NACA RM L58A02

NACA

# RESEARCH MEMORANDUM

## TWO-DIMENSIONAL CASCADE INVESTIGATION AT MACH NUMBERS UP TO 1.0 OF NACA 65-SERIES BLADE SECTIONS AT CONDITIONS TYPICAL OF COMPRESSOR TIPS

By James C. Dunavant and James C. Emery

Langley Aeronautical Laboratory
Langley Field, Va.

NATIONAL ADVISORY COMMITTEE FOR AERONAUTICS

WASHINGTON
March 17, 1958
Declassified December 1, 1959

NATIONAL ADVISORY COMMITTEE FOR AERONAUTICS

RESEARCH MEMORANDUM

# TWO-DIMENSIONAL CASCADE INVESTIGATION AT MACH NUMBERS UP TO 1.0 OF NACA 65-SERIES BLADE SECTIONS AT CONDITIONS TYPICAL OF COMPRESSOR TIPS

By James C. Dunavant and James C. Emery

## SUMMARY

A two-dimensional high-speed cascade investigation was made of thin low-cambered NACA 65-series blade shapes at operating conditions typical of compressor tip sections. Tests were made with porous walls being used and were repeated with solid walls; during the solid-wall tests, schlieren photographs were made. When losses were low, turning angles did not change significantly below an entering Mach number of 0.8. The low-speed design angle of attack fell within the low-loss region for Mach numbers below 0.85. At higher Mach numbers, the minimum loss was obtained at higher angles of attack. The angle-of-attack range for minimum losses was found to be very small at high Mach numbers.

## INTRODUCTION

The design of blade rows required to produce prescribed three-dimensional, compressible, viscous flow in axial-flow compressors is a problem for which complete theoretical solutions are not yet available. Hence, the designer will probably rely largely on experimental data - blade tests either in cascade or single-stage rotor - for the necessary information. The effects of varying blade parameters such as camber, inlet angle, solidity, and angle of attack have been studied at low speeds in systematic, two-dimensional cascade tests. (For example, see ref. 1.) Compilation of the results of tests of this type (as, for example, in ref. 2) provides a simple, quick, and accurate method of blade design where Mach number effects do not void the relatively inexpensive low-speed test results.

Inherently, limits of weight flow and pressure ratio on compressor performance are almost directly dependent upon limiting blade

relative Mach numbers. Thus, Mach number effects and limitations are of major importance in applying cascade data to the design of blade rows as well as to the design of new and improved blade sections.

Previous tests in the 7-inch high-speed cascade tunnel at the Langley Laboratory have been designed partially to extend to higher speeds some of the systematic low-speed cascade data of reference 1. For example, in reference 3 a comparison was made of the NACA 65-$\left(12A_{10}\right)$10 blade section of reference 1 with the NACA 65-$\left(12A_2I_{8b}\right)$10 blade section designed for high speed, and in reference 4 test results were reported of the NACA 65-$\left(C_{l_o}A_{10}\right)$10 blade section (designated NACA 65-$\left(C_{l_o}\right)$10 blade section in ref. 1) at typical compressor blade root conditions. These previous tests indicated that low-speed test results could be used for the design of high-speed compressor blades if the critical speed of the blades was not exceeded (refs. 3 and 4). However, the design angle of attack determined from low-speed tests was found to be lower than the optimum angle of attack for high Mach numbers.

For this report, blade sections at conditions typical of compressor rotor tip sections were tested in the 7-inch high-speed cascade tunnel at Mach numbers as high as 1.0. Typical compressor blade tip sections are thin and low cambered. The solidity is low and the inlet-flow angles high. Differences in blade configuration, particularly with regard to the ratio of throat area to upstream area, between typical root configurations (ref. 4) and typical tip configurations reported herein were expected to cause considerable difference in high-speed performance trends.

In this investigation, extensive use was made of schlieren techniques to give a qualitative picture of the flow. It is believed that a fundamental understanding of the nature of shock boundary-layer interaction is necessary to the understanding of cascade-blade capabilities and the limitations necessary in applying low-speed cascade data in the design of high-speed compressors. Hence, most of the two-dimensional porous-wall tests of the typical tip sections were repeated for the same angle-of-attack range with solid walls being used and for these solid-wall tests schlieren photographs were taken and are presented herein.

## SYMBOLS

| | |
|---|---|
| $c$ | blade chord |
| $C_{l_o}$ | camber, expressed as design lift coefficient of isolated airfoil |

$C_w$ momentum-loss coefficient

$F_c$ ratio of wake momentum loss to integrated total-pressure loss in wake

M Mach number

p static pressure

P total pressure

q dynamic pressure, $\frac{1}{2}\rho V^2$

s tangential spacing between blades

S pressure coefficient, $\frac{P_1 - p_l}{q_1}$

t blade thickness

V velocity

w wake width

$\alpha$ angle of attack, angle between entering flow direction and chord

$\beta$ air angle measured from perpendicular to blade row

$\delta$ wake blockage

$\theta$ turning angle

$\rho$ density

$\sigma$ solidity, chord-spacing ratio, c/s

Subscripts:

1 upstream of blade row, undisturbed stream

2 downstream of blade row

d low-speed design (from ref. 1)

$l$ local, as on blade surface

## APPARATUS AND METHODS

### Apparatus

The blades were tested in the 7-inch high-speed cascade tunnel at the Langley Laboratory. (See fig. 1.) The tunnel is designed to produce two-dimensional flow through the cascade; that is, no spanwise convergence or divergence of the stream tubes. For this purpose, protruding boundary-layer removal slots are contained in the four walls ahead of the blade row, and the blade-passage end walls were of a porous material permitting flow removal to maintain the two-dimensionality. The tunnel is capable of producing entering Mach numbers from low speed to 1.0 for most blade configurations. In several tests of very low solidity and low inlet-flow angles, the main air supply was of insufficient quantity to reach the required Mach number. These tests will be noted in the section entitled "Discussion of Results."

The blade models were of 7-inch span. The 10-percent-thick NACA $65\text{-}\left(8A_{10}\right)10$ blade section had a 3.5-inch chord and the 6-percent-thick NACA $65\text{-}\left(4A_{10}\right)06$ and $65\text{-}\left(8A_{10}\right)06$ blade sections had 2.8-inch chords. (The part of the designation of these blade sections within parentheses follows a system used explicitly for compressor and turbine profiles. In this system the number within parentheses represents the design lift coefficient $C_{l_o}$ in tenths. The letter A is identified with the mean line $a = 1.0$, and the subscript indicates the fraction (in tenths) of the lift coefficient associated with the particular mean line. (See ref. 5.) Seven blades were used in most of the cascade tests; however, in some of the lower solidity tests, as few as five blades were used so as to obtain the required Mach number. At all times, flexible wall fairings were used at the top and bottom to simulate an infinite series of blades.

Schlieren photographs were taken during the solid-wall rather than the porous-wall tests. Only two or three blades in the center of the blade passage were visible. The entire apparatus is described more completely in reference 3.

### Test Procedure

In making these tests, the same test procedure and instrumentation were used as in reference 3. Briefly, two-dimensional flow was established by controlling the amount of flow removed through the porous side walls. Thus, velocity and pressure changes across the cascade were made to conform to values calculated from turning angle, Mach number,

and wake measurements. With the two-dimensional flow conditions established, the blade-surface static pressures, upstream and downstream flow angles and pressures, and total pressure in the wake were recorded.

The tests were run at two-dimensional conditions wherever possible. Usually, as the blade passage chokes or the blade losses become very high, two-dimensional flow could not be achieved. Blade turning angles change as the pressure rise across the cascade is varied from two-dimensional, and usually increase as the pressure rise decreases. In order to indicate the magnitude of this change, two test points approximately at critical speed, one having pressure rise greater and one less than two-dimensional, were recorded in most tests. Arbitrarily, all test points not having a minimum of 90 percent of the two-dimensional pressure rise are not considered to be two-dimensional and the turning-angle test-point symbols are flagged for such cases.

The procedure used during the schlieren tests was different in that no control over the two-dimensionality of the tests was possible with the solid side walls. The usual test quantities were recorded at whatever pressure and velocity change were obtained for the test. In spite of the absence of porous walls, the values of pressure rise across the blade rows for the solid end walls approximate those for the porous walls.

## Reduction of Data

A momentum-loss coefficient was calculated from the measured total-pressure loss by a method like that of reference 6 for calculating drag. Momentum loss is calculated from downstream conditions and is expressed in coefficient form based upon the dynamic pressure upstream of the cascade. Hence,

$$C_{w_1} = F_c \int_0^w \frac{P_1 - P_2}{q_1 c} \, dw$$

where $F_c$ (determined from a method like that of ref. 6) is the ratio of the momentum-loss coefficient to the total-pressure-loss coefficient for an assumed wake shape as a function of the maximum total-pressure loss and Mach number.

A calculated check of the two-dimensionality of the flow was made for all the porous-wall tests. Arbitrarily, tests are considered to

be two-dimensional if the test pressure rise $\frac{P_2 - P_1}{q_1}$ is greater than 90 percent of the ideal pressure rise calculated from entering Mach number, inlet-air angle, turning angle, and wake blockage of the particular test. The wake blockages for a number of tests were calculated and plotted against the integrated total-pressure loss and the following relationship for the wake blockage $\delta$ was indicated:

$$\frac{\delta}{c} = 0.51 \int_0^w \frac{P_1 - P_2}{q_2 c} dw$$

The ideal pressure rise was obtained for this displacement thickness with the use of isentropic relationships. The test pressure rise was compared with this calculated ideal pressure rise to determine whether the tests were to be considered two-dimensional.

## BLADE TESTS AND PRESENTATION OF RESULTS

### Blade Tests

Previous cascade blade tests in the 7-inch high-speed cascade tunnel (refs. 3 and 4) and low-speed cascade tests (ref. 1) have been made at a constant inlet-air angle $\beta_1$. Blade angle-of-attack variation was made relative to the flow and the stagger line. In the present tests, the blades were fixed relative to the stagger line (fig. 1) and angle-of-attack variation was obtained by rotation of the blade assembly. Thus, both inlet-flow angle and angle of attack relative to the blades are changed; however, $\beta - \alpha$ is a constant value for each range of angle of attack of the test. This condition corresponds to blade operation in a rotor under varying throttle conditions. The range of angle of attack was determined by the increase in losses at high and low angles of attack.

Blades tested were limited to configurations typical of compressor blade tip sections designed for high subsonic entering Mach numbers. The majority of the tests were of the NACA 65-$\left(4A_{10}\right)$06 and 65-$\left(8A_{10}\right)$06 blade sections, which are typical of present high-speed and some transonic tip blade sections. The NACA 65-$\left(8A_{10}\right)$10 blade section used in some of the configurations is presently considered excessively thick. Blade sections were set approximately at low-speed design angle of attack at $\beta_1 = 47^\circ$ or $\beta_1 = 57^\circ$ and for two solidities, 0.6 and 1.0. A few tests

were made at $\sigma = 0.8$. The low-speed design angle of attack, as specified in reference 2, is the angle at which a peak-free pressure distribution is obtained on the blade surface. The angle varies with both camber and solidity but is constant for all inlet-air angles. Solid-wall schlieren tests were run for the NACA 65-$(4A_{10})$06 and 65-$(8A_{10})$06 blade sections at the 47° inlet-air-angle condition and for all the NACA 65-$(8A_{10})$10 configurations.

Reynolds numbers based on the chord were between 500,000 and 1,700,000, which is well above the ordinary range of critical Reynolds numbers at which high losses and decreases in turning angle occur in cascade.

## Presentation of Results

Performance of the blade sections in the porous-wall test, for each angle of attack is given in figures 2 to 62. Test conditions and corresponding figure numbers are listed in table I. These figures are composed of four pressure distributions, parts (a) to (d), measured at four representative entering Mach numbers. On each pressure distribution, the peak blade-surface Mach number (assuming no total-pressure loss) is given and the downstream static pressure is indicated by the horizontal line at the 100-percent-chord station. Part (e) of each figure presents the variation of turning angle, momentum-loss coefficient, and pressure rise with Mach number. Turning angles measured in tests not having two-dimensional pressure rises are shown in these figures by flagged test points.

Schlieren photographs are shown in figures 63 to 104. Four or five representative schlieren photographs were selected from each blade test configuration and are presented in the first parts of each of these figures. The last part of each of these figures gives the variation of momentum-loss coefficient, turning angle, and pressure rise with entering Mach number measured during the test.

The variation of turning angle and momentum-loss coefficient with angle of attack is shown in figures 105 to 116 and figures 117 to 128, respectively. The variation is plotted for eight constant Mach numbers. It must be noted that inlet-air angle is not constant in these figures, but varies as angle of attack changes; however, $\beta_1 - \alpha$ is constant.

## DISCUSSION OF RESULTS

### Variation of Turning Angle With Mach Number

Turning angles for the typical tip sections operating in the low-loss angle-of-attack regions did not change significantly with Mach number for speeds below about $M_1 = 0.8$ (figs. 105 to 116). This result is the same as previously reported for speeds below critical in other tests of the NACA 65-series blade sections (ref. 4). At Mach numbers of 0.8 and above, turning angles decreased with Mach number. Shocks that formed on blade sections increased in strength with entering Mach number and decreased the turning angle. Turning angles remained quite high at Mach numbers for which the losses indicated considerable separation to be present.

### Variation of Turning Angle With Angle of Attack

The variation of turning angle with angle of attack as presented in this report is different from the usual presentation of the variation as found in references 1, 3, and 4. The manner in which the tests were run, at constant $\beta - \alpha$, is similar to blade section operation in a rotor. In this system as the angle of attack increases, the inlet-flow angle increases. The slopes of the curves of $\theta$ plotted against $\alpha$ presented herein are, as expected, less than 1.0. In general, the rate of change of $\theta$ with $\alpha$ is independent of Mach number. An exception is to be noted in figure 114 where the turning angle increased with Mach number near design angle of attack.

### Momentum Loss

At low speeds, the losses are a result of viscous losses from the upper and lower surfaces of the blade. These losses are small unless the flow separates due to large pressure rises along the blade surface. Typical blade configurations have losses which increase rapidly at an angle of attack where a blade surface has a very high peak velocity, and hence low pressure. The peak velocity occurs on the lower surface at low angles of attack and on the upper surface at high angles of attack. Inasmuch as compressibility effects accentuate these peaks, it would be expected that high-speed separation would occur at angles of attack nearer the design value than at low speeds and would thus have the net effect of a decrease in the low-loss angle-of-attack range. Reduction of useful range is attributed largely to this reason since all passage areas at and above design angle of attack were greater than upstream areas and choking was not expected at these low-solidity,

high-inlet-angle conditions. At the highest Mach numbers, the useful range of angle of attack may be less than 5° as in figures 120 and 121. Blade-surface pressure rises were also caused by shocks at the higher speeds. The difference of the effects of the steeper pressure rise through the shock and of the more gradual rise subsonically on the boundary layer and associated losses is not fully understood. When the shock is located near the leading edge, the boundary layer is thin and higher Mach numbers may be tolerated without excessive losses. On the other hand, location of the peak Mach number near the trailing edge with the usually thick boundary layer is more likely to incur high losses. The development of the NACA 65-$\left(C_{l_o} A_2 I_{8b}\right)$10 blade series was made on the premise of having a higher critical speed by locating the surface pressure rise near the trailing edge. Comparison of this blade section with the NACA 65-$\left(C_{l_o} A_{10}\right)$10 blade which generally has the minimum pressure near the leading edge showed no advantage in the use of the unique shape of the NACA 65-$\left(C_{l_o} A_2 I_{8b}\right)$10 blade (ref. 3).

Some part of the losses measured is attributed to shock losses and not associated with the boundary layer. This was readily shown by the shapes of the wake total-pressure distributions recorded. Viscous and shock boundary-layer losses are grouped in a narrow but high-loss region just behind the blade, whereas shock losses are distributed over the entire passage width. No attempt has been made to isolate or differentiate between these two losses inasmuch as no significant or measurable shock loss occurred until after shock boundary-layer interaction had caused high viscous and shock boundary-layer losses. Such may not be the case for other blade sections.

Variation of the momentum-loss coefficient at several Mach numbers is shown in figures 117 to 128 and, owing to the decrease in angle-of-attack range already discussed, the variation provides a basis for estimating the mimimum-loss angle of attack at high speeds. Selection of the minimum-loss angle of attack in figures 117 to 128 is aided by the dashed lines between some angles of attack. In order to obtain the dashed lines, trends of increasing losses with Mach number were assumed to continue beyond the highest test Mach number. For the tip section blade tests, the low-speed design angle of attack fell within the low-loss region for Mach numbers below 0.85. At $M_1 = 0.9$, several of the blade sections showed minimum loss to occur at angles of attack greater than low-speed design. At $M_1 = 0.95$, an even greater shift in the low-loss range is shown. Test results of references 3 and 4 have shown that at high speeds the minimum-loss angle of attack is greater than the low-speed design angle. At low inlet-flow angles, the difference in angles at critical speed (where sonic velocity first occurs on blade surface) was approximately 6°. This difference was less at higher

inlet-flow angles and appeared to decrease to 0° at inlet-flow angles of about 65°. These previous tests were made with blades having a value of $t/c = 0.10$ and many of the blade passages were choked, particularly at the lower inlet-flow angles. Increasing the angle of attack opened the blade passages permitting higher entering Mach numbers. This was the primary reason for the shift in the optimum angle of attack at low inlet-flow angle. Tests of the NACA 65-$\left(12A_{10}\right)$10 blade section at open passage conditions (no passage throat) also showed an increase in the optimum angle of attack at high speeds and this was believed to be a result of several contributing factors. (See ref. 3.) The blades used in the present tests are of lower camber and thickness, hence, they would have reduced interference and induced effects which would decrease the shift in the low-loss angle-of-attack range. In general, the shift in low-loss angle-of-attack range was found to be less than would have been predicted from the results of references 3 and 4 and apparently is more a function of Mach number than of inlet-flow angle.

## Schlieren Photographs

A schlieren system was used to examine qualitatively the high-speed flow. In order to take the schlieren photographs, the porous side walls to the tunnel were necessarily removed and replaced with solid (nonporous) walls containing glass windows. Hence, the flow during schlieren tests is different from that during porous-wall tests. Turning angle, wakes, and pressure rise were recorded as the schlieren photographs were made and the data may be compared with the porous-wall test results. As would be expected, the pressure rise across the blade row in the solid-wall schlieren tests is less than that of the porous-wall test. As a result of this, the turning angle is usually a degree or so higher and the wake losses are lower. Differences are particularly noticeable at critical angles of attack where the lower pressure rise during the schlieren test extends the angle-of-attack range. In spite of these very significant differences in the solid and porous-wall test results, the gross effects of compressibility and shock waves seen in the photographs of the solid-wall tests should depict the flow conditions of the porous-wall tests. As an indication that this is true, positions of shock waves in photographs agree quite closely with static-pressure rises obtained in blade-surface pressure-distribution measurements made during porous-wall tests. (Compare schlieren photograph of figure 77 (parts (b) and (c)) with pressure distribution of figure 17 (parts (c) and (d)); also compare figure 94(d) with figure 54(d).)

The schlieren photographs give an excellent picture of the flow variation at high speeds over a range of angles of attack. At low angles of attack, low inlet-flow angles, and high solidities, the blade passage throat is nearly equal to the upstream

flow area. As for typical blade root sections (ref. 4), shocks form in the passage at relatively low upstream Mach numbers. At the low angle of attack, as the Mach number is increased, a normal shock first forms on the lower surface just behind the leading edge with the oblique foot of the shock extending to the leading edge, as shown in figure 100. Increasing the Mach number, when possible, or decreasing the pressure behind the blade row increases the shock strength, moves it downstream, and extends it to the upper surface of the blade below. In figure 73 at $M_1 = 0.702$, only a small region of shock is visible; yet, at $M_1 = 0.750$, a normal shock extends across the passage and no significant increase in upstream Mach number is possible. Passage shocks form quite abruptly and to this factor is attributed the abrupt rise in losses at low angles of attack. At this point the passage is choked, and further decreasing the back pressure would only move the shock downstream and increase the shock strength, and hence the separation.

Increases in the angle of attack and inlet angle increase the ratio of the throat area to the upstream area; thus, higher upstream Mach numbers are permitted before choking. While the passage shock may still exist, the flow over the upper surface, particularly for higher blade cambers, may become supersonic over the forward portion. As this supersonic flow region becomes extensive, shocks on the upper surface of the blade extend to form a bow wave ahead of the blade above. A quite similar condition to the bow wave and passage shock configuration which may also occur at higher angles of attack is that for which the bow wave may produce large separation on the upper surface of the blade below. Between the large separated region and the lower surface of the blade, a throat exists and the passage shock may stand between the lower surface and separated region. (See fig. 92.) With this type of flow, two peak velocities on the upper surface of a pressure distribution would be expected; however, the large amount of separation probably prevented this from being seen in any of the pressure distributions.

The high angle-of-attack condition is the usual operating condition for tip blade sections. The entering flow may be well below sonic and the induced effects of a blade upper surface may cause a supersonic field ahead of the blade above. This flow is decelerated through a normal shock or bow wave standing ahead of the leading edge of the blade above. The shock extends from the upper surface where frequently the flow is separated (fig. 87). The pressure rise across the blade row is accomplished by the shock and a subsonic diffusion behind the shock. Thus, the intersection of this shock with the blade-surface boundary layer will largely determine blade viscous losses and be of major importance. The possibility exists of shaping the upper surface of the blade in the region where the foot of the shock stands so as to decrease the Mach number and keep the pressure rise across the shock low to prevent

separation. Variations in blade-surface boundary layer might also be studied with the idea of increasing the allowable pressure rise without separation.

## CONCLUDING REMARKS

Two-dimensional high-speed cascade tests were made of thin low-camber NACA 65-series blade shapes at operating conditions typical of compressor tip sections. From these tests and comparison with previously reported tests, the following results are summarized:

1. Turning angles for typical tip sections operating in the low-loss angle-of-attack regions did not change significantly with Mach number below an entering Mach number of approximately 0.8. Higher Mach numbers caused the turning angle to decrease.

2. The low-speed design angle of attack selected to have a peak-free pressure distribution fell within the low-loss region for Mach numbers below 0.85. At higher Mach numbers, the low-loss region occurred at angles of attack greater than low-speed design. A greater shift in the low-loss region would have been predicted from previous high-speed test results.

3. The angle-of-attack range for minimum losses was found to be very small at high Mach numbers, frequently being less than $5^{\circ}$.

Langley Aeronautical Laboratory,
National Advisory Committee for Aeronautics,
Langley Field, Va., December 12, 1957.

## REFERENCES

1. Herrig, L. Joseph, Emery, James C., and Erwin, John R.: Systematic Two-Dimensional Cascade Tests of NACA 65-Series Compressor Blades At Low Speeds. NACA TN 3916, 1957. (Supersedes NACA RM L51G31.)

2. Felix, A. Richard: Summary of 65-Series Compressor-Blade Low-Speed Cascade Data by Use of the Carpet-Plotting Technique. NACA TN 3913, 1957. (Supersedes NACA RM L54H18a.)

3. Dunavant, James C., Emery, James C., Walch, Howard C., and Westphal, Willard R.: High-Speed Cascade Tests of the NACA 65-$\left(12A_{10}\right)10$ and NACA 65-$\left(12A_2I_{8b}\right)10$ Compressor Blade Sections. NACA RM L55I08, 1955.

4. Emery, James C., and Dunavant, James C.: Two-Dimensional Cascade Tests of NACA 65-$\left(C_{l_o}A_{10}\right)10$ Blade Sections at Typical Compressor Hub Conditions for Speeds up to Choking. NACA RM L57H05, 1957.

5. Erwin, John R., and Yacobi, Laura A.: Method of Estimating the Incompressible-Flow Pressure Distribution of Compressor Blade Sections at Design Angle of Attack. NACA RM L53F17, 1953.

6. Heaslet, Max. A.: Theoretical Investigation of Methods for Computing Drag From Wake Surveys at High Subsonic Speeds. NACA WR W-1, 1945. (Formerly NACA ARR 5C21.)

TABLE I.- CASCADE CONFIGURATIONS TESTED

(a) Porous-wall tests

| NACA blade section | Figure | Angle of attack, $\alpha$, deg | Inlet-air angle, $\beta_1$, deg | Solidity, $\sigma$ | $\beta_1 - \alpha$, deg | $\alpha_d$, deg |
|---|---|---|---|---|---|---|
| 65-$(4A_{10})$06 | 2 | 1.7 | 44.0 | 0.6 | 42.3 | 4.6 |
| | 3 | 4.7 | 47.0 | | | |
| | 4 | 7.7 | 50.0 | | | |
| | 5 | 10.7 | 53.0 | | | |
| | 6 | 13.7 | 56.0 | | | |
| | 7 | 1.0 | 41.0 | 0.8 | 40.0 | 5.6 |
| | 8 | 4.0 | 44.0 | | | |
| | 9 | 7.0 | 47.0 | | | |
| | 10 | 10.0 | 50.0 | | | |
| | 11 | 13.0 | 53.0 | | | |
| | 12 | 16.0 | 56.0 | | | |
| | 13 | 0.4 | 41.0 | 1.0 | 40.6 | 6.5 |
| | 14 | 3.4 | 44.0 | | | |
| | 15 | 6.4 | 47.0 | | | |
| | 16 | 9.4 | 50.0 | | | |
| | 17 | 12.4 | 53.0 | | | |
| | 18 | 15.4 | 56.0 | | | |
| | 19 | 1.5 | 54.0 | 0.6 | 52.5 | 4.6 |
| | 20 | 4.5 | 57.0 | | | |
| | 21 | 7.5 | 60.0 | | | |
| | 22 | 10.5 | 63.0 | | | |
| | 23 | 0.5 | 51.0 | 1.0 | 50.5 | 6.5 |
| | 24 | 3.5 | 54.0 | | | |
| | 25 | 6.5 | 57.0 | | | |
| | 26 | 9.5 | 60.0 | | | |
| | 27 | 12.5 | 63.0 | | | |
| 65-$(8A_{10})$06 | 28 | 1.0 | 41.0 | 0.6 | 40.0 | 6.9 |
| | 29 | 4.0 | 44.0 | | | |
| | 30 | 7.0 | 47.0 | | | |
| | 31 | 10.0 | 50.0 | | | |
| | 32 | 13.0 | 53.0 | | | |
| | 33 | 16.0 | 56.0 | | | |
| | 34 | 3.2 | 41.0 | 0.8 | 37.8 | 8.3 |
| | 35 | 6.2 | 44.0 | | | |
| | 36 | 9.2 | 47.0 | | | |
| | 37 | 12.2 | 50.0 | | | |
| | 38 | 15.2 | 53.0 | | | |
| | 39 | 3.5 | 41.0 | 1.0 | 37.5 | 9.4 |
| | 40 | 6.5 | 44.0 | | | |
| | 41 | 9.5 | 47.0 | | | |
| | 42 | 12.5 | 50.0 | | | |
| | 43 | 15.5 | 53.0 | | | |
| | 44 | 1.0 | 51.0 | 0.6 | 50.0 | 6.9 |
| | 45 | 4.0 | 54.0 | | | |
| | 46 | 7.0 | 57.0 | | | |
| | 47 | 10.0 | 60.0 | | | |
| | 48 | 13.0 | 63.0 | | | |
| | 49 | 3.5 | 51.0 | 1.0 | 47.5 | 9.4 |
| | 50 | 6.5 | 54.0 | | | |
| | 51 | 9.5 | 57.0 | | | |
| | 52 | 12.5 | 60.0 | | | |
| | 53 | 15.5 | 63.0 | | | |
| 65-$(8A_{10})$10 | 54 | 5.2 | 47.0 | 1.0 | 41.8 | 9.4 |
| | 55 | 8.2 | 50.0 | | | |
| | 56 | 11.2 | 53.0 | | | |
| | 57 | 14.2 | 56.0 | | | |
| | 58 | 17.2 | 59.0 | | | |
| | 59 | 5.2 | 54.0 | 1.0 | 48.8 | 9.4 |
| | 60 | 8.2 | 57.0 | | | |
| | 61 | 11.2 | 60.0 | | | |
| | 62 | 14.2 | 63.0 | | | |

TABLE I.- CASCADE CONFIGURATIONS TESTED - Concluded

(b) Schlieren tests

| NACA blade section | Figure | Angle of attack, $\alpha$, deg | Inlet-air angle, $\beta_1$, deg | Solidity, $\sigma$ | $\beta_1 - \alpha$, deg | $\alpha_d$, deg |
|---|---|---|---|---|---|---|
| $65-(4A_{10})06$ | 63 | -1.1 | 41.0 | 0.6 | 42.1 | 4.6 |
| | 64 | 1.9 | 44.0 | | | |
| | 65 | 4.9 | 47.0 | | | |
| | 66 | 7.9 | 50.0 | | | |
| | 67 | 10.9 | 53.0 | | | |
| | 68 | -0.2 | 41.0 | 0.8 | 41.2 | 5.6 |
| | 69 | 2.8 | 44.0 | | | |
| | 70 | 5.8 | 47.0 | | | |
| | 71 | 8.8 | 50.0 | | | |
| | 72 | 14.8 | 56.0 | | | |
| | 73 | 0.8 | 41.0 | 1.0 | 40.2 | 6.5 |
| | 74 | 3.8 | 44.0 | | | |
| | 75 | 6.8 | 47.0 | | | |
| | 76 | 9.8 | 50.0 | | | |
| | 77 | 12.8 | 53.0 | | | |
| | 78 | 15.8 | 56.0 | | | |
| $65-(8A_{10})06$ | 79 | 1.0 | 41.0 | 0.6 | 40.0 | 6.9 |
| | 80 | 4.0 | 44.0 | | | |
| | 81 | 7.0 | 47.0 | | | |
| | 82 | 10.0 | 50.0 | | | |
| | 83 | 13.0 | 53.0 | | | |
| | 84 | 2.0 | 41.0 | 0.8 | 39.0 | 8.3 |
| | 85 | 5.0 | 44.0 | | | |
| | 86 | 8.0 | 47.0 | | | |
| | 87 | 11.0 | 50.0 | | | |
| | 88 | 14.0 | 53.0 | | | |
| | 89 | 4.0 | 41.0 | 1.0 | 37.0 | 9.4 |
| | 90 | 7.0 | 44.0 | | | |
| | 91 | 10.0 | 47.0 | | | |
| | 92 | 13.0 | 50.0 | | | |
| | 93 | 16.0 | 53.0 | | | |
| $65-(8A_{10})10$ | 94 | 5.2 | 47.0 | 1.0 | 41.8 | 9.4 |
| | 95 | 8.2 | 50.0 | | | |
| | 96 | 11.2 | 53.0 | | | |
| | 97 | 14.2 | 56.0 | | | |
| | 98 | 17.2 | 59.0 | | | |
| | 99 | 20.2 | 62.0 | | | |
| | 100 | 5.0 | 54.0 | 1.0 | 49.0 | 9.4 |
| | 101 | 8.0 | 57.0 | | | |
| | 102 | 11.0 | 60.0 | | | |
| | 103 | 14.0 | 63.0 | | | |
| | 104 | 17.0 | 66.0 | | | |

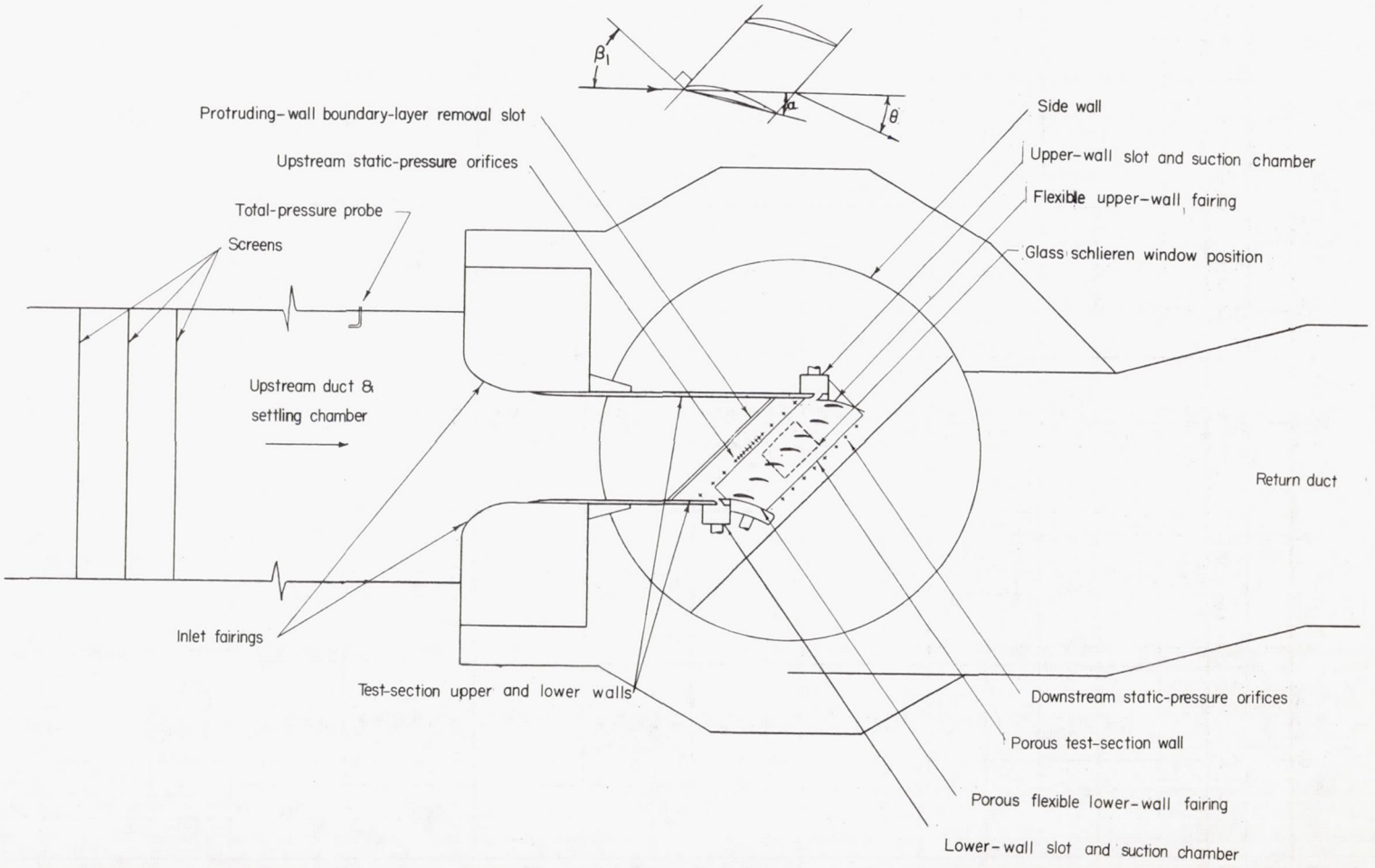



Figure 1.- Cross-sectional view of the 7-inch high-speed cascade tunnel.

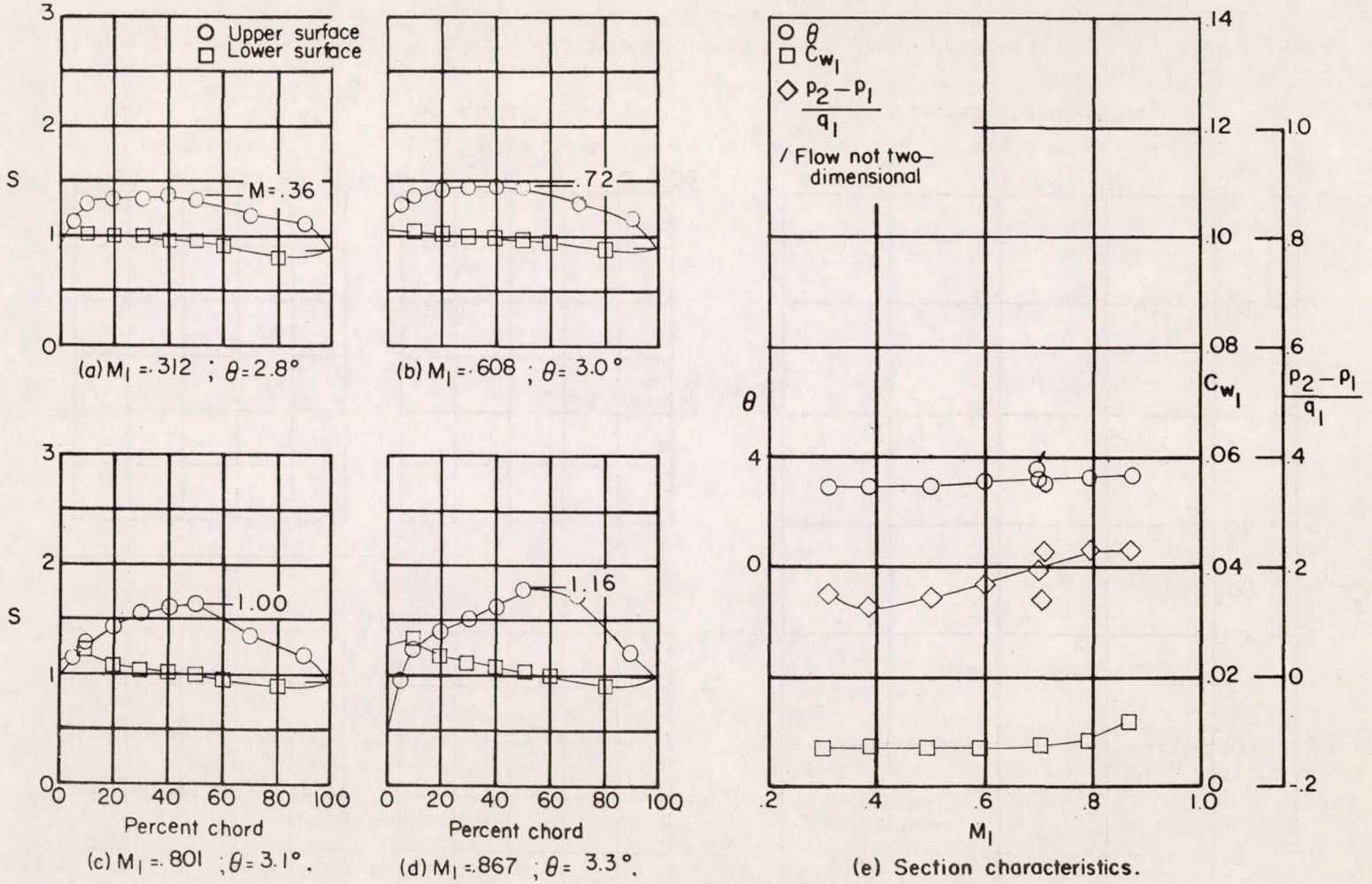



Figure 2.- Blade-surface pressure distributions and section characteristics for the cascade combination $\beta_1 = 44.0°$, $\alpha = 1.7°$, $\sigma = 0.6$, and NACA 65-$(^{4}A_{10})$06 blade section.

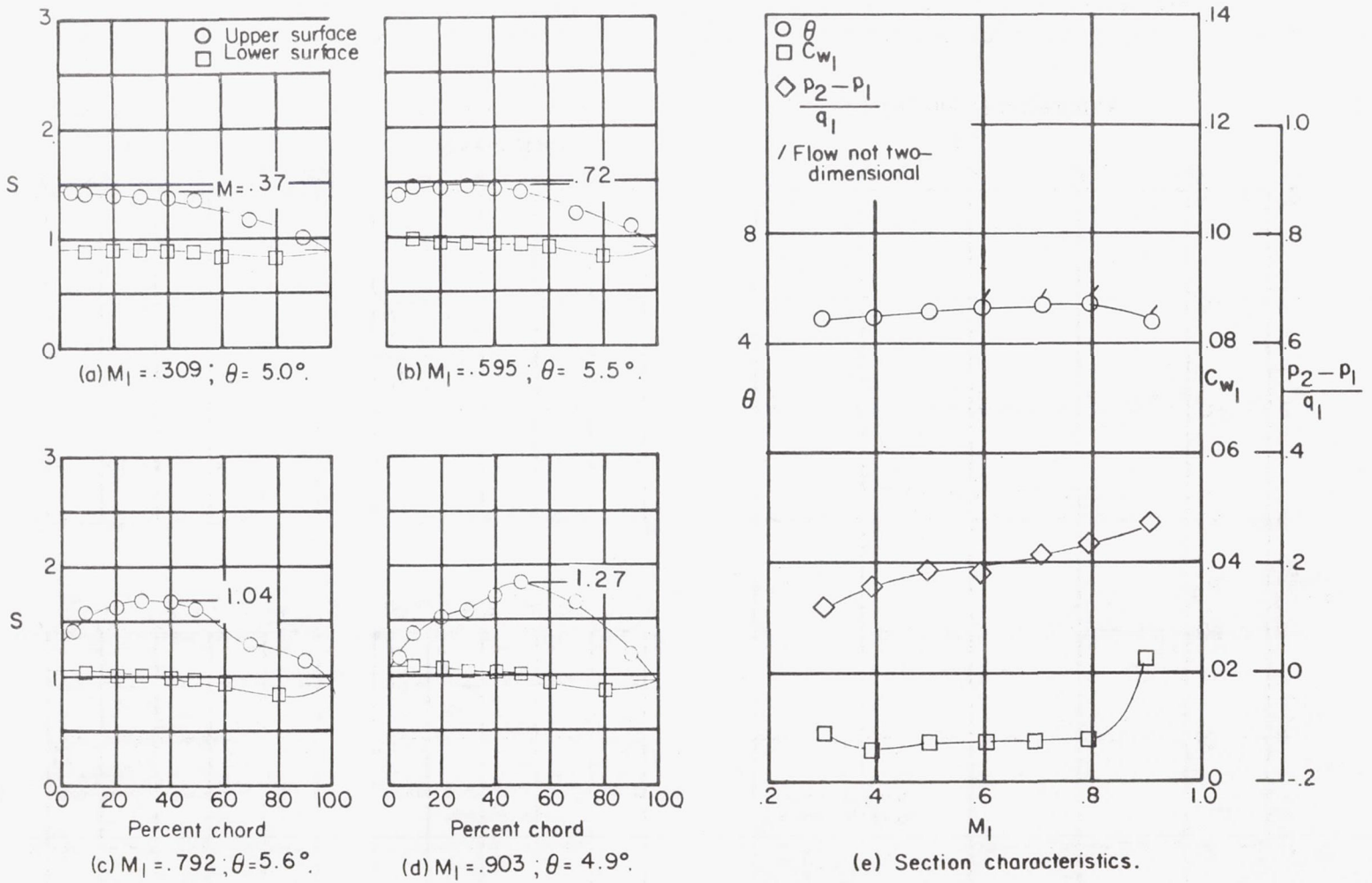



Figure 3.- Blade-surface pressure distributions and section characteristics for the cascade combination $\beta_1 = 47.0^\circ$, $\alpha = 4.7^\circ$, $\sigma = 0.6$, and NACA 65-$(4A_{10})$06 blade section.

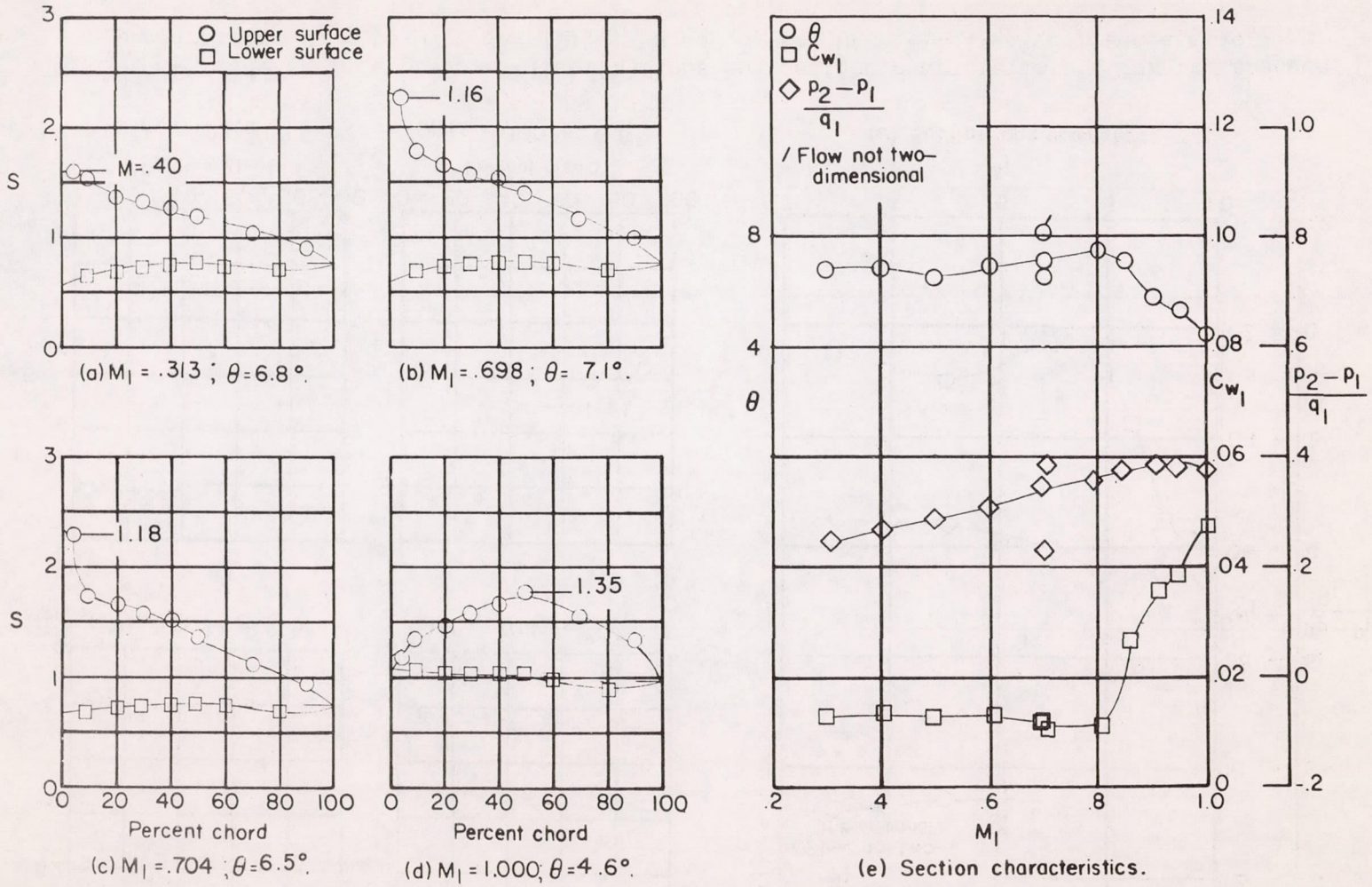



Figure 4.- Blade-surface pressure distributions and section characteristics for the cascade combination $\beta_1 = 50.0^\circ$, $\alpha = 7.7^\circ$, $\sigma = 0.6$, and NACA 65-$(4A_{10})$06 blade section.

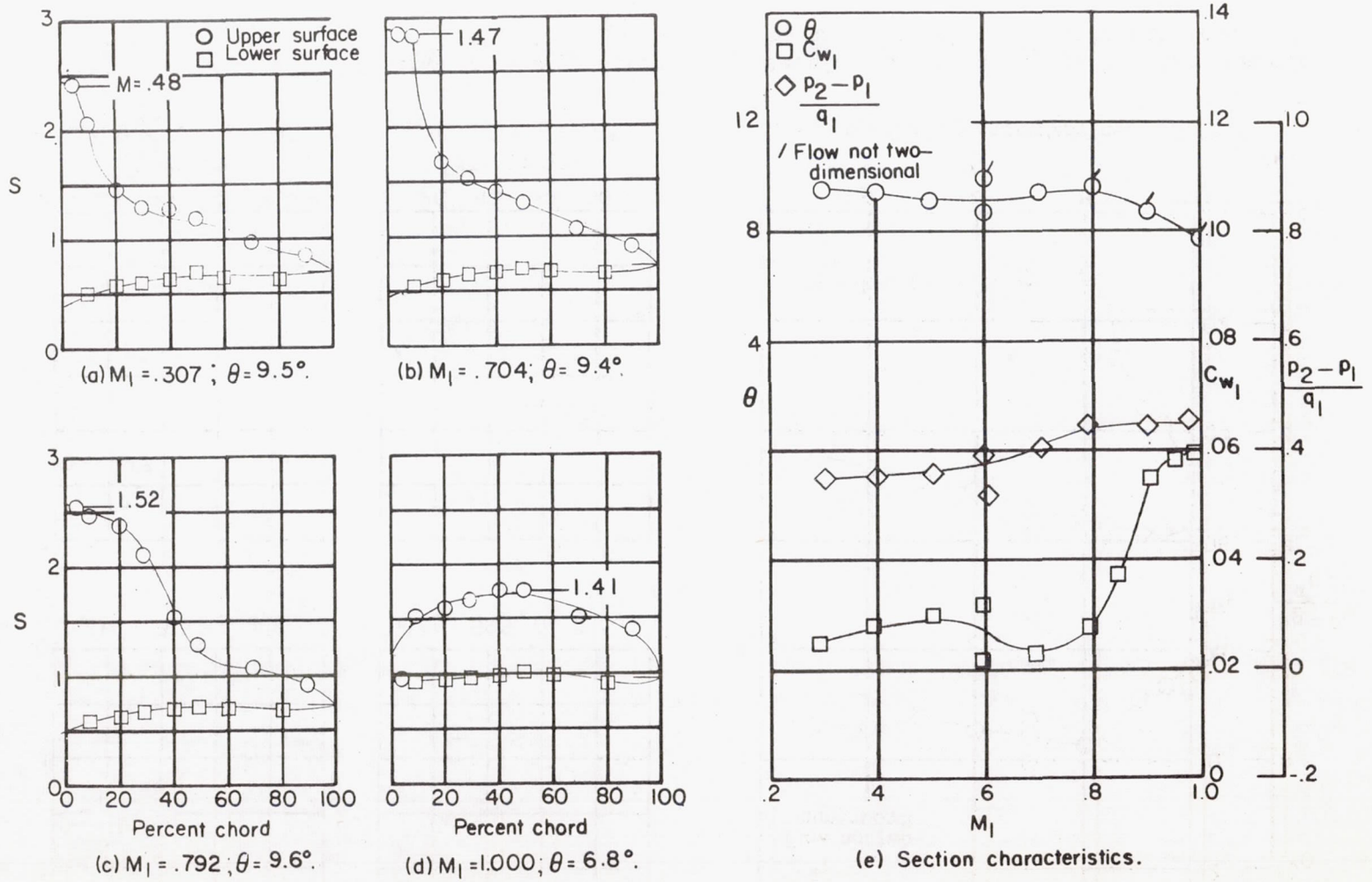



Figure 5.- Blade-surface pressure distributions and section characteristics for the cascade combination $\beta_1 = 53.0^\circ$, $\alpha = 10.7^\circ$, $\sigma = 0.6$, and NACA 65-$(4A_{10})$06 blade section.

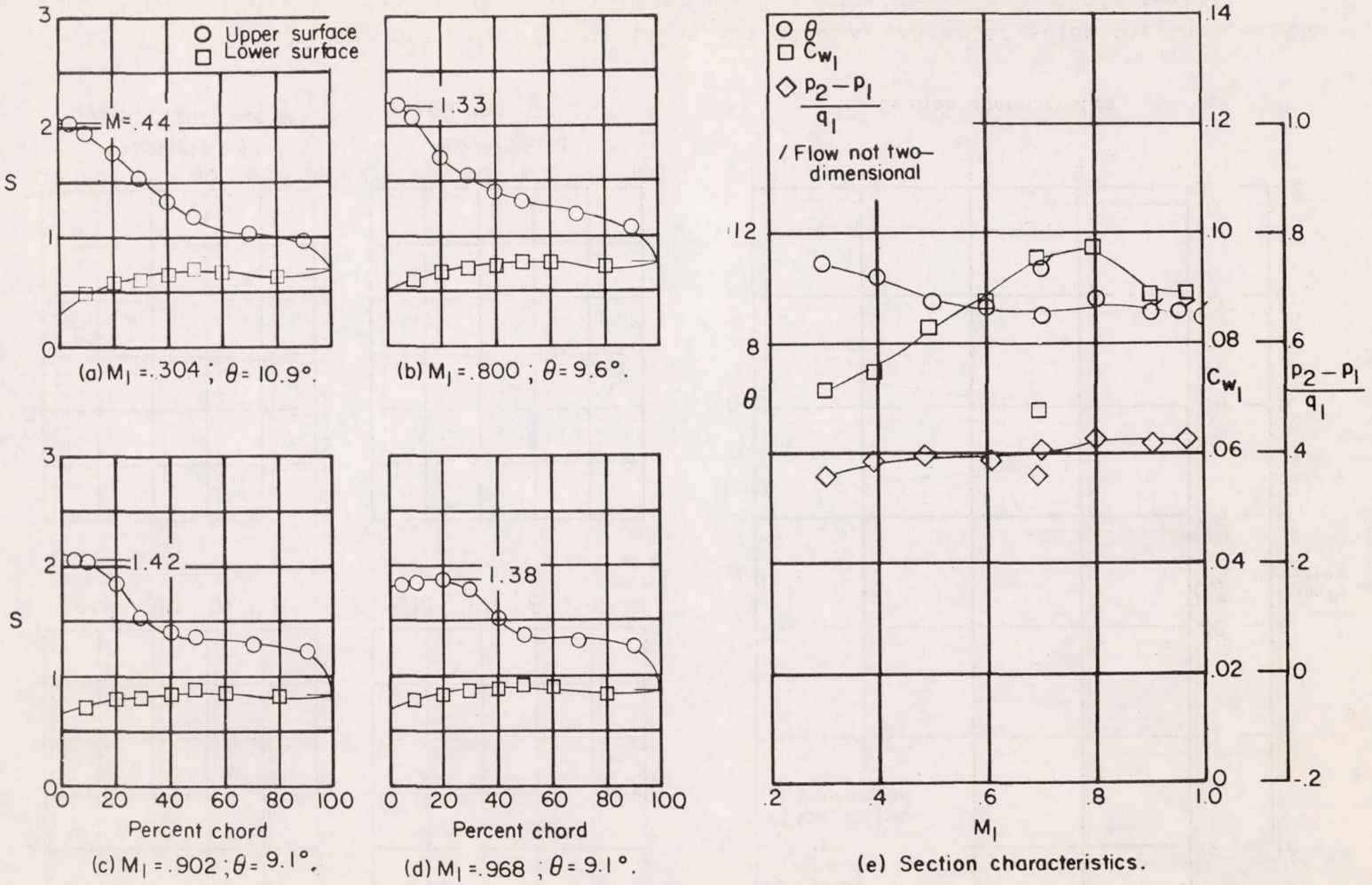



Figure 6.- Blade-surface pressure distributions and section characteristics for the cascade combination $\beta_1 = 56.0°$, $\alpha = 13.7°$, $\sigma = 0.6$, and NACA 65-$(4A_{10})$06 blade section.

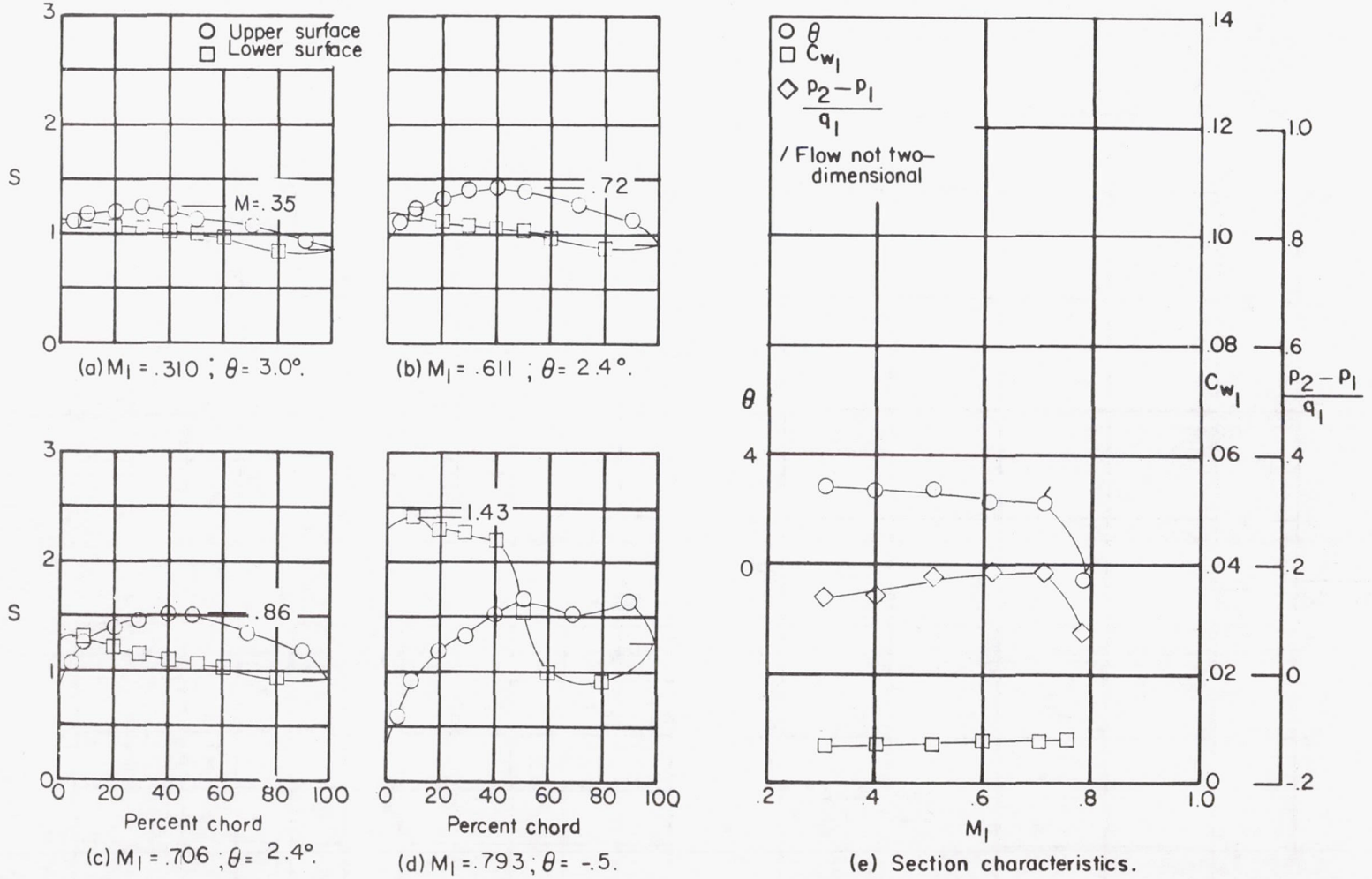



Figure 7.- Blade-surface pressure distributions and section characteristics for the cascade combination $\beta_1 = 41.0^\circ$, $\alpha = 1.0^\circ$, $\sigma = 0.8$, and NACA 65-$(4A_{10})$06 blade section.

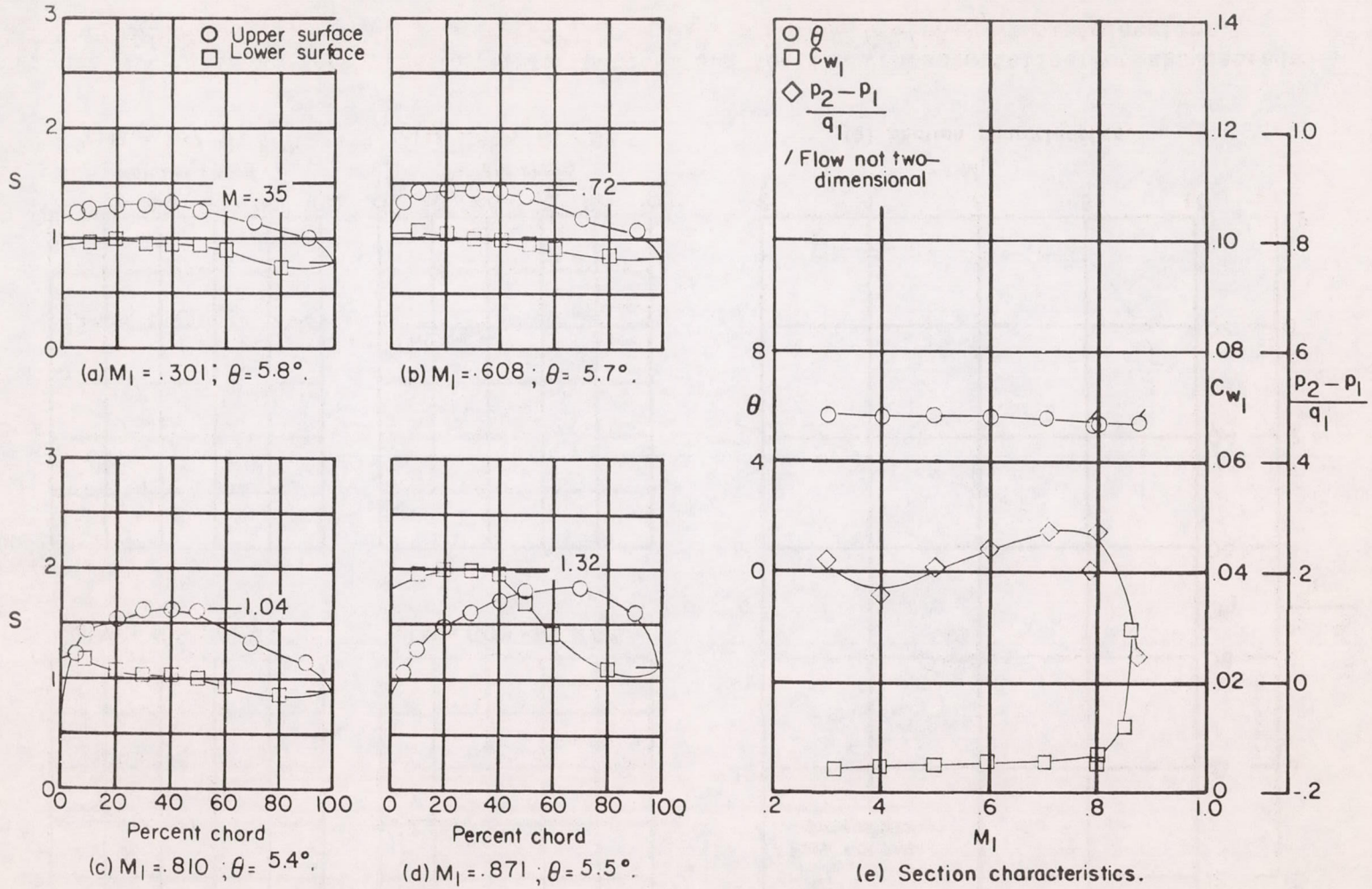



Figure 8.- Blade-surface pressure distributions and section characteristics for the cascade combination $\beta_1 = 44.0^\circ$, $\alpha = 4.0^\circ$, $\sigma = 0.8$, and NACA 65-$(4A_{10})$06 blade section.

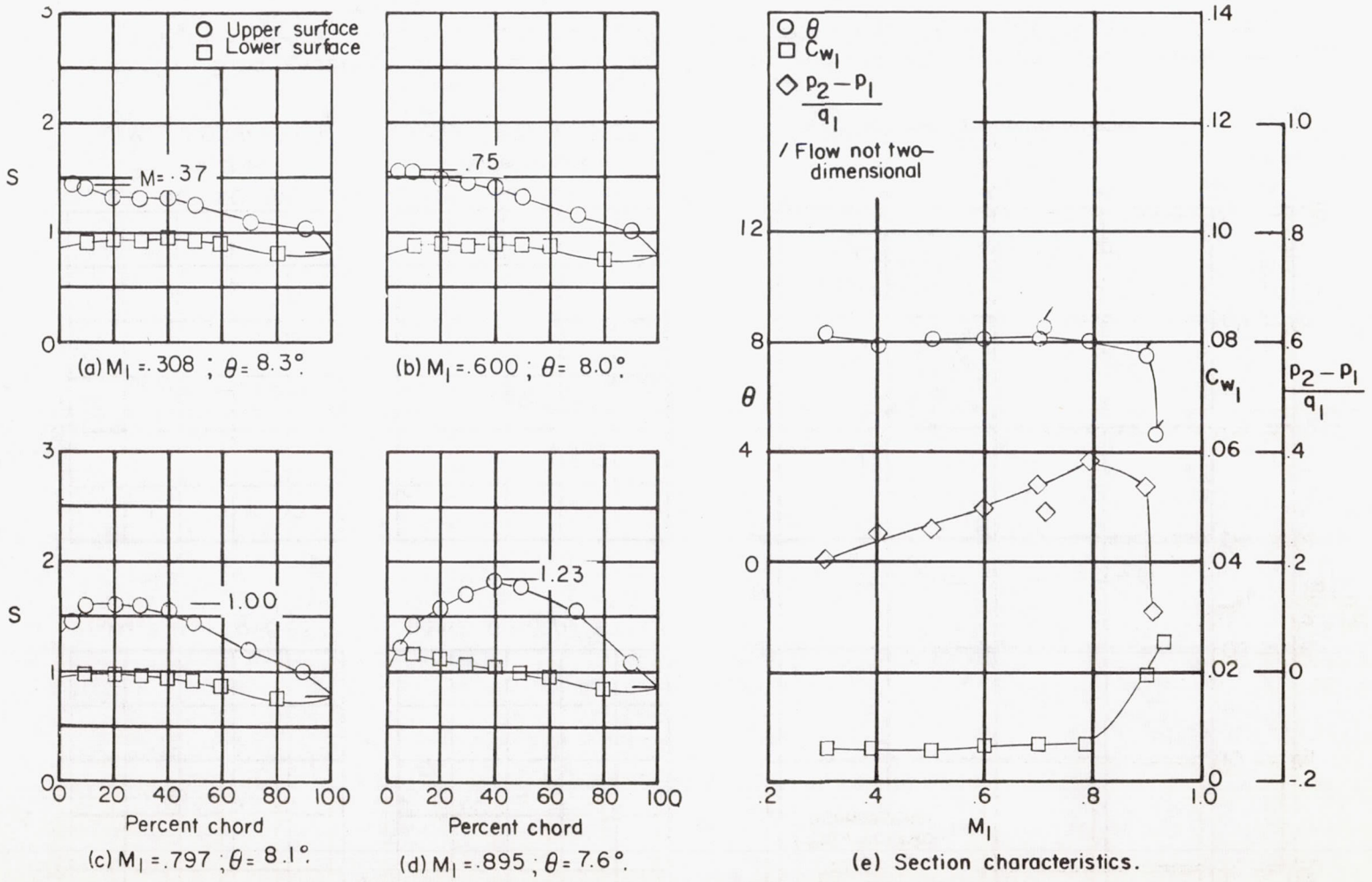



Figure 9.- Blade surface pressure distributions and section characteristics for the cascade combination $\beta_1 = 47.0^\circ$, $\alpha = 7.0^\circ$, $\sigma = 0.8$, and NACA 65-$(4A_{10})$06 blade section.

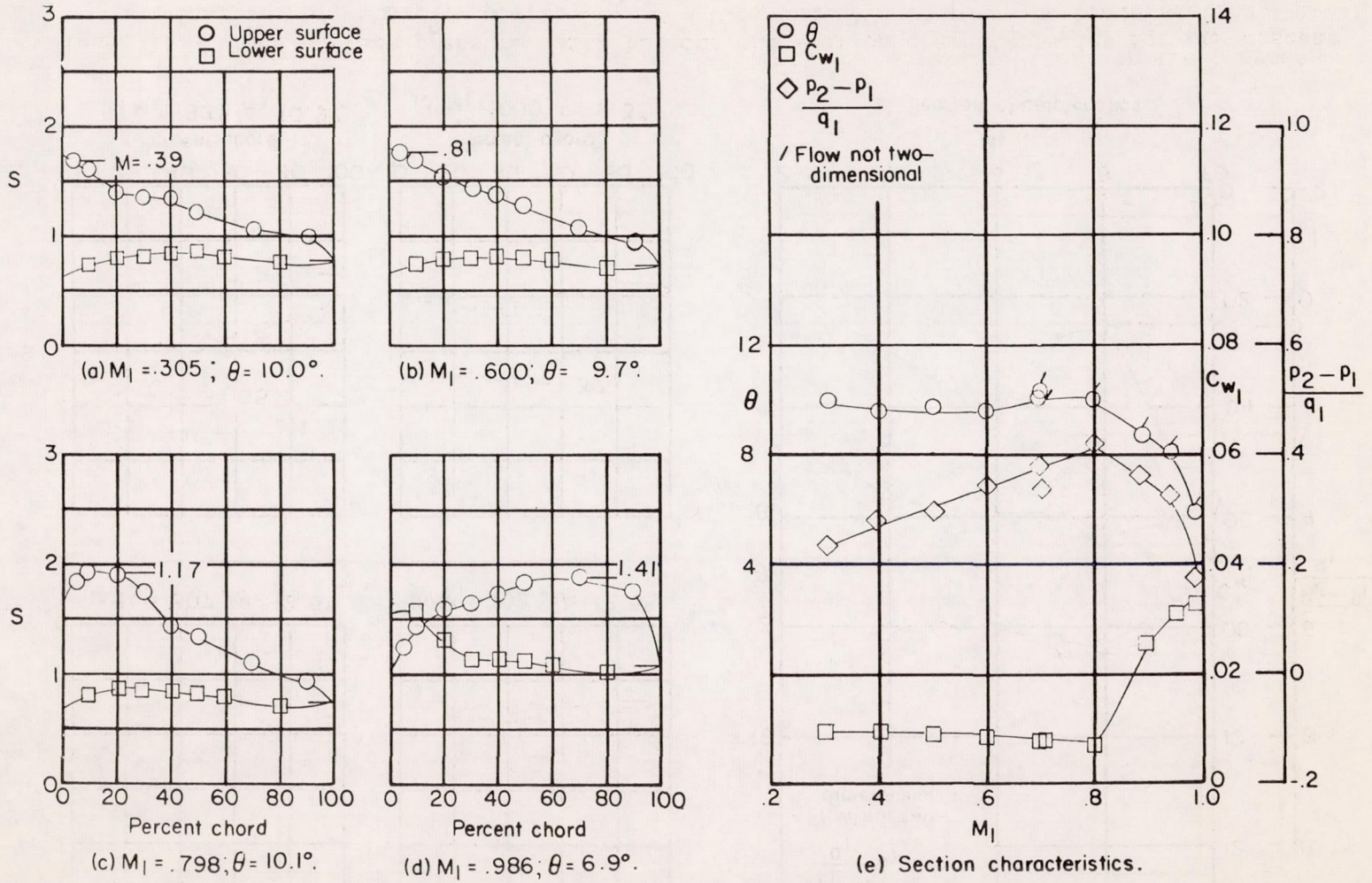



Figure 10.- Blade-surface pressure distributions and section characteristics for the cascade combination $\beta_1 = 50.0°$, $\alpha = 10.0°$, $\sigma = 0.8$, and NACA 65-$(^4A_{10})$06 blade section.

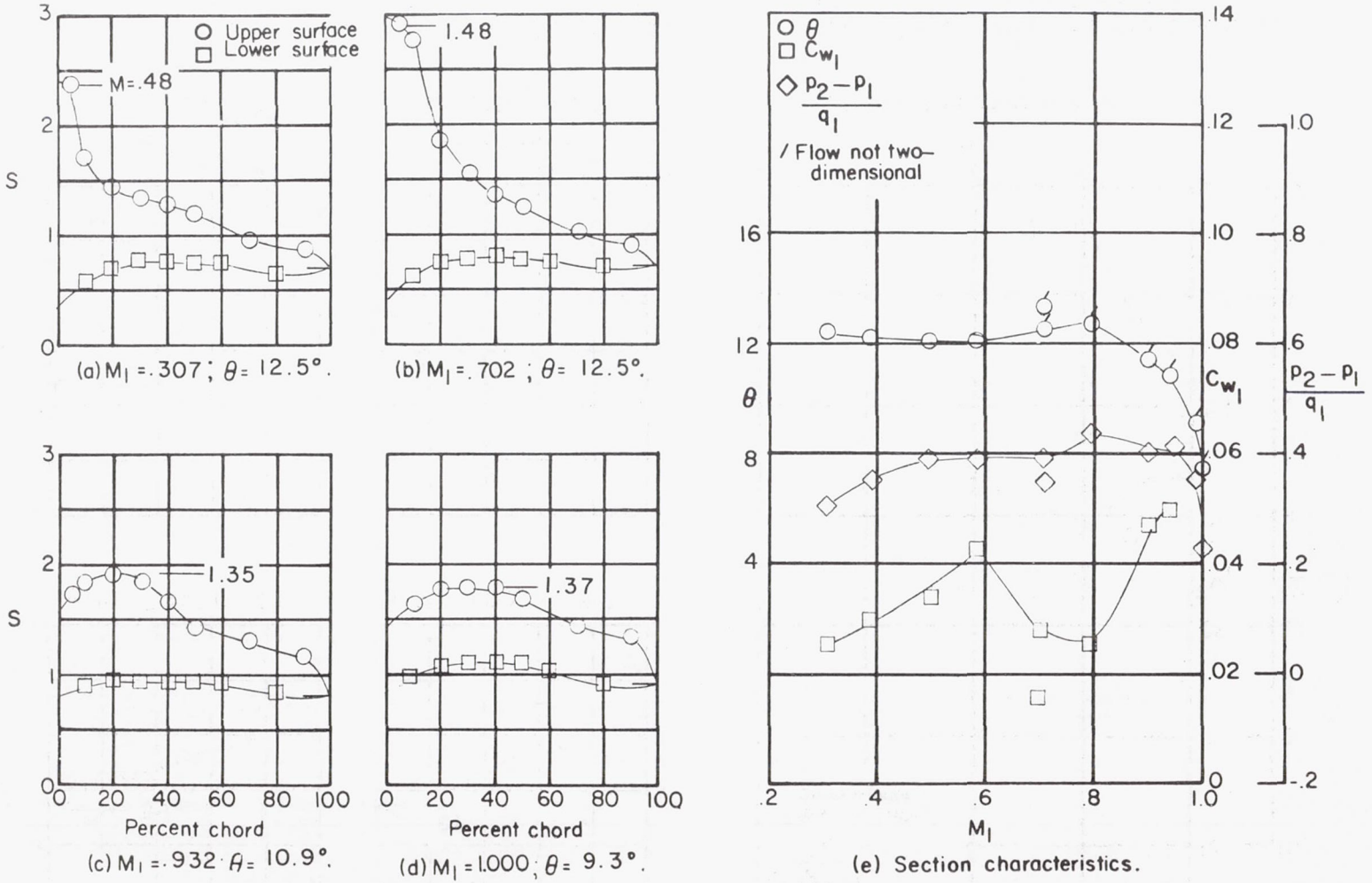



Figure 11.- Blade-surface pressure distributions and section characteristics for the cascade combination $\beta_1 = 53.0°$, $\alpha = 13.0°$, $\sigma = 0.8$, and NACA 65-$(4A_{10})$06 blade section.

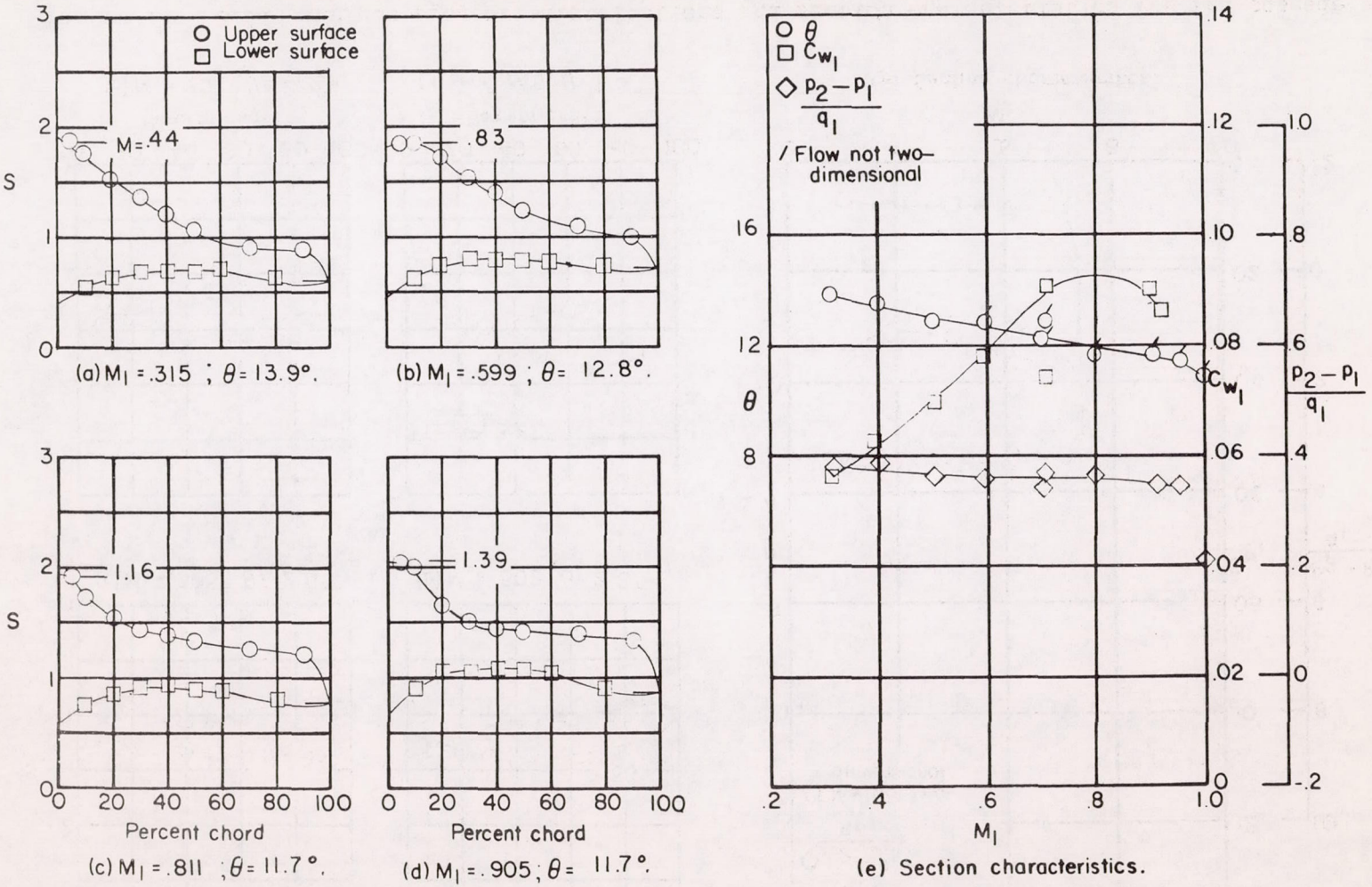



Figure 12.- Blade-surface pressure distributions and section characteristics for the cascade combination $\beta_1 = 56.0^\circ$, $\alpha = 16.0^\circ$, $\sigma = 0.8$, and NACA 65-$(4A_{10})$06 blade section.

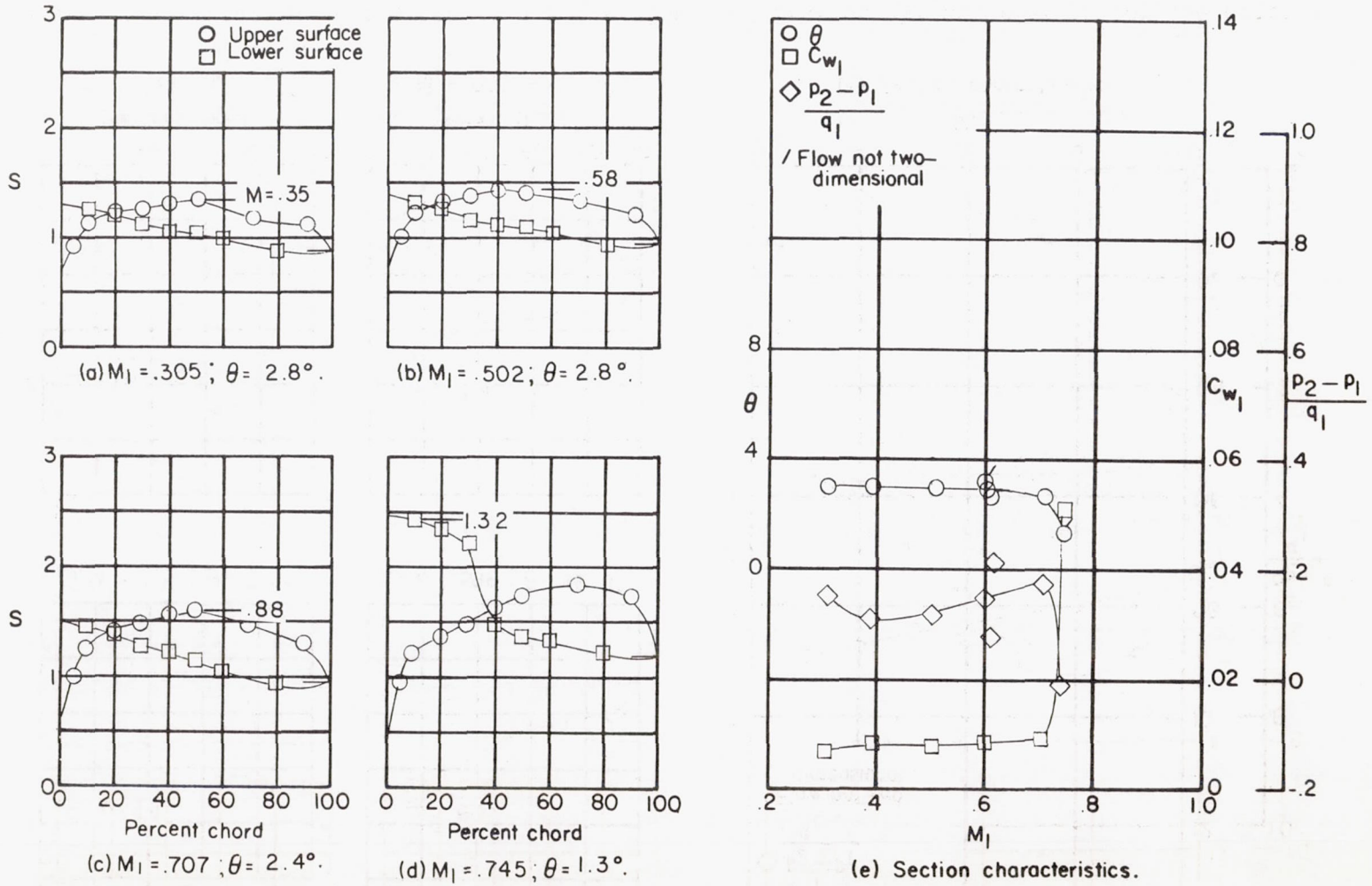



Figure 13.- Blade-surface pressure distributions and section characteristics for the cascade combination $\beta_1 = 41.0^\circ$, $\alpha = 0.4^\circ$, $\sigma = 1.0$, and NACA 65-$(4A_{10})$06 blade section.

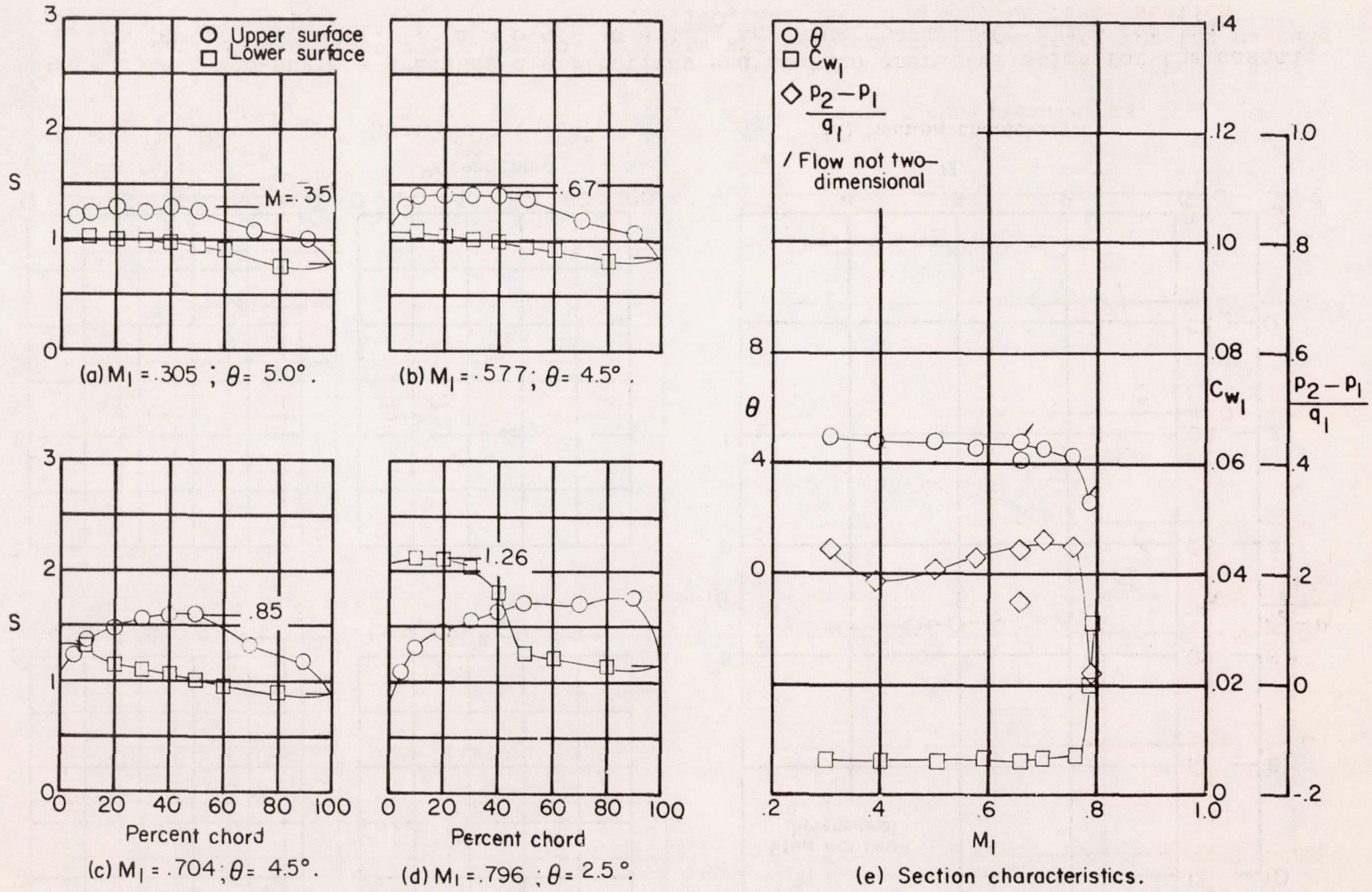



Figure 14.- Blade-surface pressure distributions and section characteristics for the cascade combination $\beta_1 = 44.0^\circ$, $\alpha = 3.4^\circ$, $\sigma = 1.0$, and NACA 65-$\left(^{4}A_{10}\right)$06 blade section.

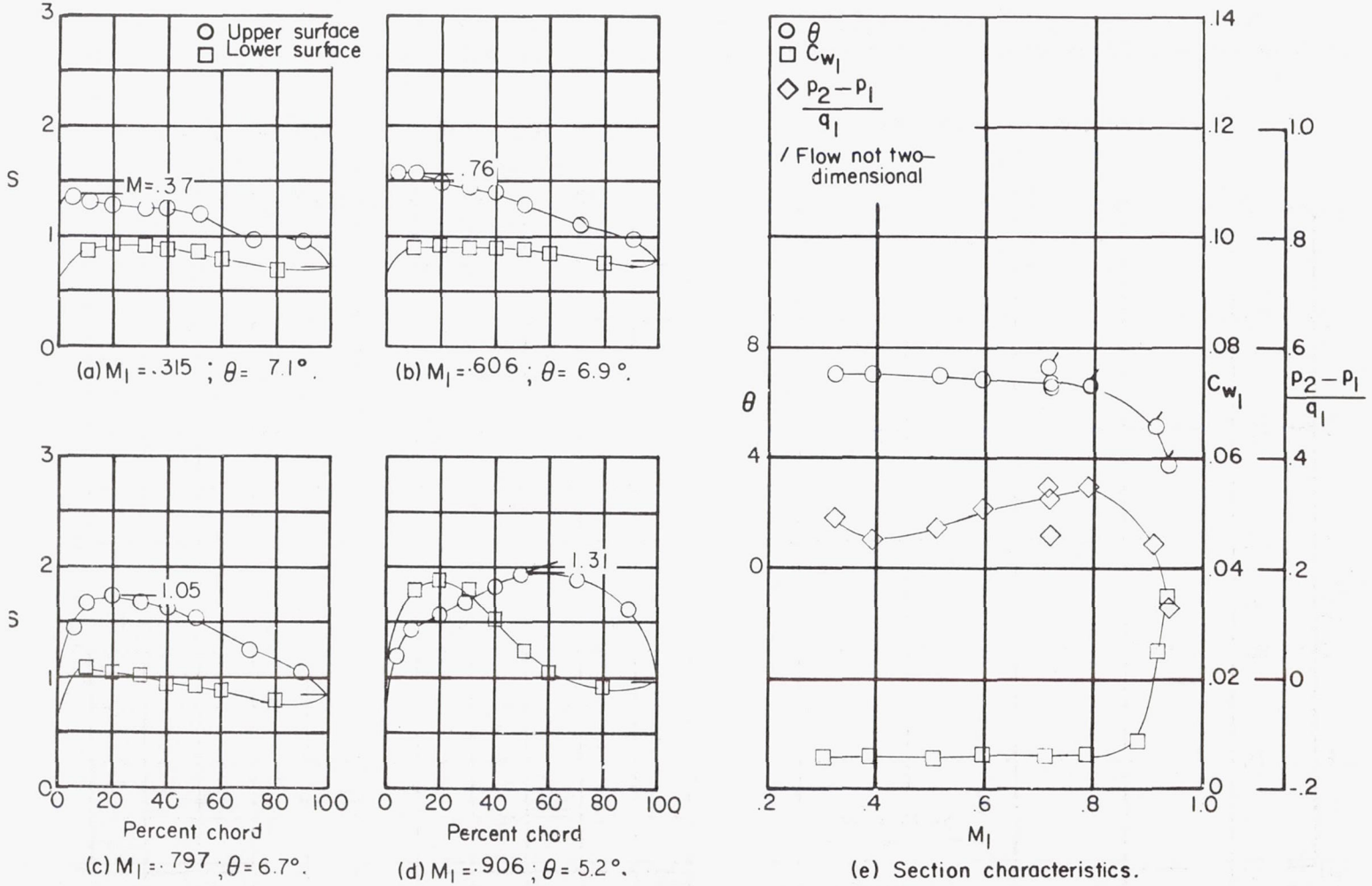



Figure 15.- Blade-surface pressure distributions and section characteristics for the cascade combination $\beta_1 = 47.0^\circ$, $\alpha = 6.4^\circ$, $\sigma = 1.0$, and NACA 65-$(4A_{10})$06 blade section.

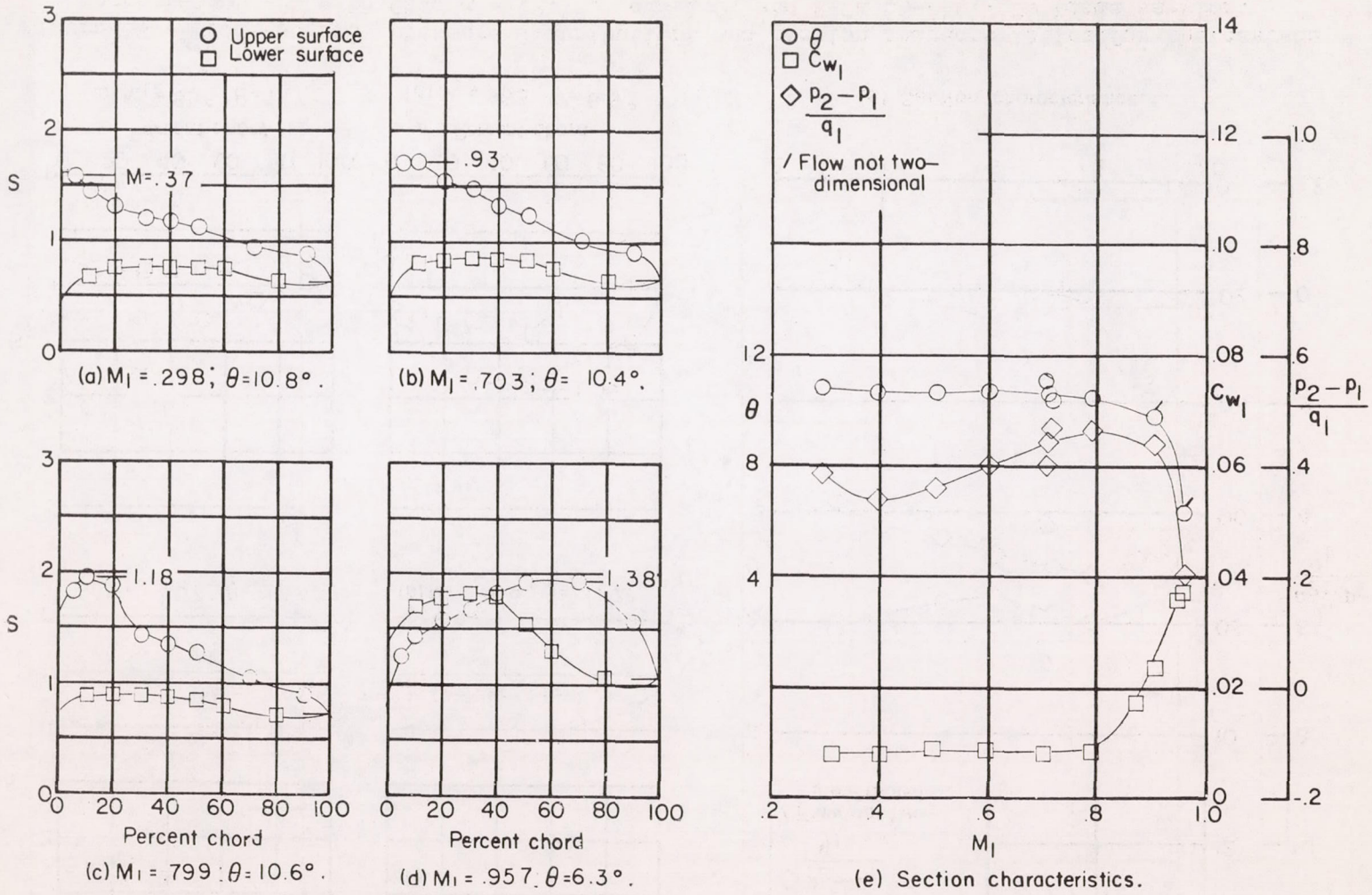



Figure 16.- Blade-surface pressure distributions and section characteristics for the cascade combination $\beta_1 = 50.0°$, $\alpha = 9.4°$, $\sigma = 1.0$, and NACA 65-$\left(4A_{10}\right)$06 blade section.

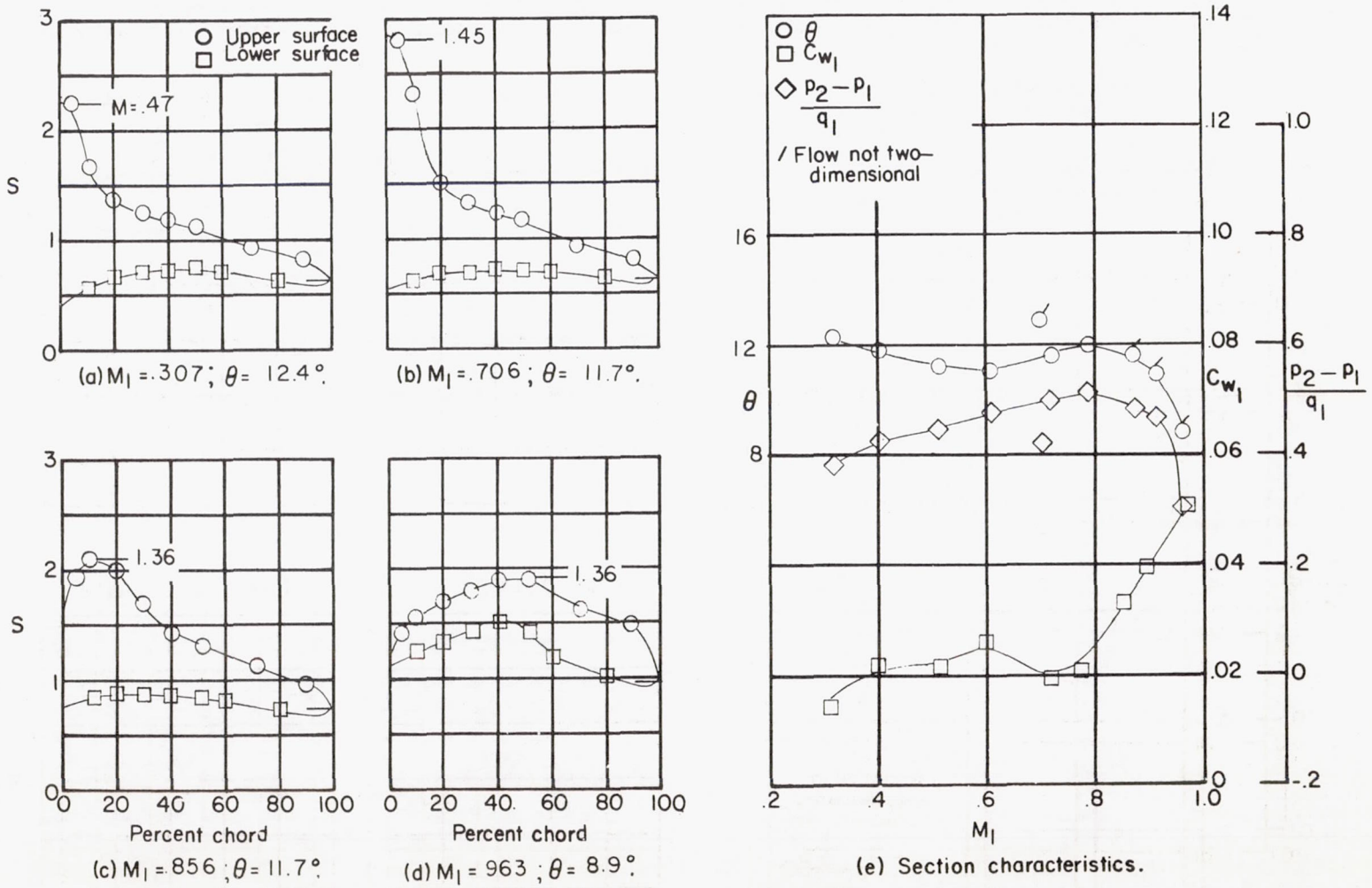



Figure 17.- Blade-surface pressure distributions and section characteristics for the cascade combination $\beta_1 = 53.0°$, $\alpha = 12.4°$, $\sigma = 1.0$, and NACA 65-$\left(^{4}A_{10}\right)$06 blade section.

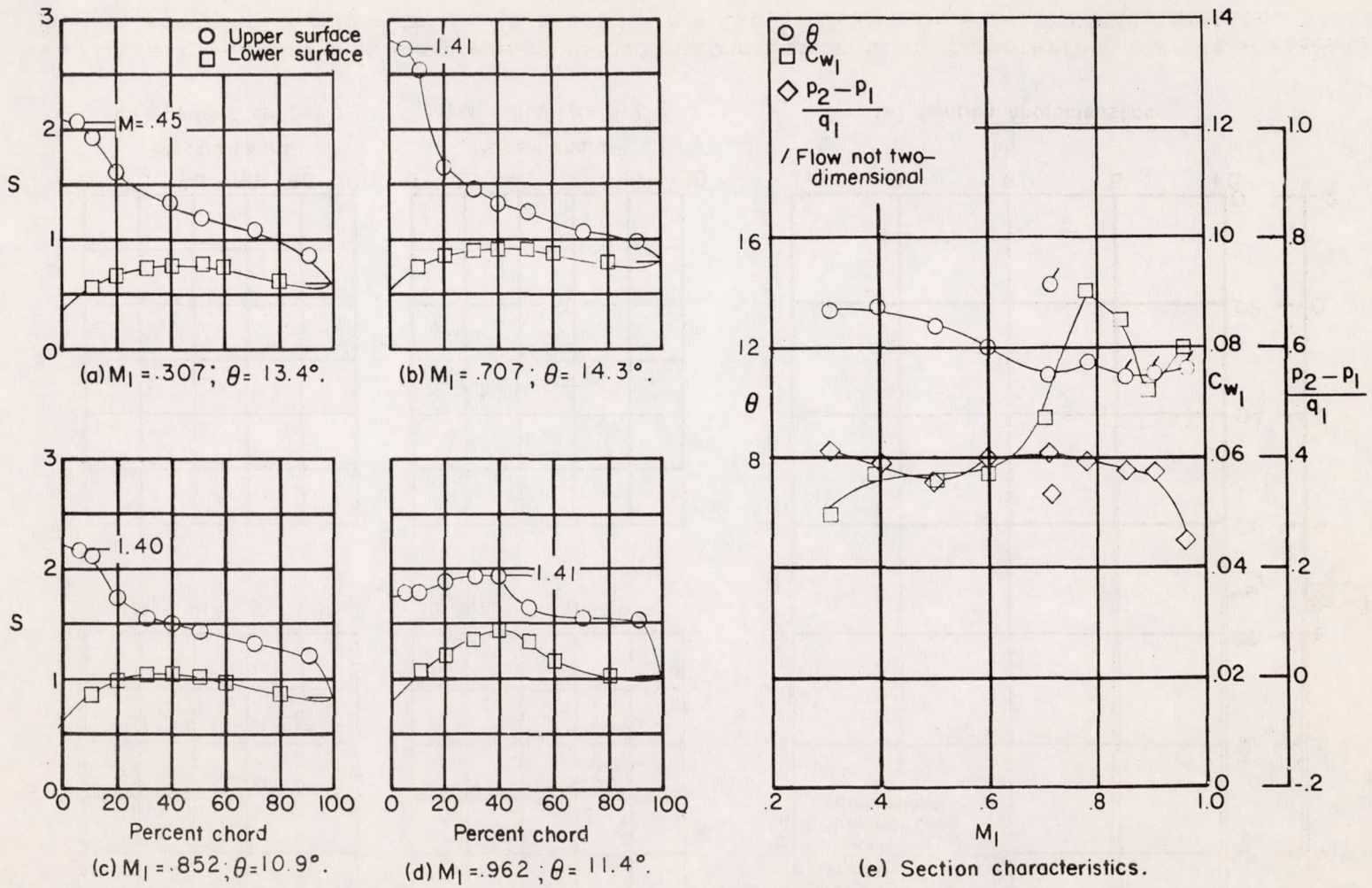



Figure 18.- Blade-surface pressure distributions and section characteristics for the cascade combination $\beta_1 = 56.0°$, $\alpha = 15.4°$, $\sigma = 1.0$, and NACA 65-$(^4A_{10})$06 blade section.

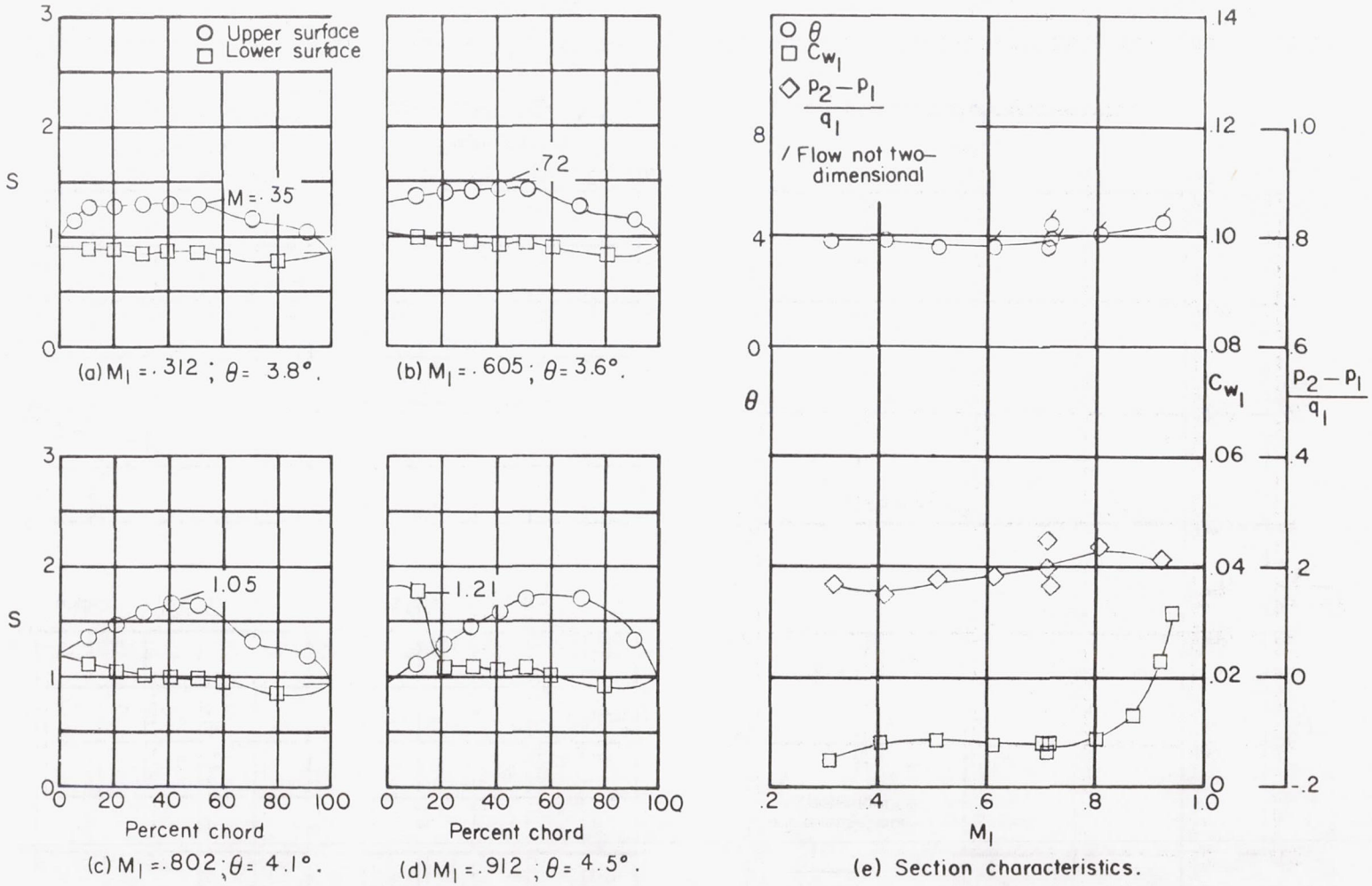



Figure 19.- Blade-surface pressure distributions and section characteristics for the cascade combination $\beta_1 = 54.0°$, $\alpha = 1.5°$, $\sigma = 0.6$, and NACA 65-$(4A_{10})$06 blade section.

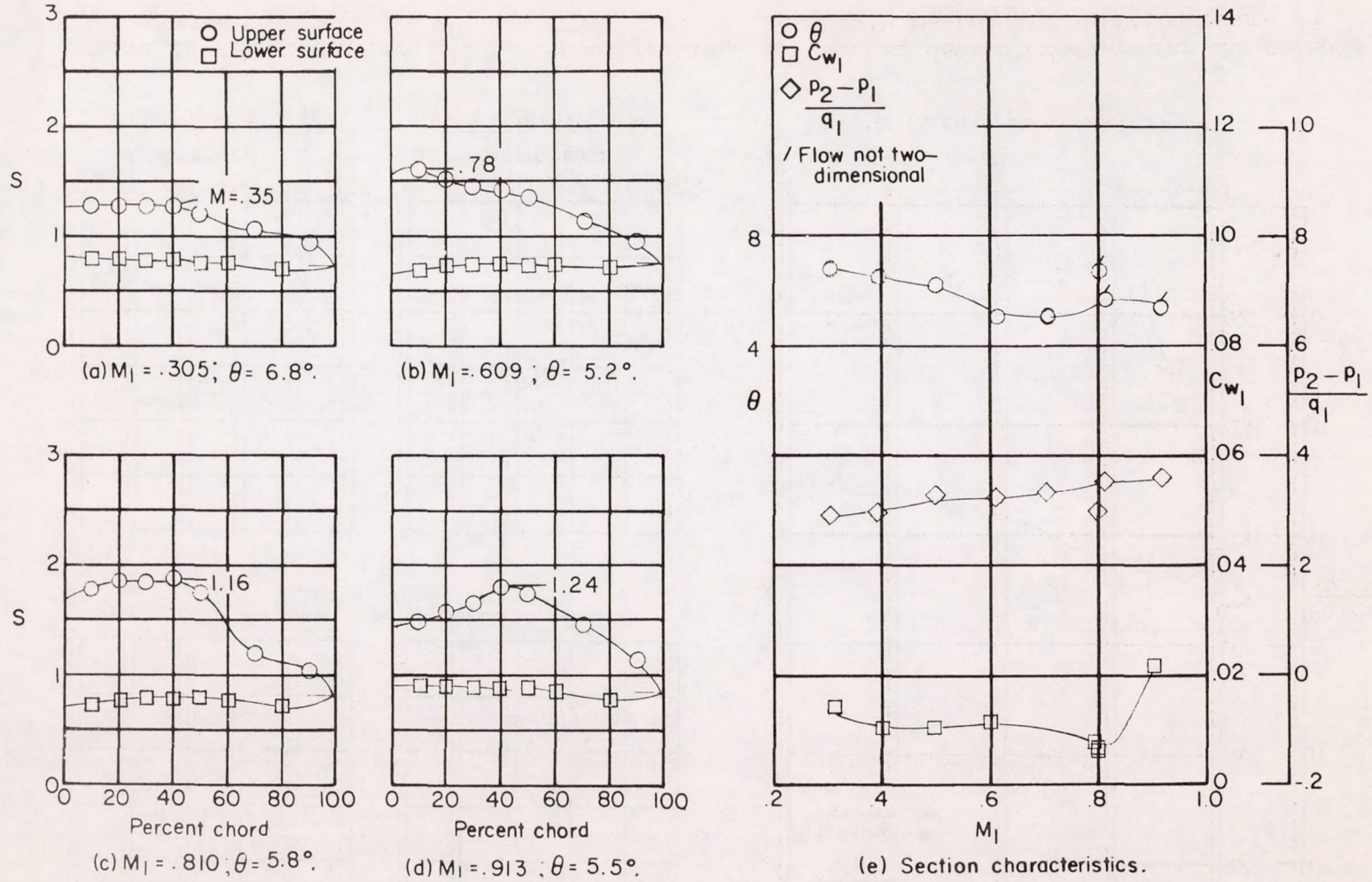



Figure 20.- Blade-surface pressure distributions and section characteristics for the cascade combination $\beta_1 = 57.0^\circ$, $\alpha = 4.5^\circ$, $\sigma = 0.6$, and NACA 65-$(4A_{10})$06 blade section.

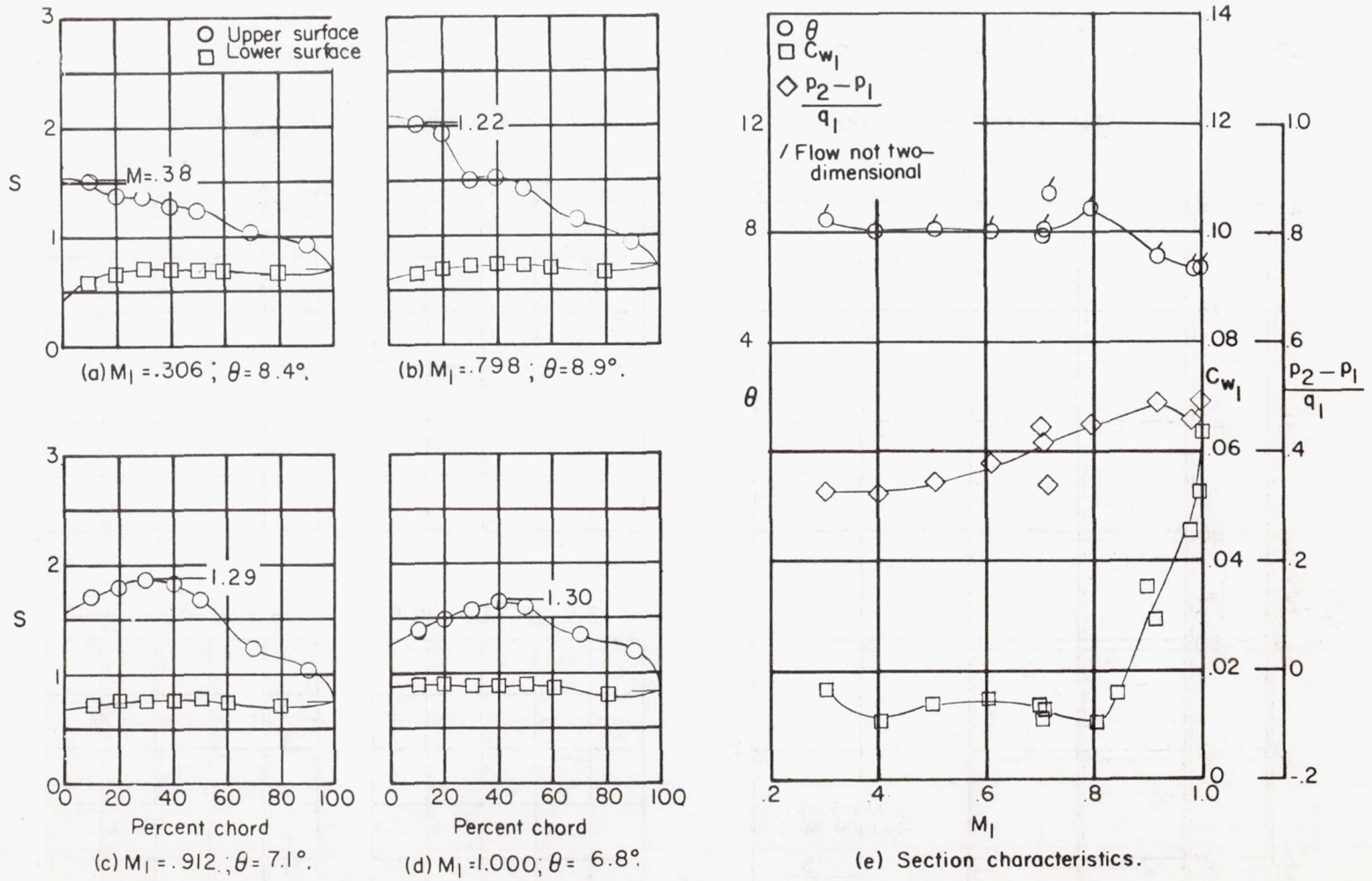



Figure 21.- Blade-surface pressure distributions and section characteristics for the cascade combination $\beta_1 = 60.0°$, $\alpha = 7.5°$, $\sigma = 0.6$, and NACA 65-$\left(^{4}A_{10}\right)$06 blade section.

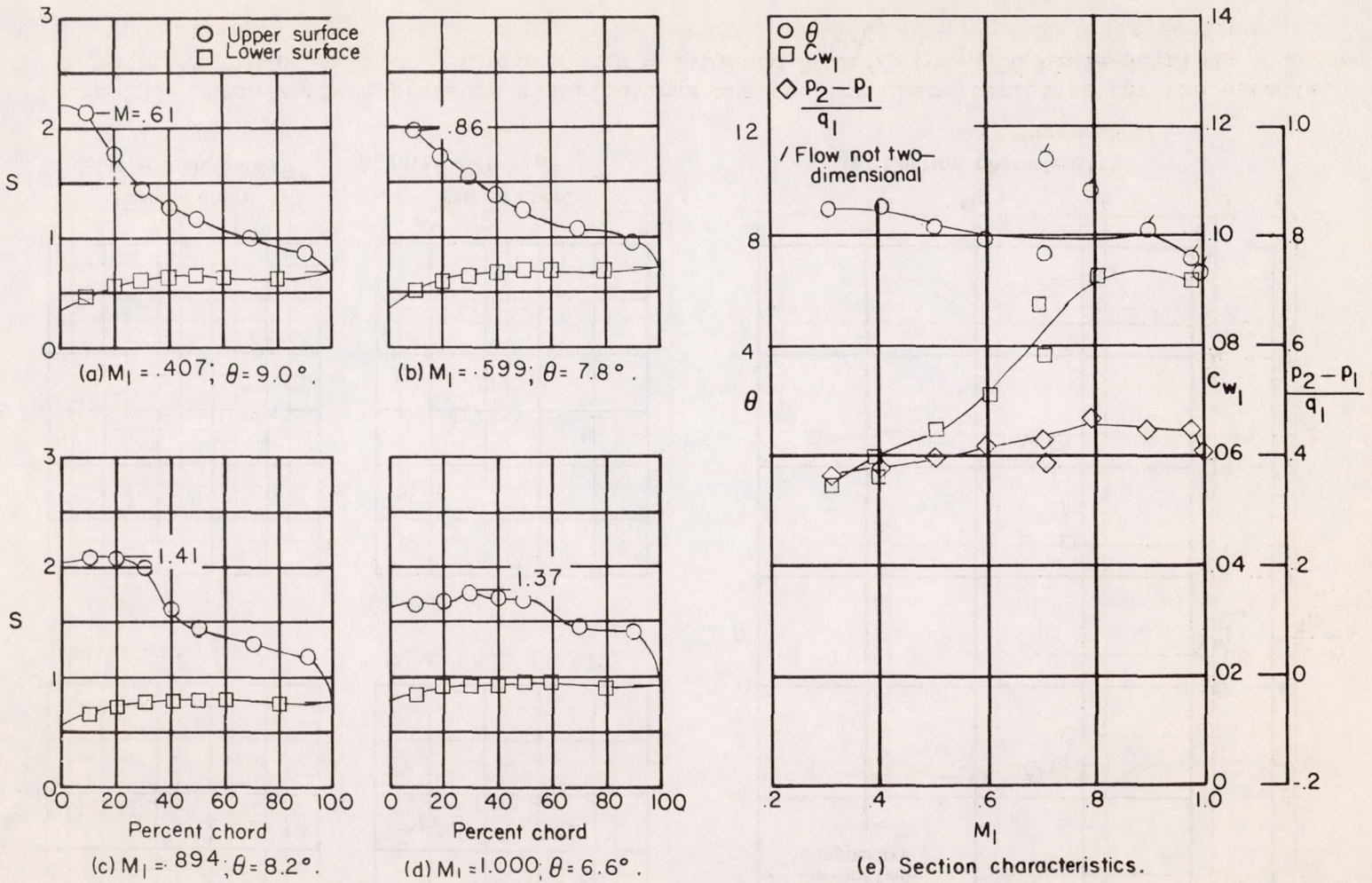



Figure 22.- Blade-surface pressure distributions and section characteristics for the cascade combination $\beta_1 = 63.0°$, $\alpha = 10.5°$, $\sigma = 0.6$, and NACA 65-$(4A_{10})$06 blade section.

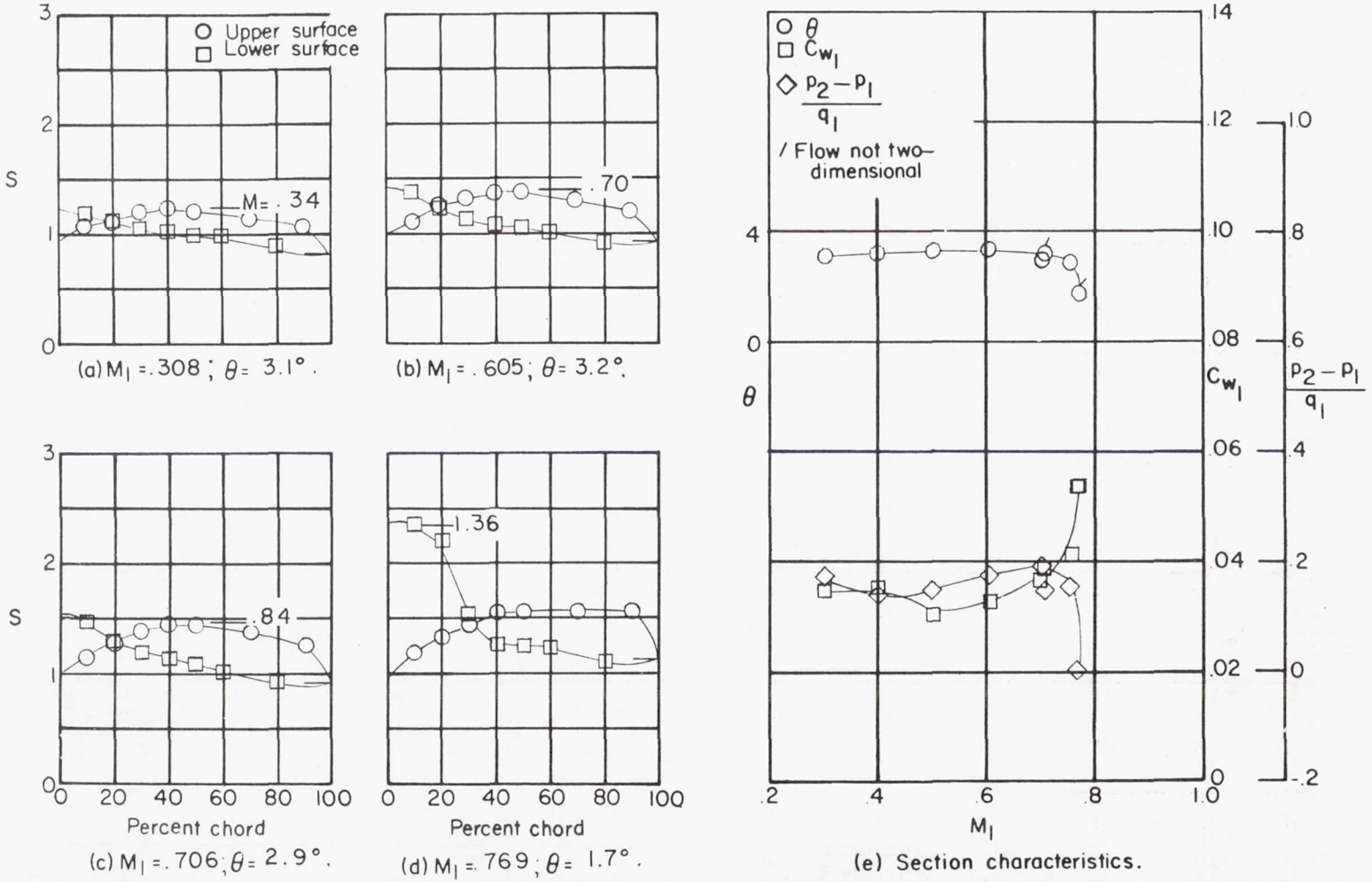



Figure 23.- Blade-surface pressure distributions and section characteristics for the cascade combination $\beta_1 = 51.0^\circ$, $\alpha = 0.5^\circ$, $\sigma = 1.0$, and NACA 65-$\left(4A_{10}\right)$06 blade section.

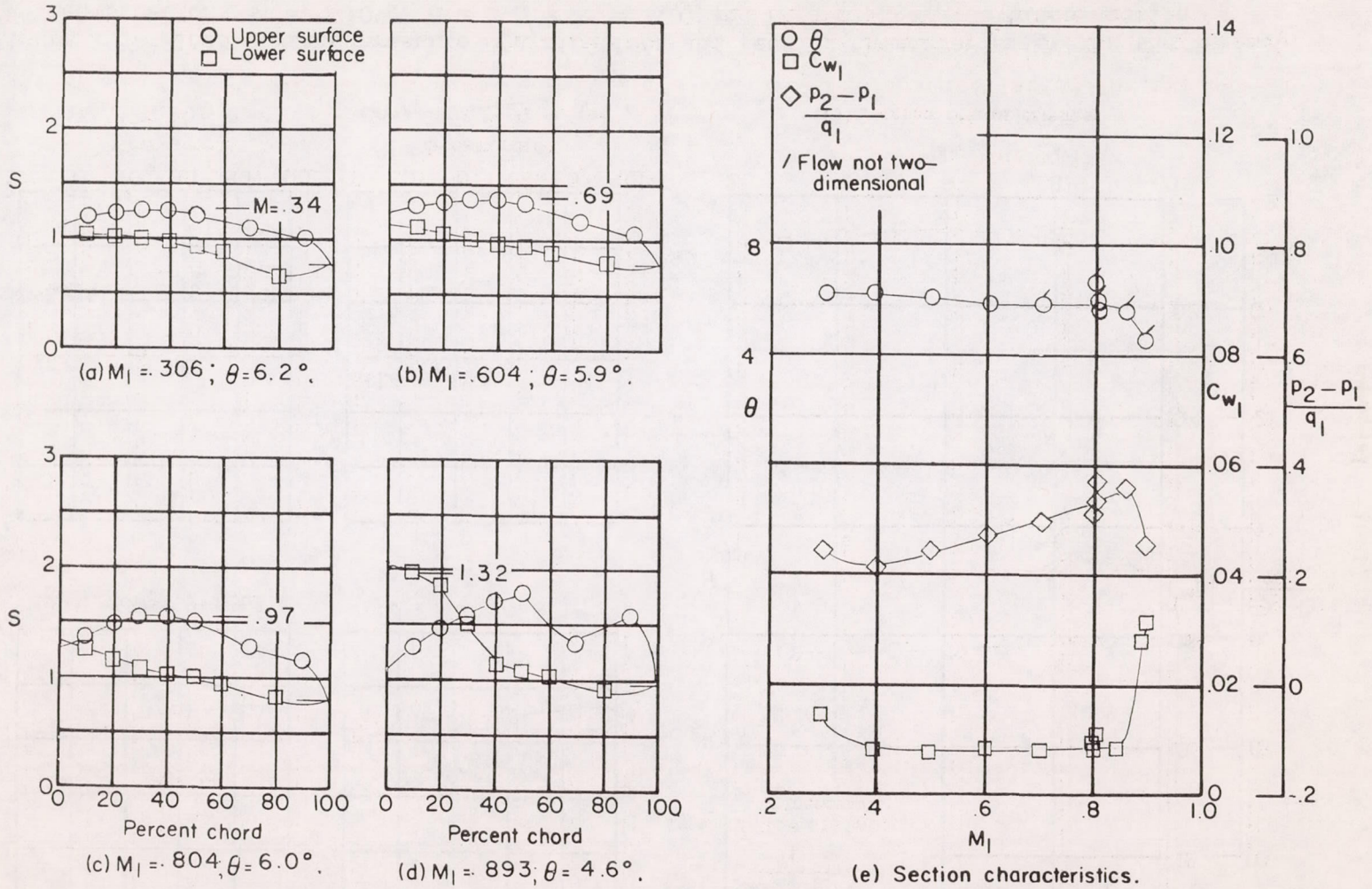



Figure 24.- Blade-surface pressure distributions and section characteristics for the cascade combination $\beta_1 = 54.0°$, $\alpha = 3.5°$, $\sigma = 1.0$, and NACA 65-$(4A_{10})$06 blade section.

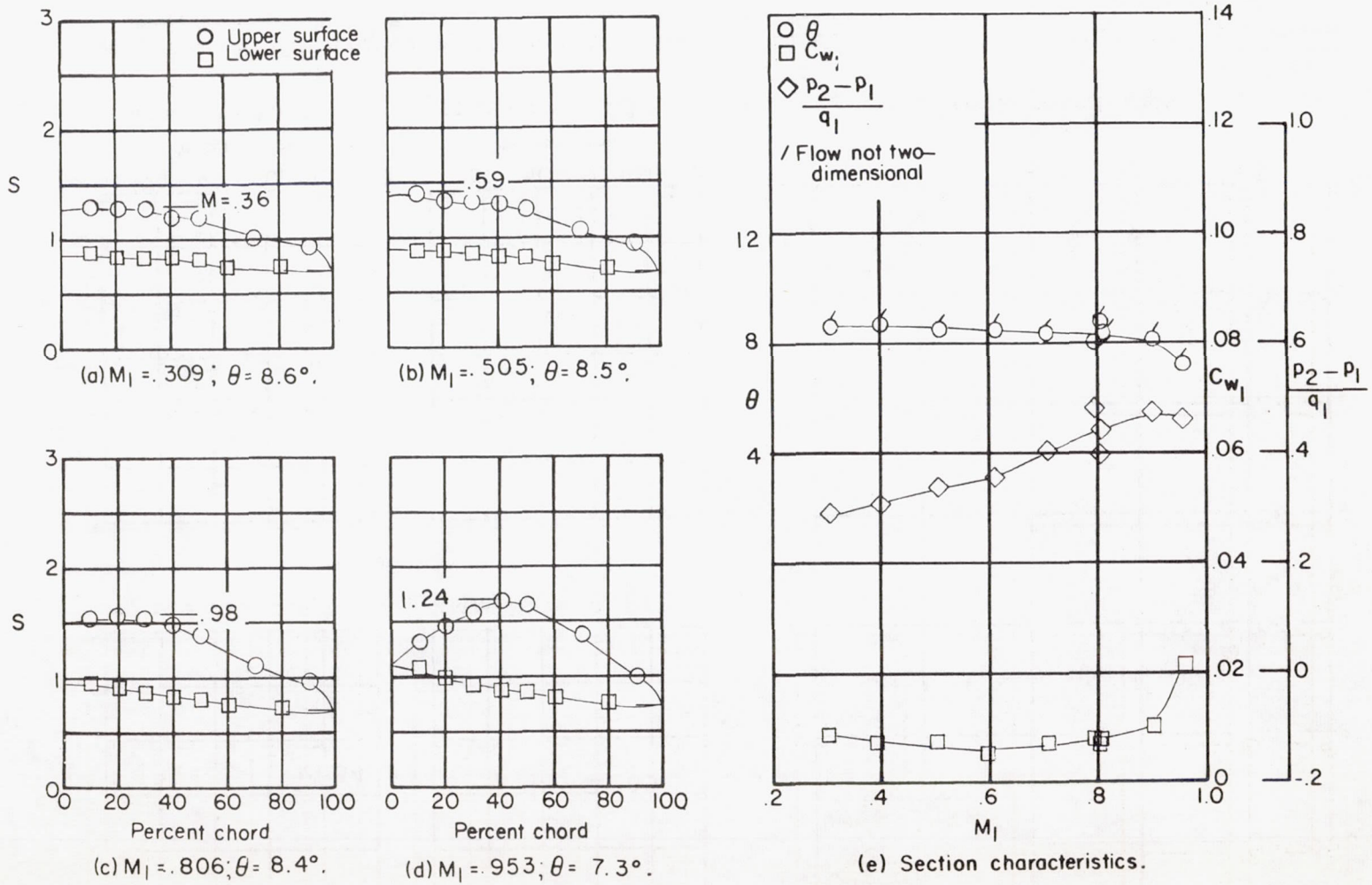



Figure 25.- Blade-surface pressure distributions and section characteristics for the cascade combination $\beta_1 = 57.0^\circ$, $\alpha = 6.5^\circ$, $\sigma = 1.0$, and NACA 65-$(^4A_{10})$06 blade section.

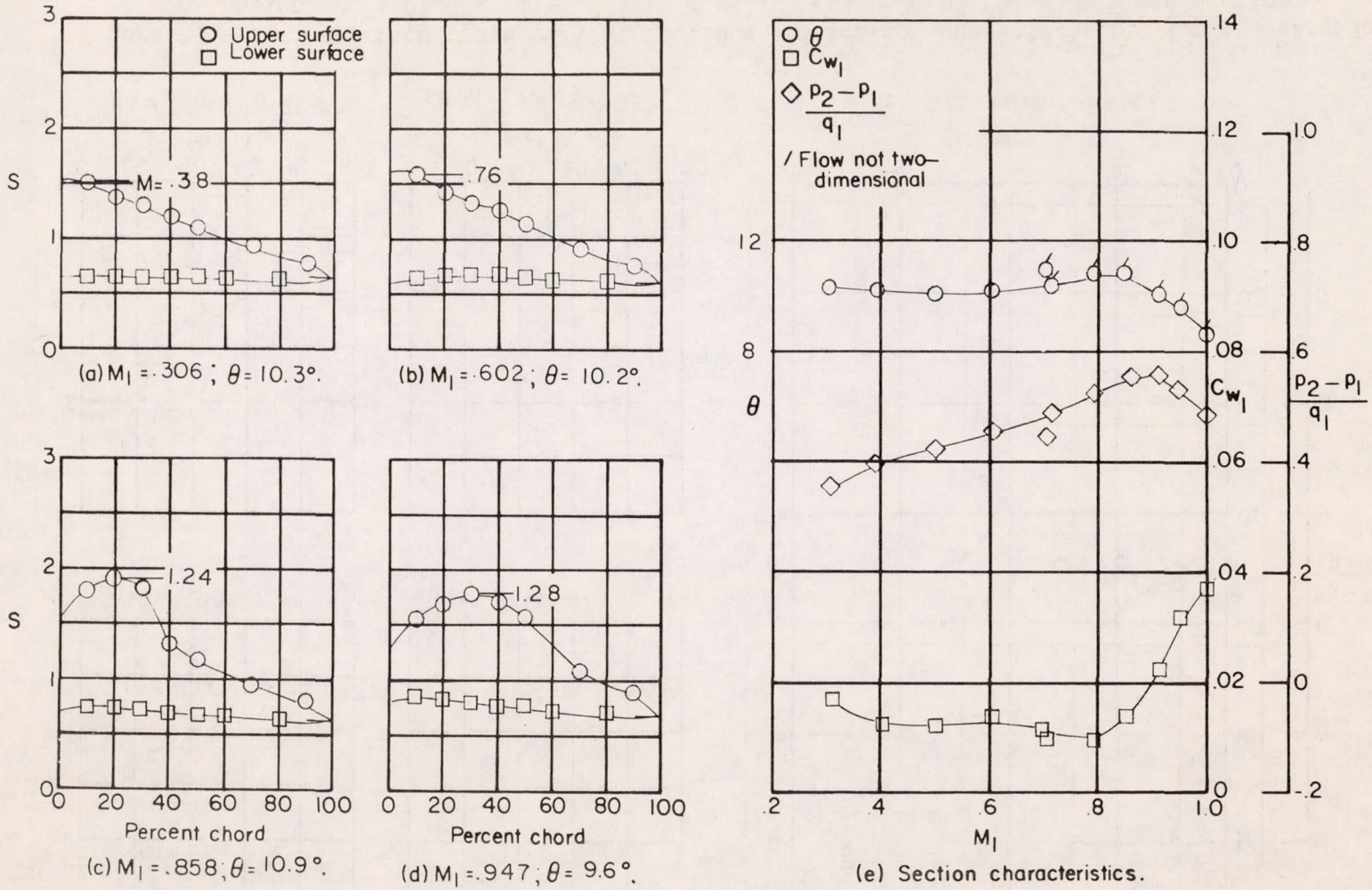



Figure 26.- Blade-surface pressure distributions and section characteristics for the cascade combination $\beta_1 = 60.0°$, $\alpha = 9.5°$, $\sigma = 1.0$, and NACA 65-$\left(4A_{10}\right)$06 blade section.

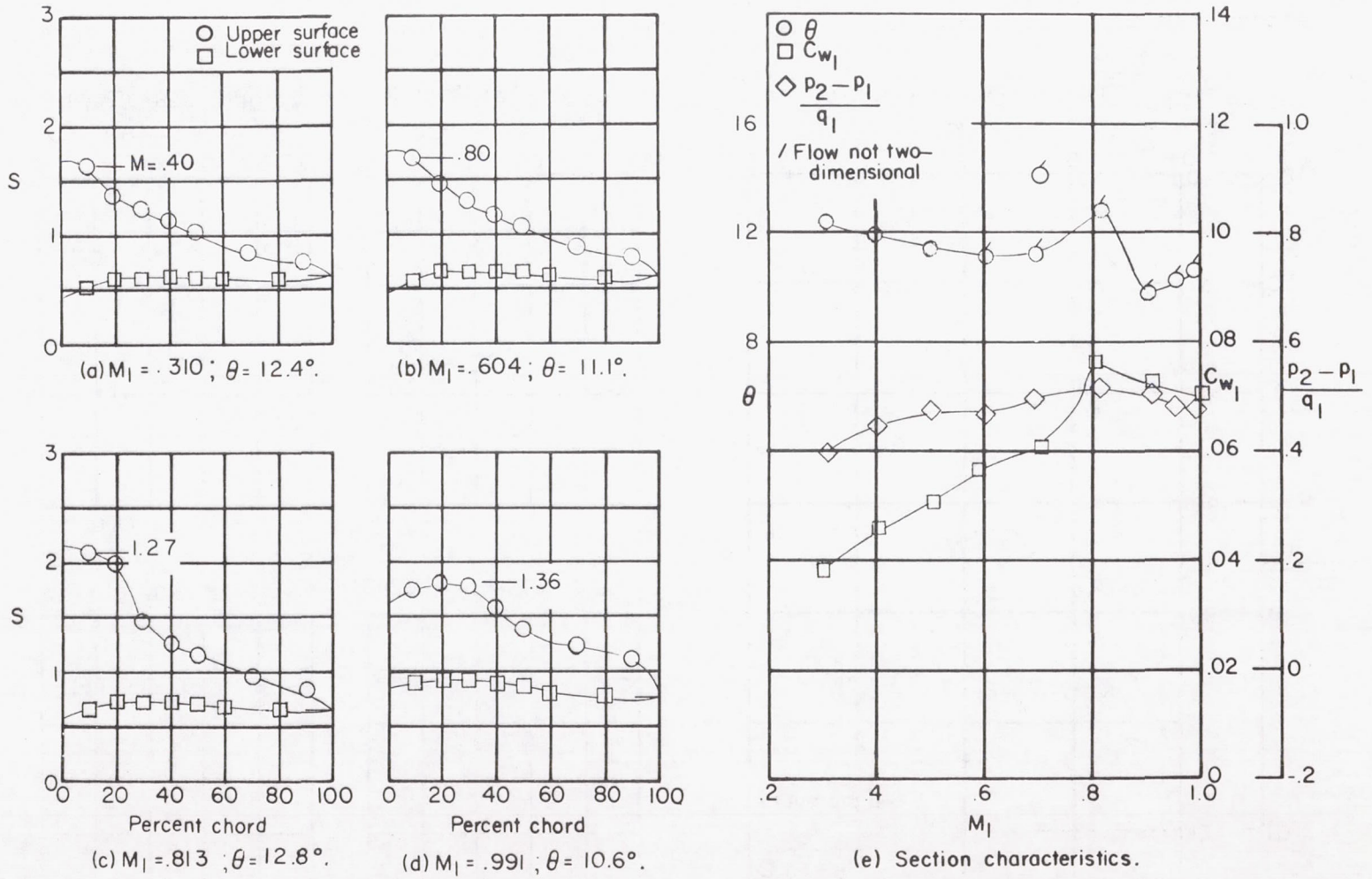



Figure 27.- Blade-surface pressure distributions and section characteristics for the cascade combination $\beta_1 = 63.0°$, $\alpha = 12.5°$, $\sigma = 1.0$, and NACA 65-$(4A_{10})$06 blade section.

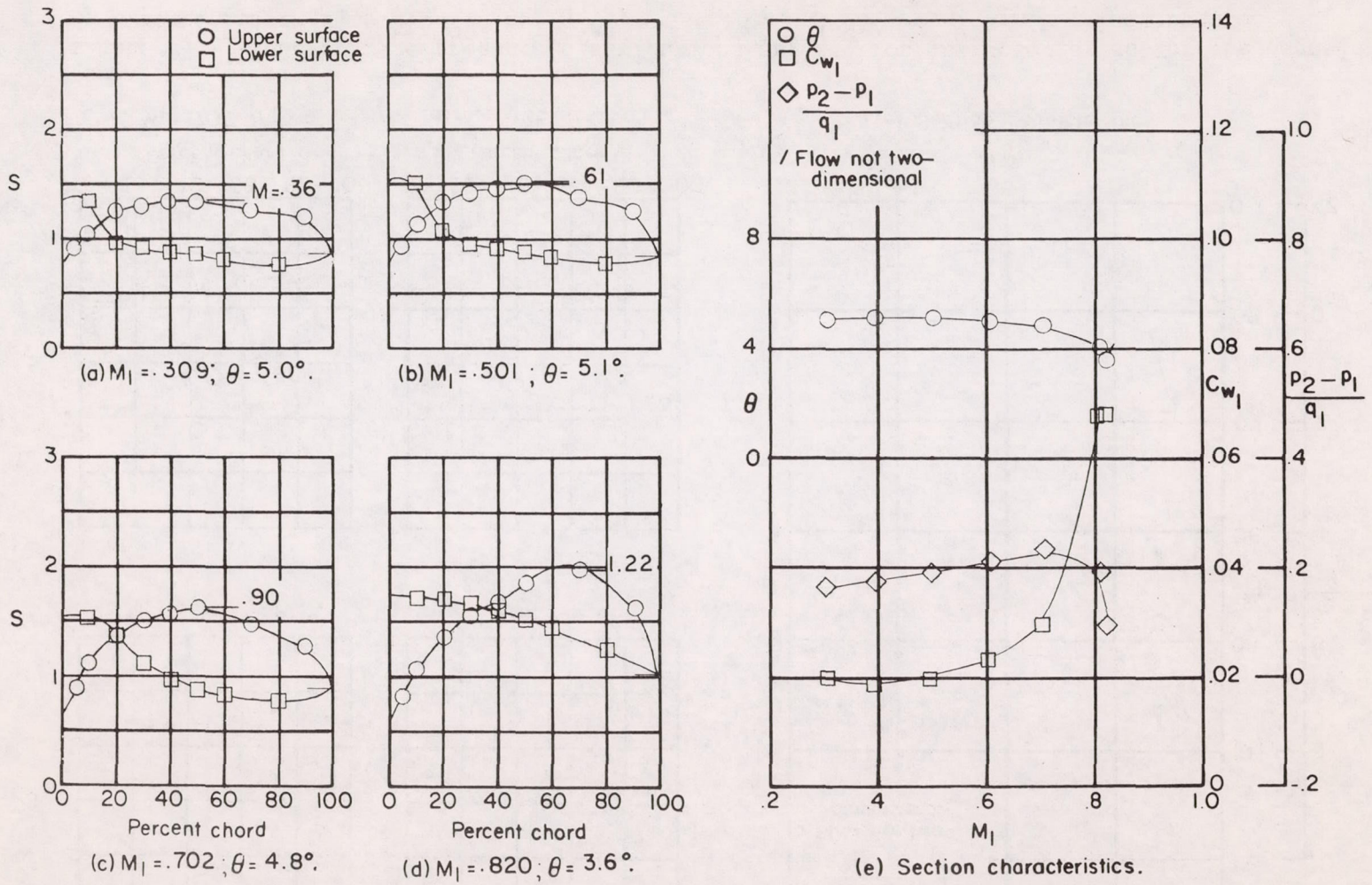



Figure 28.- Blade-surface pressure distributions and section characteristics for the cascade combination $\beta_1 = 41.0^\circ$, $\alpha = 1.0^\circ$, $\sigma = 0.6$, and NACA 65-$(8A_{10})$06 blade section.

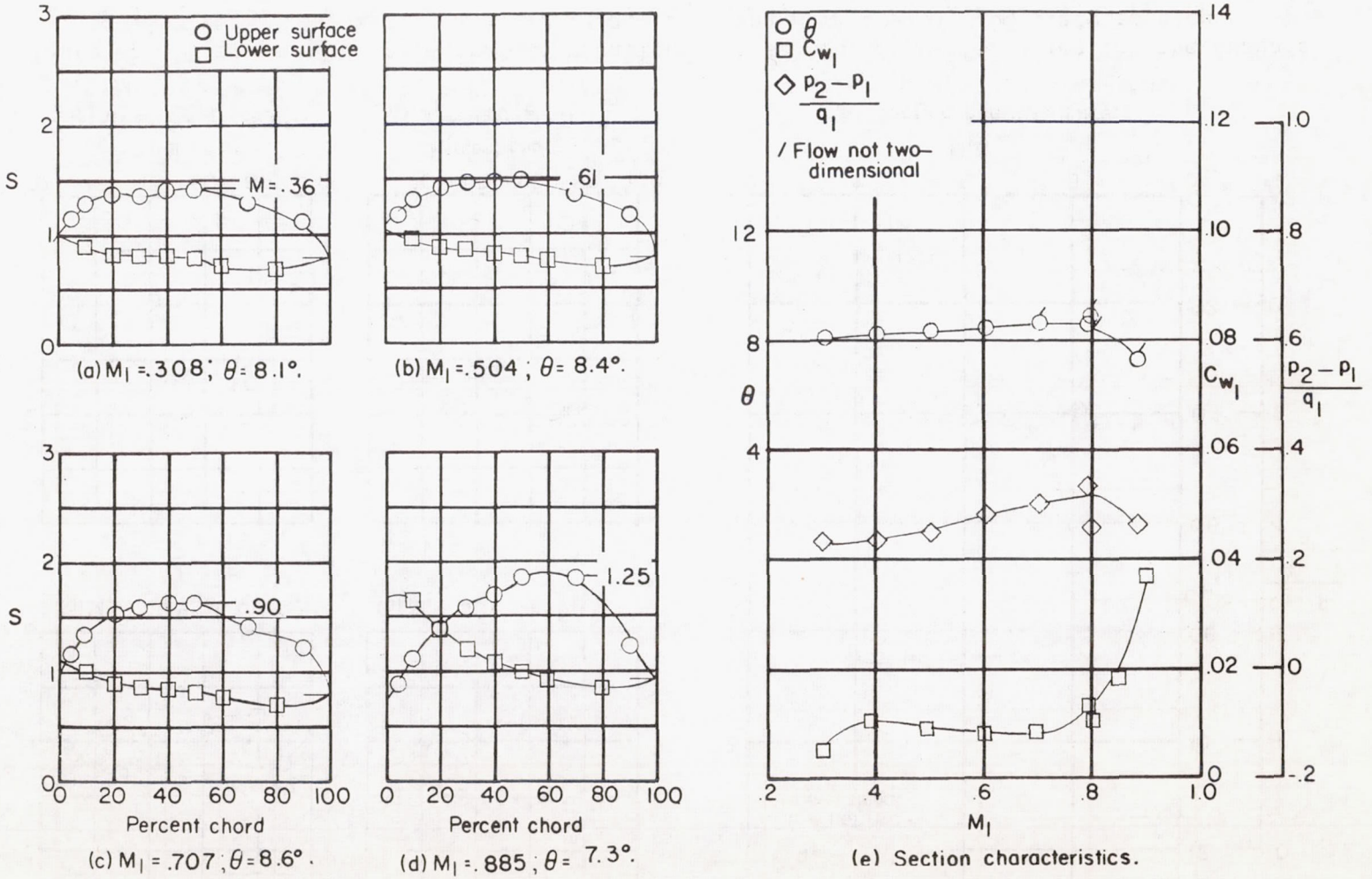



Figure 29.- Blade-surface pressure distributions and section characteristics for the cascade combination $\beta_1 = 44.0°$, $\alpha = 4.0°$, $\sigma = 0.6$, and NACA 65-$(8A_{10})$06 blade section.

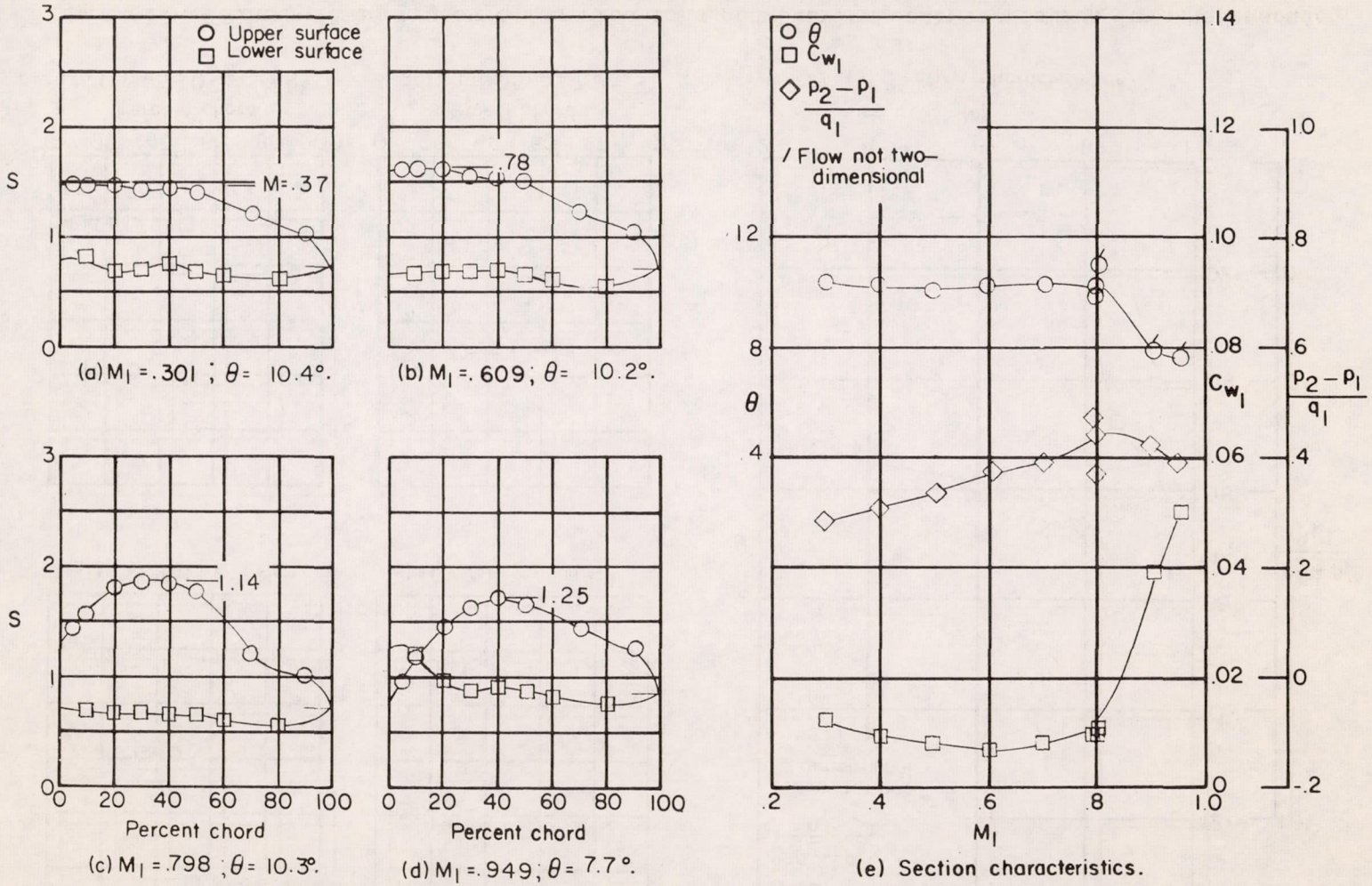



Figure 30.- Blade-surface pressure distributions and section characteristics for the cascade combination $\beta_1 = 47.0^\circ$, $\alpha = 7.0^\circ$, $\sigma = 0.6$, and NACA 65-$\left(8A_{10}\right)$06 blade section.

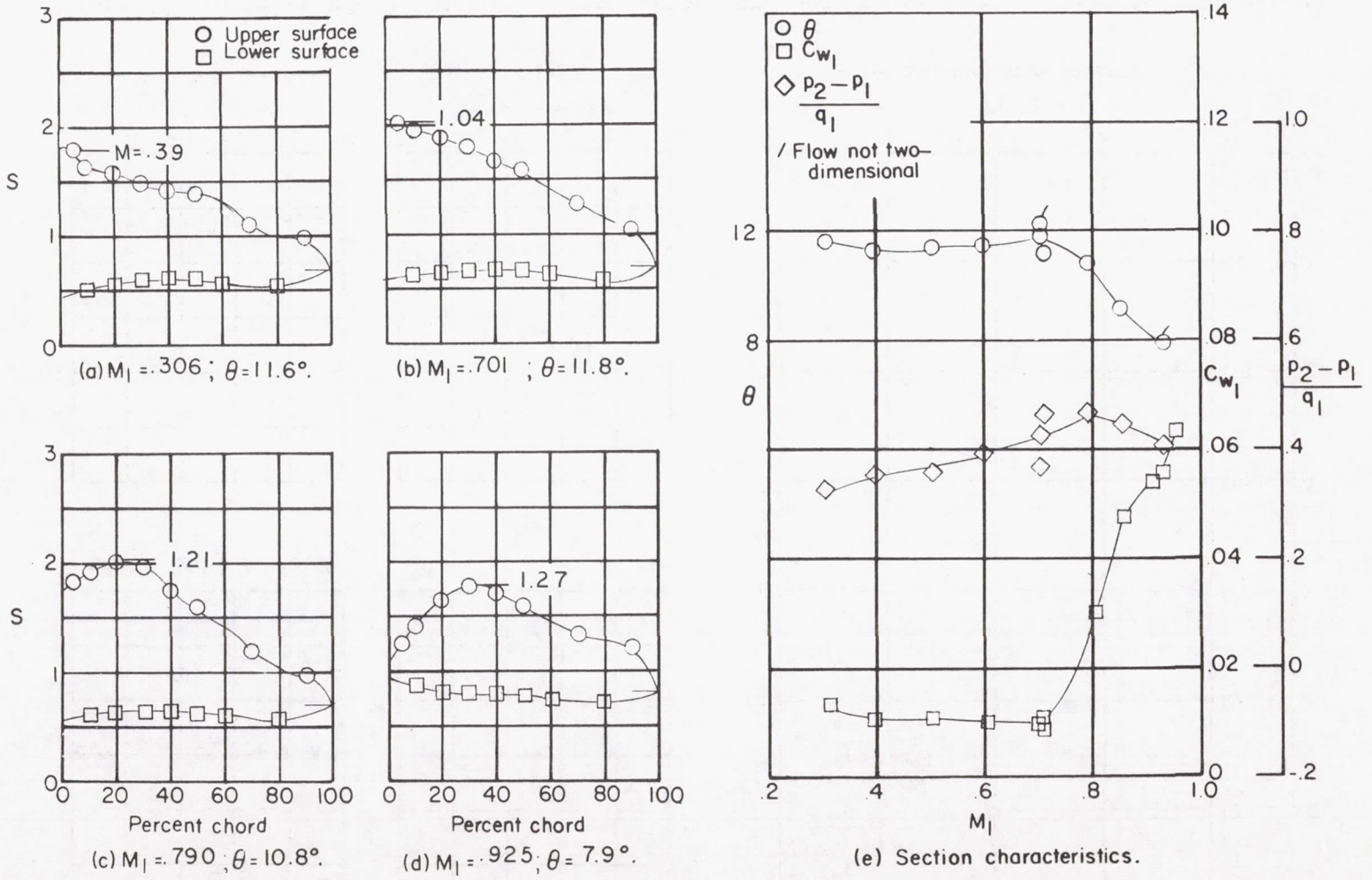



Figure 31.- Blade-surface pressure distributions and section characteristics for the cascade combination $\beta_1 = 50.0^\circ$, $\alpha = 10.0^\circ$, $\sigma = 0.6$, and NACA 65-$(8A_{10})$10 blade section.

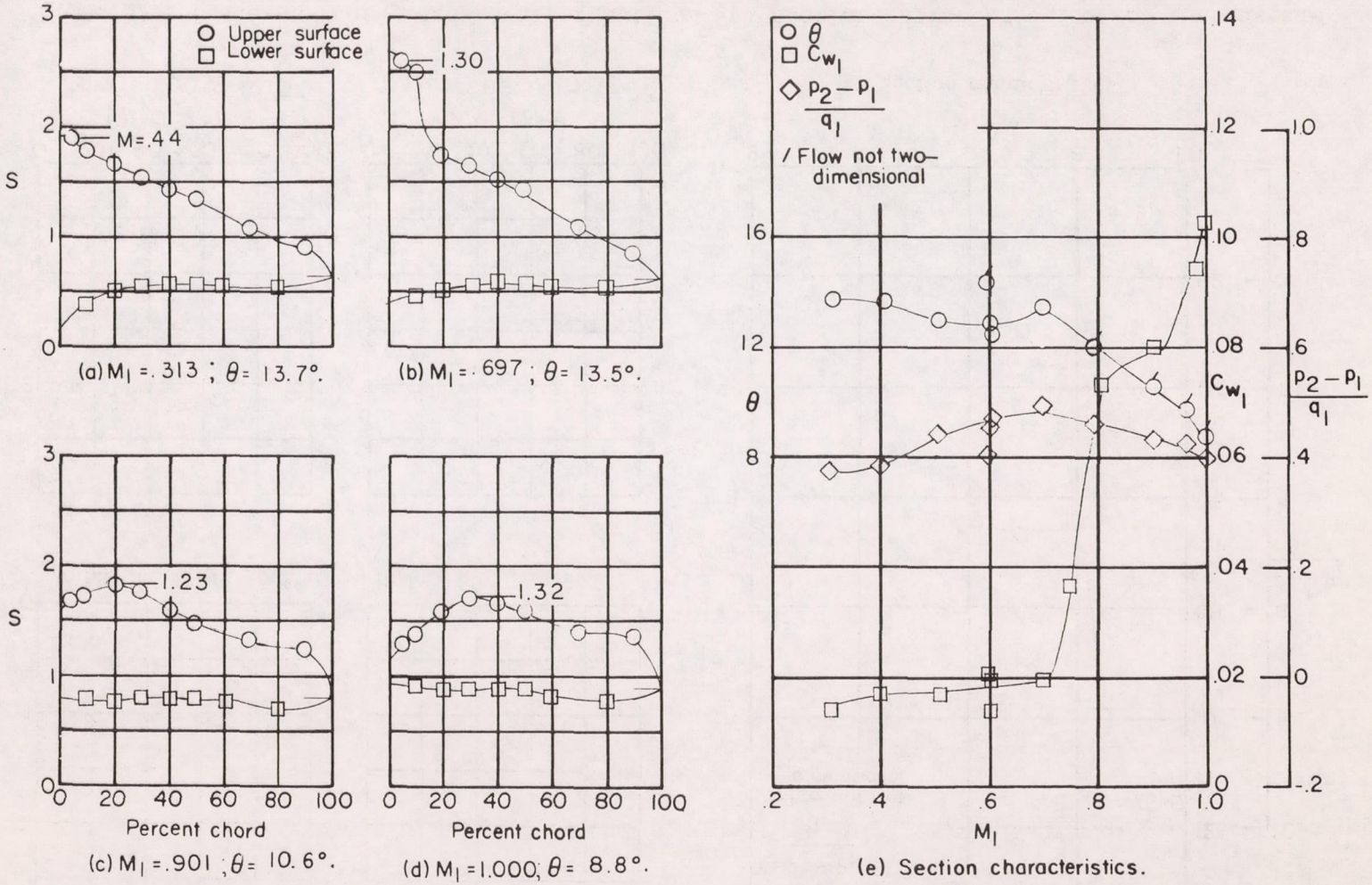



Figure 32.- Blade-surface pressure distributions and section characteristics for the cascade combination $\beta_1 = 53.0°$, $\alpha = 13.0°$, $\sigma = 0.6$, and NACA 65-$(8A_{10})$06 blade section.

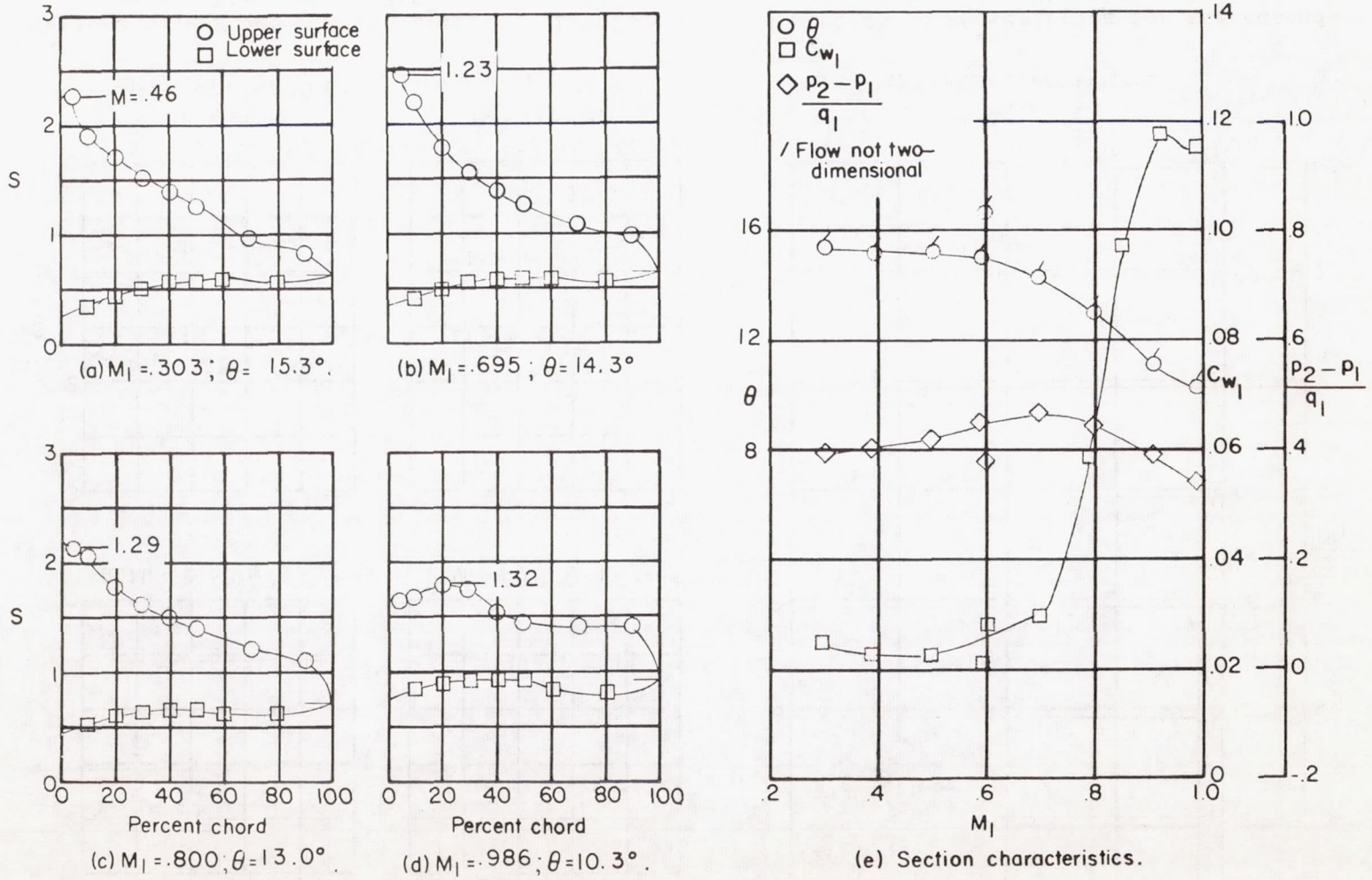



Figure 33.- Blade-surface pressure distributions and section characteristics for the cascade combination $\beta_1 = 56.0°$, $\alpha = 16.0°$, $\sigma = 0.6$, and NACA 65-$\left(8A_{10}\right)$06 blade section.

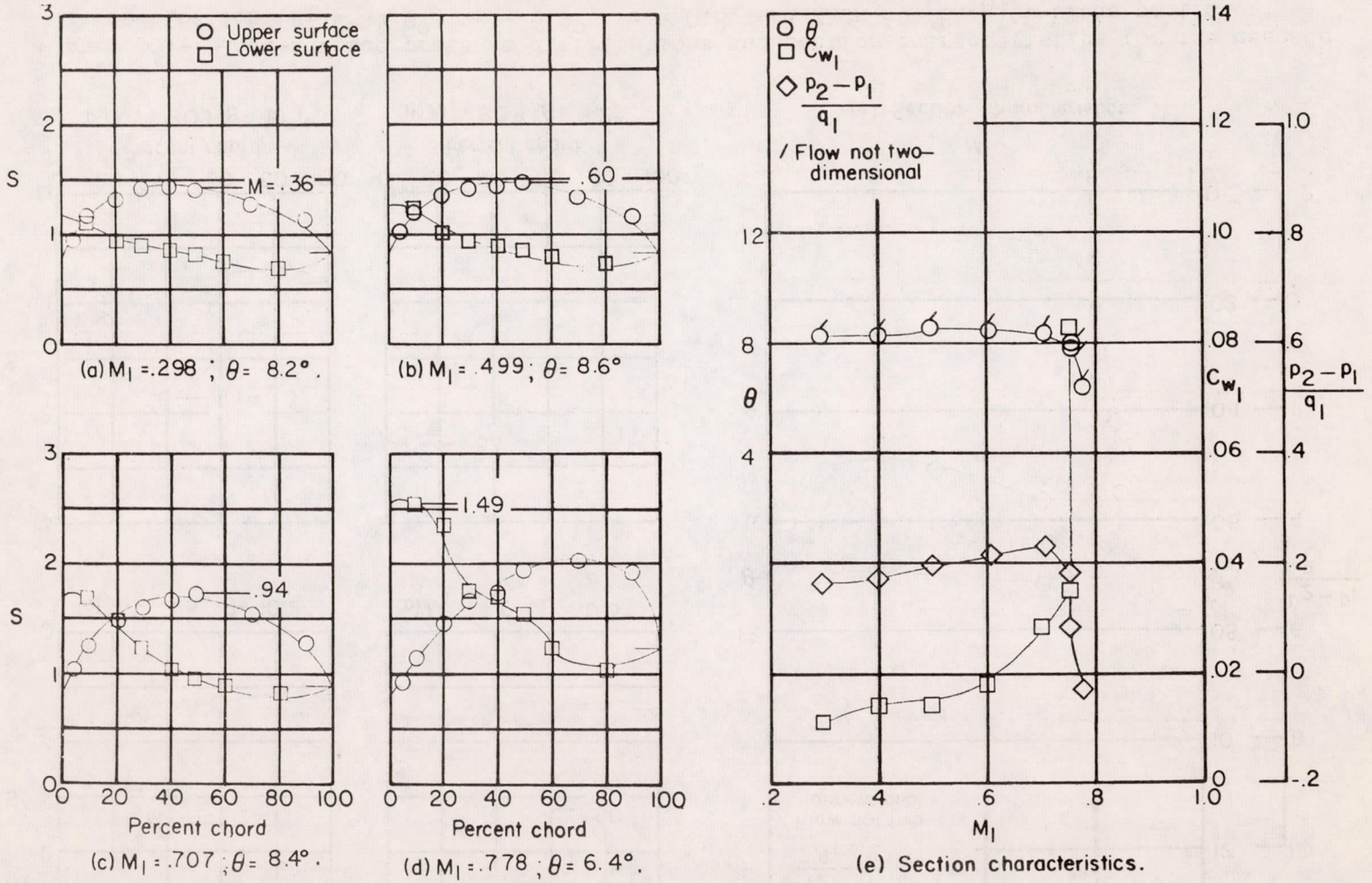



Figure 34.- Blade-surface pressure distributions and section characteristics for the cascade combination $\beta_1 = 41.0°$, $\alpha = 3.2°$, $\sigma = 0.8$, and NACA 65-$(8A_{10})$06 blade section.

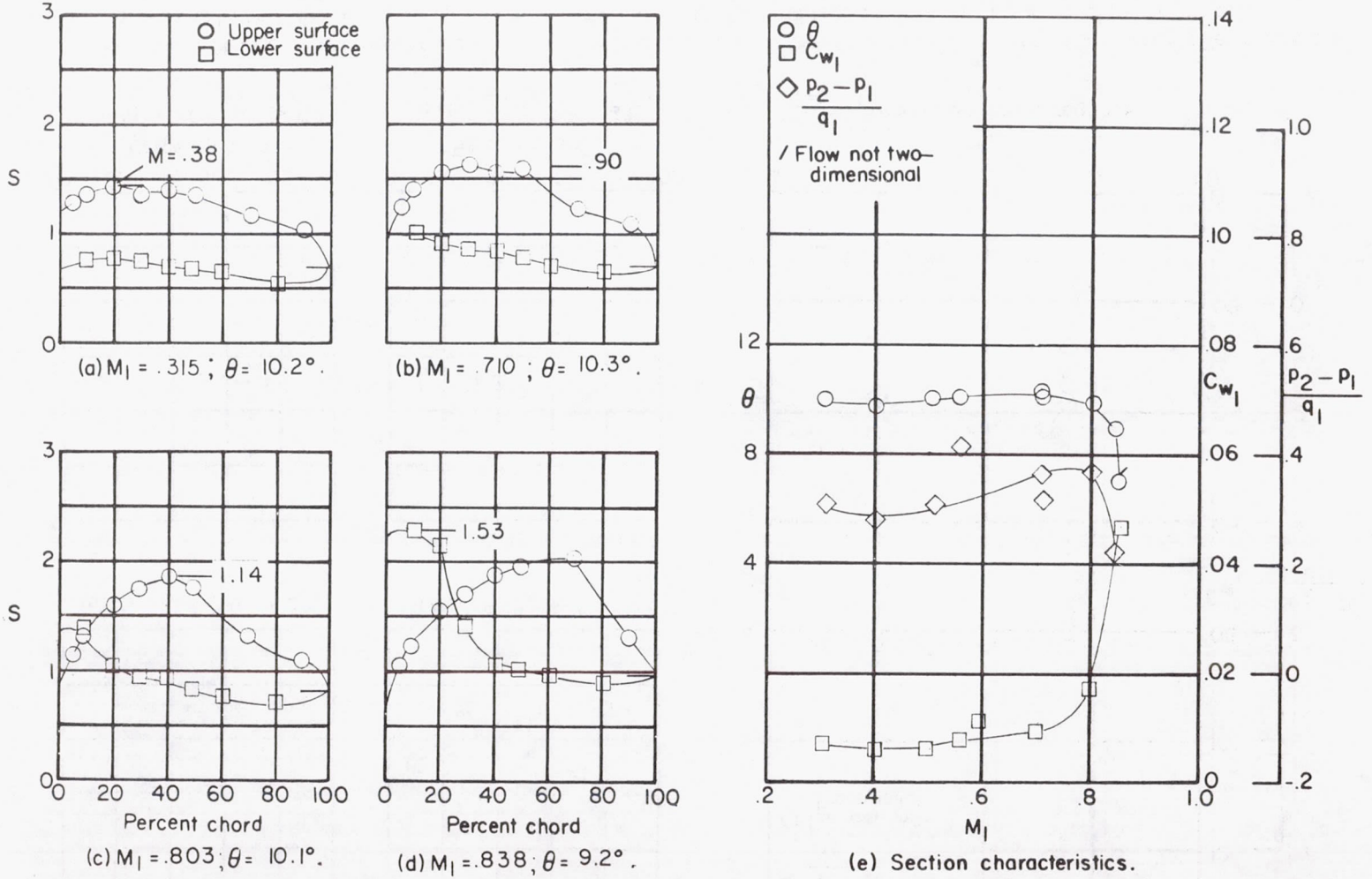



Figure 35.- Blade-surface pressure distributions and section characteristics for the cascade combination $\beta_1 = 44.0°$, $\alpha = 6.2°$, $\sigma = 0.8$, and NACA 65-$(8A_{10})$06 blade section.

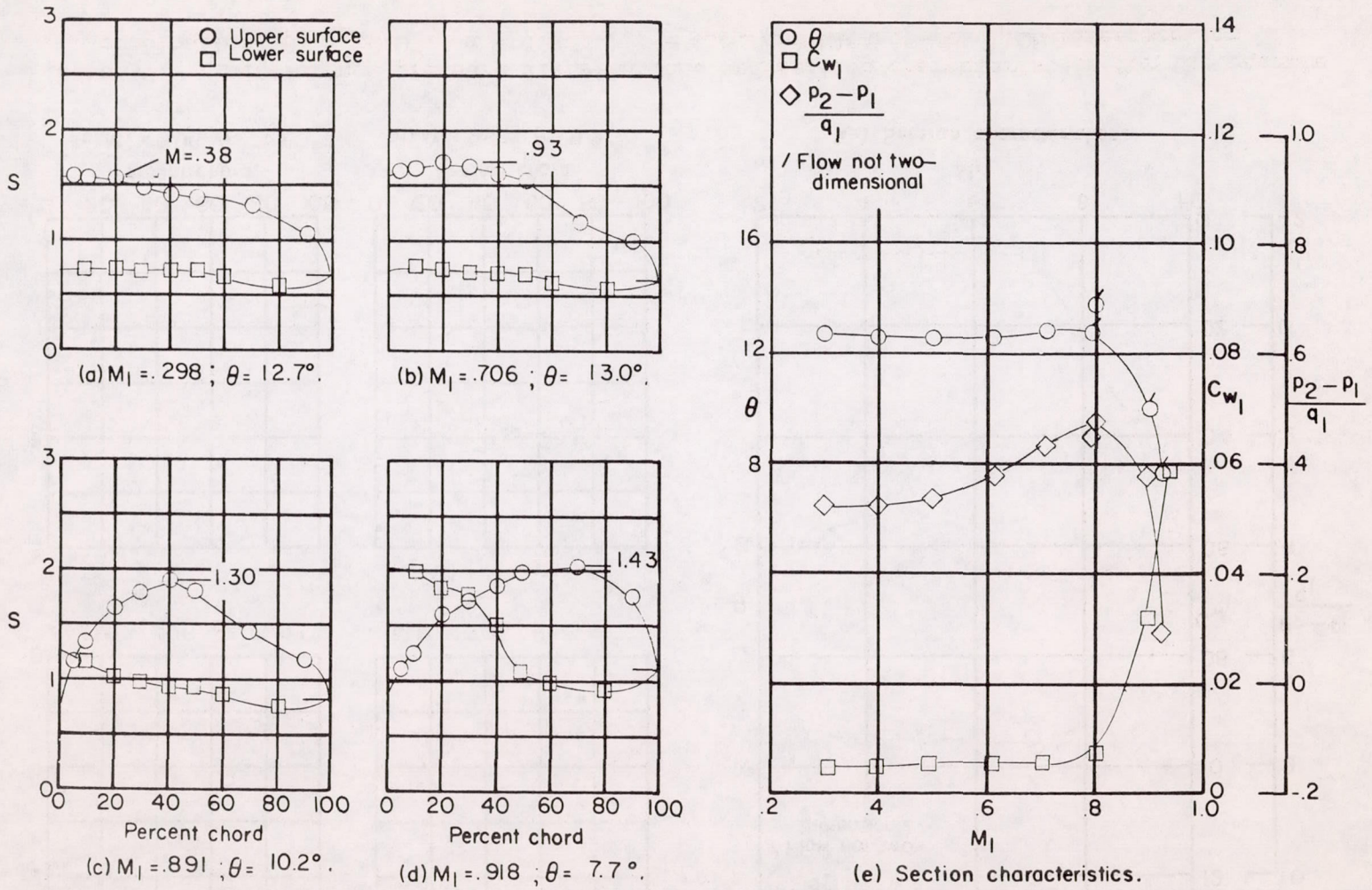



Figure 36.- Blade-surface pressure distributions and section characteristics for the cascade combination $\beta_1 = 47.0°$, $\alpha = 9.2°$, $\sigma = 0.8$, and NACA 65-$(8A_{10})$06 blade section.

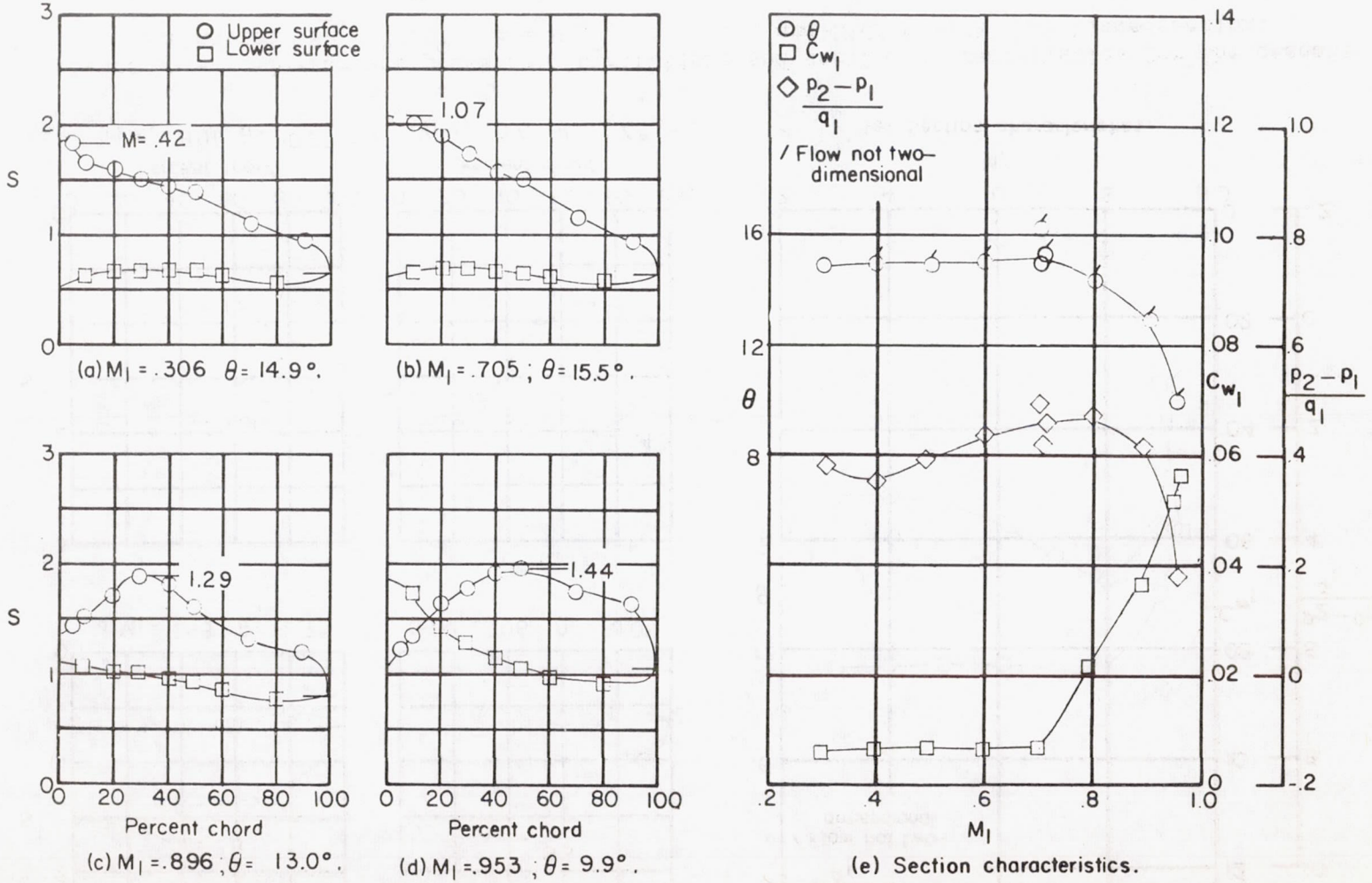



Figure 37.- Blade-surface pressure distributions and section characteristics for the cascade combination $\beta_1 = 50.0^\circ$, $\alpha = 12.2^\circ$, $\sigma = 0.8$, and NACA 65-$(8A_{10})$06 blade section.

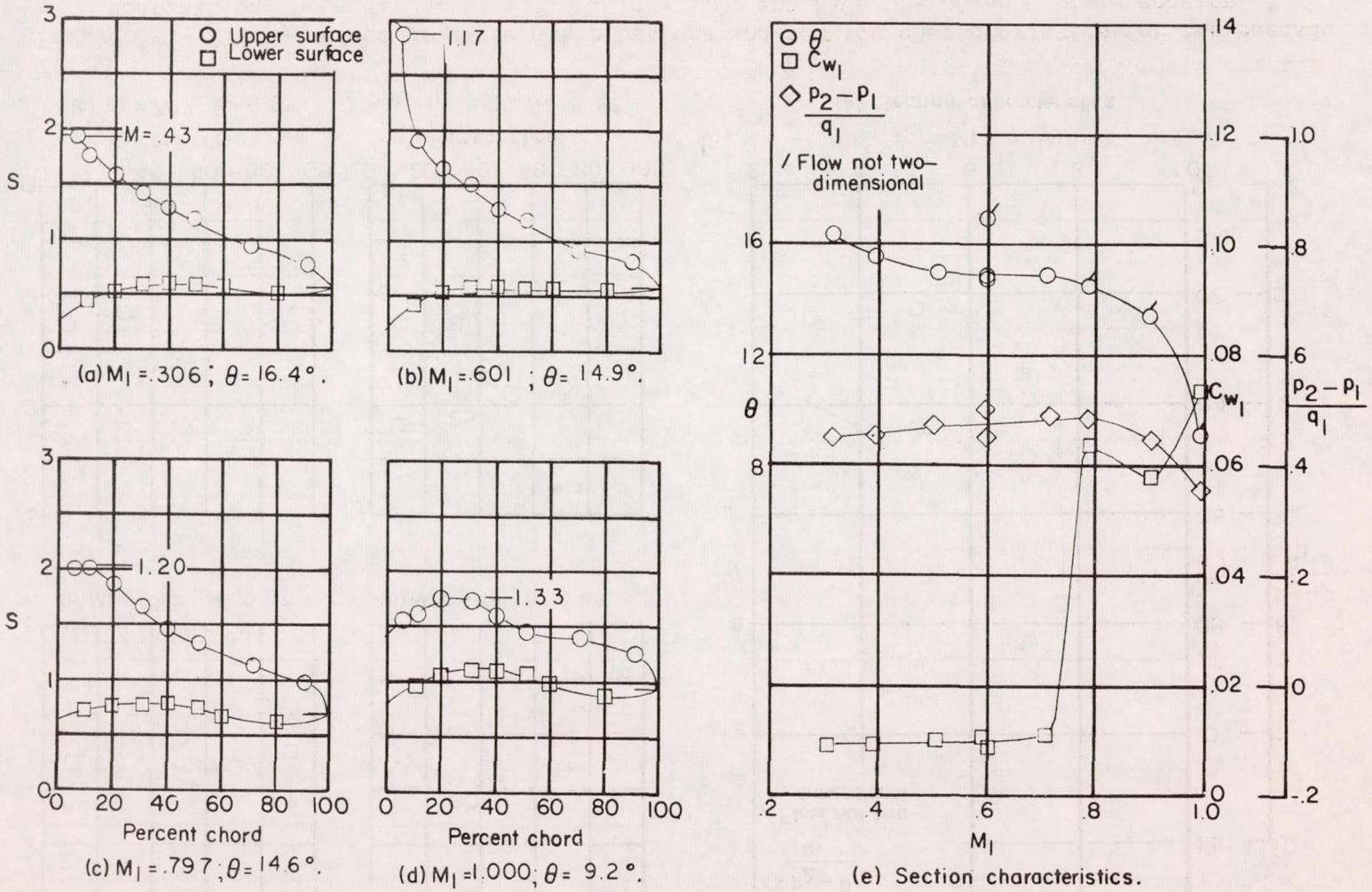



Figure 38.- Blade-surface pressure distributions and section characteristics for the cascade combination $\beta_1 = 53.0°$, $\alpha = 15.2°$, $\sigma = 0.8$, and NACA 65-$(8A_{10})$06 blade section.

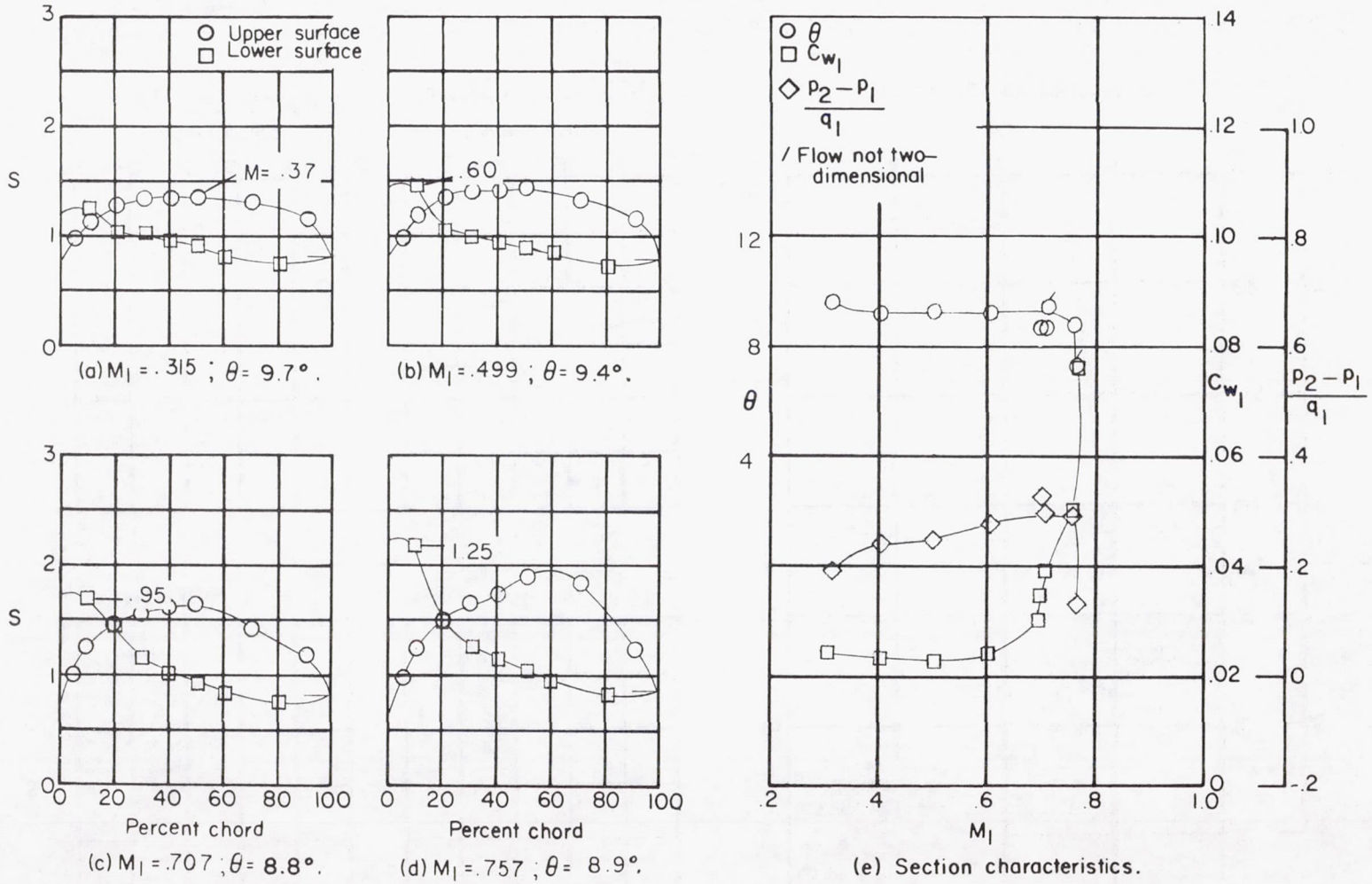



Figure 39.- Blade-surface pressure distributions and section characteristics for the cascade combination $\beta_1 = 41.0°$, $\alpha = 3.5°$, $\sigma = 1.0$, and NACA 65-$(8A_{10})$06 blade section.

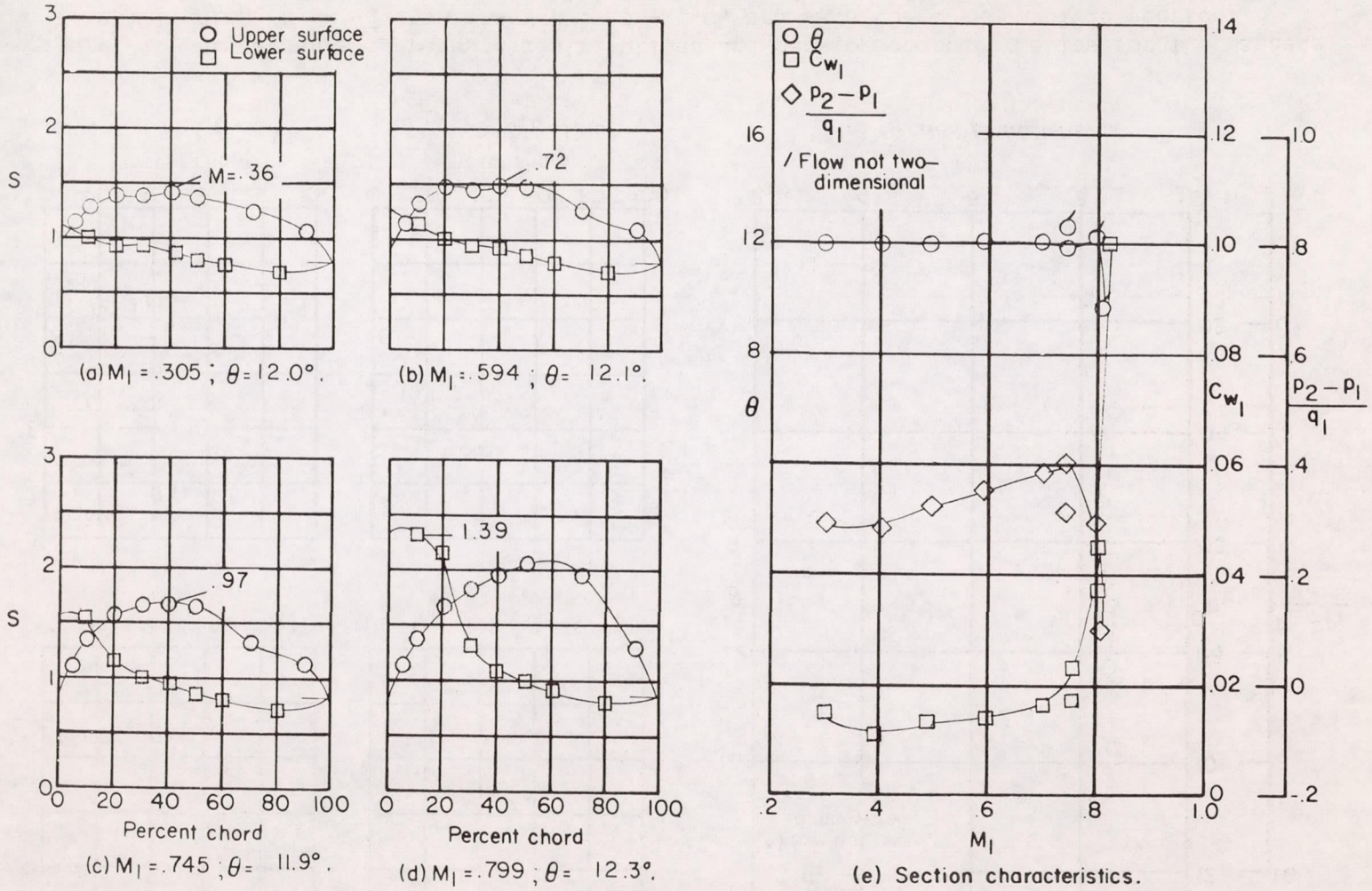



Figure 40.- Blade-surface pressure distributions and section characteristics for the cascade combination $\beta_1 = 44.0°$, $\alpha = 6.5°$, $\sigma = 1.0$, and NACA 65-$(8A_{10})$06 blade section.

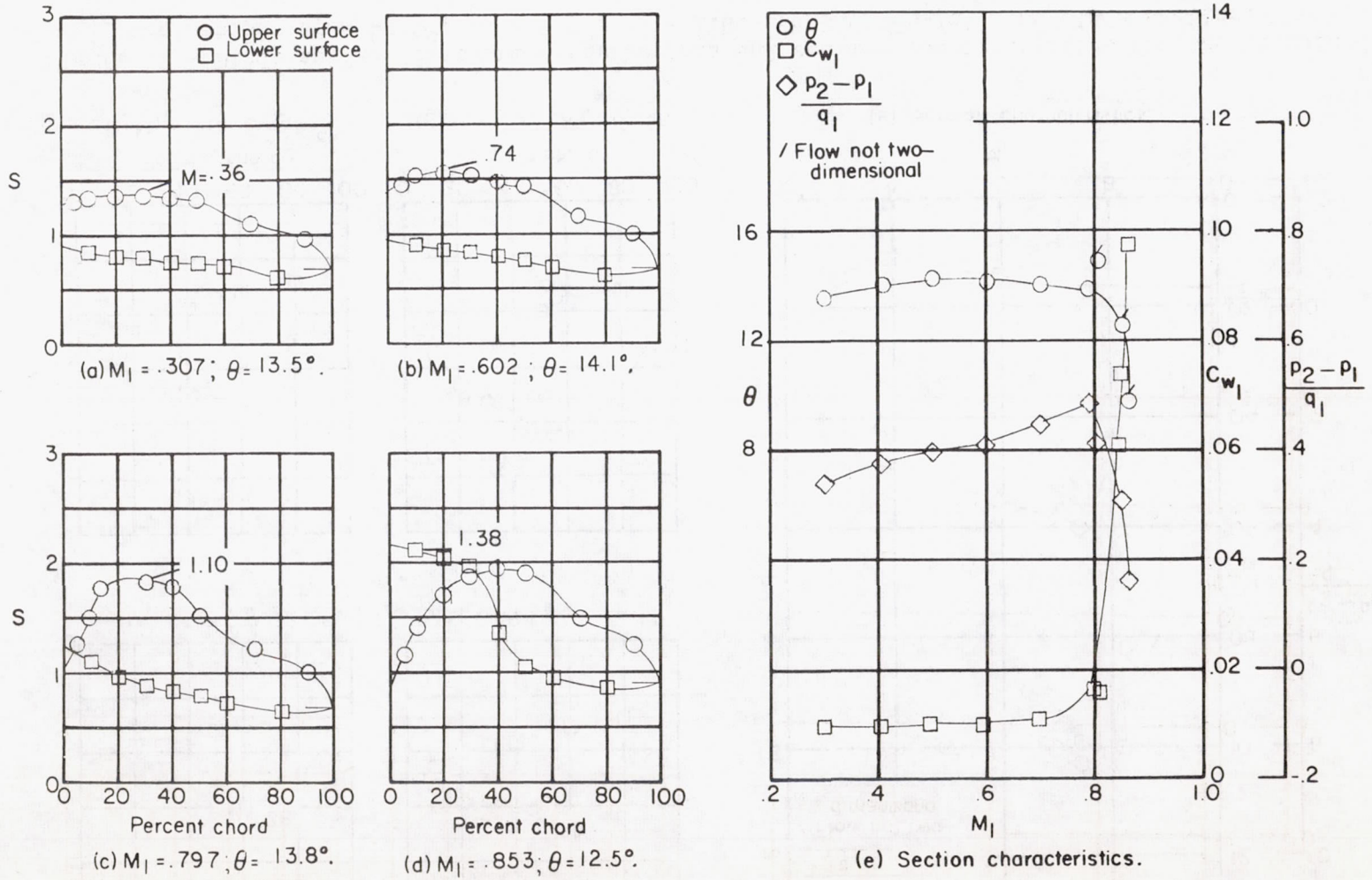



Figure 41.- Blade-surface pressure distributions and section characteristics for the cascade combination $\beta_1 = 47.0°$, $\alpha = 9.5°$, $\sigma = 1.0$, and NACA 65-$(8A_{10})$06 blade section.

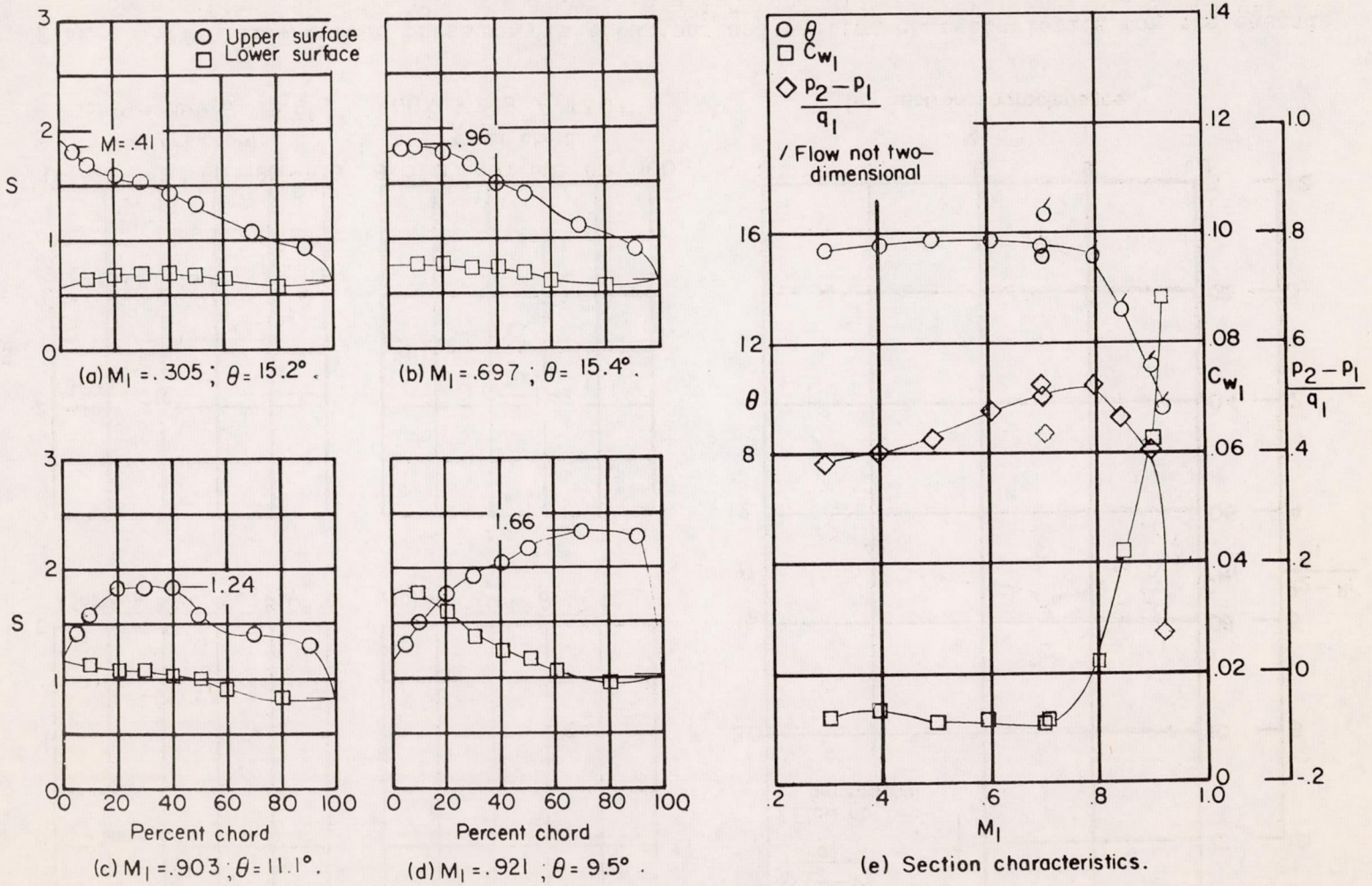



Figure 42.- Blade-surface pressure distributions and section characteristics for the cascade combination $\beta_1 = 50.0°$, $\alpha = 12.5°$, $\sigma = 1.0$, and NACA 65-$(8A_{10})$06 blade section.

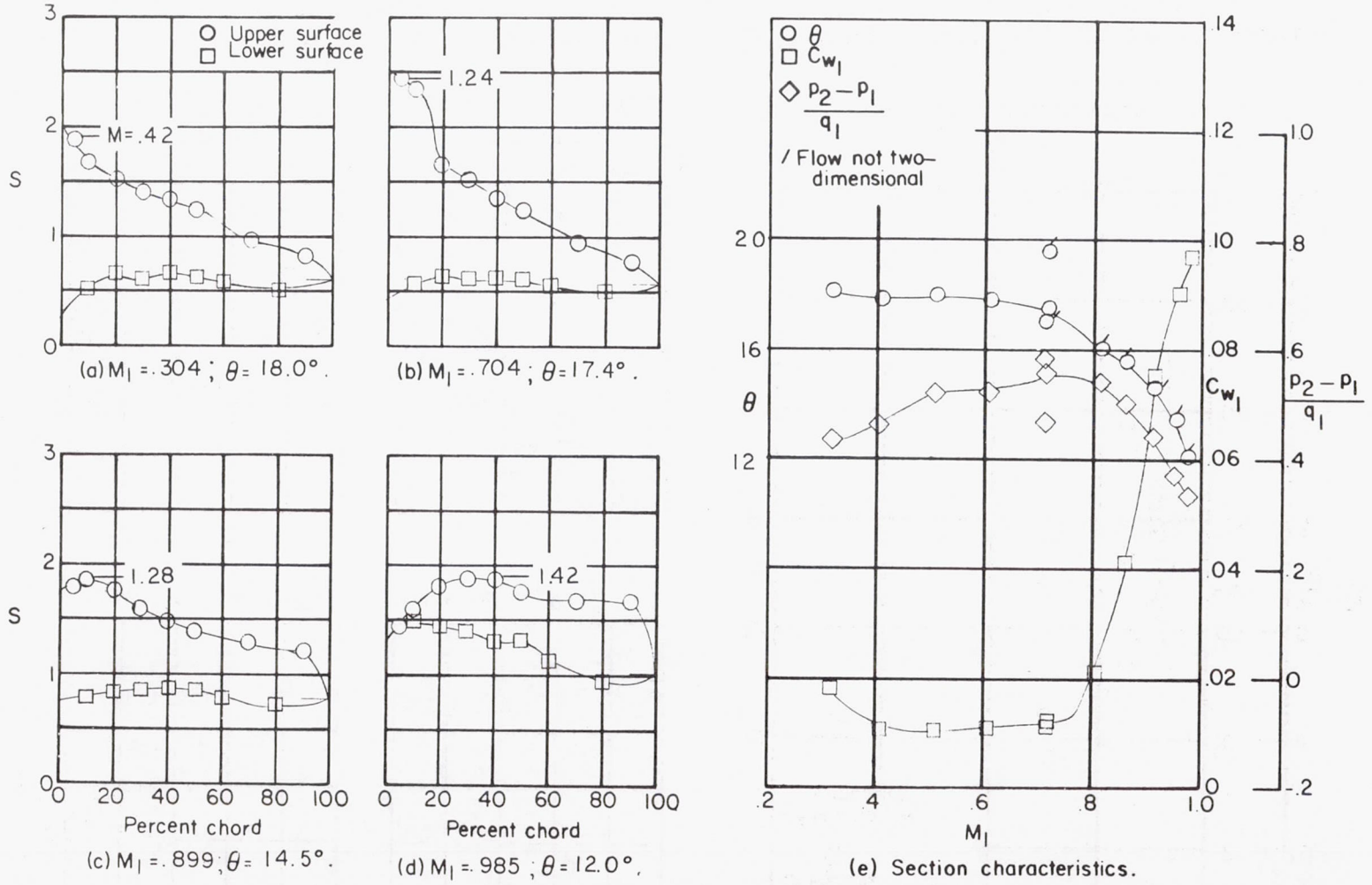



Figure 43.- Blade-surface pressure distributions and section characteristics for the cascade combination $\beta_1 = 53.0^\circ$, $\alpha = 15.5^\circ$, $\sigma = 1.0$, and NACA 65-$(8A_{10})$06 blade section.

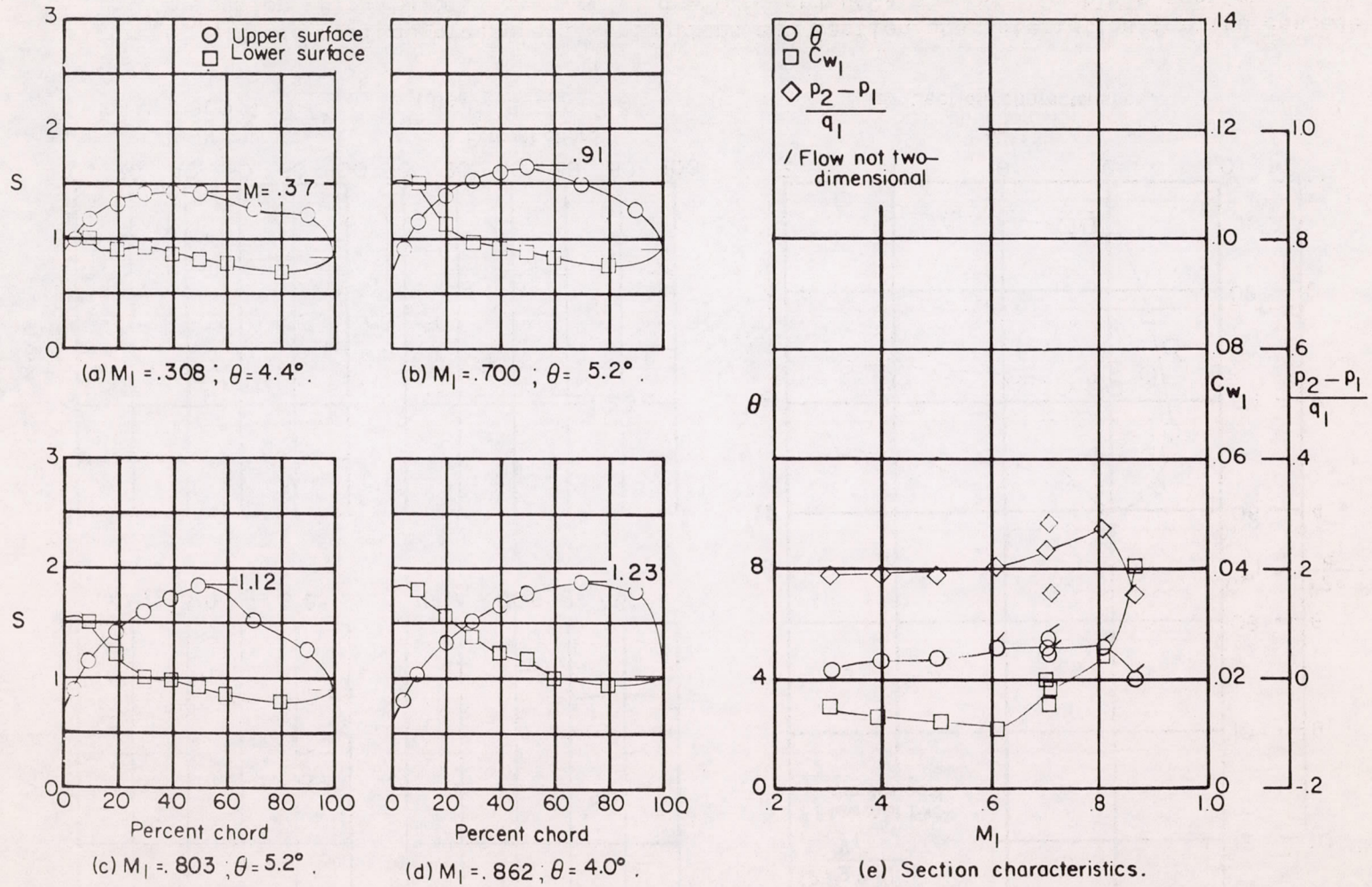



Figure 44.- Blade-surface pressure distributions and section characteristics for the cascade combination $\beta_1 = 51.0^\circ$, $\alpha = 1.0^\circ$, $\sigma = 0.6$, and NACA 65-$(8A_{10})$06 blade section.

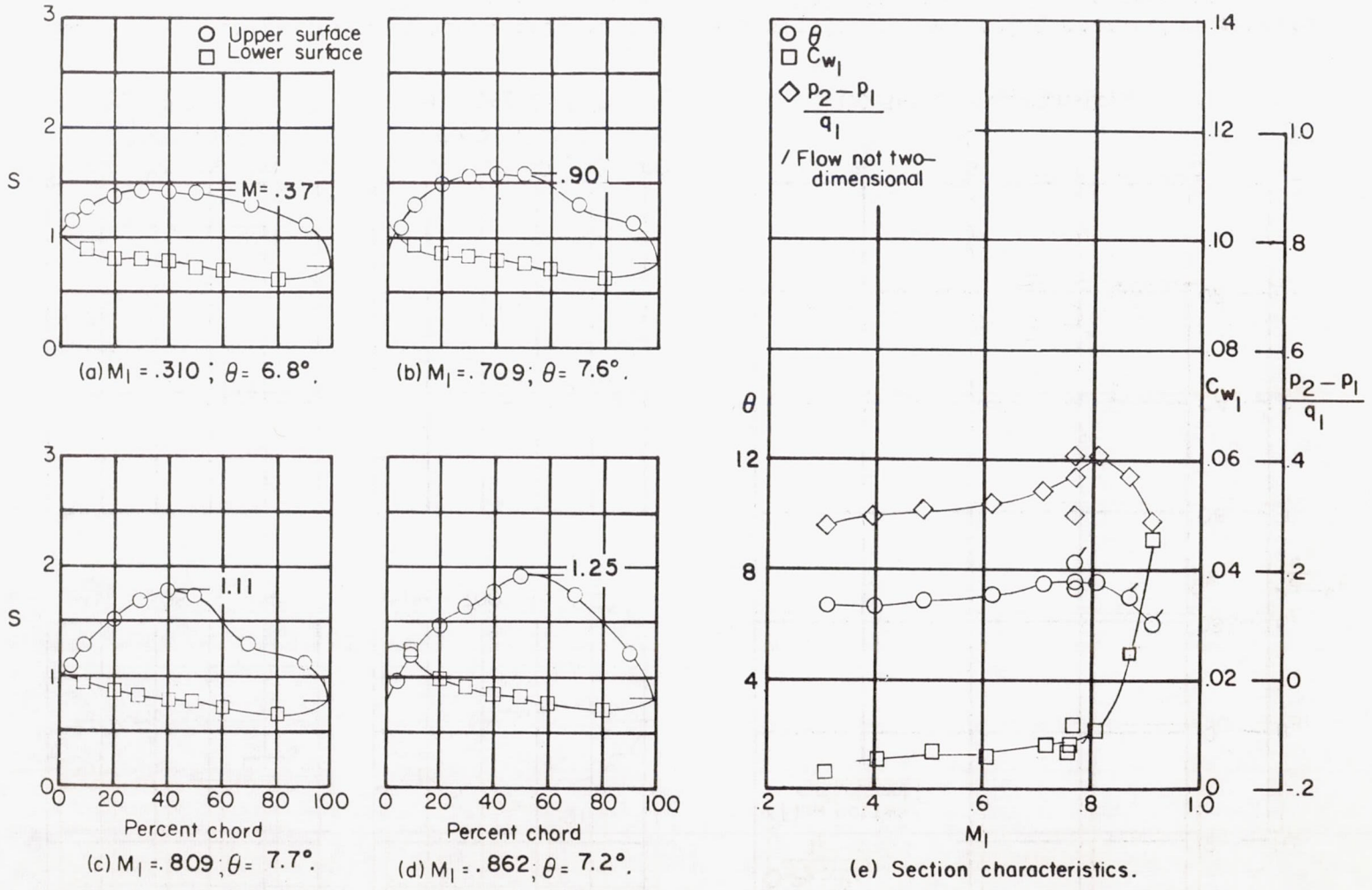



Figure 45.- Blade-surface pressure distributions and section characteristics for the cascade combination $\beta_1 = 54.0°$, $\alpha = 4.0°$, $\sigma = 0.6$, and NACA 65-$(8A_{10})$06 blade section.

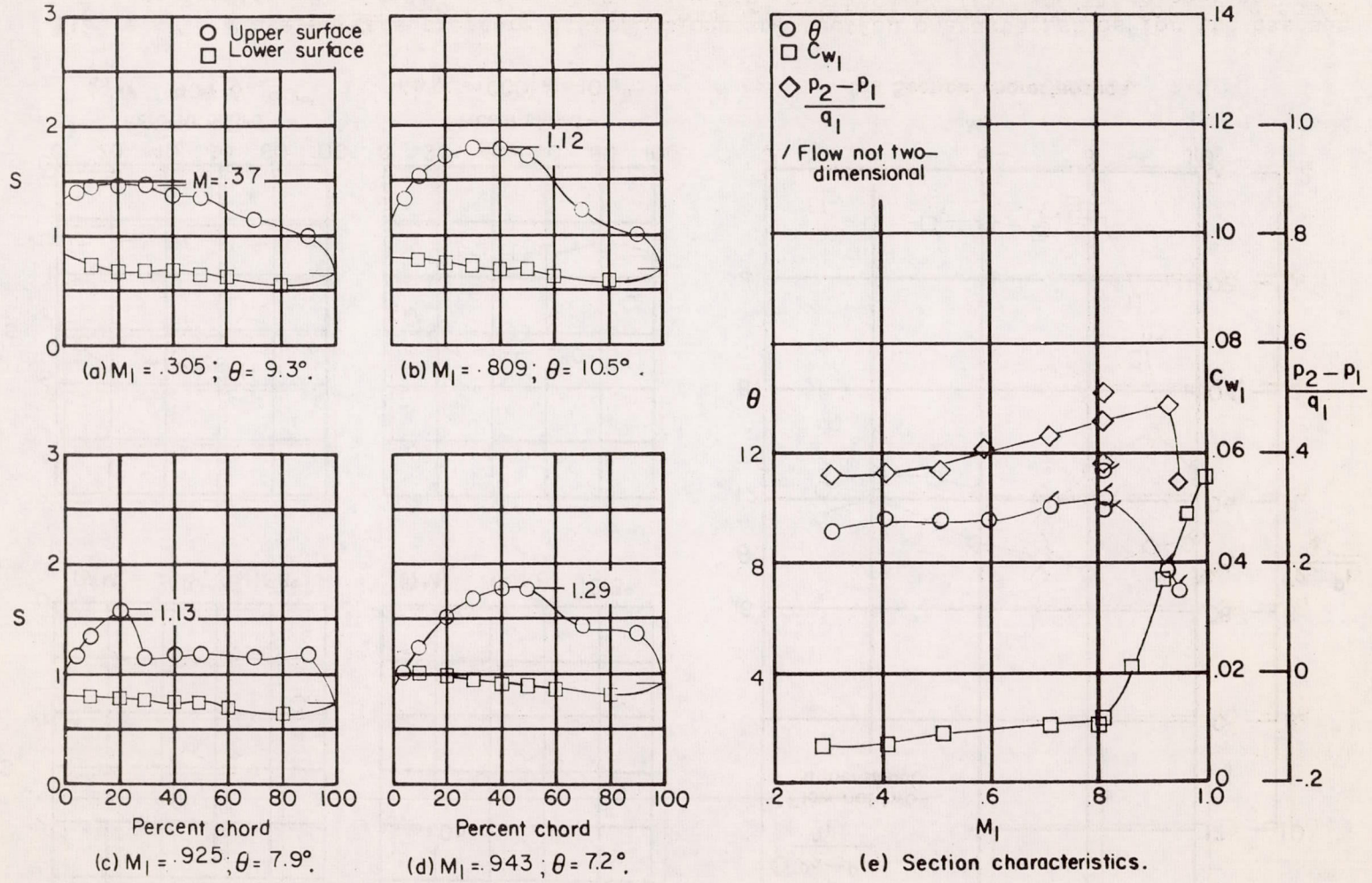



Figure 46.- Blade-surface pressure distributions and section characteristics for the cascade combination $\beta_1 = 57.0^\circ$, $\alpha = 7.0^\circ$, $\sigma = 0.6$, and NACA 65-$(8A_{10})$06 blade section.

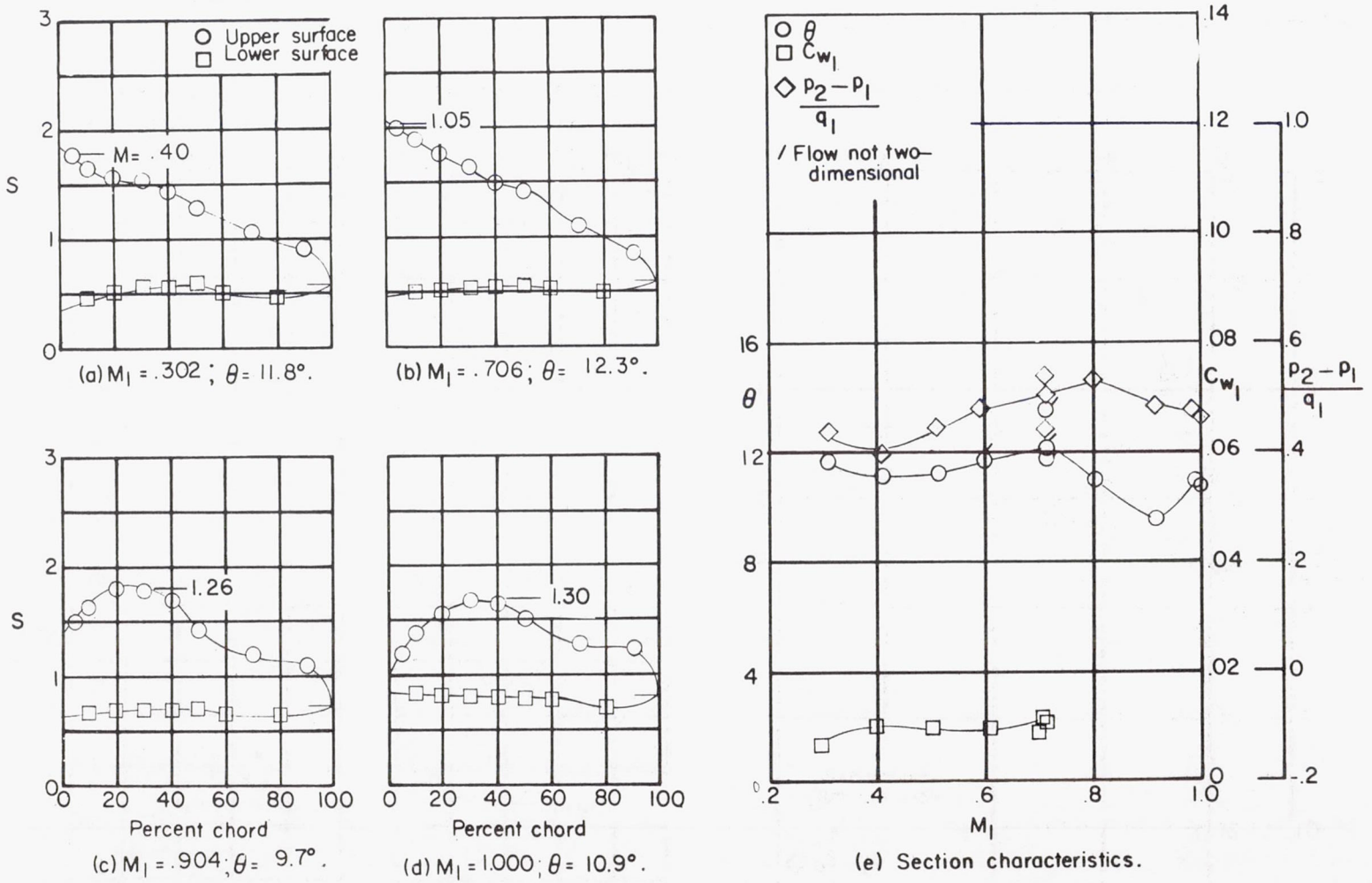



Figure 47.- Blade-surface pressure distributions and section characteristics for the cascade combination $\beta_1 = 60.0^\circ$, $\alpha = 10.0^\circ$, $\sigma = 0.6$, and NACA 65-$(8A_{10})$06 blade section.

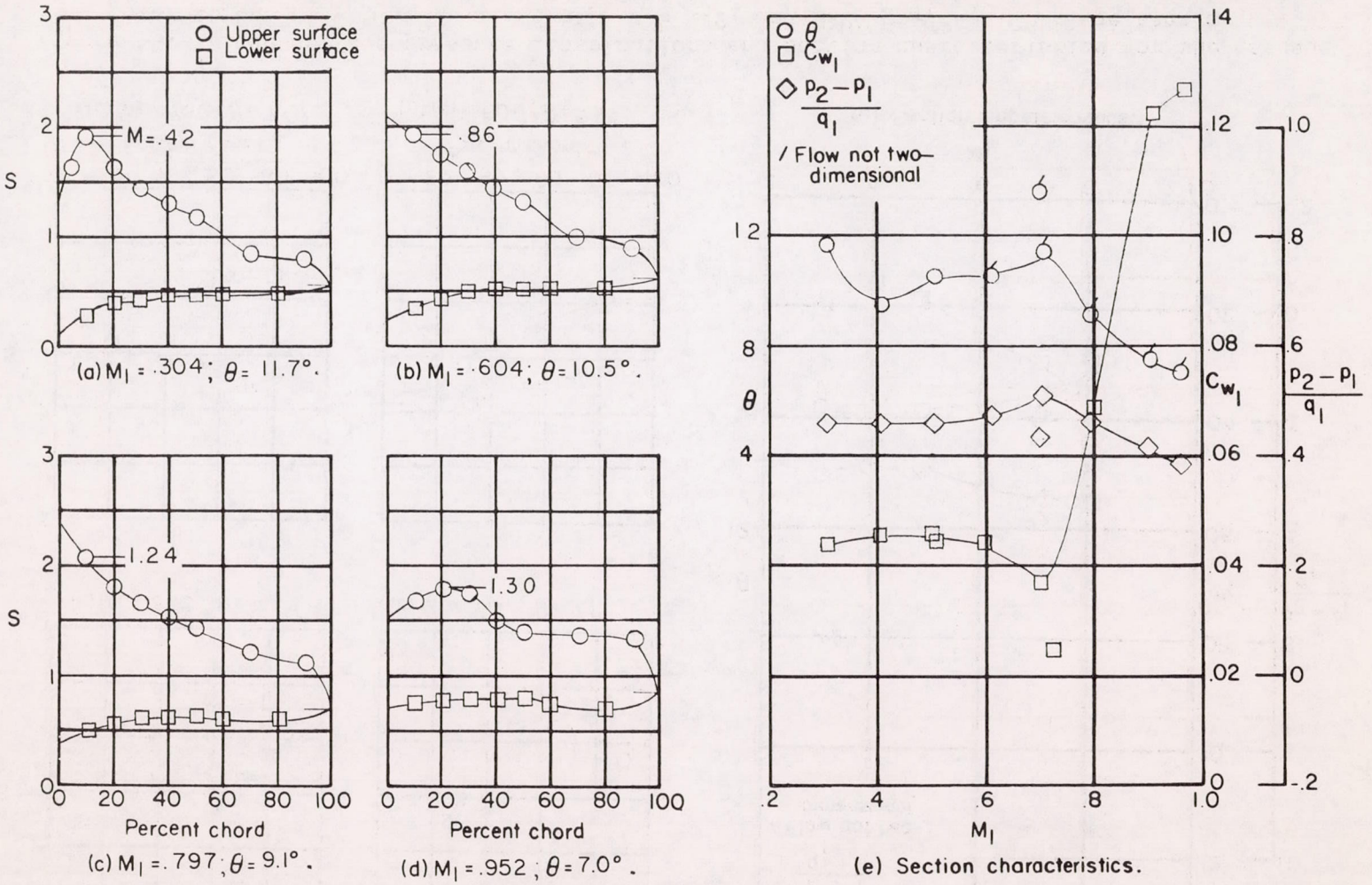



Figure 48.- Blade-surface pressure distributions and section characteristics for the cascade combination $\beta_1 = 63.0°$, $\alpha = 13.0°$, $\sigma = 0.6$, and NACA 65-$\left(8A_{10}\right)$06 blade section.

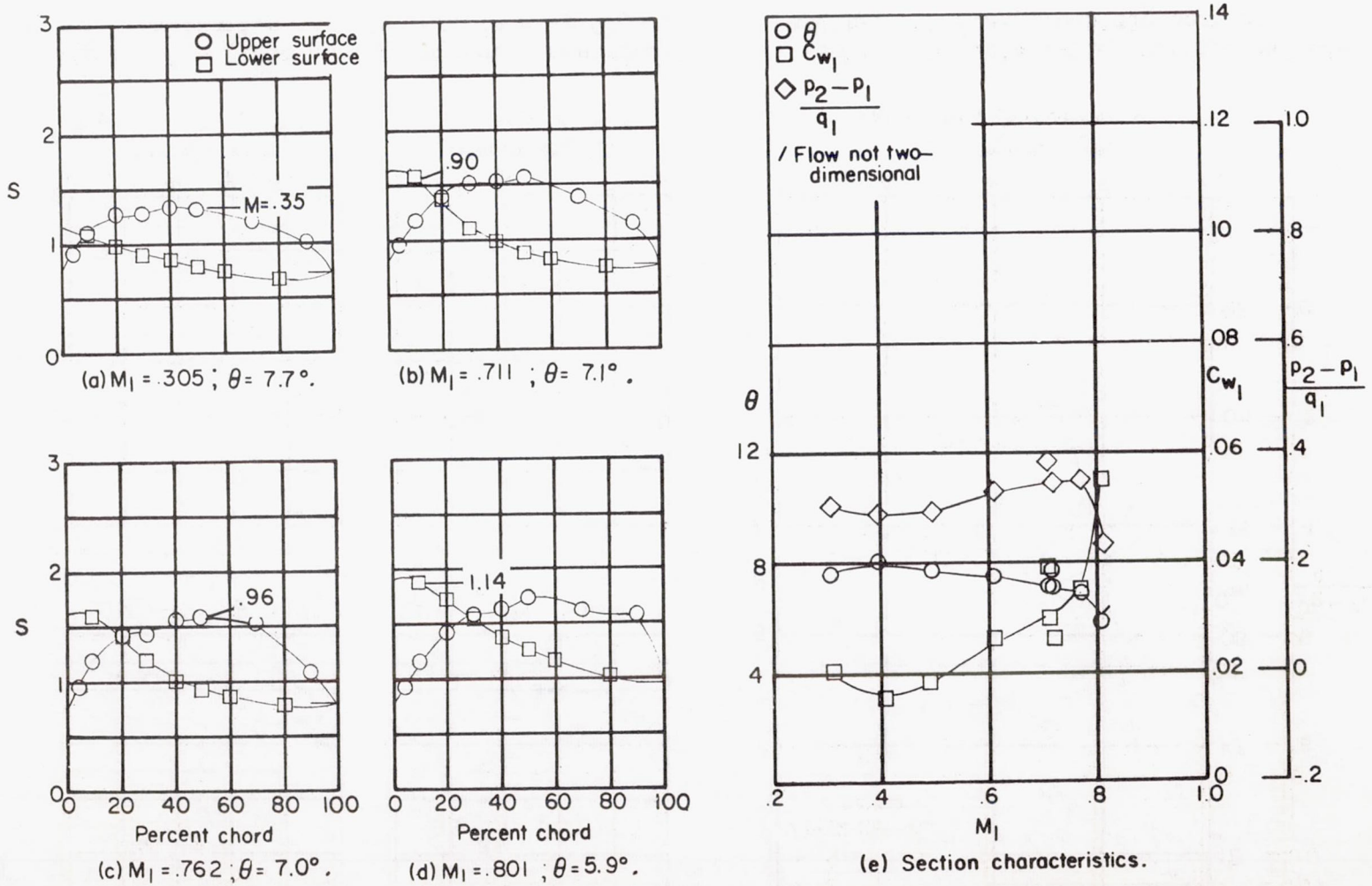



Figure 49.- Blade-surface pressure distributions and section characteristics for the cascade combination $\beta_1 = 51.0^\circ$, $\alpha = 3.5^\circ$, $\sigma = 1.0$, and NACA 65-$(8A_{10})$06 blade section.

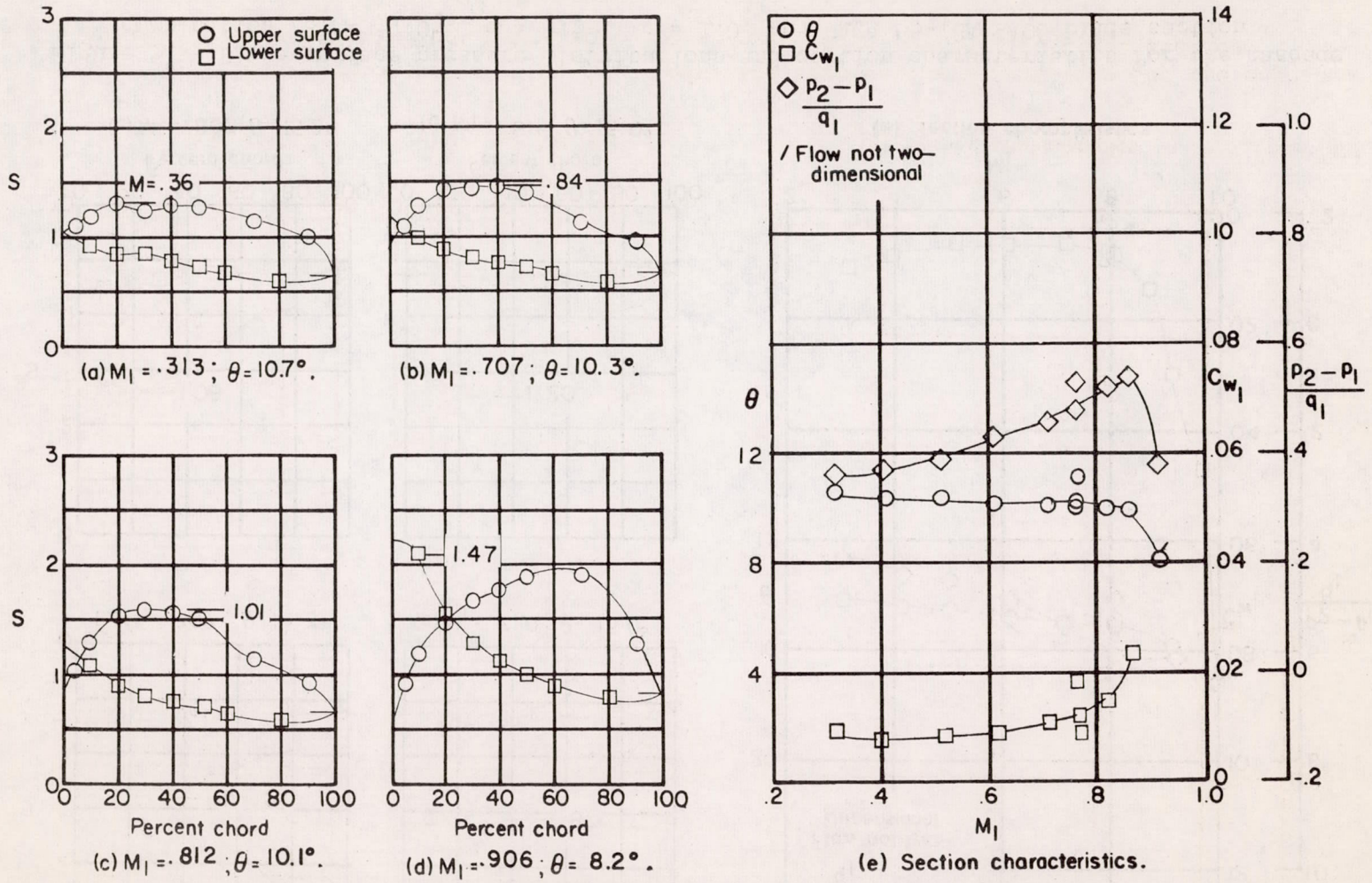



Figure 50.- Blade-surface pressure distributions and section characteristics for the cascade combination $\beta_1 = 54.0°$, $\alpha = 6.5°$, $\sigma = 1.0$, and NACA 65-$(8A_{10})$06 blade section.

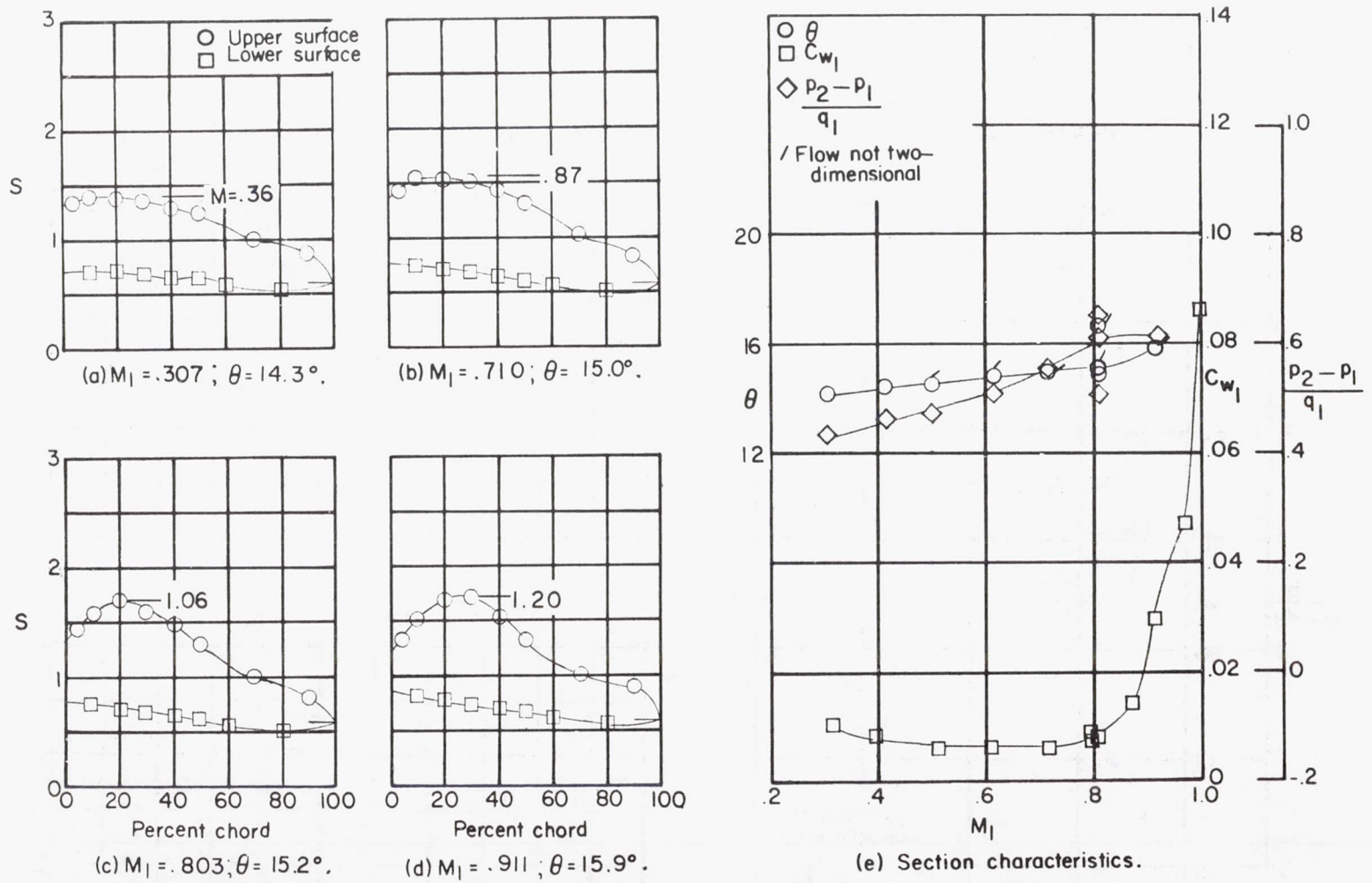



Figure 51.- Blade-surface pressure distributions and section characteristics for the cascade combination $\beta_1 = 57.0°$, $\alpha = 9.5°$, $\sigma = 1.0$, and NACA 65-$(8A_{10})$06 blade section.

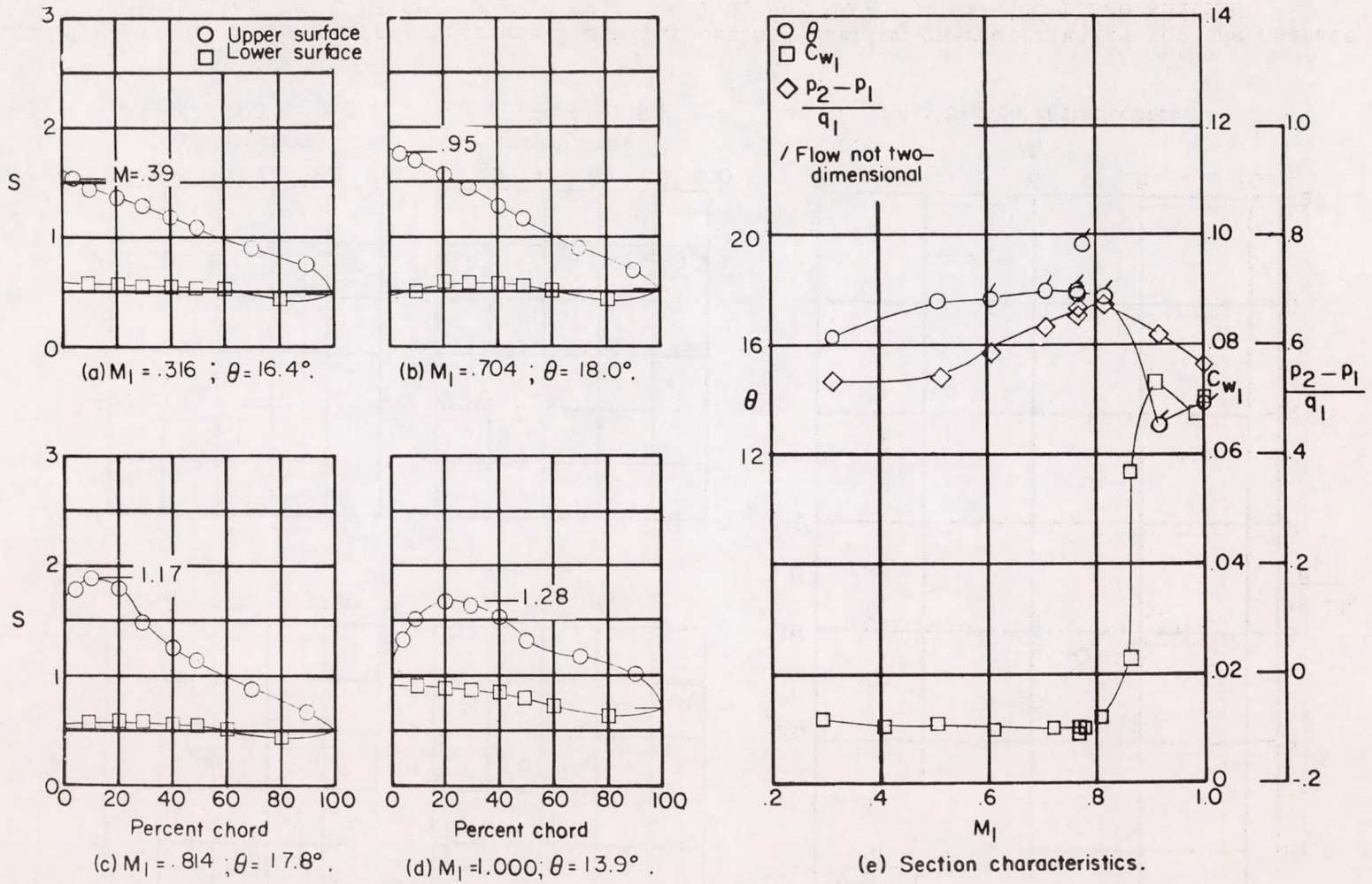



Figure 52.- Blade-surface pressure distributions and section characteristics for the cascade combination $\beta_1 = 60.0^\circ$, $\alpha = 12.5^\circ$, $\sigma = 1.0$, and NACA 65-$(8A_{10})$06 blade section.

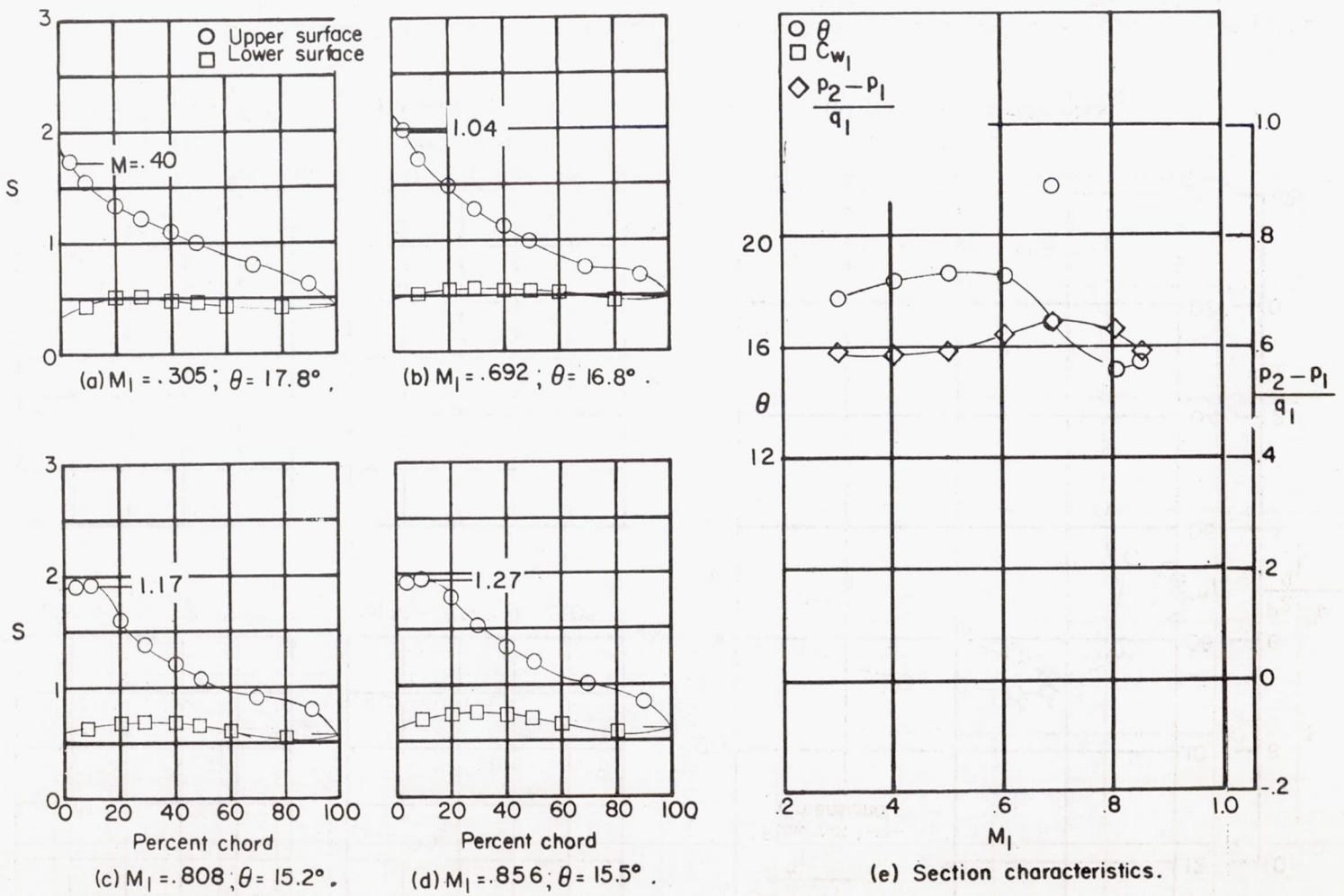



Figure 53.- Blade-surface pressure distributions and section characteristics for the cascade combination $\beta_1 = 63.0°$, $\alpha = 15.5°$, $\sigma = 1.0$, and NACA 65-$(8A_{10})$06 blade section. (Losses were not measured due to repeated blade failure.)

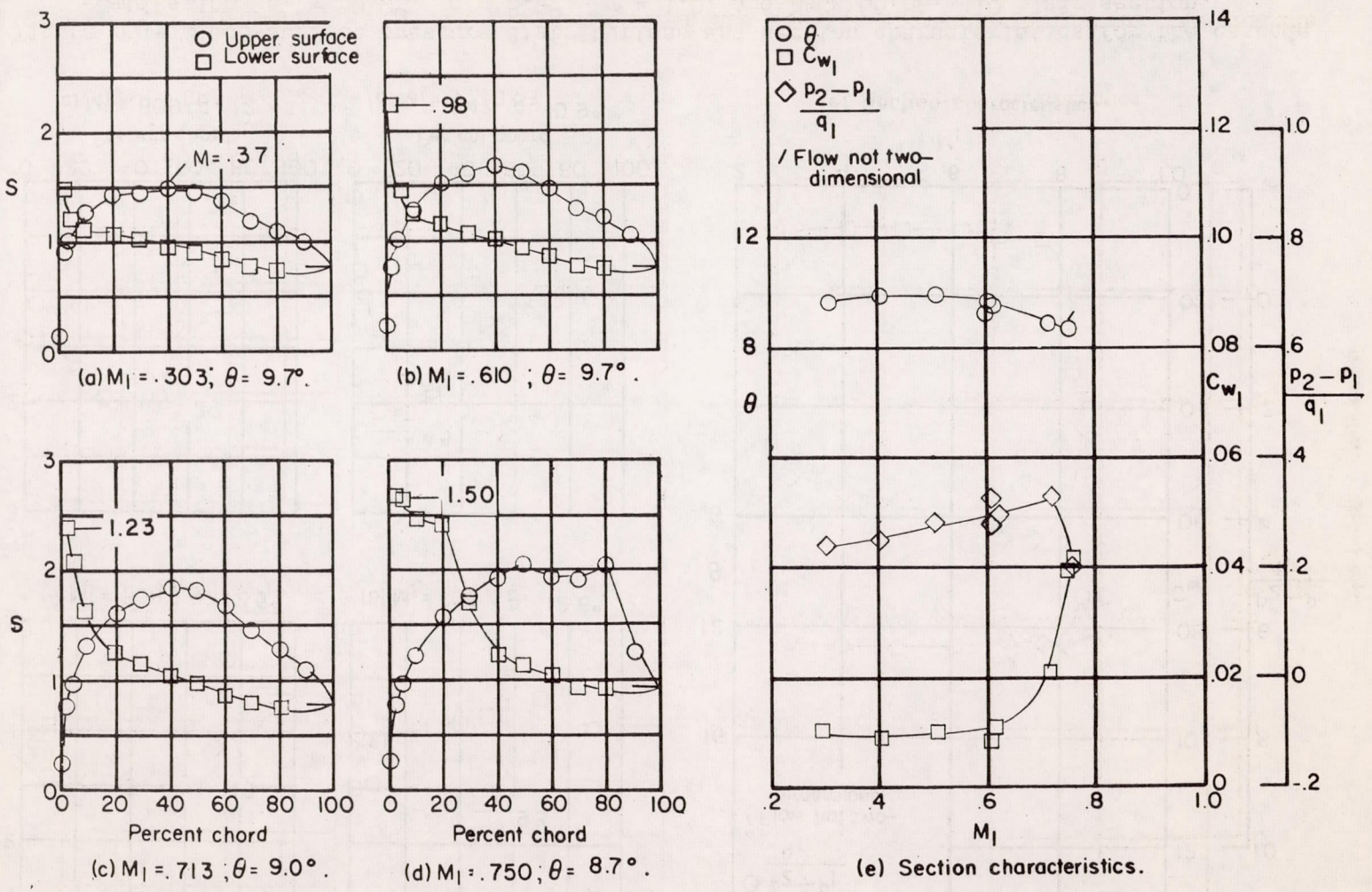



Figure 54.- Blade-surface pressure distributions and section characteristics for the cascade combination $\beta_1 = 47.0°$, $\alpha = 5.2°$, $\sigma = 1.0$, and NACA 65-$\left(8A_{10}\right)$10 blade section.

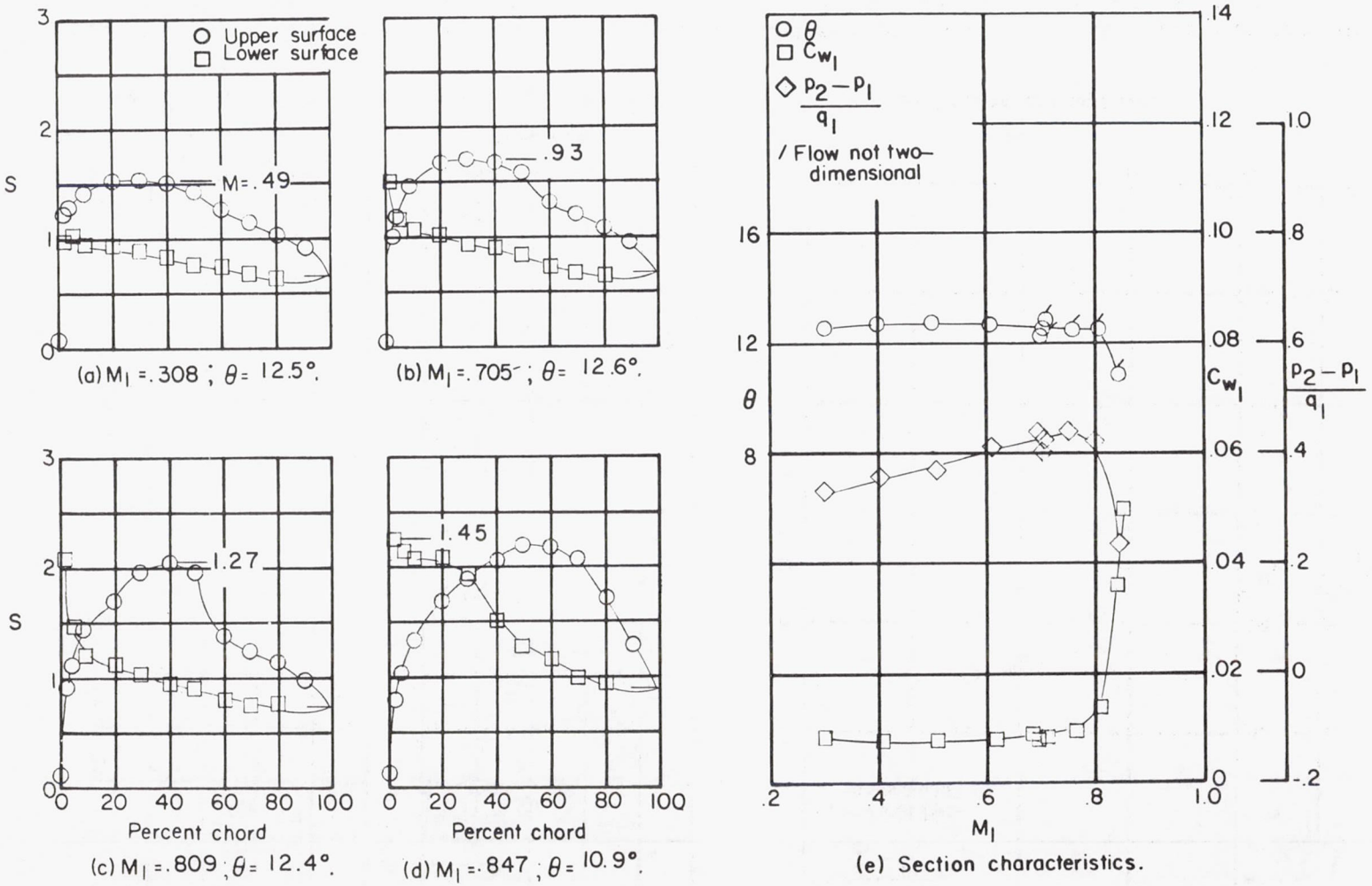



Figure 55.- Blade-surface pressure distributions and section characteristics for the cascade combination $\beta_1 = 50.0°$, $\alpha = 8.2°$, $\sigma = 1.0$, and NACA $65\left(8A_{10}\right)10$ blade section.

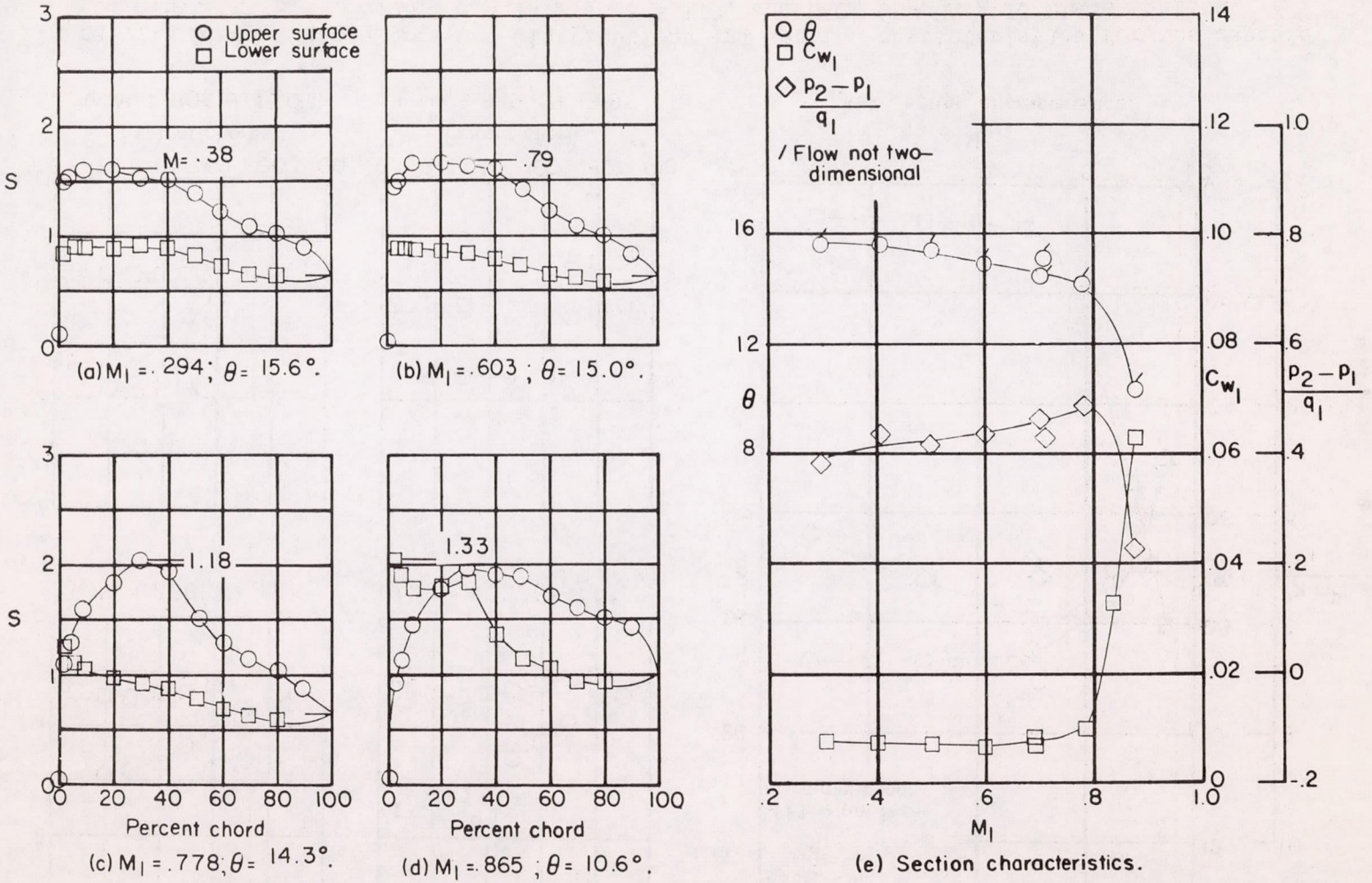



Figure 56.- Blade-surface pressure distributions and section characteristics for the cascade combination $\beta_1 = 53.0^\circ$, $\alpha = 11.2^\circ$, $\sigma = 1.0$, and NACA 65-$(8A_{10})$10 blade section.

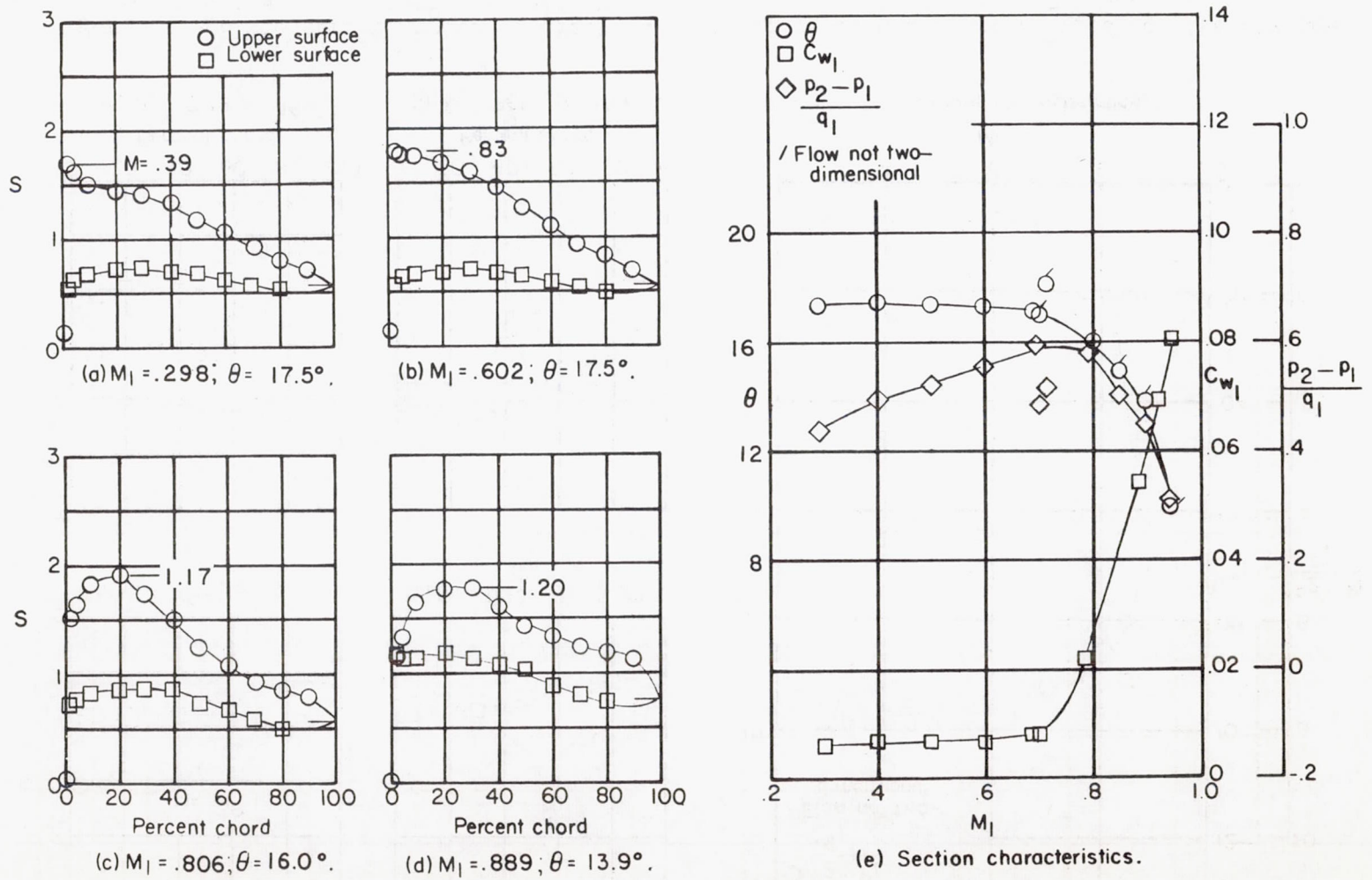



Figure 57.- Blade-surface pressure distributions and section characteristics for the cascade combination $\beta_1 = 56.0°$, $\alpha = 14.2°$, $\sigma = 1.0$, and NACA 65-$(8A_{10})$10 blade section.

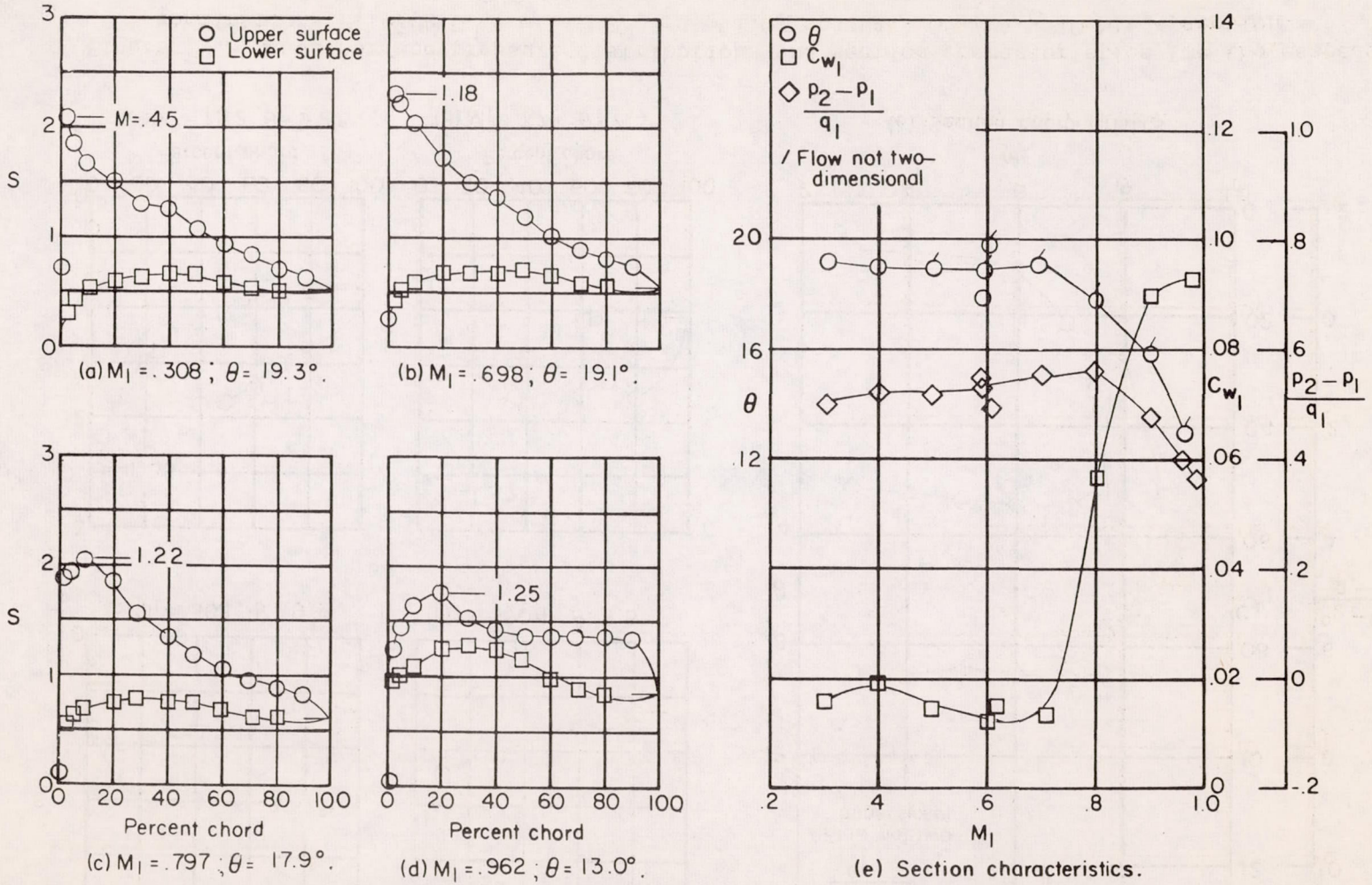



Figure 58.- Blade-surface pressure distributions and section characteristics for the cascade combination $\beta_1 = 59.0^\circ$, $\alpha = 17.2^\circ$, $\sigma = 1.0$, and NACA 65-$(8A_{10})$10 blade section.

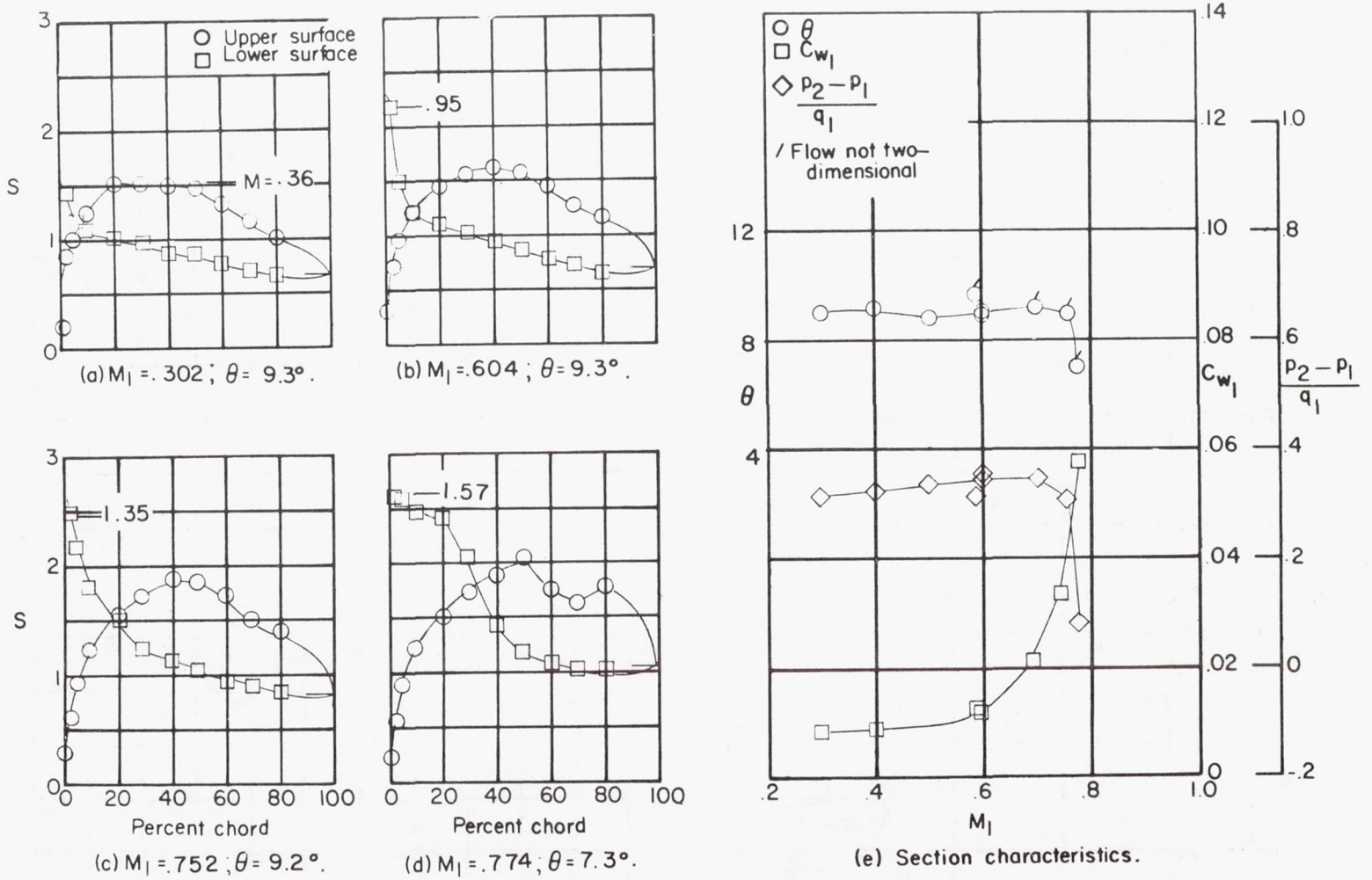



Figure 59.- Blade-surface pressure distributions and section characteristics for the cascade combination $\beta_1 = 54.0^\circ$, $\alpha = 5.2^\circ$, $\sigma = 1.0$, and NACA 65-$(8A_{10})$10 blade section.

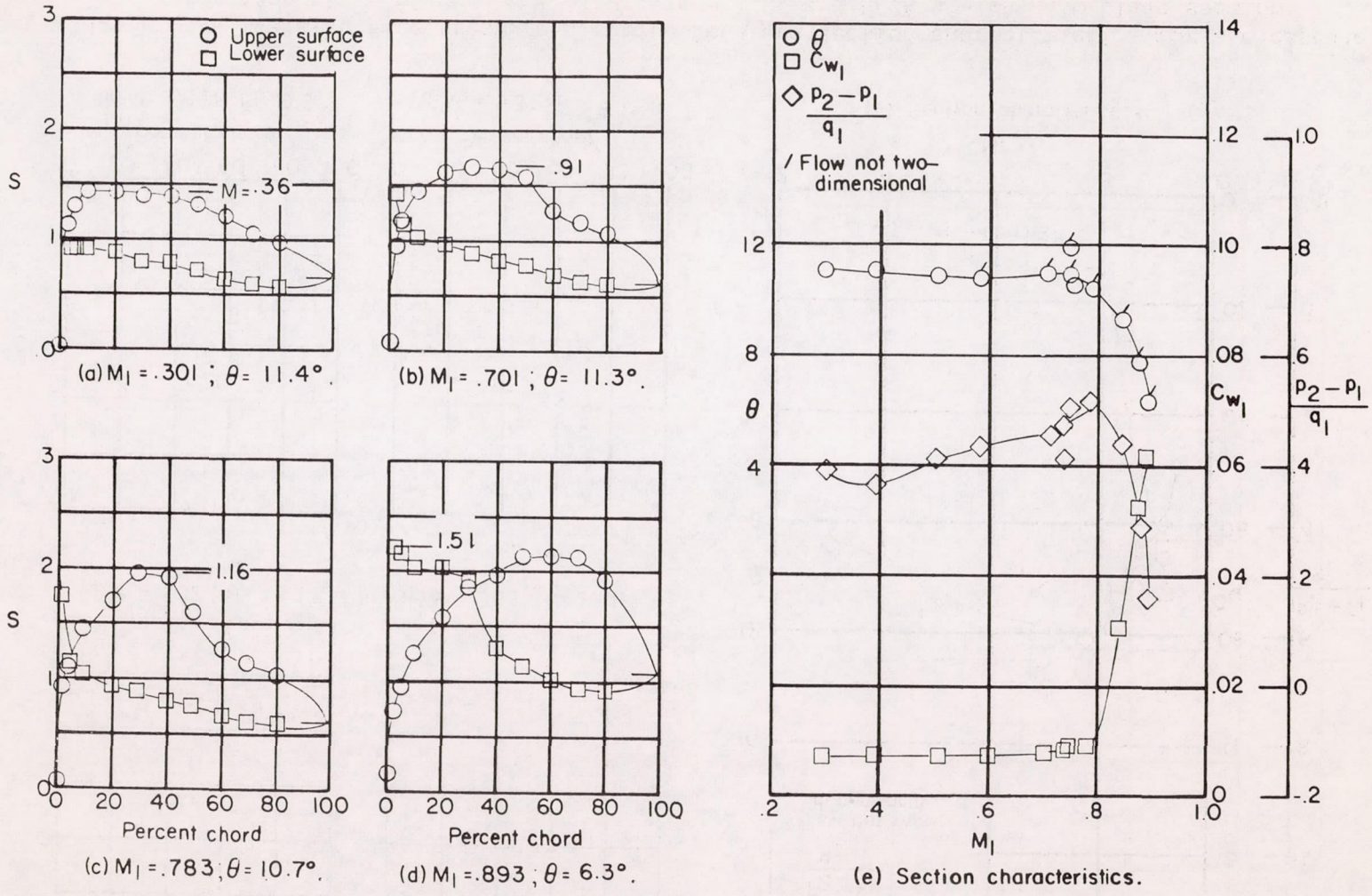



Figure 60.- Blade-surface pressure distributions and section characteristics for the cascade combination $\beta_1 = 57.0^\circ$, $\alpha = 8.2^\circ$, $\sigma = 1.0$, and NACA 65-$(8A_{10})$10 blade section.

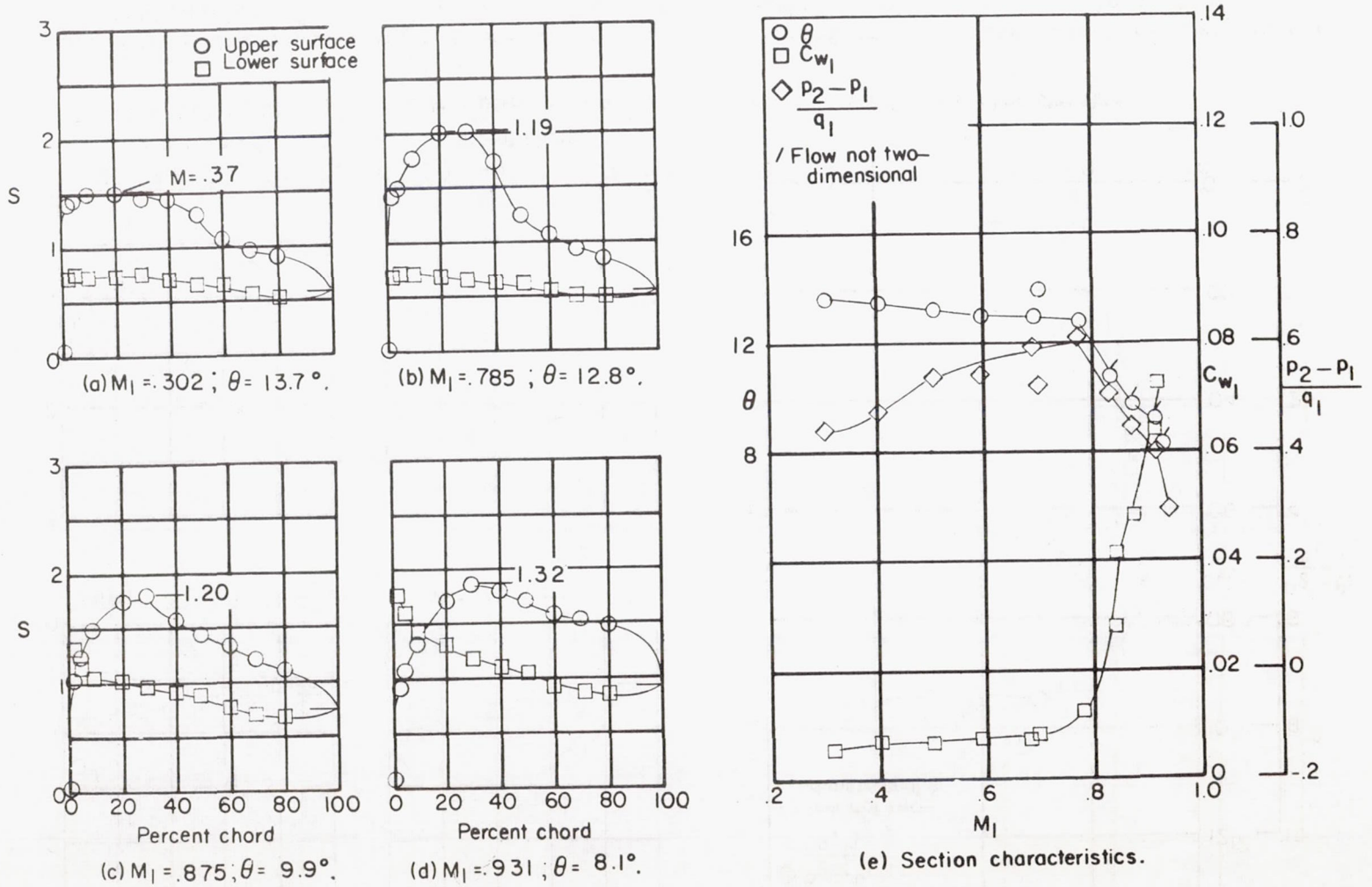



Figure 61.- Blade-surface pressure distributions and section characteristics for the cascade combination $\beta_1 = 60.0°$, $\alpha = 11.2°$, $\sigma = 1.0$, and NACA 65-$(8A_{10})$10 blade section.

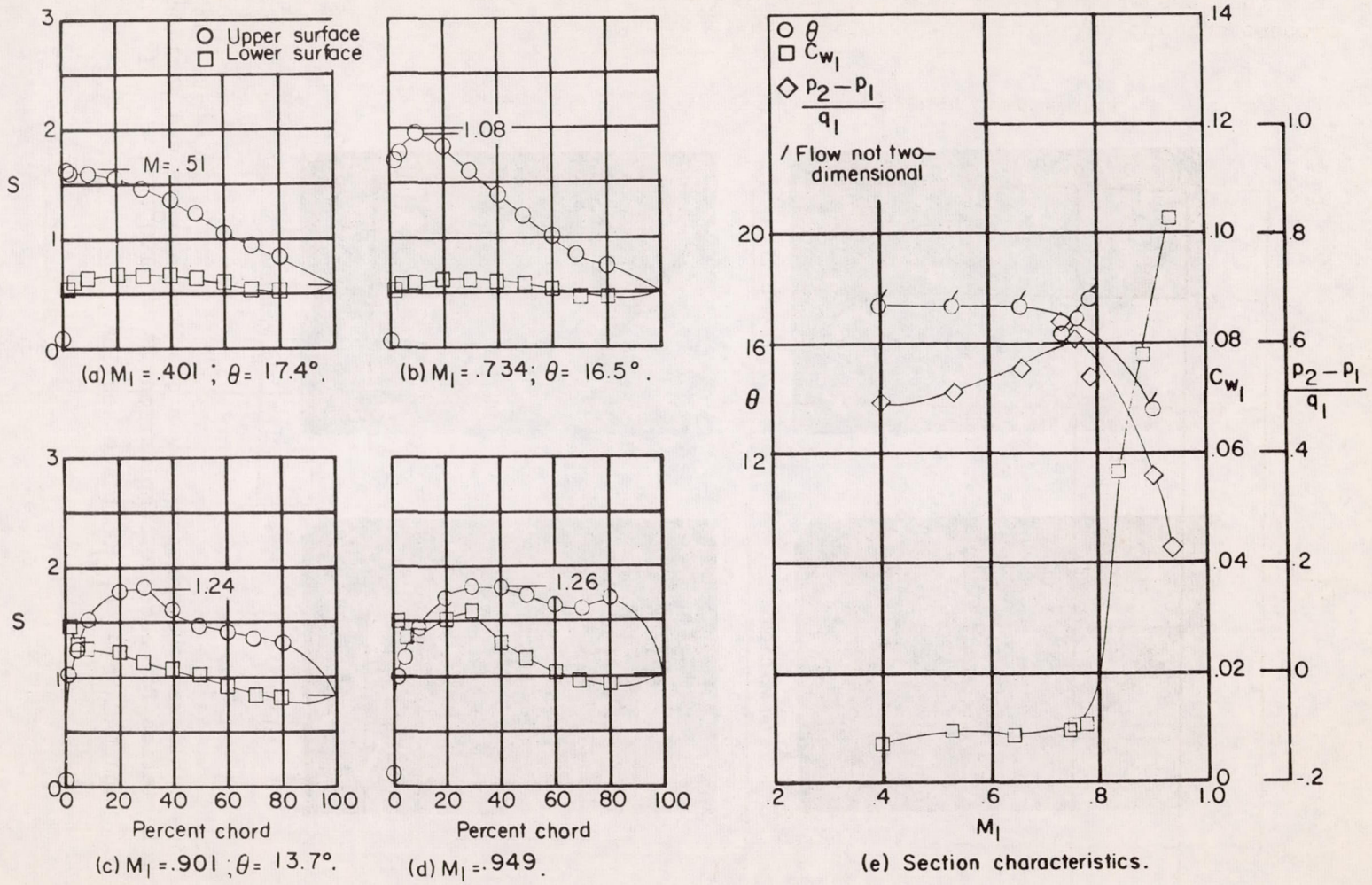
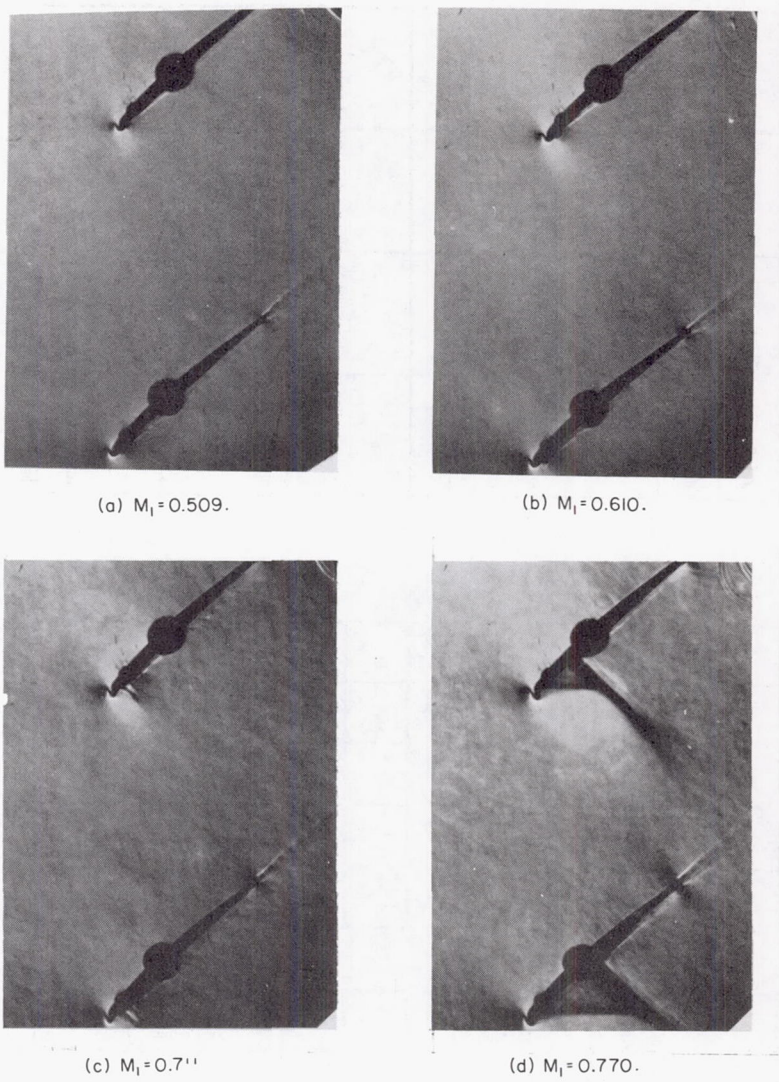



Figure 62.- Blade-surface pressure distributions and section characteristics for the cascade combination $\beta_1 = 63.0^\circ$, $\alpha = 14.2^\circ$, $\sigma = 1.0$, and NACA 65-$(8A_{10})$10 blade section.



(a) $M_1 = 0.509$.

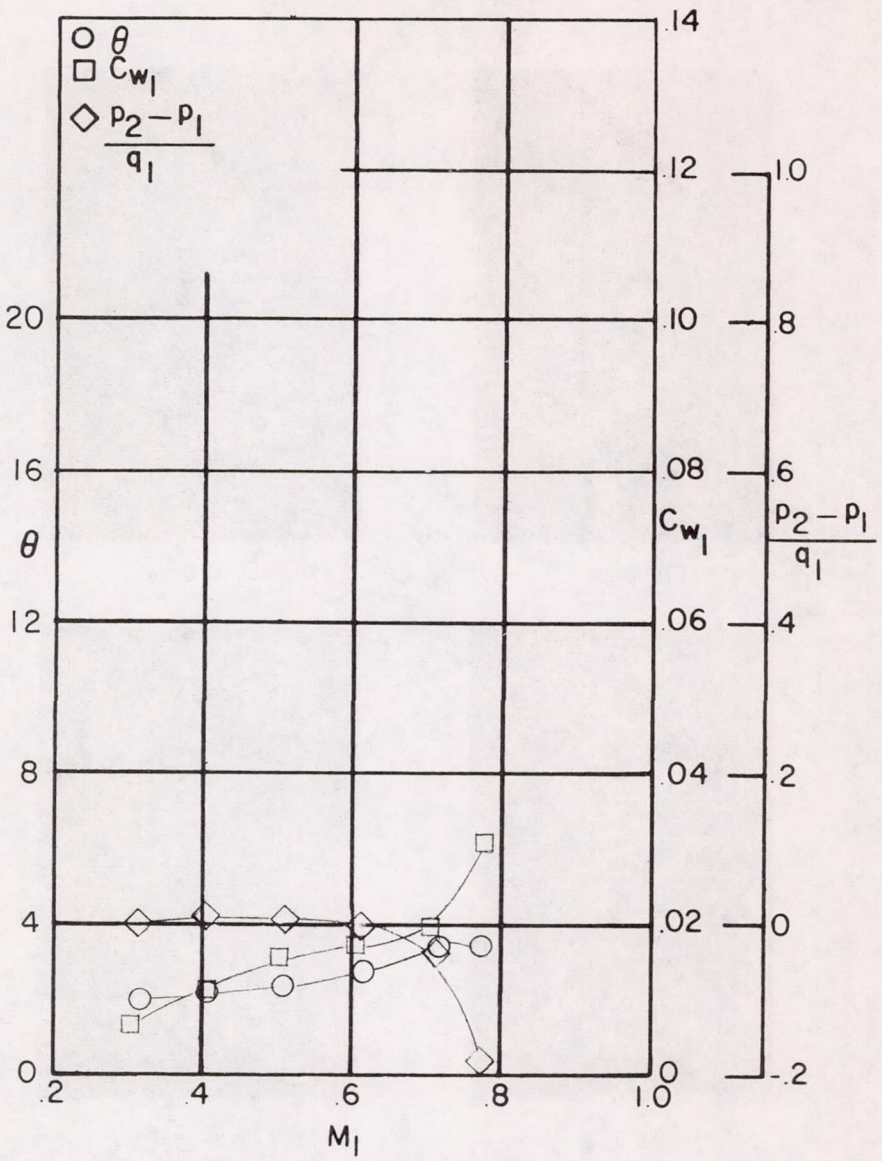
(b) $M_1 = 0.610$.

(c) $M_1 = 0.711$

(d) $M_1 = 0.770$.

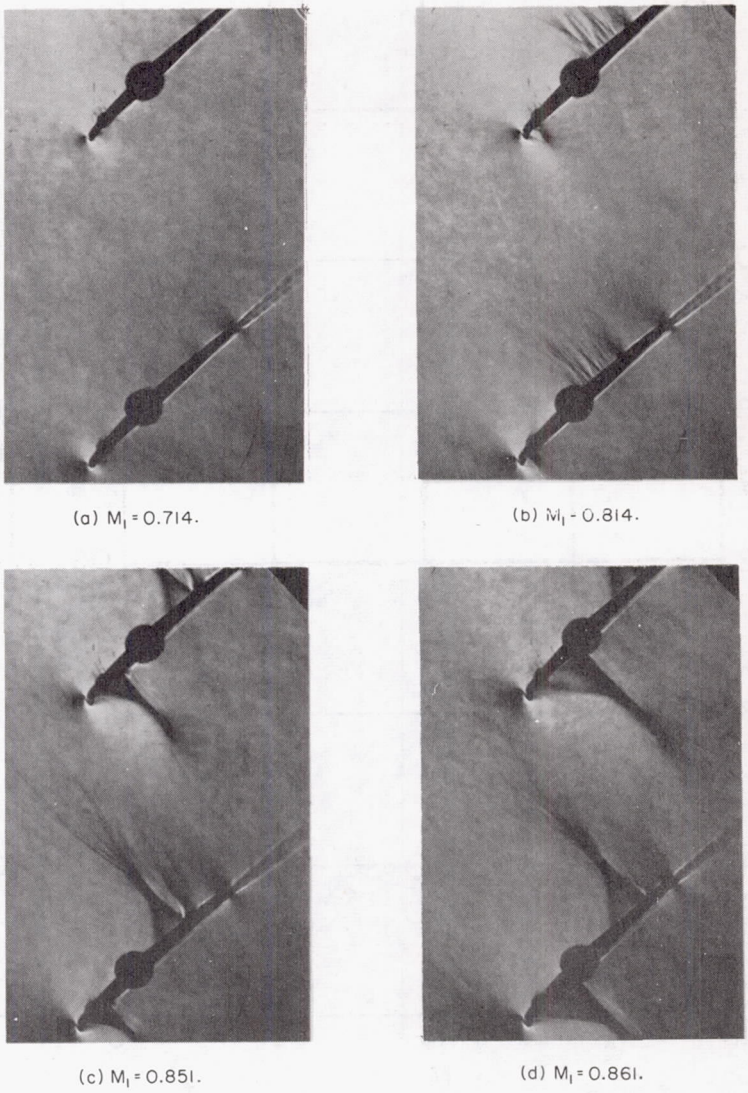
L-57-4455

Figure 63.- Schlieren photographs at various Mach numbers and section characteristics for cascade combination $\beta_1 = 41.0^\circ$, $\alpha = -1.1^\circ$ $\sigma = 0.6$, and NACA 65-$(4A_{10})$06 blade section.




(e) Section characteristics.

Figure 63.- Concluded.



(a) $M_1 = 0.714$.

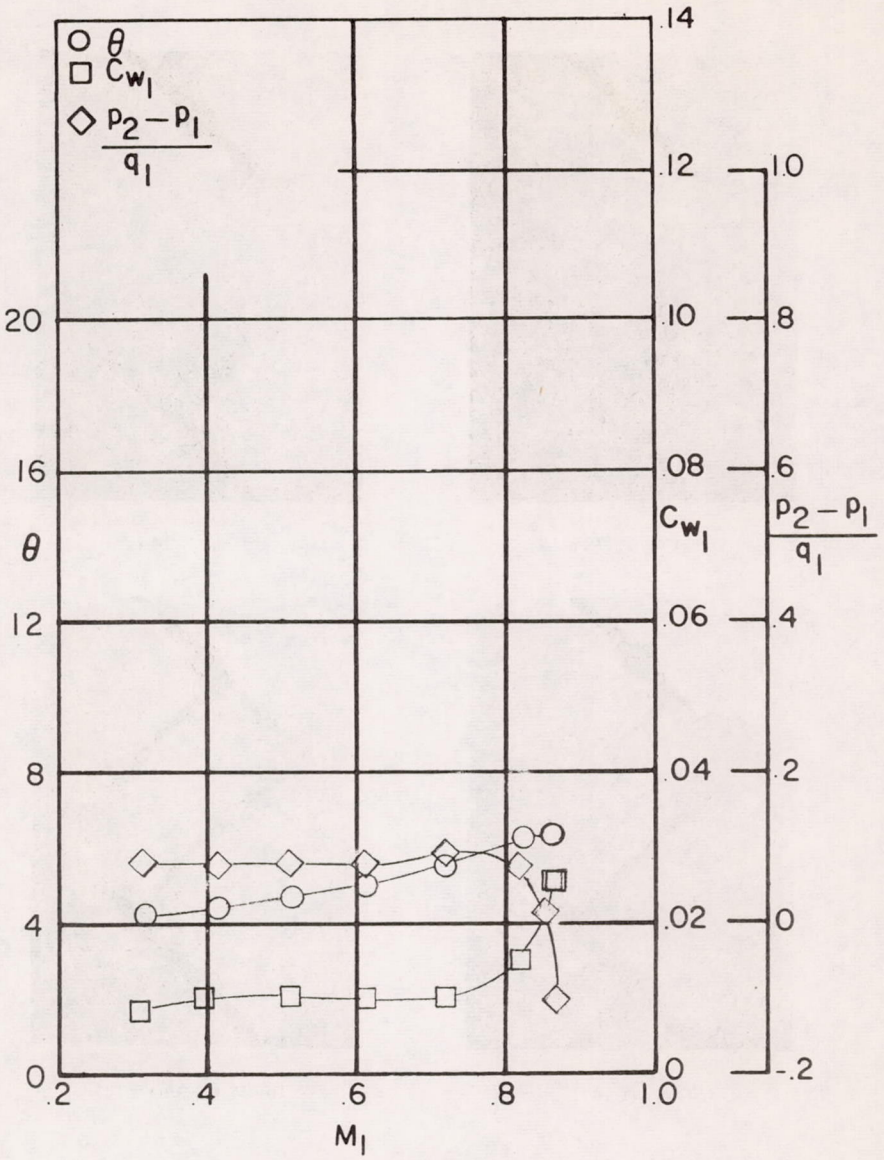
(b) $M_1 = 0.814$.

(c) $M_1 = 0.851$.

(d) $M_1 = 0.861$.

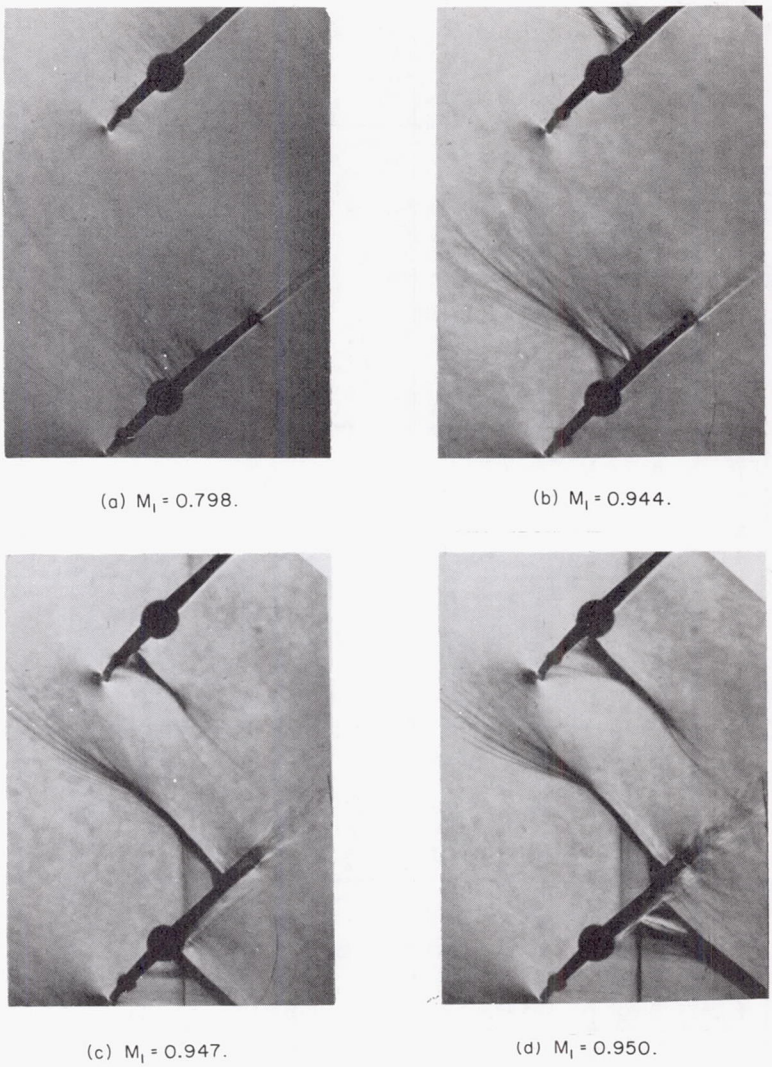
L-57-4456

Figure 64.- Schlieren photographs at various Mach numbers and section characteristics for cascade combination $\beta_1 = 44.0^\circ$, $\alpha = 1.9^\circ$, $\sigma = 0.6$, and NACA 65-$\left(4A_{10}\right)$06 blade section.




(e) Section characteristics.

Figure 64.- Concluded.



(a) $M_1 = 0.798$.

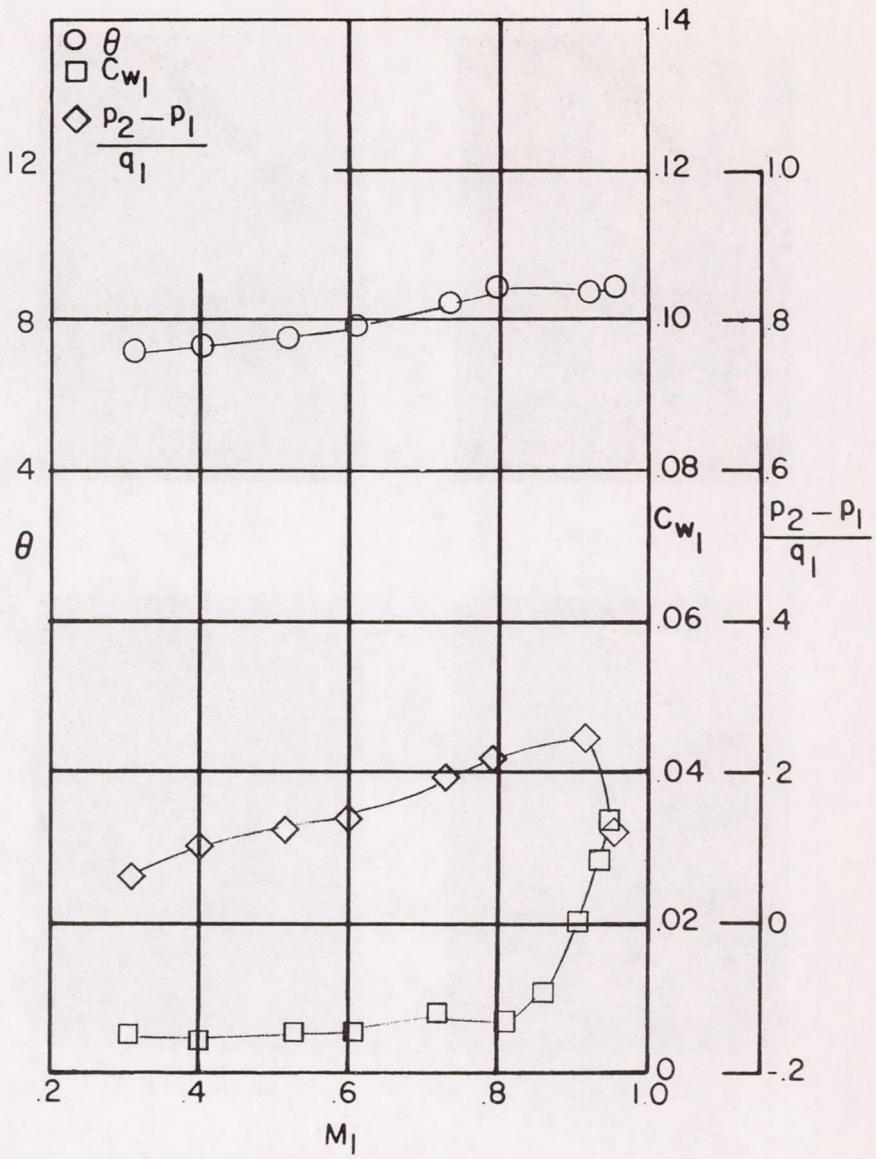
(b) $M_1 = 0.944$.

(c) $M_1 = 0.947$.

(d) $M_1 = 0.950$.

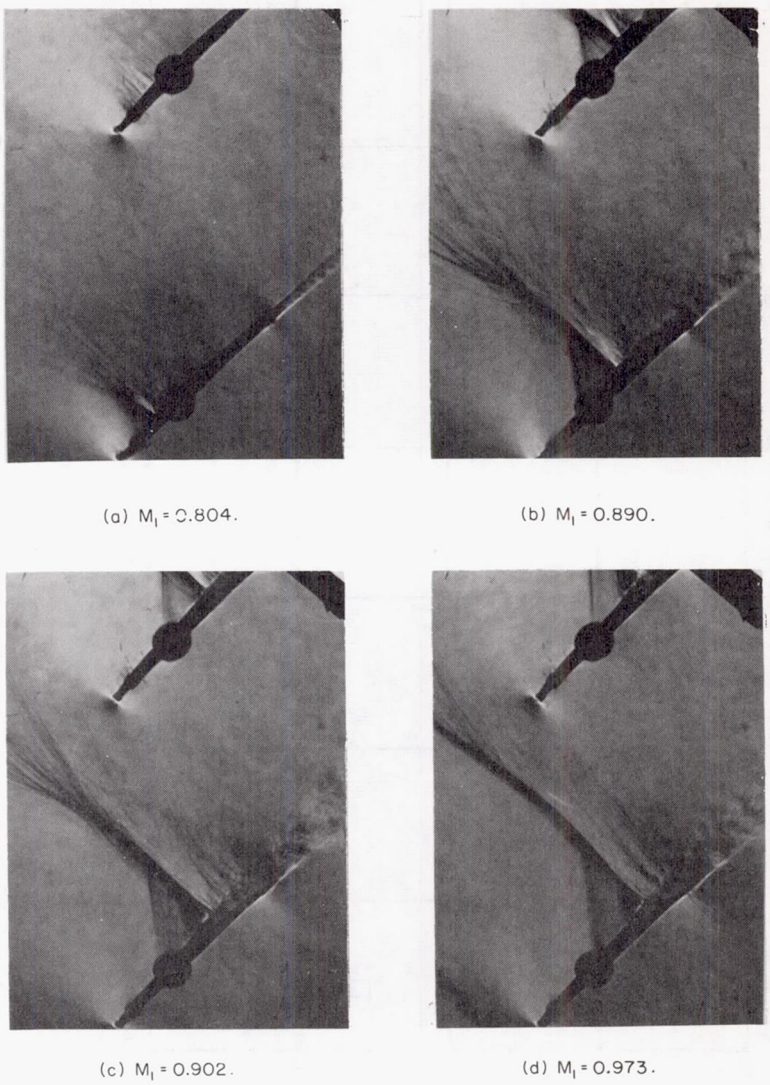
L-57-4457

Figure 65.- Schlieren photographs at various Mach numbers and section characteristics for cascade combination $\beta_1 = 47.0^\circ$, $\alpha = 4.9^\circ$, $\sigma = 0.6$, and NACA 65-$(4A_{10})$06 blade section.




(e) Section characteristics.

Figure 65.- Concluded.



(a) $M_1 = 0.804$.

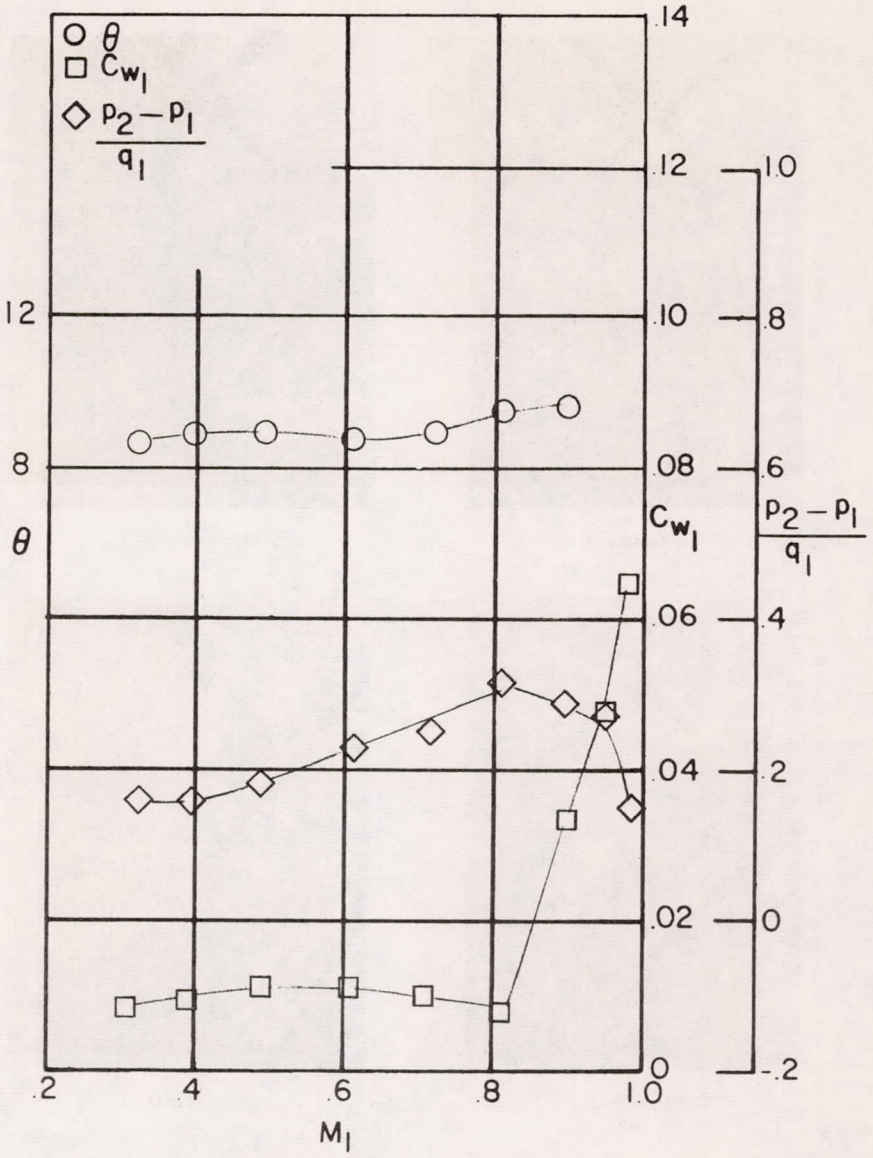
(b) $M_1 = 0.890$.

(c) $M_1 = 0.902$.

(d) $M_1 = 0.973$.

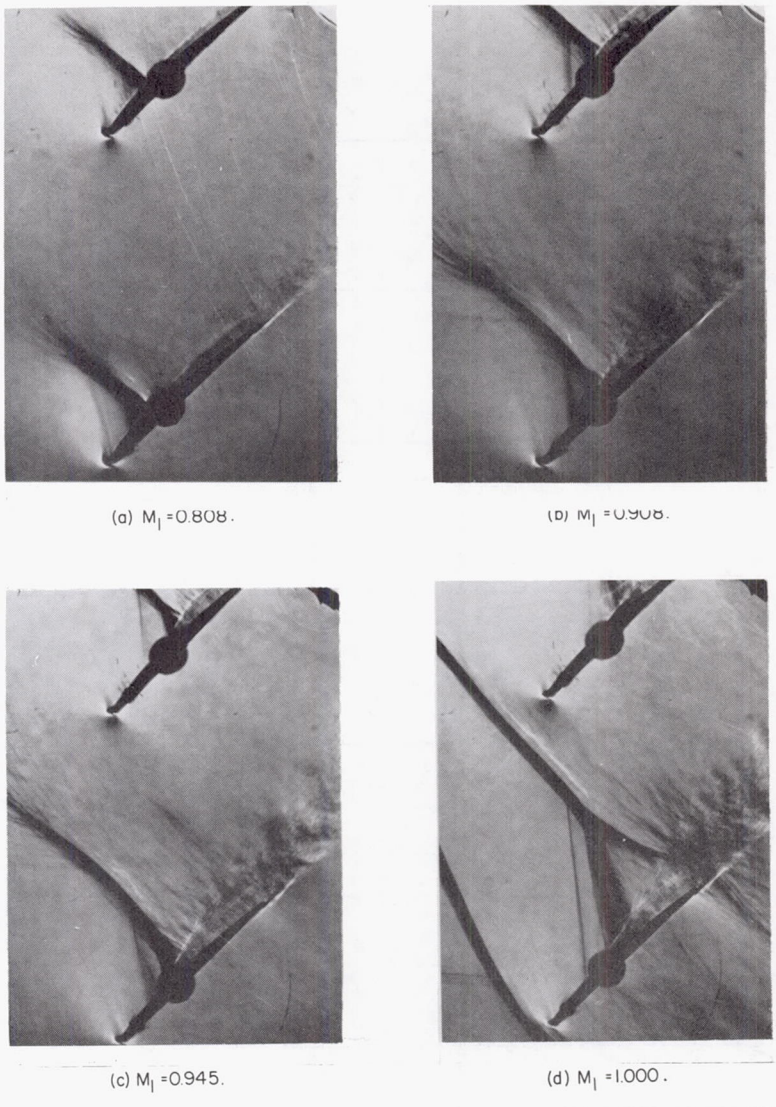
L-57-4458

Figure 66.- Schlieren photographs at various Mach numbers and section characteristics for cascade combination $\beta_1 = 50.0^\circ$, $\alpha = 7.9^\circ$, $\sigma = 0.6$, and NACA 65-$\left(4A_{10}\right)$06 blade section.




(e) Section characteristics.

Figure 66.- Concluded.



(a) $M_1 = 0.808$.

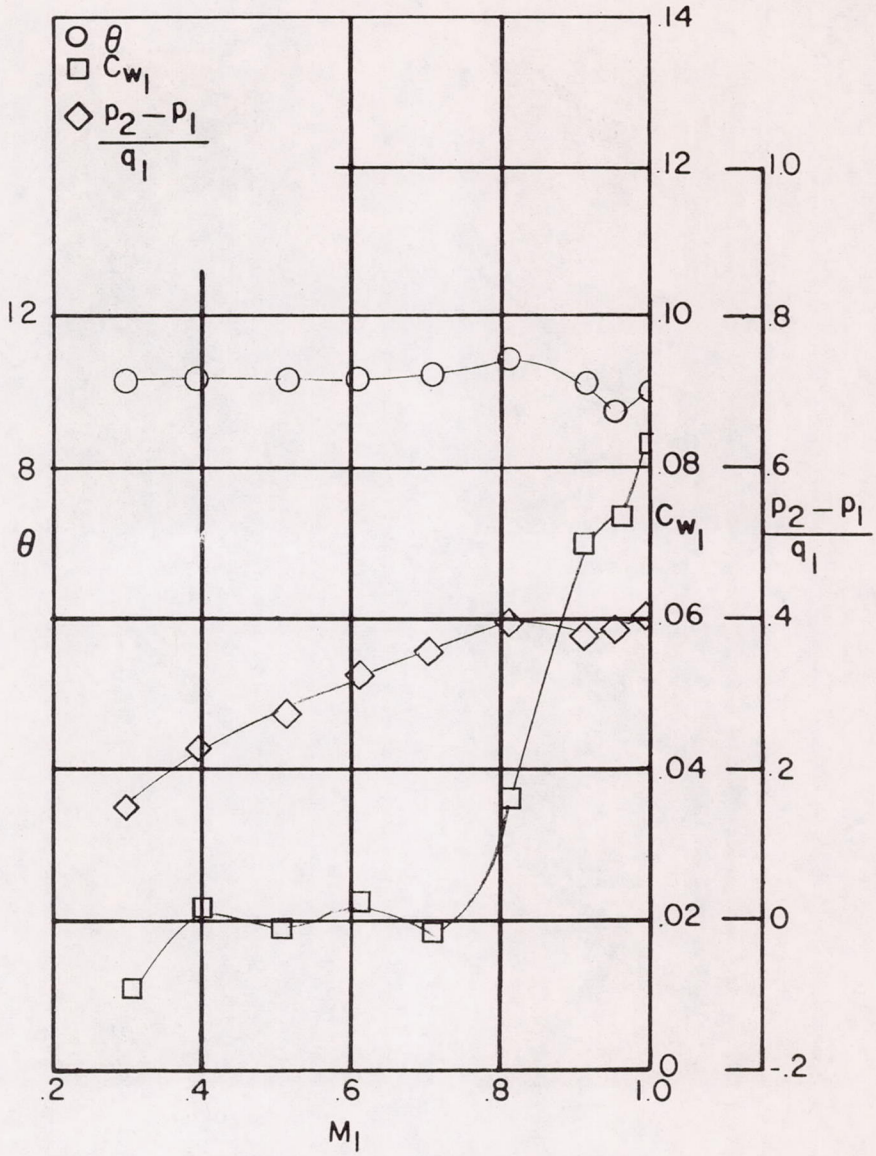
(b) $M_1 = 0.908$.

(c) $M_1 = 0.945$.

(d) $M_1 = 1.000$.

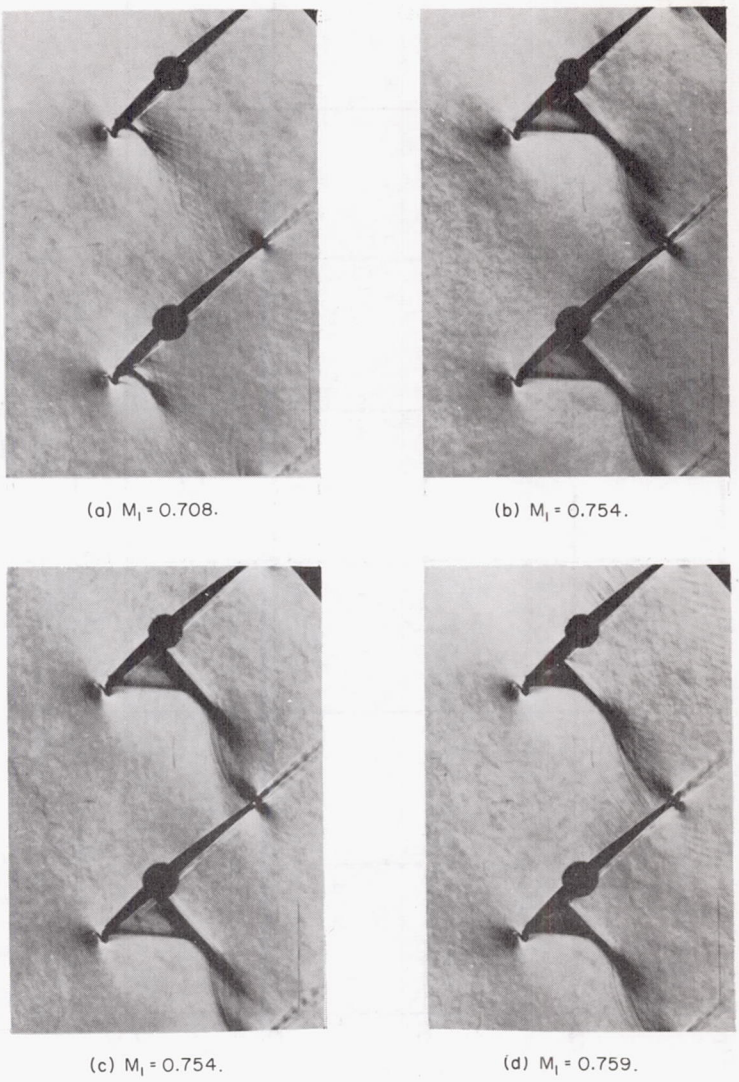
L-57-4459

Figure 67.- Schlieren photographs at various Mach numbers and section characteristics for cascade combination $\beta_1 = 53.0^\circ$, $\alpha = 10.9^\circ$, $\sigma = 0.6$, and NACA 65-$(4A_{10})$06 blade section.




(e) Section characteristics.

Figure 67.- Concluded.



(a) $M_1 = 0.708$.

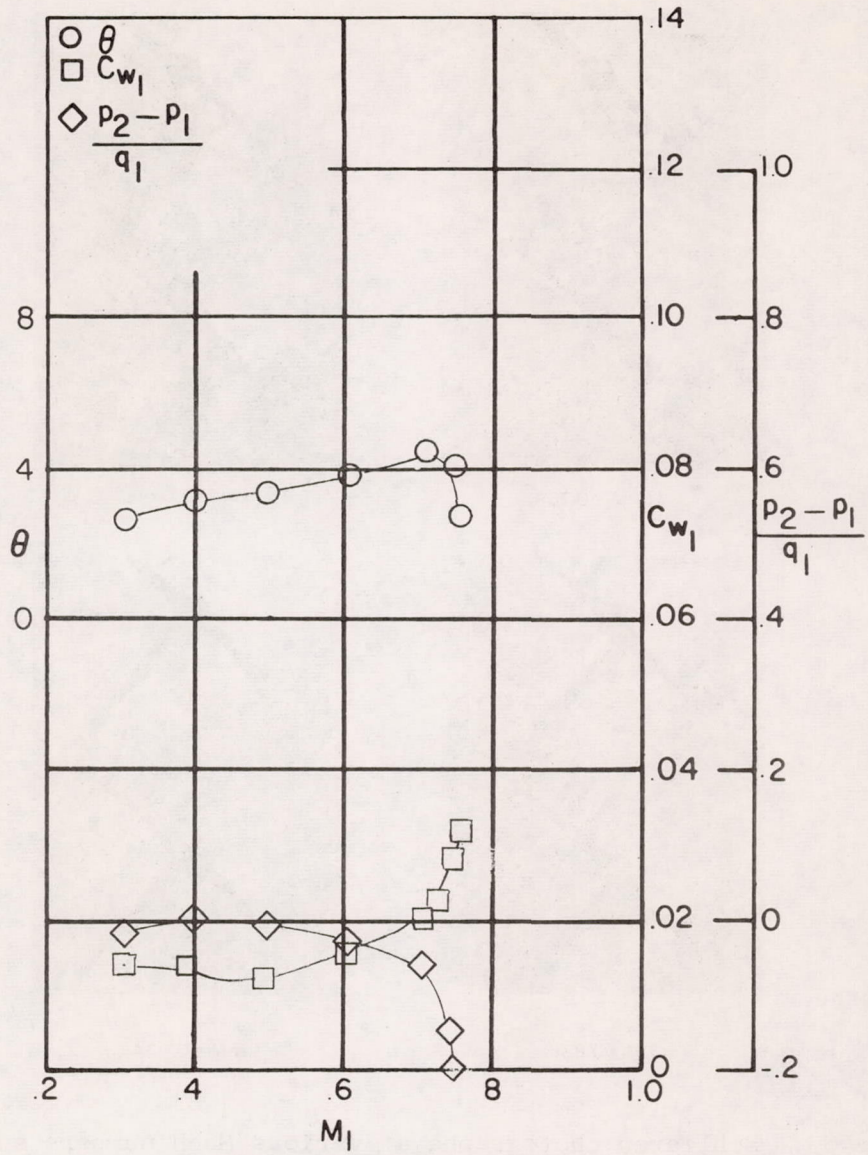
(b) $M_1 = 0.754$.

(c) $M_1 = 0.754$.

(d) $M_1 = 0.759$.

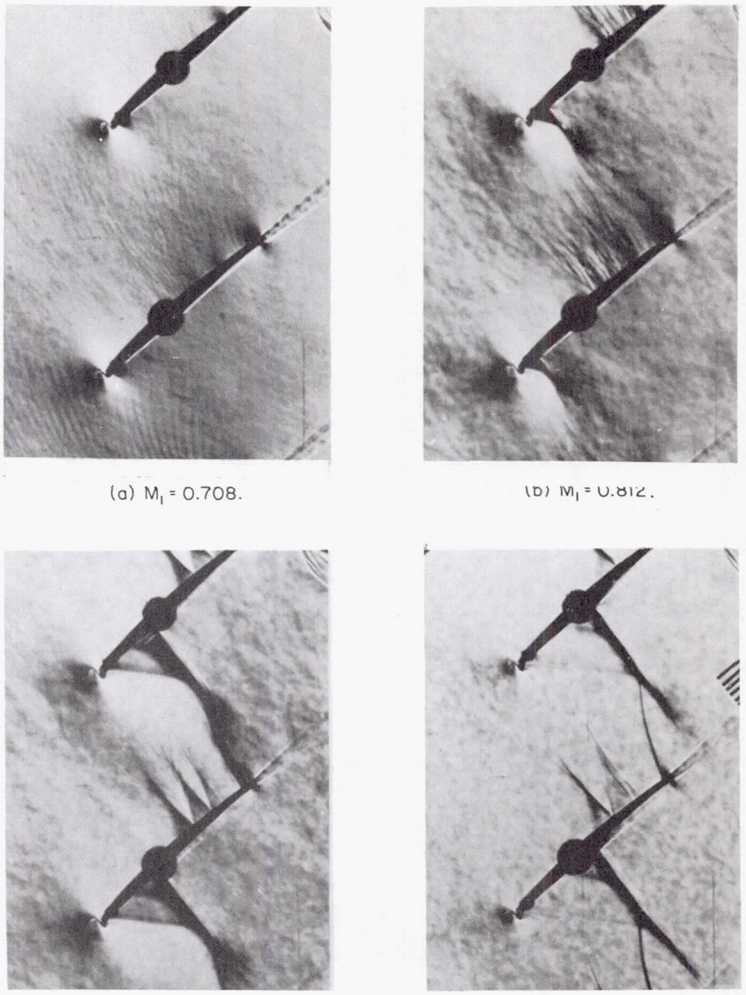
L-57-4460

Figure 68.- Schlieren photographs at various Mach numbers and section characteristics for cascade combination $\beta_1 = 41.0^\circ$, $\alpha = -0.2^\circ$, $\sigma = 0.8$, and NACA 65-$\left(4A_{10}\right)$06 blade section.




(e) Section characteristics.

Figure 68.- Concluded.



(a) $M_1 = 0.708$.

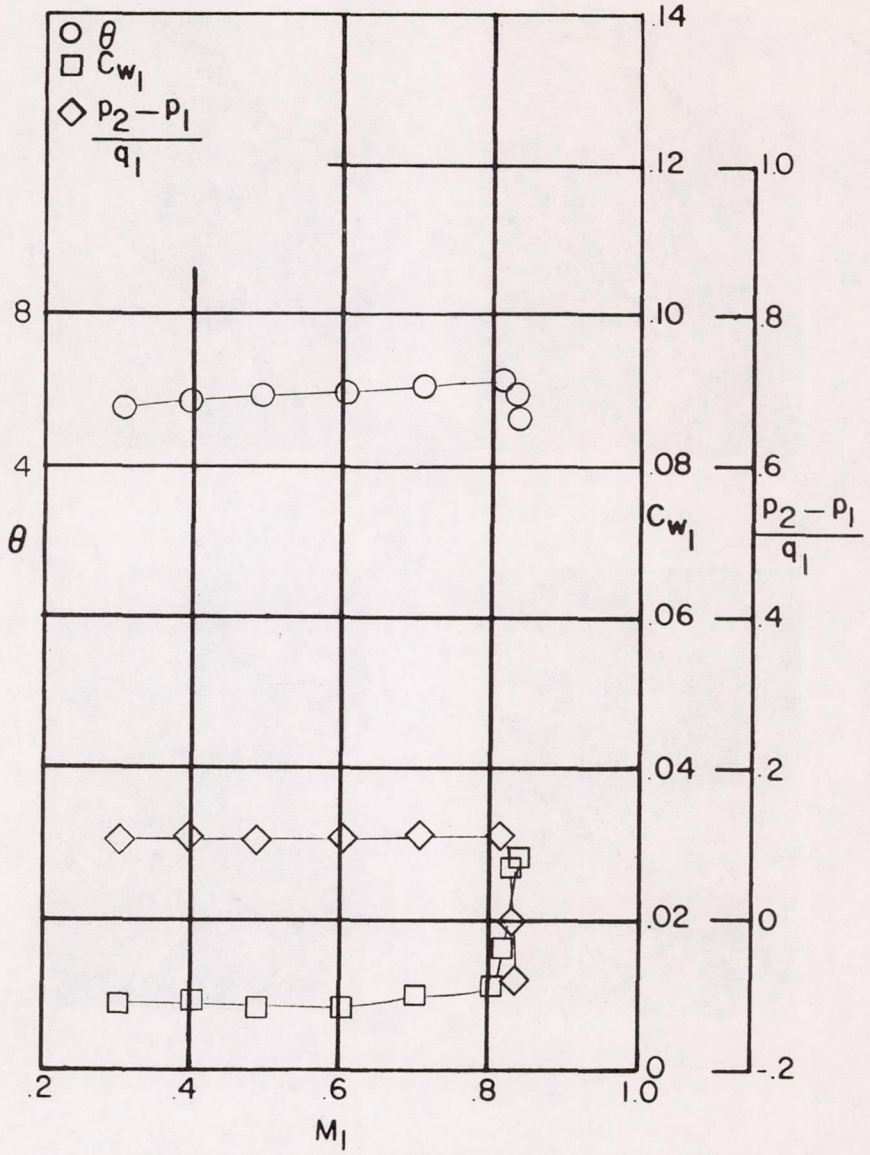
(b) $M_1 = 0.812$.

(c) $M_1 = 0.831$.

(d) $M_1 = 0.834$.

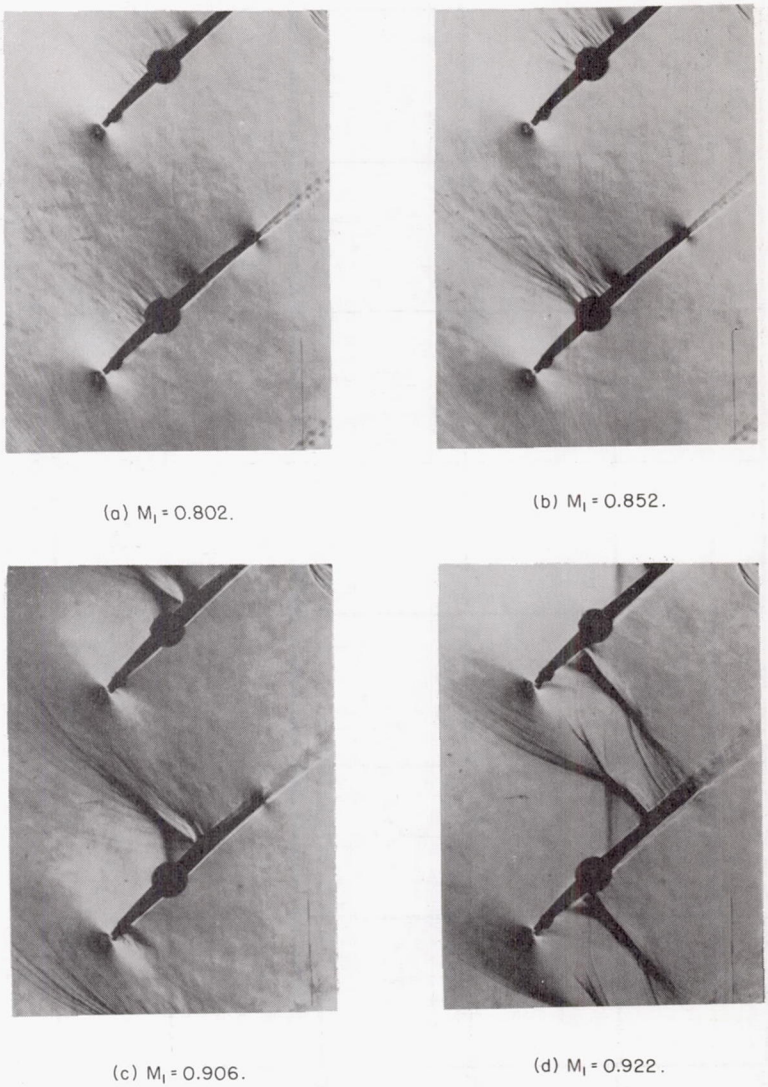
L-57-4461

Figure 69.- Schlieren photographs at various Mach numbers and section characteristics for cascade combination $\beta_1 = 44.0^\circ$, $\alpha = 2.8^\circ$, $\sigma = 0.8$, and NACA 65-$\left(4A_{10}\right)$06 blade section.




(e) Section characteristics.

Figure 69.- Concluded.



(a) $M_1 = 0.802$.

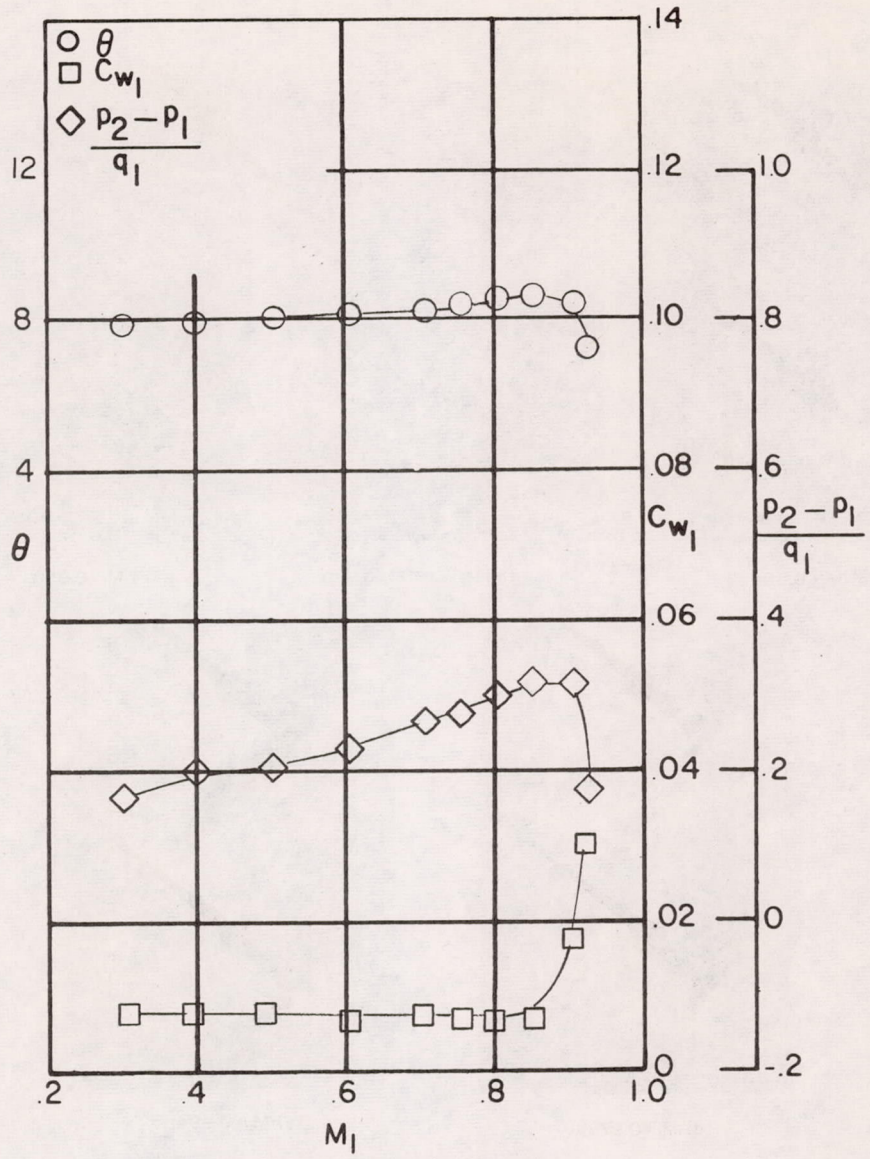
(b) $M_1 = 0.852$.

(c) $M_1 = 0.906$.

(d) $M_1 = 0.922$.

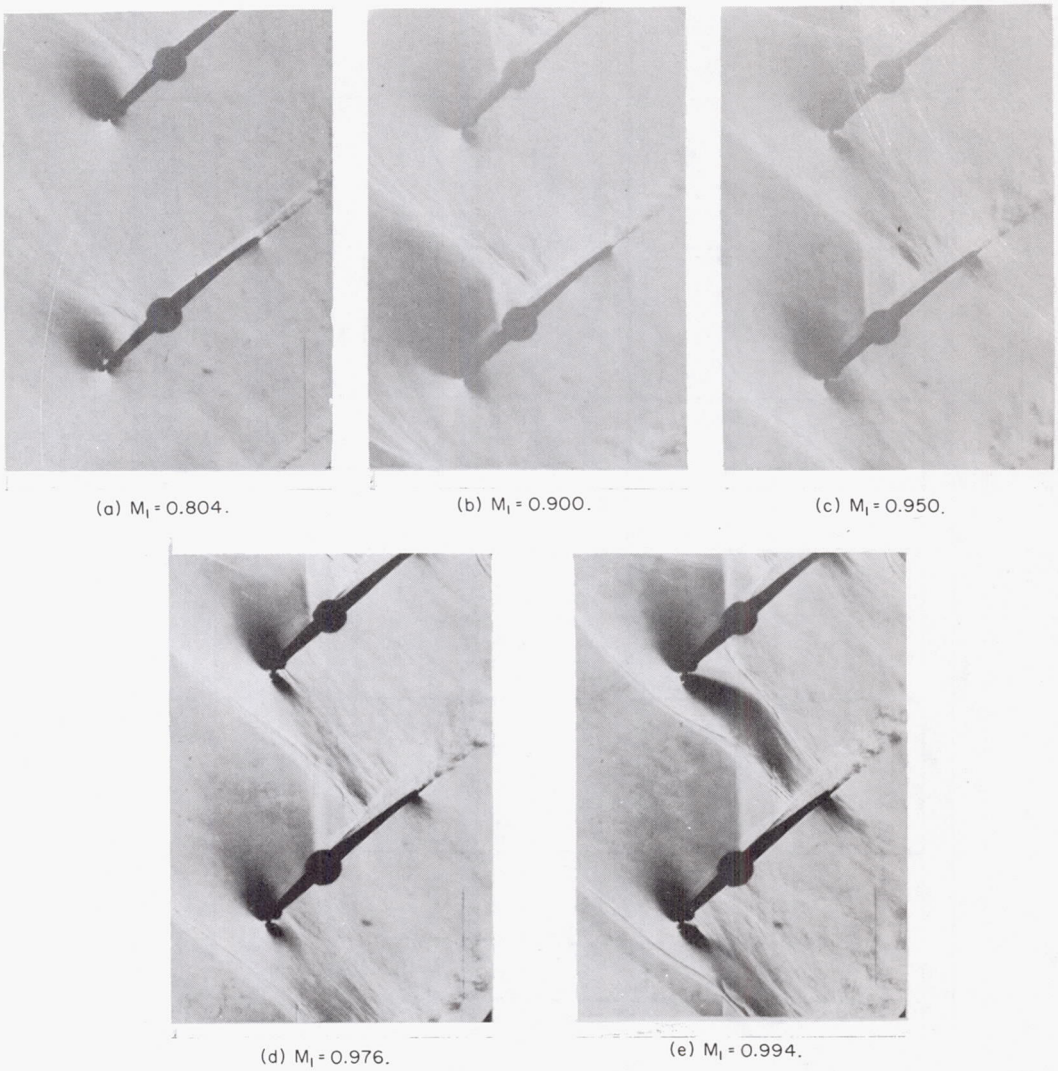
L-57-4462

Figure 70.- Schlieren photographs at various Mach numbers and section characteristics for cascade combination $\beta_1 = 47.0^\circ$, $\alpha = 5.8^\circ$, $\sigma = 0.8$, and NACA 65-$\left(4A_{10}\right)$06 blade section.




(e) Section characteristics.

Figure 70.- Concluded.

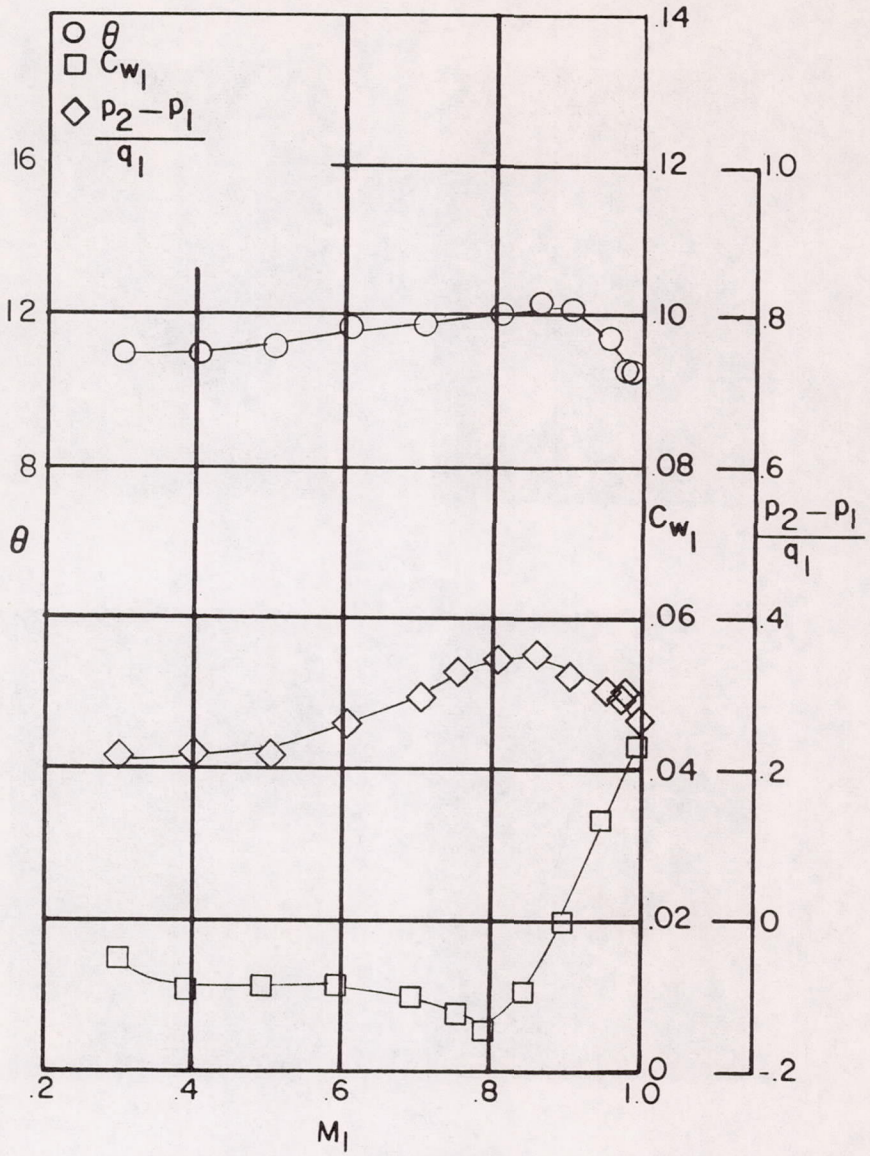


(a) $M_1 = 0.804$. (b) $M_1 = 0.900$. (c) $M_1 = 0.950$.

(d) $M_1 = 0.976$. (e) $M_1 = 0.994$.

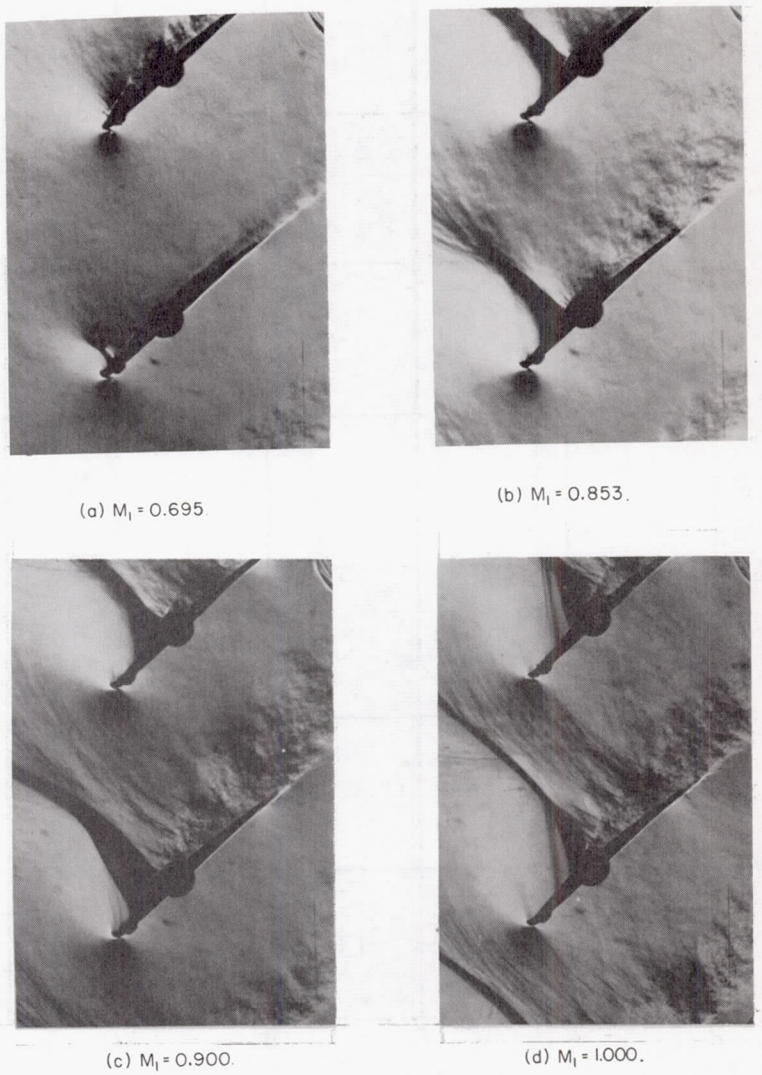
L-57-4463

Figure 71.- Schlieren photographs at various Mach numbers and section characteristics for cascade combination $\beta_1 = 50.0^\circ$, $\alpha = 8.8^\circ$, $\sigma = 0.8$, and NACA 65-$\left(4A_{10}\right)$06 blade section.




(f) Section characteristics.

Figure 71.- Concluded.



(a) $M_1 = 0.695$.

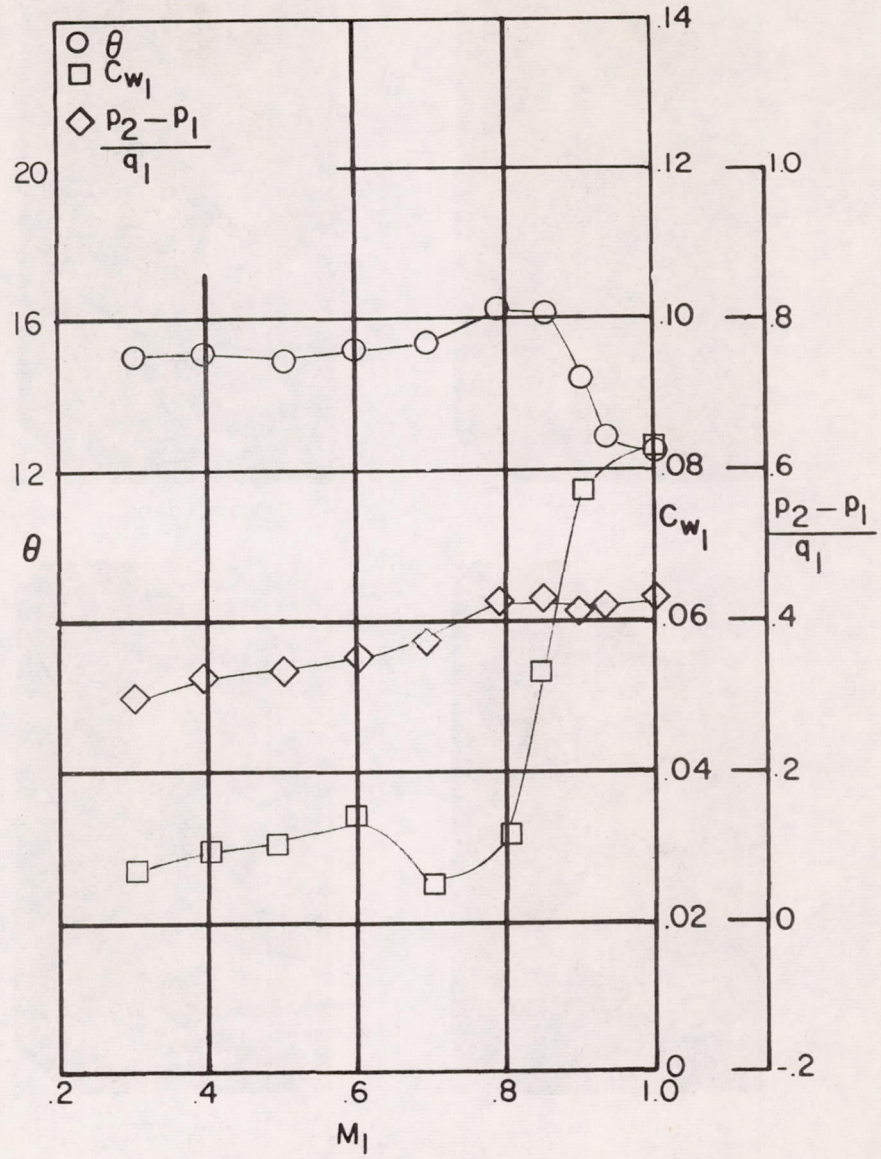
(b) $M_1 = 0.853$.

(c) $M_1 = 0.900$.

(d) $M_1 = 1.000$.

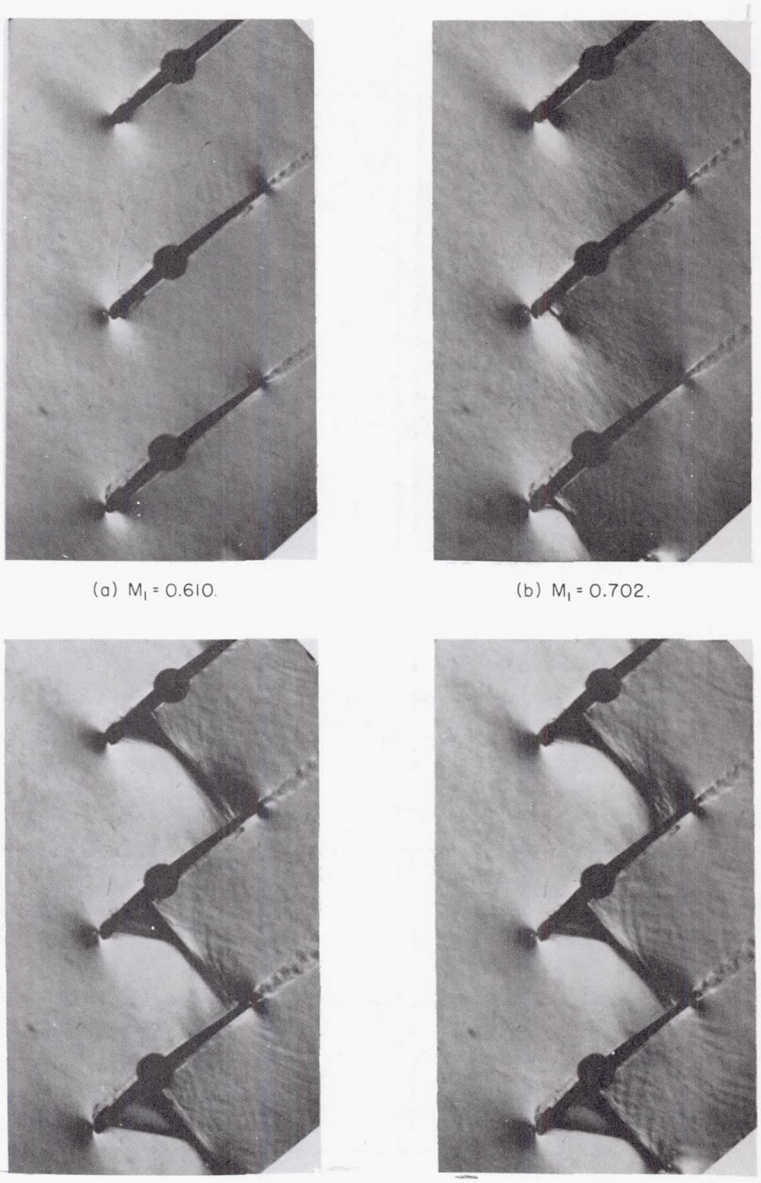
L-57-4464

Figure 72.- Schlieren photographs at various Mach numbers and section characteristics for cascade combination $\beta_1 = 56.0^\circ$, $\alpha = 14.8^\circ$, $\sigma = 0.8$, and NACA 65-$(4A_{10})$06 blade section.




(e) Section characteristics.

Figure 72.- Concluded.



(a) $M_1 = 0.610$.

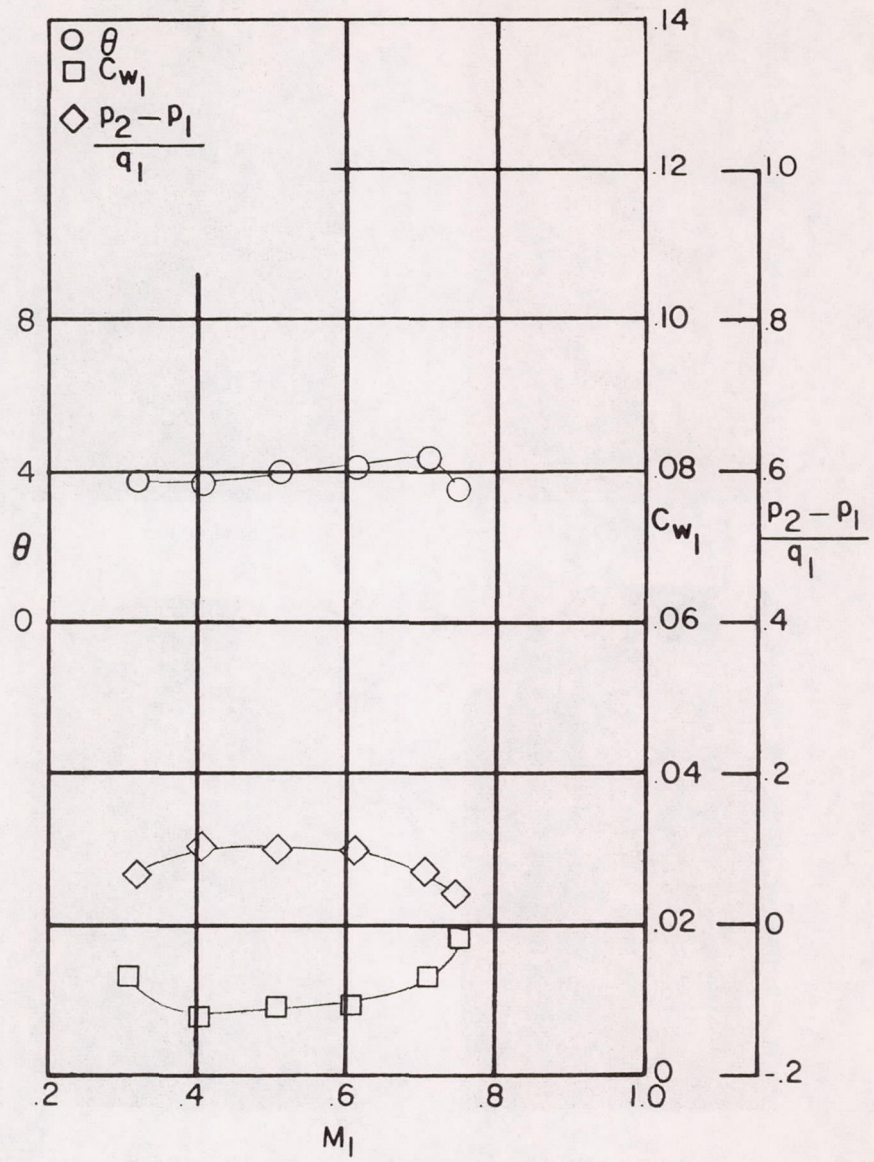
(b) $M_1 = 0.702$.

(c) $M_1 = 0.745$

(d) $M_1 = 0.750$.

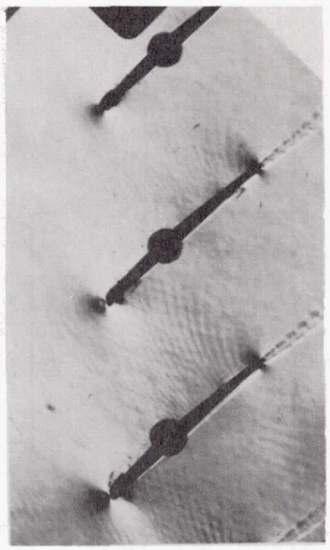
L-57-4465

Figure 73.- Schlieren photographs at various Mach numbers and section characteristics for cascade combination $\beta_1 = 41.0^\circ$, $\alpha = 0.8^\circ$, $\sigma = 1.0$, and NACA 65-$(4A_{10})$06 blade section.

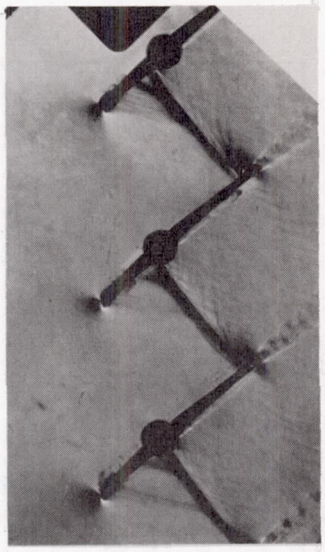



(e) Section characteristics.

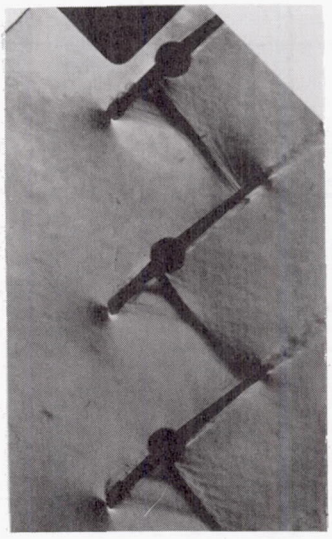
Figure 73.- Concluded.



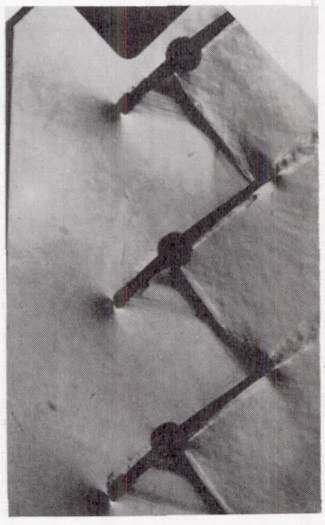
(a) $M_1 = 0.709$.



(b) $M_1 = 0.813$.



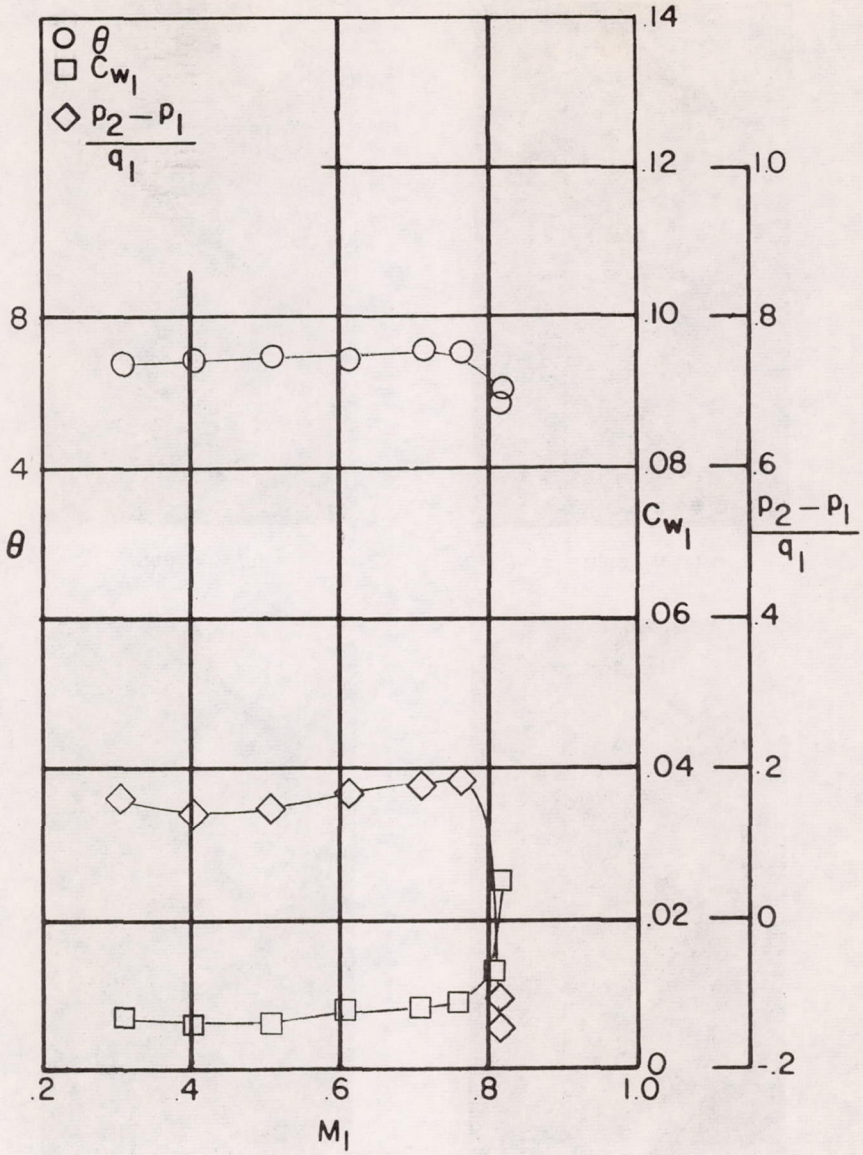
(c) $M_1 = 0.815$.



(d) $M_1 = 0.818$.

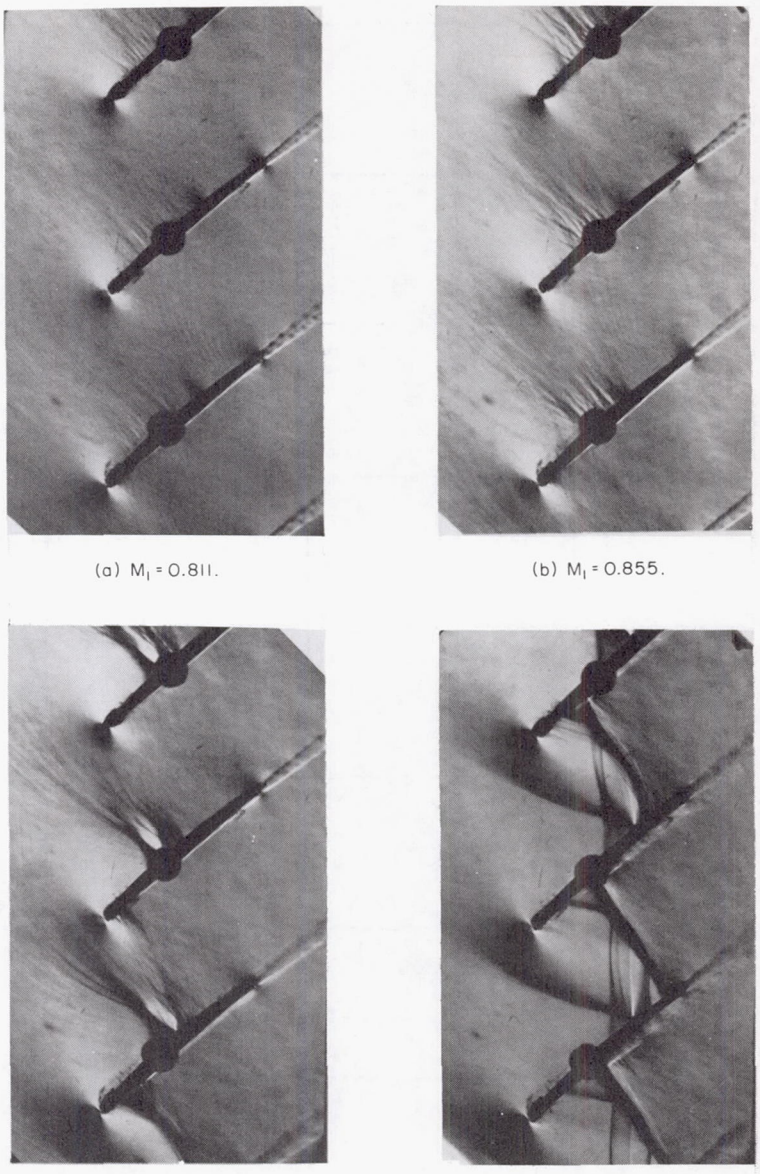
L-57-4466

Figure 74.- Schlieren photographs at various Mach numbers and section characteristics for cascade combination $\beta_1 = 44.0^\circ$, $\alpha = 3.8^\circ$, $\sigma = 1.0$, and NACA 65-$\left(4A_{10}\right)$06 blade section.




(e) Section characteristics.

Figure 74.- Concluded.



(a) $M_1 = 0.811$.

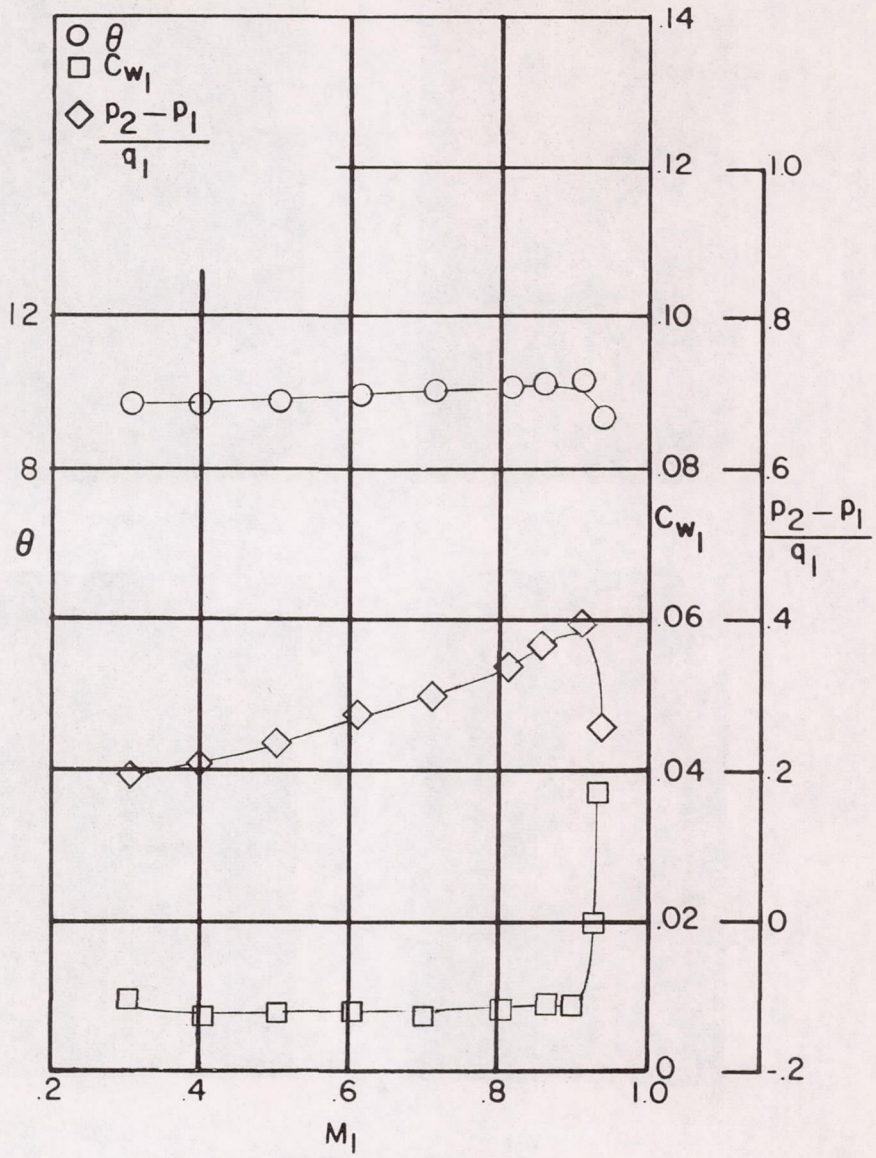
(b) $M_1 = 0.855$.

(c) $M_1 = 0.906$.

(d) $M_1 = 0.930$.

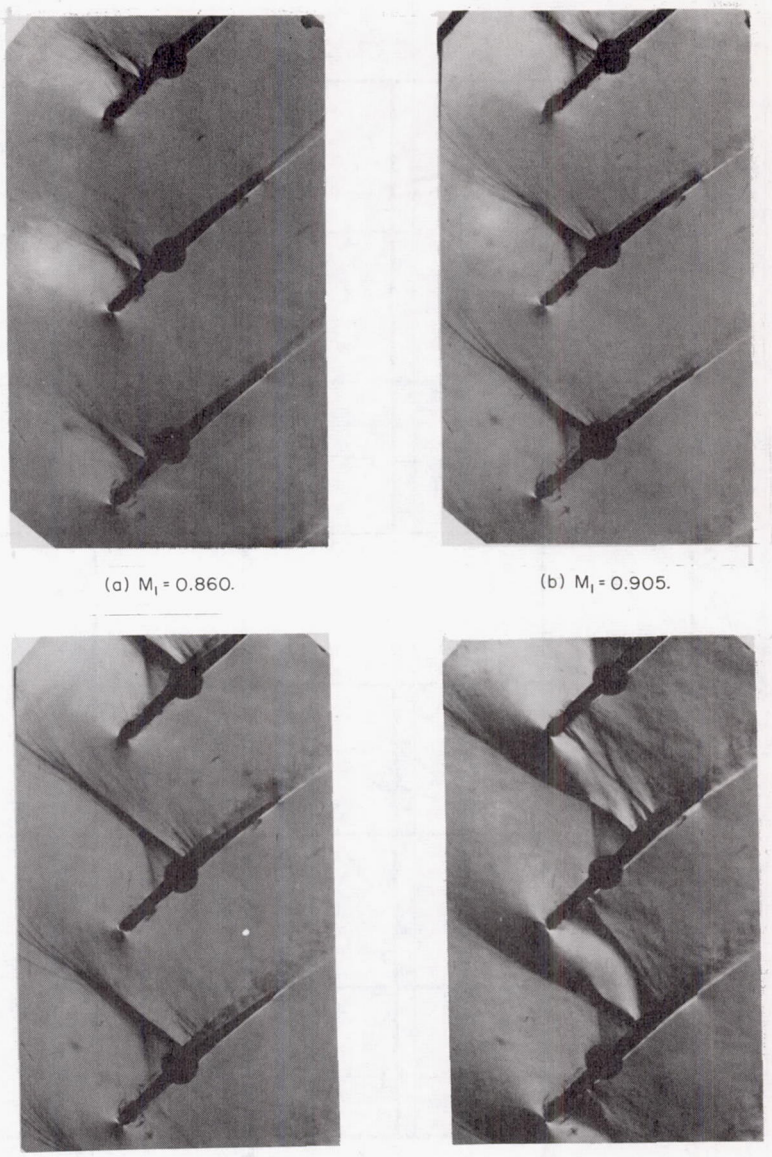
L-57-4467

Figure 75.- Schlieren photographs at various Mach numbers and section characteristics for cascade combination $\beta_1 = 47.0^\circ$, $\alpha = 6.8^\circ$, $\sigma = 1.0$, and NACA 65-$\left(4A_{10}\right)$06 blade section.




(e) Section characteristics.

Figure 75.- Concluded.



(a) $M_1 = 0.860$.

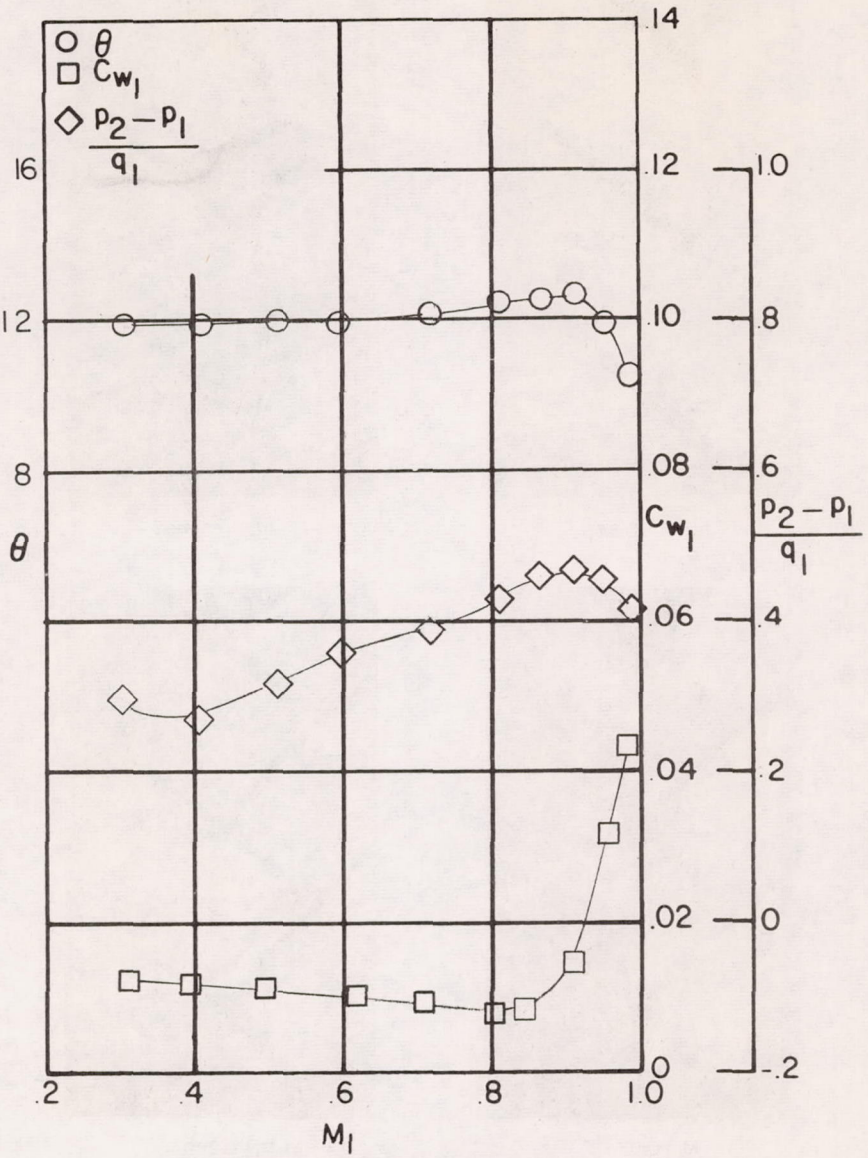
(b) $M_1 = 0.905$.

(c) $M_1 = 0.946$.

(d) $M_1 = 0.985$.

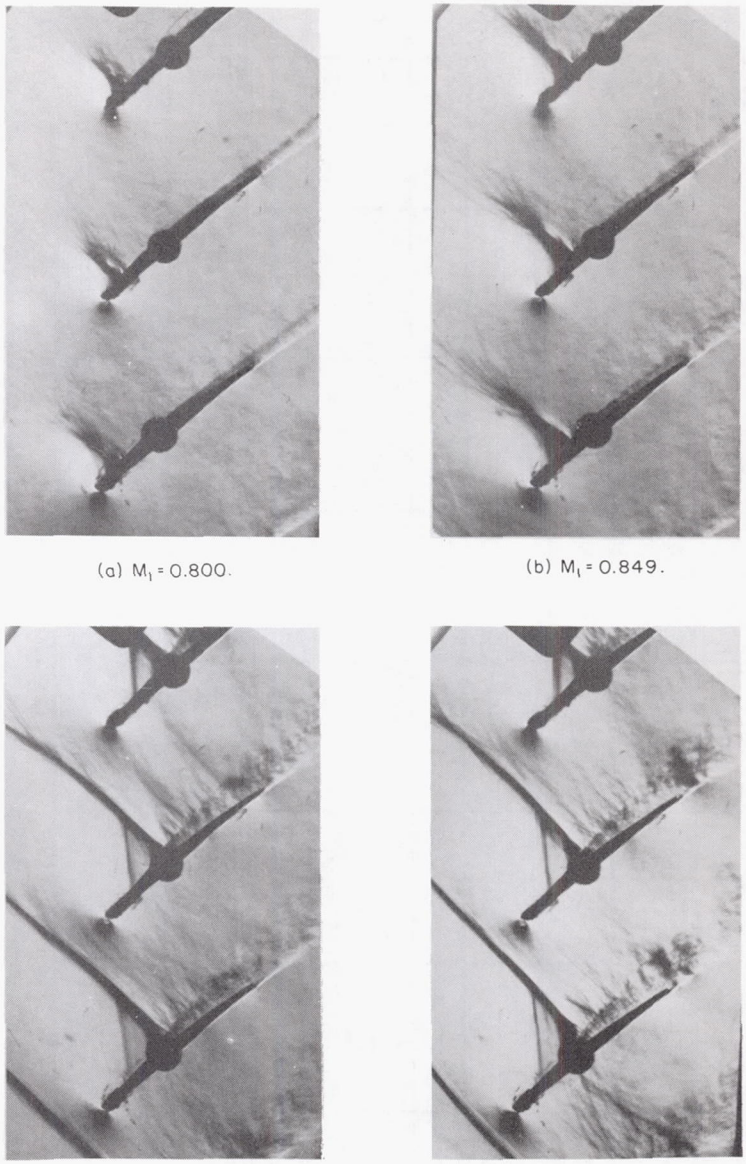
L-57-4468

Figure 76.- Schlieren photographs at various Mach numbers and section characteristics for cascade combination $\beta_1 = 50.0^\circ$, $\alpha = 9.8^\circ$, $\sigma = 1.0$, and NACA 65-$\left(4A_{10}\right)$06 blade section.




(e) Section characteristics.

Figure 76.- Concluded.



(a) $M_1 = 0.800$.

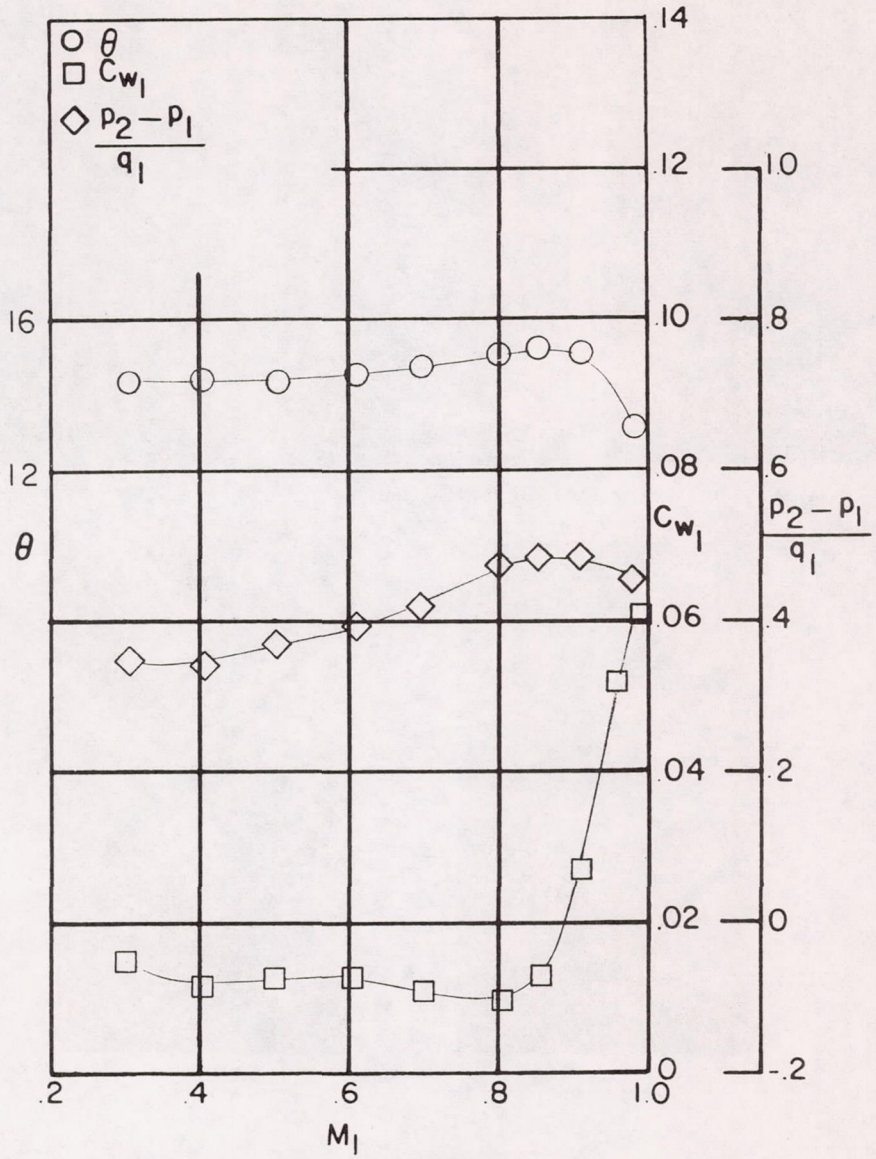
(b) $M_1 = 0.849$.

(c) $M_1 = 0.974$.

(d) $M_1 = 0.989$.

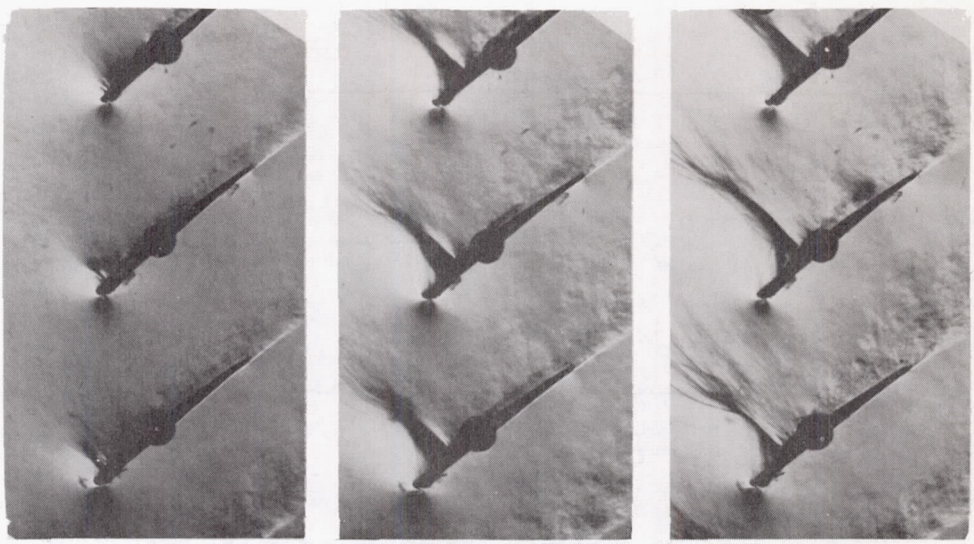
L-57-4469

Figure 77.- Schlieren photographs at various Mach numbers and section characteristics for cascade combination $\beta_1 = 53.0^\circ$, $\alpha = 12.8^\circ$, $\sigma = 1.0$, and NACA 65-$(4A_{10})$06 blade section.

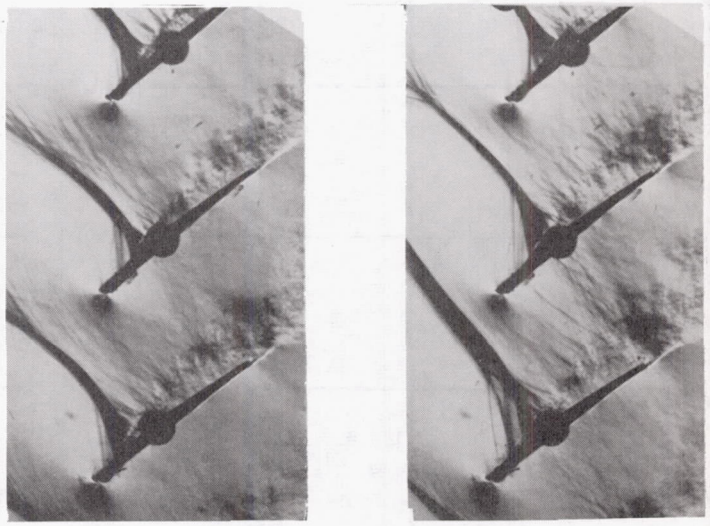



(e) Section characteristics.

Figure 77.- Concluded.



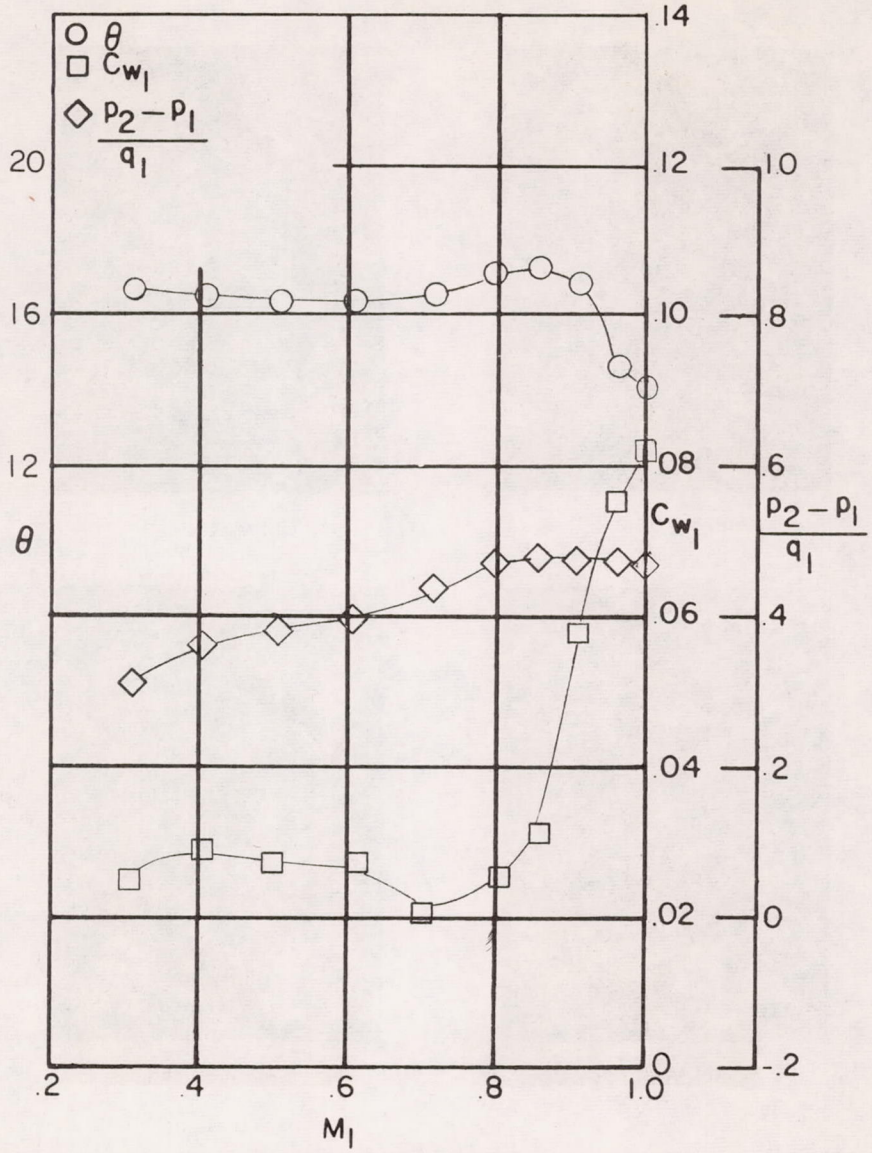
(a) $M_1 = 0.711$. (b) $M_1 = 0.851$. (c) $M_1 = 0.902$.



(d) $M_1 = 0.957$. (e) $M_1 = 1.000$

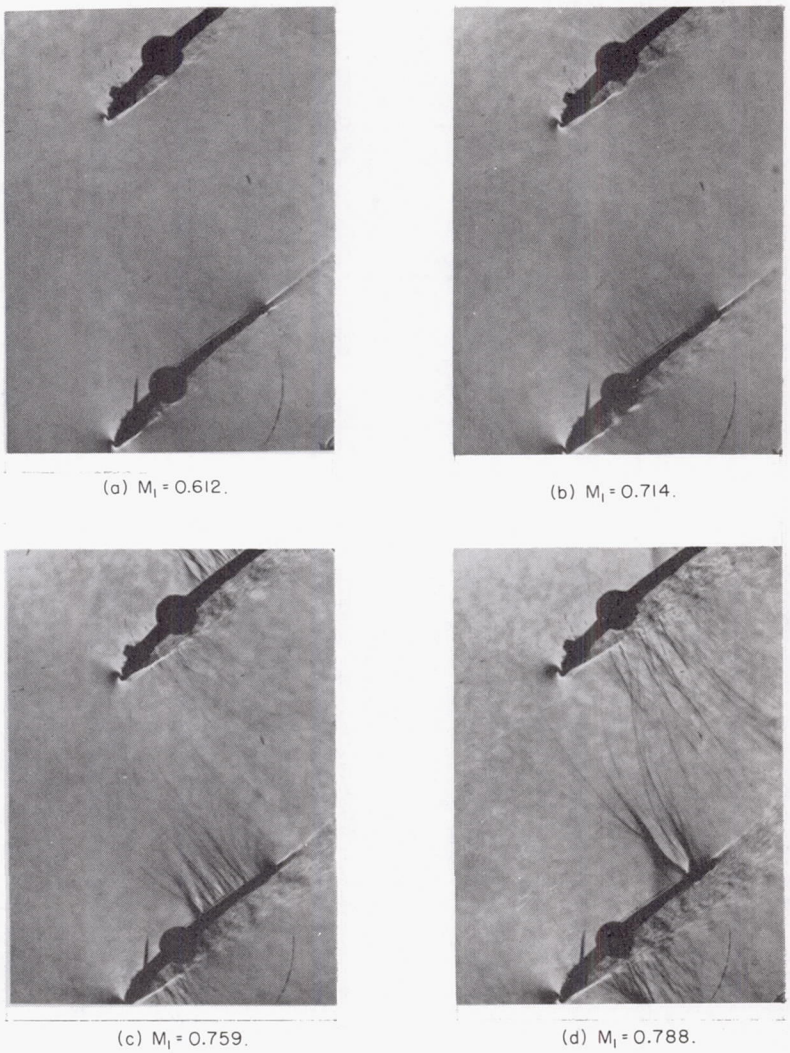
L-57-4470

Figure 78.- Schlieren photographs at various Mach numbers and section characteristics for cascade combination $\beta_1 = 56.0^\circ$, $\alpha = 15.8^\circ$, $\sigma = 1.0$, and NACA 65-$\left(4A_{10}\right)$06 blade section.




(f) Section characteristics.

Figure 78.- Concluded.



(a) $M_1 = 0.612$.

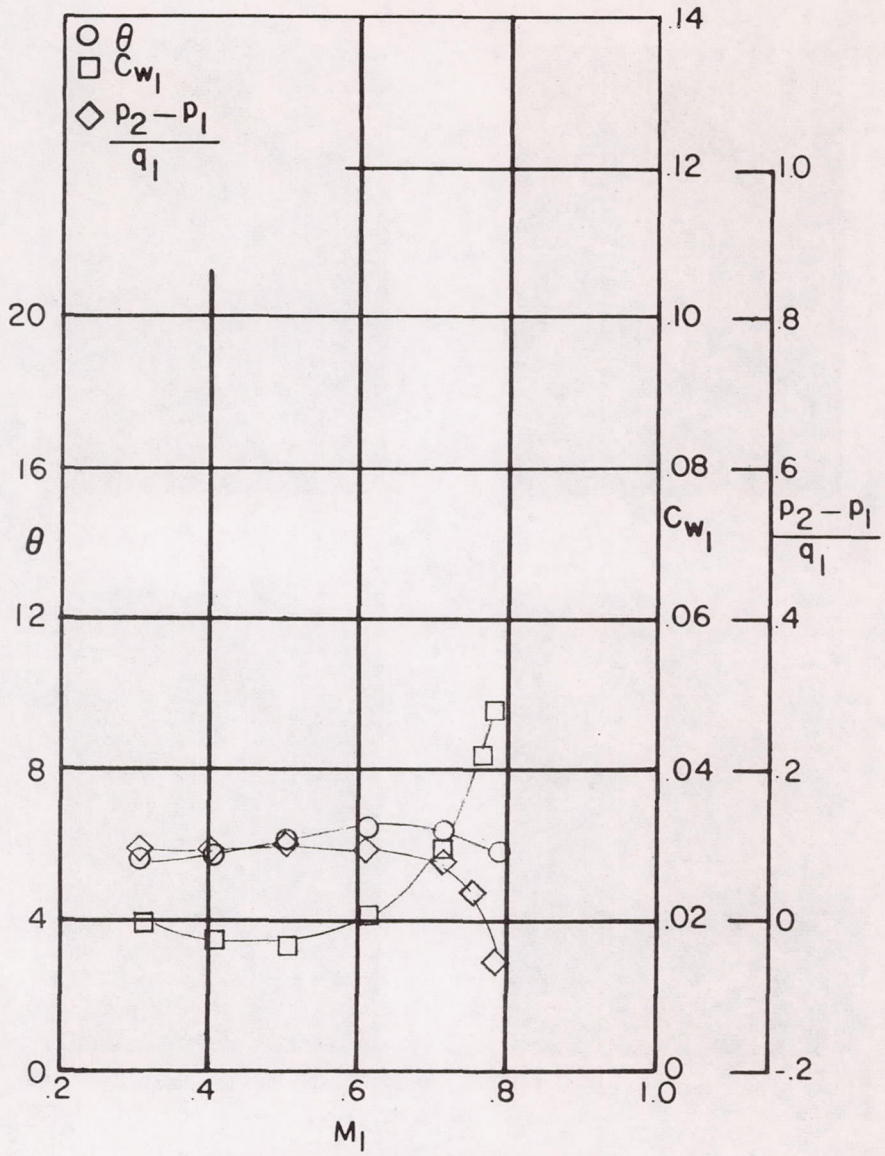
(b) $M_1 = 0.714$.

(c) $M_1 = 0.759$.

(d) $M_1 = 0.788$.

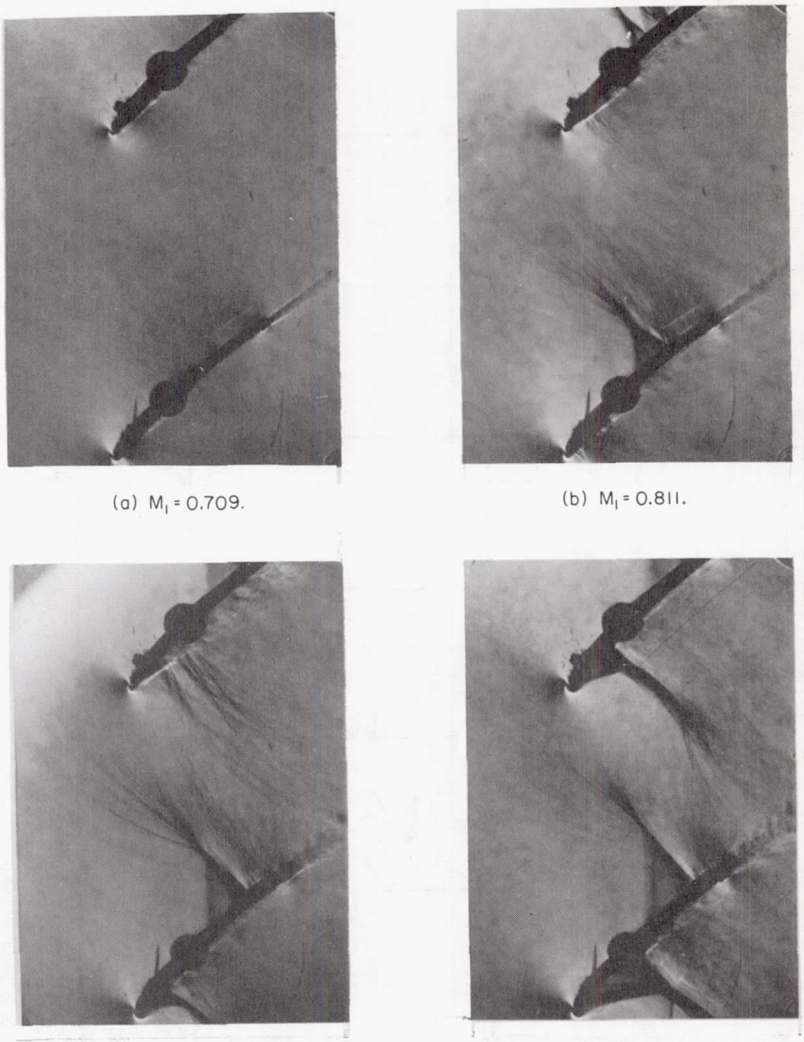
L-57-4471

Figure 79.- Schlieren photographs at various Mach numbers and section characteristics for cascade combination $\beta_1 = 41.0^\circ$, $\alpha = 1.0^\circ$, $\sigma = 0.6$, and NACA 65-$(8A_{10})$06 blade section.




(e) Section characteristics.

Figure 79.- Concluded.



(a) $M_1 = 0.709$.

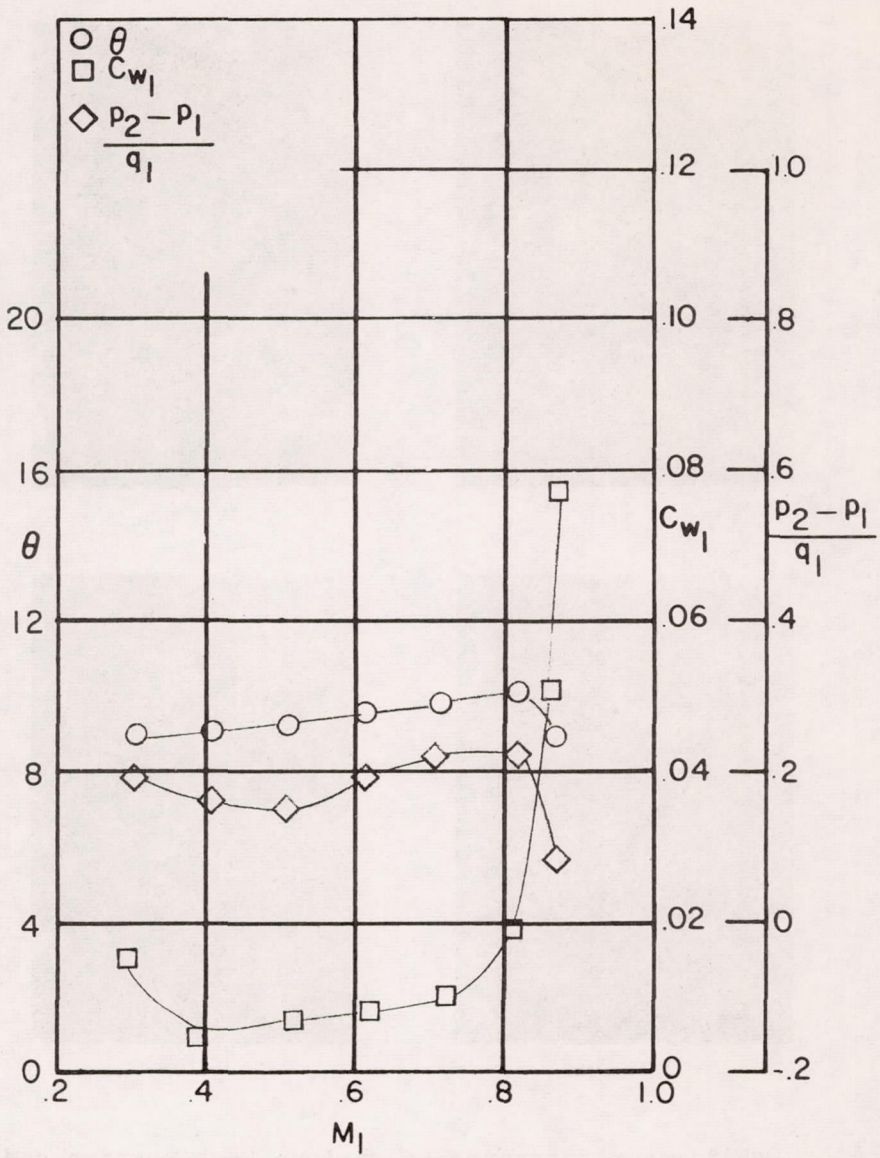
(b) $M_1 = 0.811$.

(c) $M_1 = 0.858$.

(d) $M_1 = 0.867$.

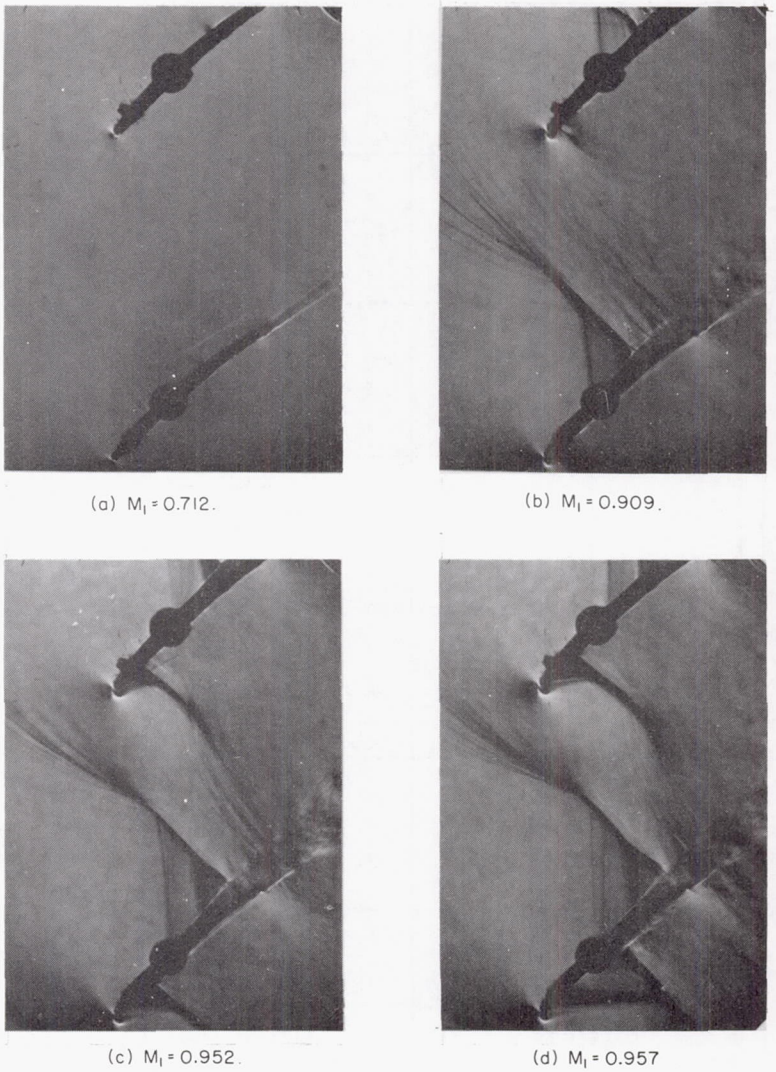
L-57-4472

Figure 80.- Schlieren photographs at various Mach numbers and section characteristics for cascade combination $\beta_1 = 44.0^\circ$, $\alpha = 4.0^\circ$, $\sigma = 0.6$, and NACA 65-$(8A_{10})$06 blade section.




(e) Section characteristics.

Figure 80.- Concluded.



(a) $M_1 = 0.712$.

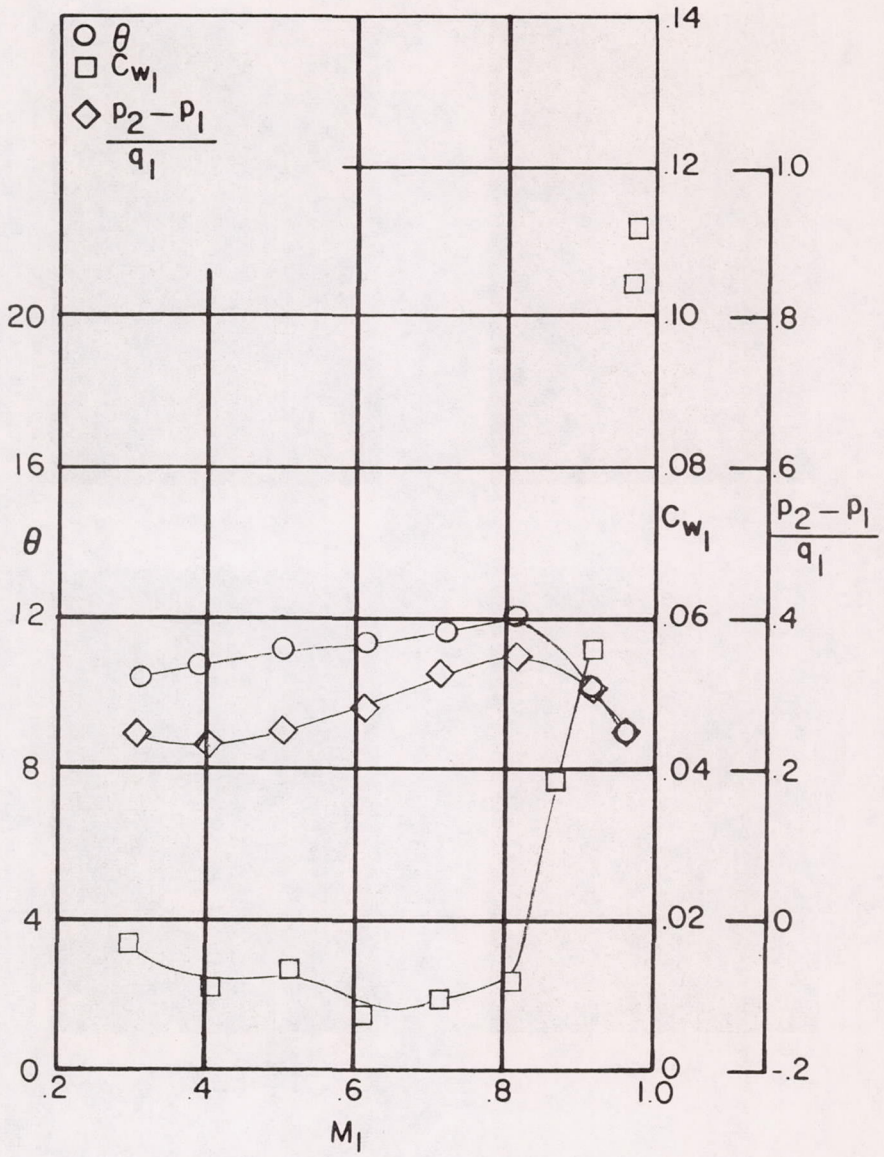
(b) $M_1 = 0.909$.

(c) $M_1 = 0.952$.

(d) $M_1 = 0.957$

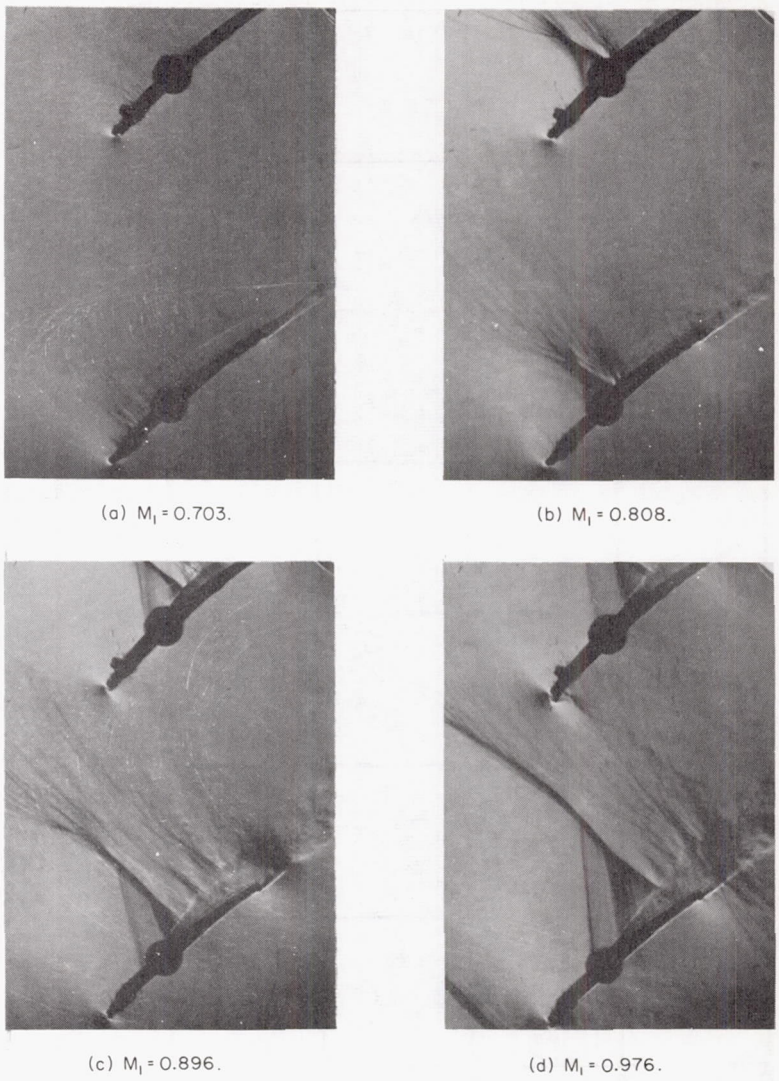
L-57-4473

Figure 81.- Schlieren photographs at various Mach numbers and section characteristics for cascade combination $\beta_1 = 47.0^\circ$, $\alpha = 7.0^\circ$, $\sigma = 0.6$, and NACA 65-$(8A_{10})$06 blade section.




(e) Section characteristics.

Figure 81.- Concluded.



(a) $M_1 = 0.703$.

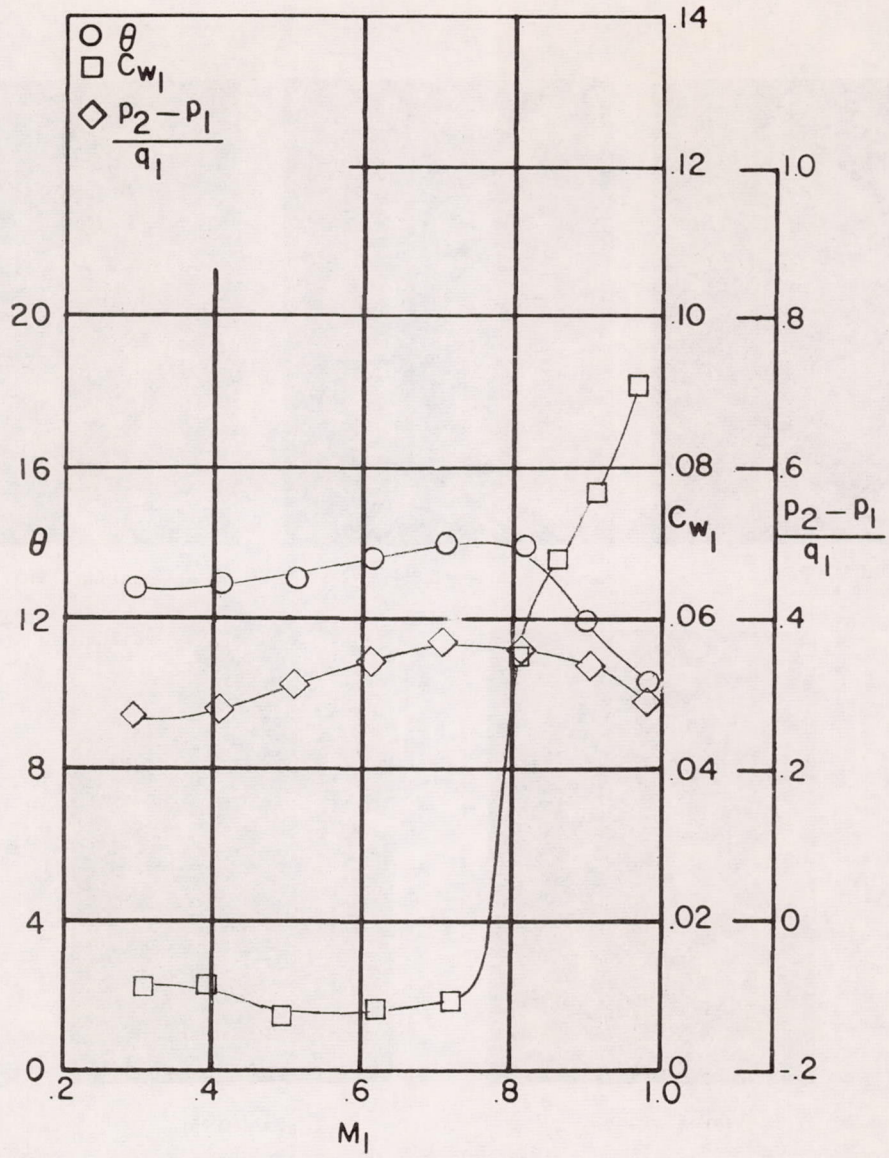
(b) $M_1 = 0.808$.

(c) $M_1 = 0.896$.

(d) $M_1 = 0.976$.

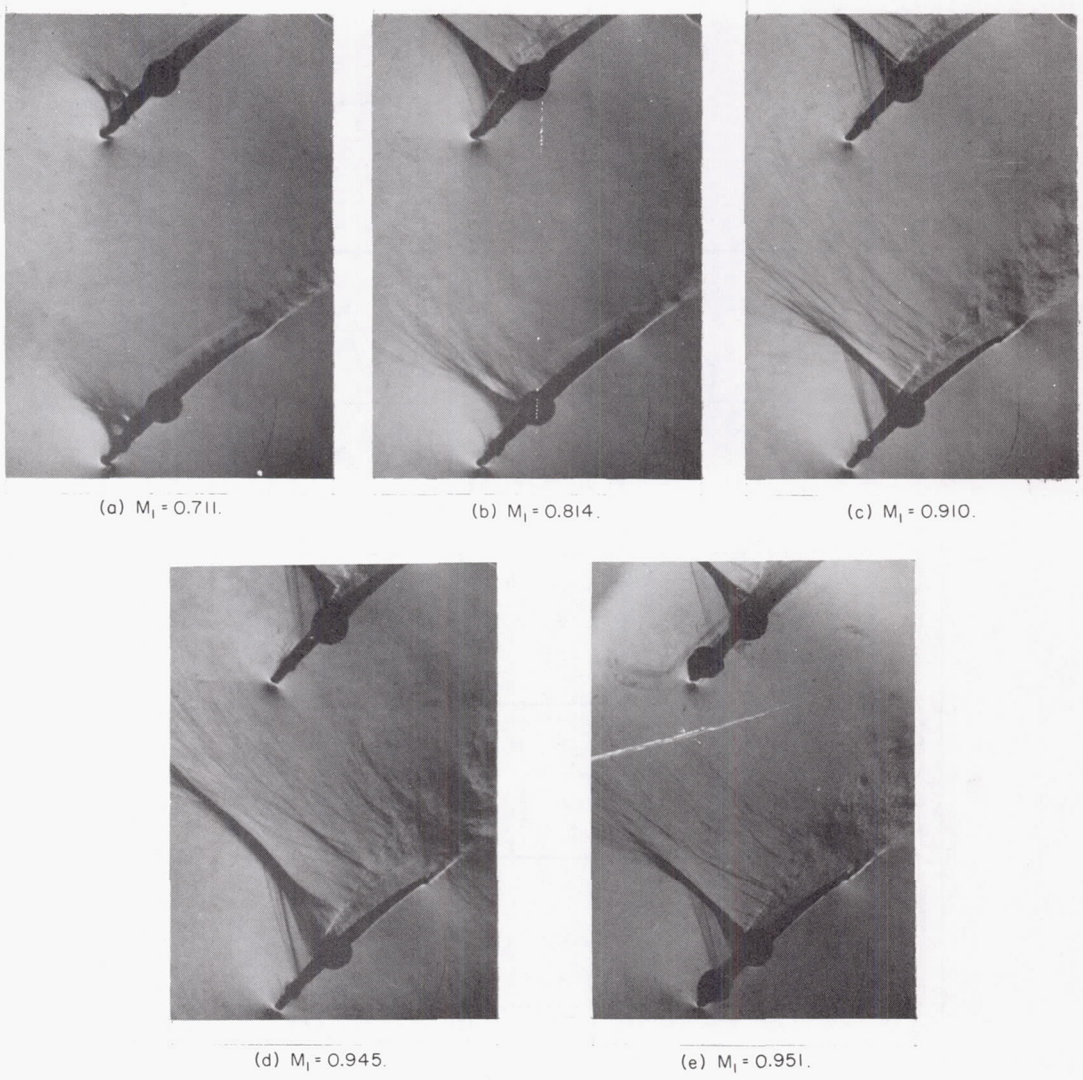
L-57-4474

Figure 82.- Schlieren photographs at various Mach numbers and section characteristics for cascade combination $\beta_1 = 50.0^\circ$, $\alpha = 10.0^\circ$, $\sigma = 0.6$, and NACA 65-$(8A_{10})$06 blade section.




(e) Section characteristics.

Figure 82.- Concluded.

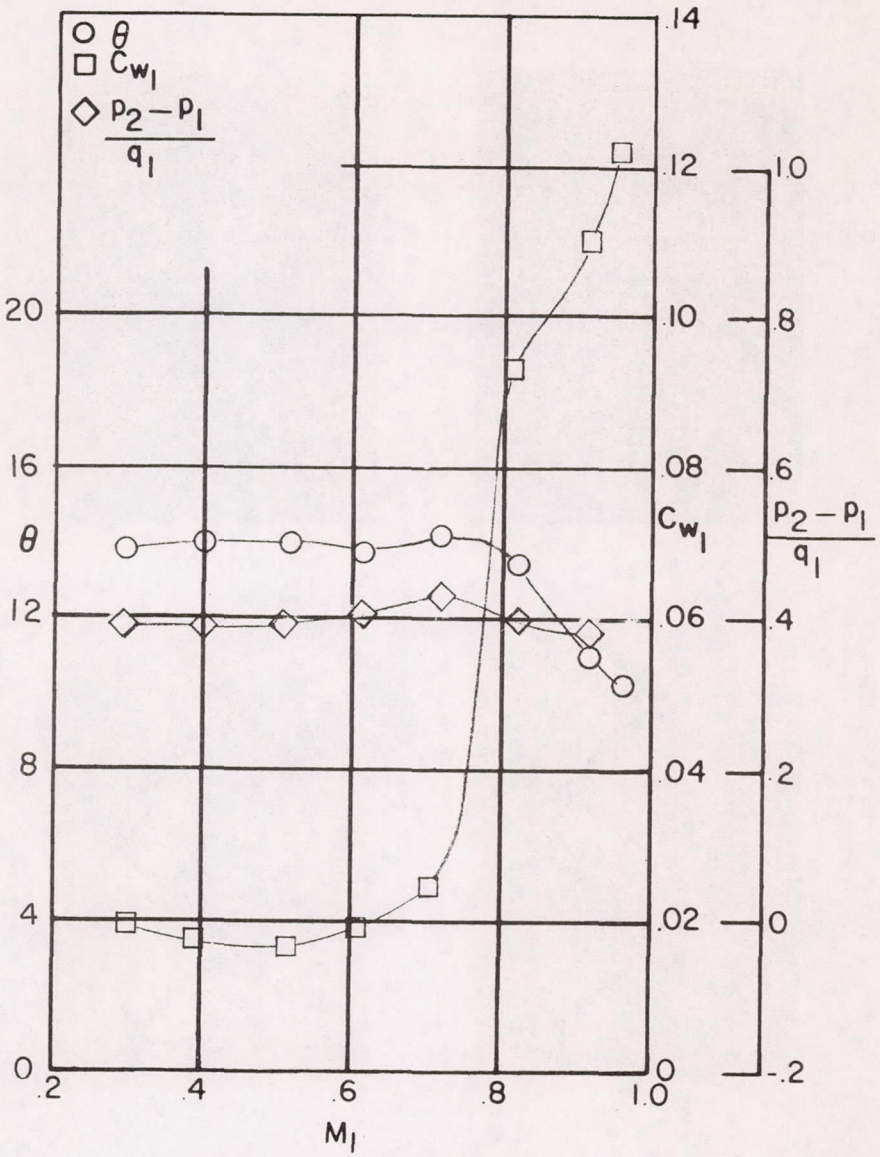


(a) $M_1 = 0.711$. (b) $M_1 = 0.814$. (c) $M_1 = 0.910$.

(d) $M_1 = 0.945$. (e) $M_1 = 0.951$.

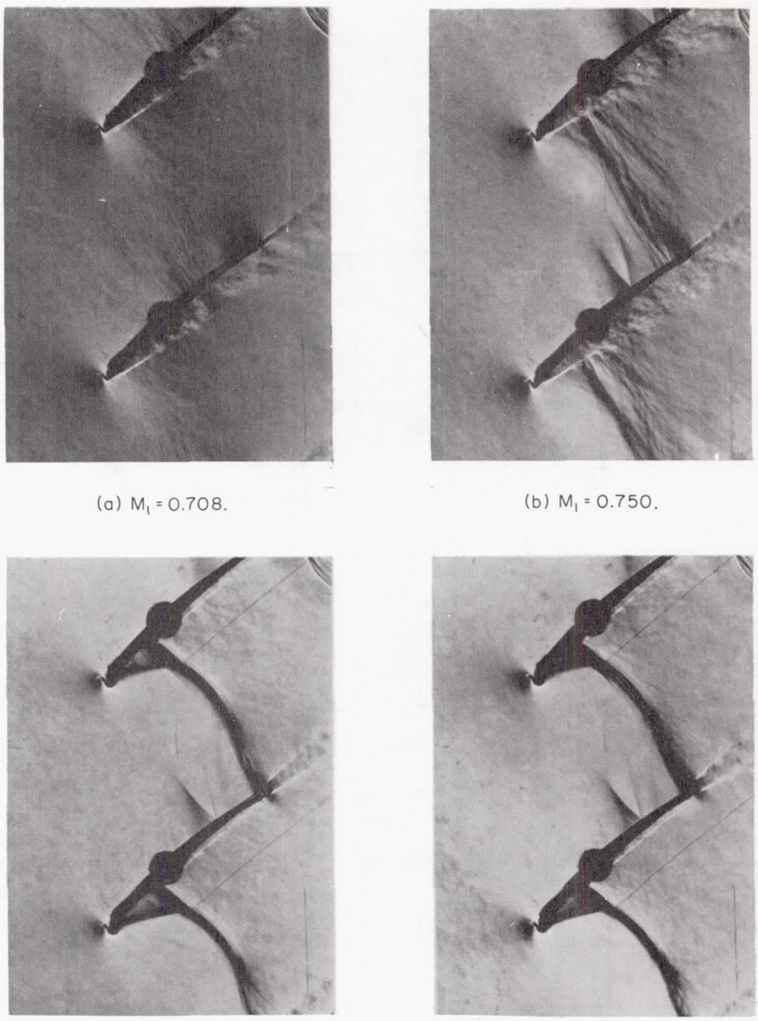
L-57-4475

Figure 83.- Schlieren photographs at various Mach numbers and section characteristics for cascade combination $\beta_1 = 53.0^\circ$, $\alpha = 13.0^\circ$, $\sigma = 0.6$, and NACA 65-$\left(8A_{10}\right)$06 blade section.




(f) Section characteristics.

Figure 83.- Concluded.



(a) $M_1 = 0.708$.

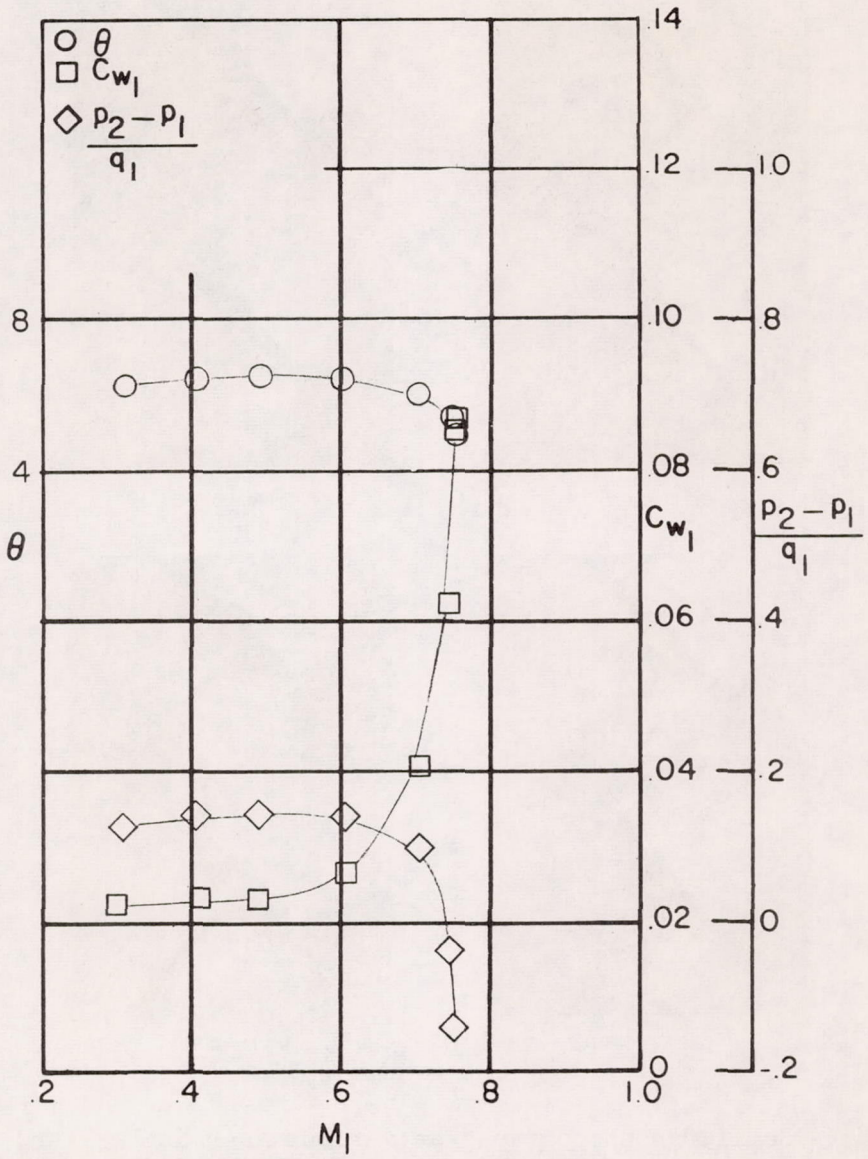
(b) $M_1 = 0.750$.

(c) $M_1 = 0.755$.

(d) $M_1 = 0.757$.

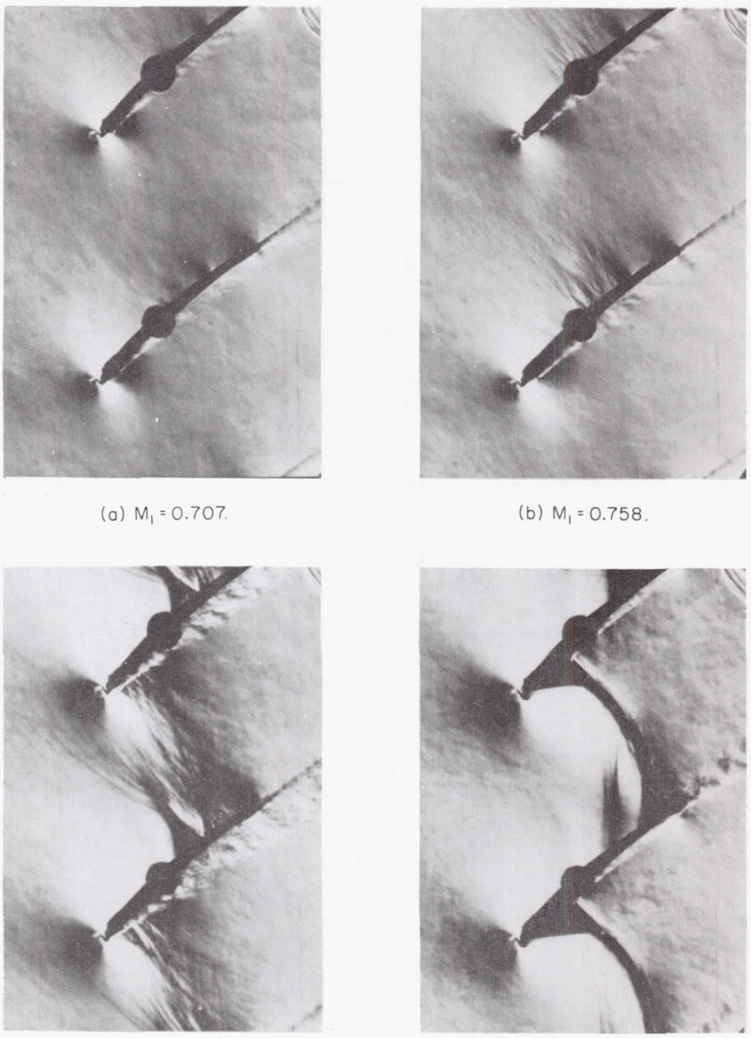
L-57-4476

Figure 84.- Schlieren photographs at various Mach numbers and section characteristics for cascade combination $\beta_1 = 41.0^\circ$, $\alpha = 2.0^\circ$, $\sigma = 0.8$, and NACA 65-$(8A_{10})$06 blade section.




(e) Section characteristics.

Figure 84.- Concluded.



(a) $M_1 = 0.707$.

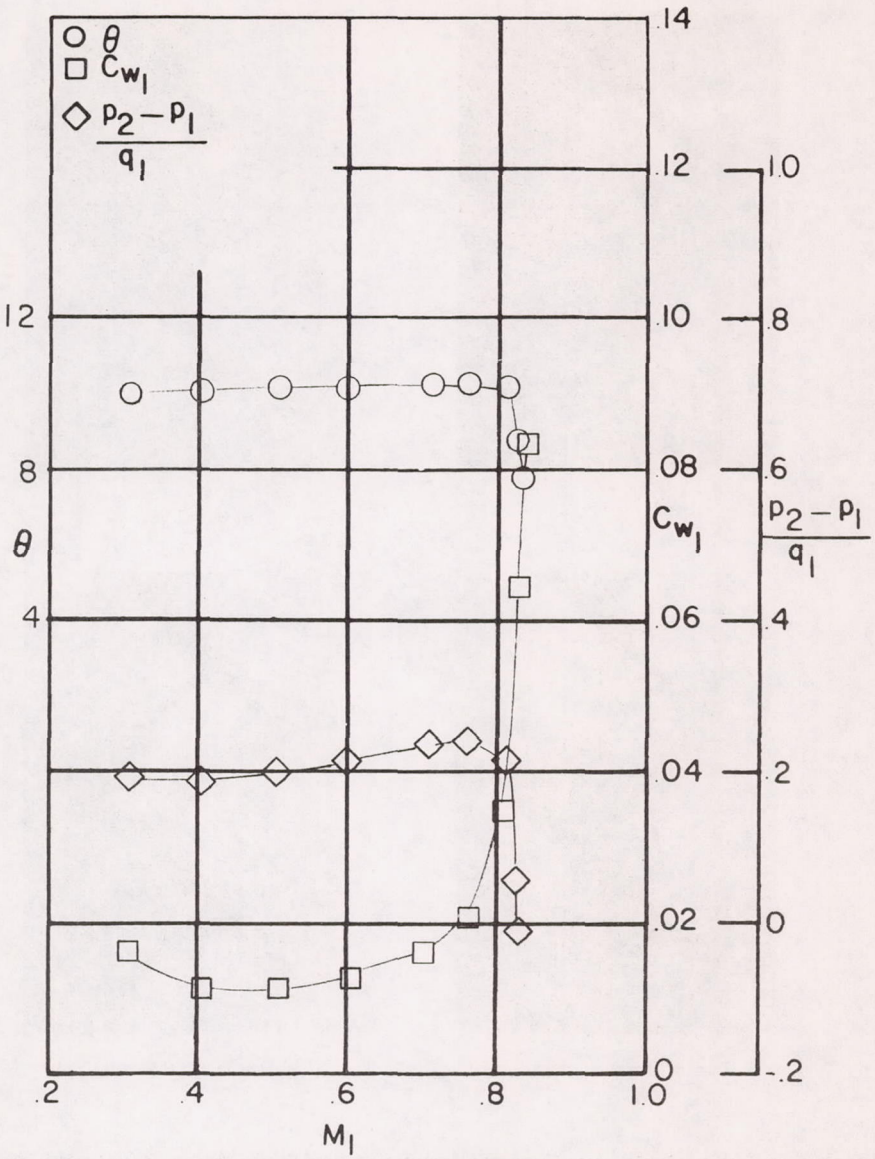
(b) $M_1 = 0.758$.

(c) $M_1 = 0.810$.

(d) $M_1 = 0.822$.

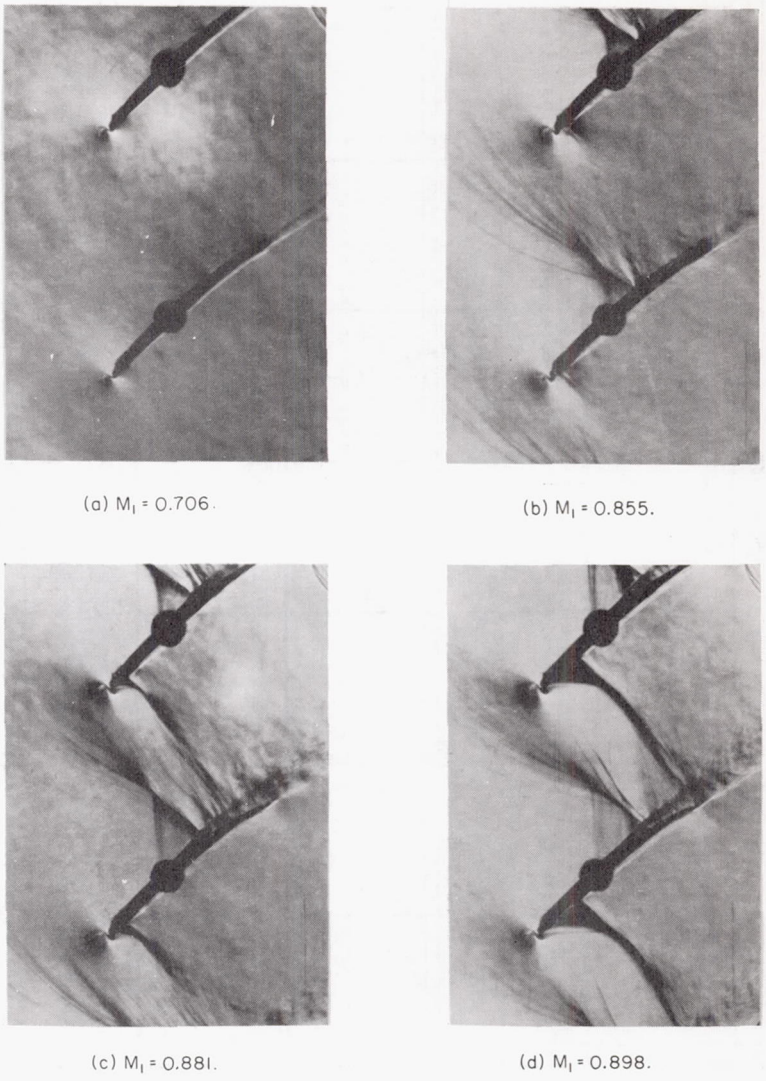
L-57-4477

Figure 85.- Schlieren photographs at various Mach numbers and section characteristics for cascade combination $\beta_1 = 44.0^\circ$, $\alpha = 5.0^\circ$, $\sigma = 0.8$, and NACA 65-$(8A_{10})$06 blade section.




(e) Section characteristics.

Figure 85.- Concluded.



(a) $M_1 = 0.706$.

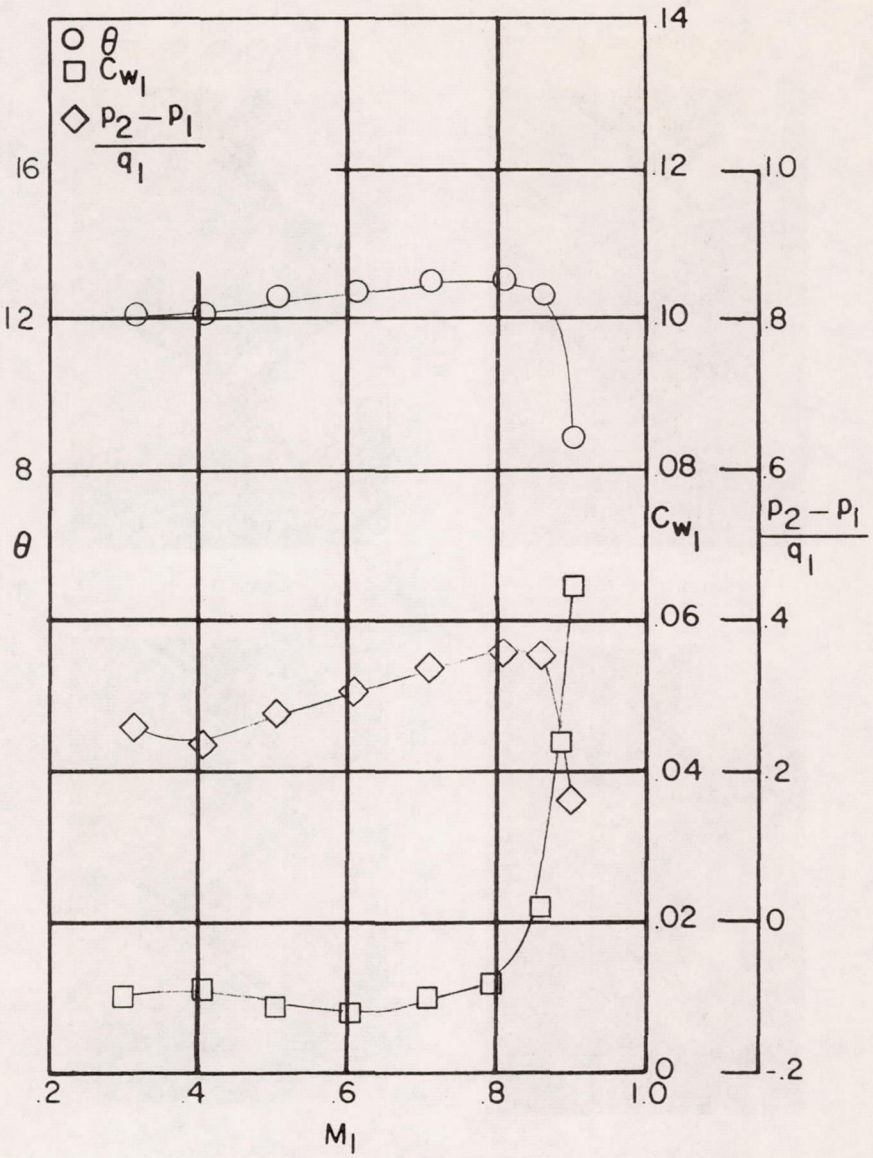
(b) $M_1 = 0.855$.

(c) $M_1 = 0.881$.

(d) $M_1 = 0.898$.

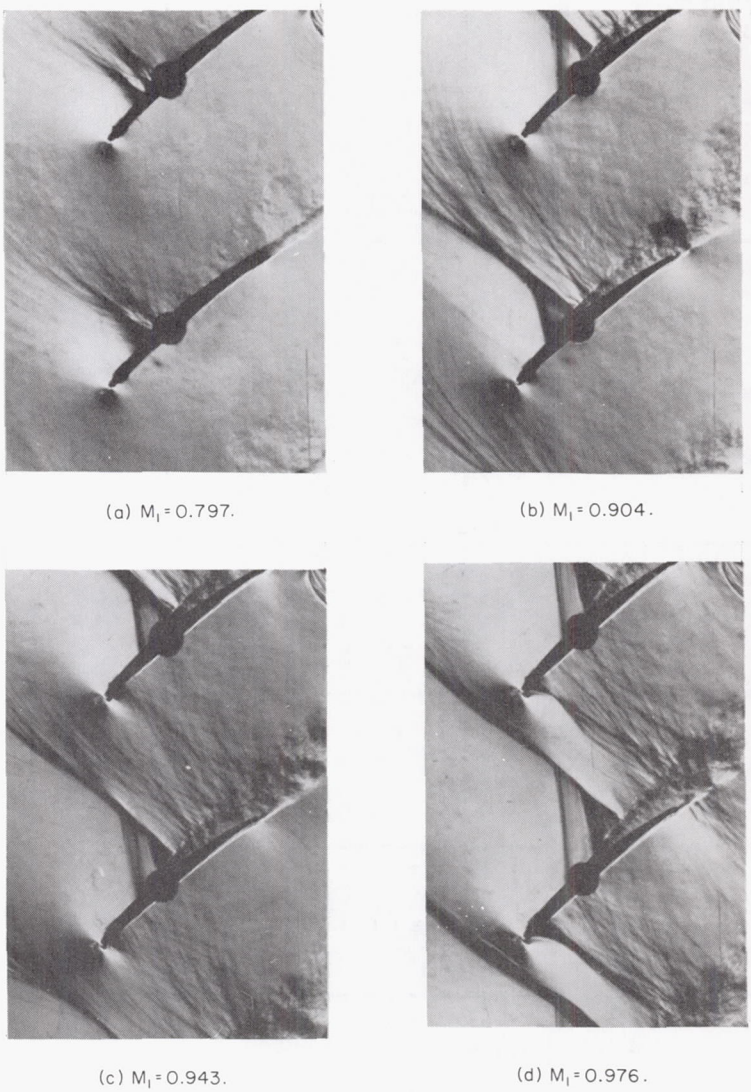
L-57-4478

Figure 86.- Schlieren photographs at various Mach numbers and section characteristics for cascade combination $\beta_1 = 47.0^\circ$, $\alpha = 8.0^\circ$, $\sigma = 0.8$, and NACA 65-$(8A_{10})$06 blade section.




(e) Section characteristics.

Figure 86.- Concluded.



(a) $M_1 = 0.797$.

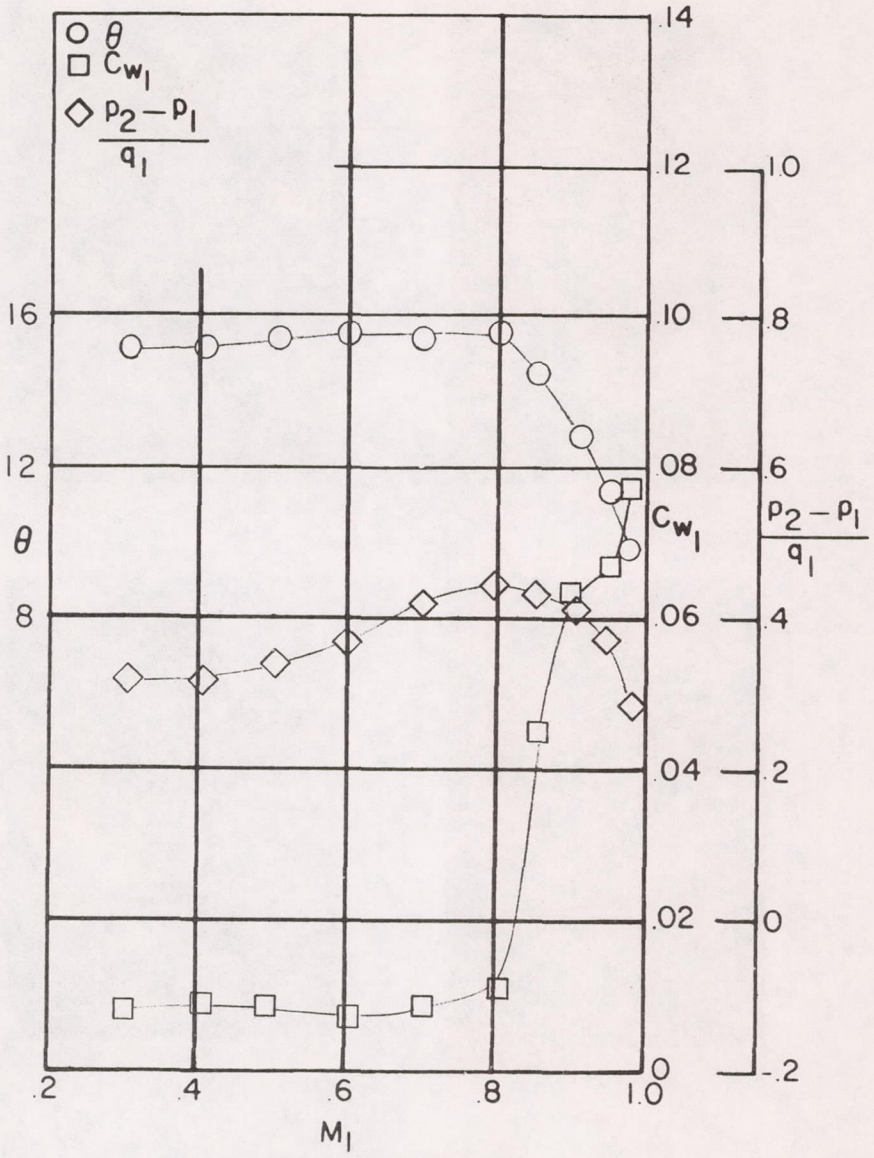
(b) $M_1 = 0.904$.

(c) $M_1 = 0.943$.

(d) $M_1 = 0.976$.

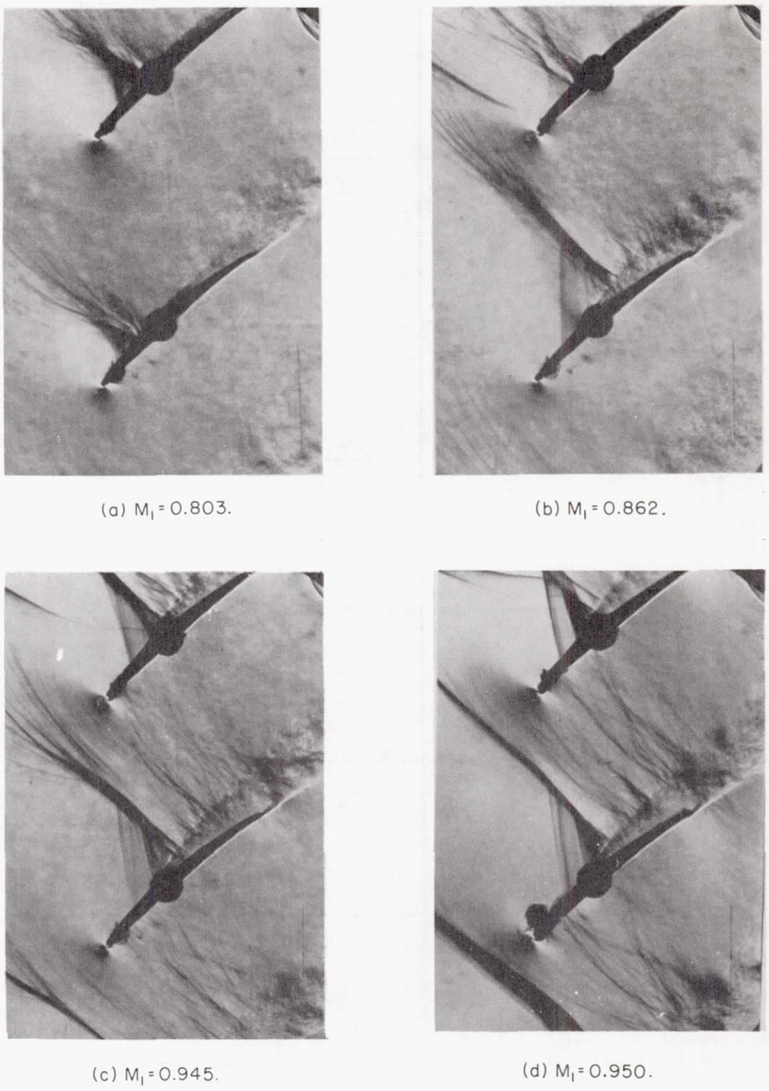
L-57-4479

Figure 87.- Schlieren photographs at various Mach numbers and section characteristics for cascade combination $\beta_1 = 50.0^\circ$, $\alpha = 11.0^\circ$, $\sigma = 0.8$, and NACA 65-$\left(8A_{10}\right)$06 blade section.




(e) Section characteristics.

Figure 87.- Concluded.



(a) $M_1 = 0.803$.

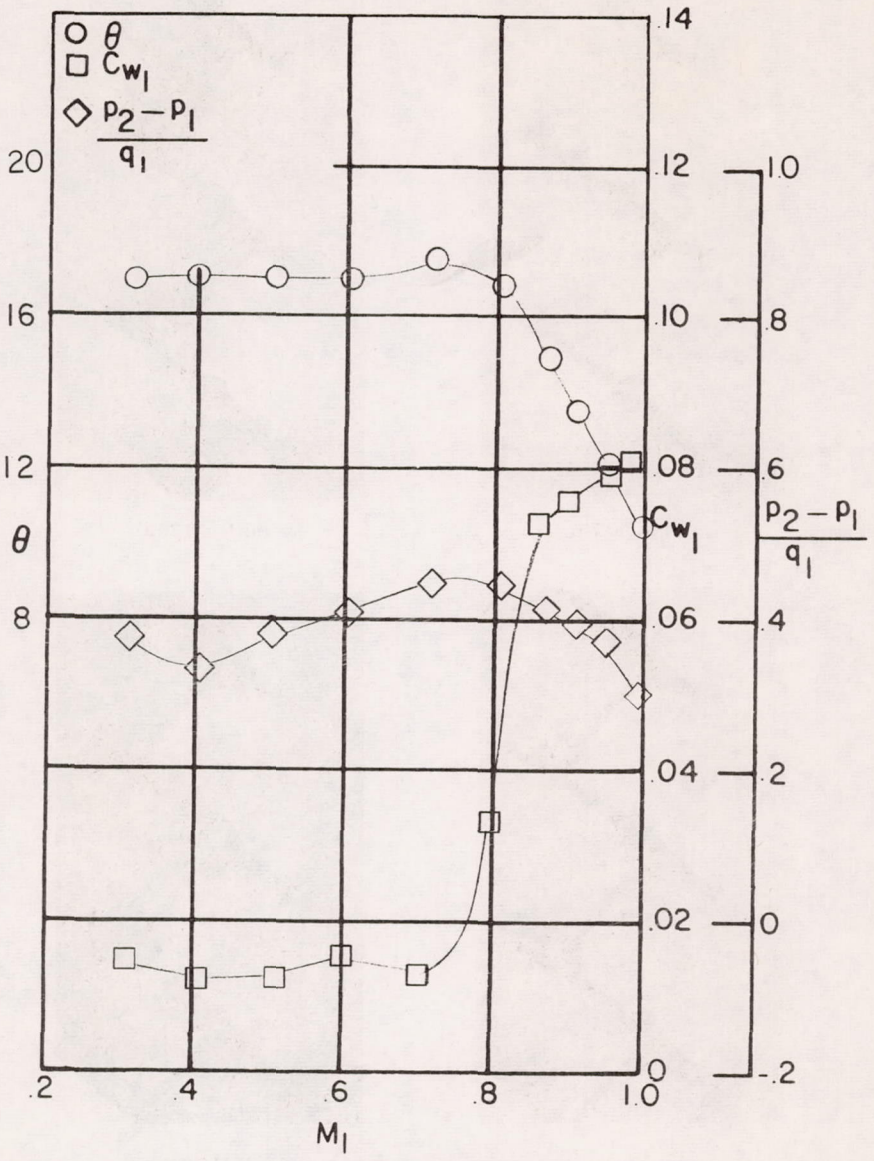
(b) $M_1 = 0.862$.

(c) $M_1 = 0.945$.

(d) $M_1 = 0.950$.

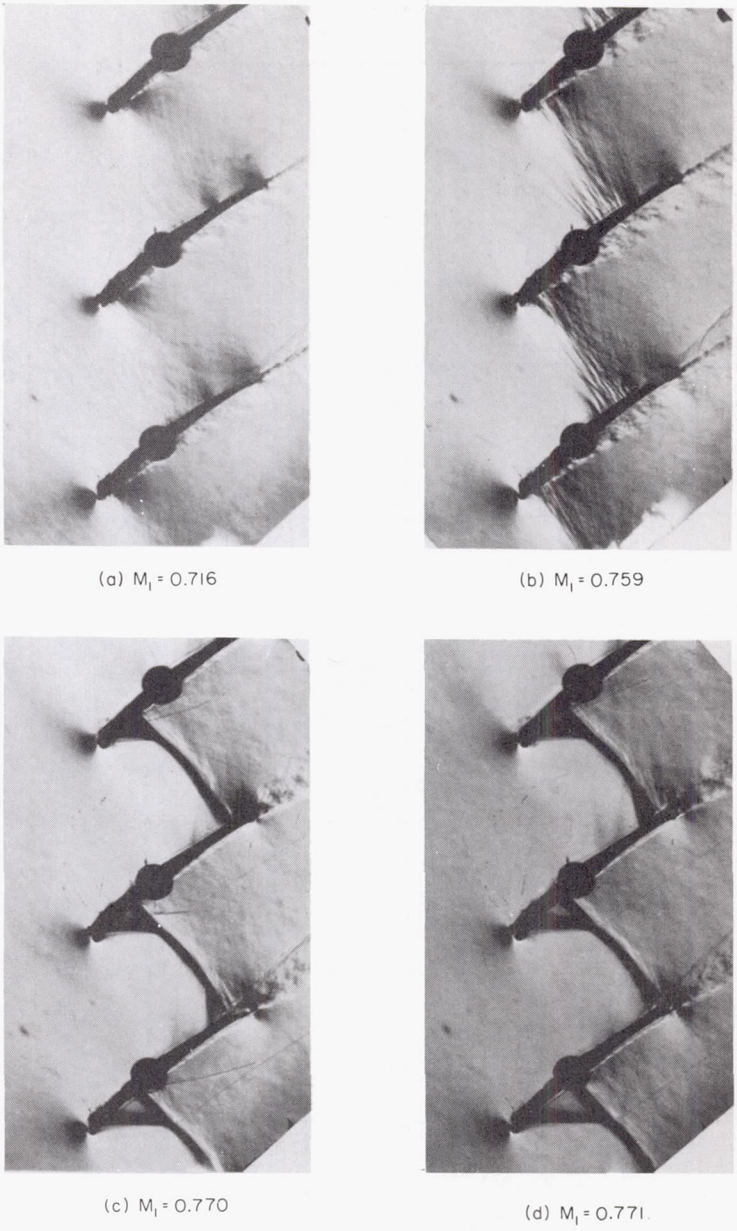
L-57-4480

Figure 88.- Schlieren photographs at various Mach numbers and section characteristics for cascade combination $\beta_1 = 53.0^\circ$, $\alpha = 14.0^\circ$, $\sigma = 0.8$, and NACA 65-$(8A_{10})$06 blade section.




(e) Section characteristics.

Figure 88.- Concluded.



(a) $M_1 = 0.716$

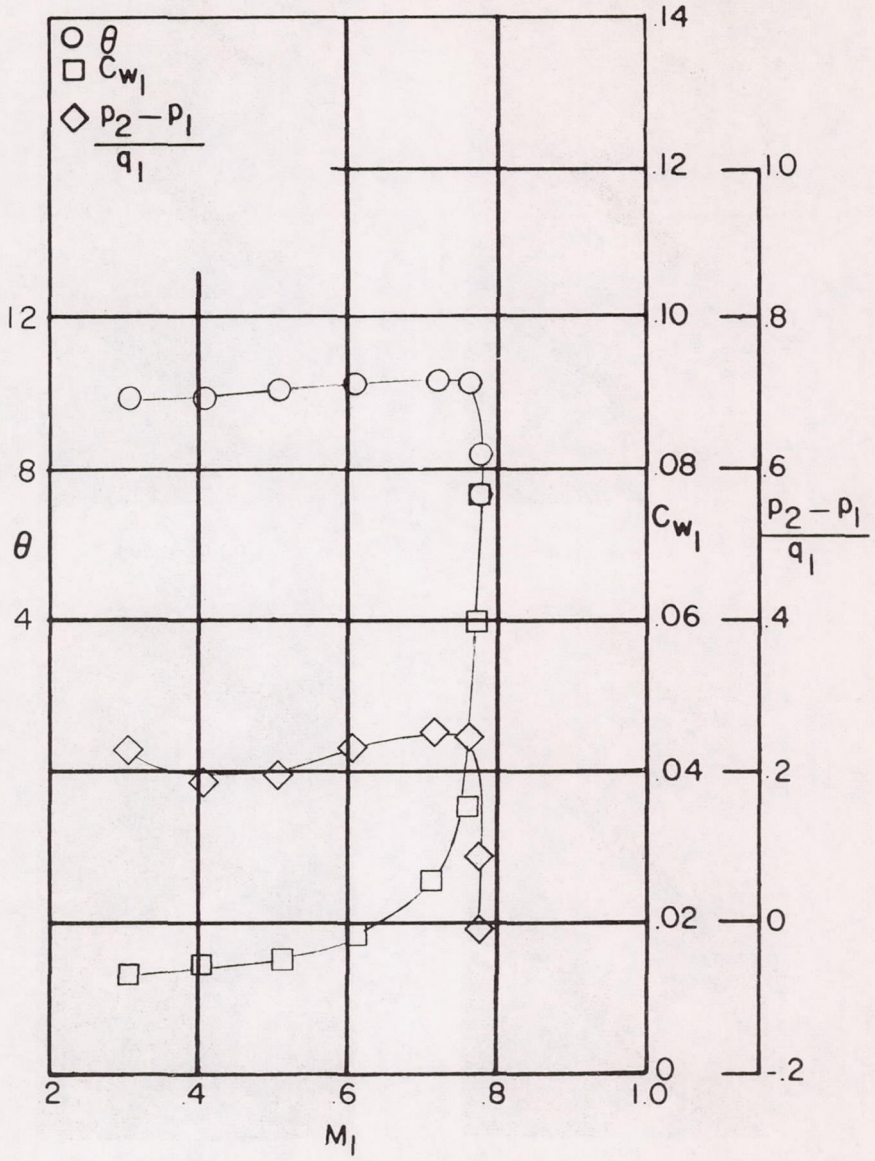
(b) $M_1 = 0.759$

(c) $M_1 = 0.770$

(d) $M_1 = 0.771$

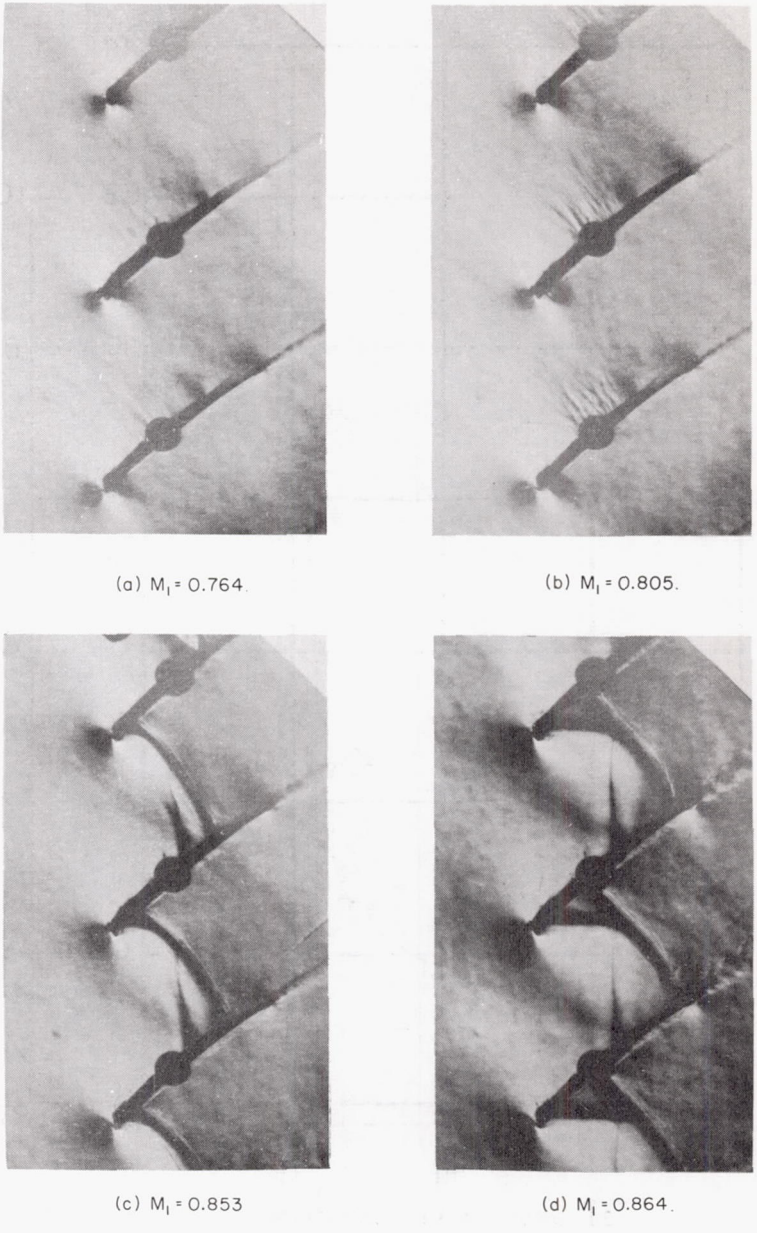
L-57-4481

Figure 89.- Schlieren photographs at various Mach numbers and section characteristics for cascade combination $\beta_1 = 41.0^\circ$, $\alpha = 4.0^\circ$, $\sigma = 1.0$, and NACA 65-$(8A_{10})$06 blade section.




(e) Section characteristics.

Figure 89.- Concluded.



(a) $M_1 = 0.764$.

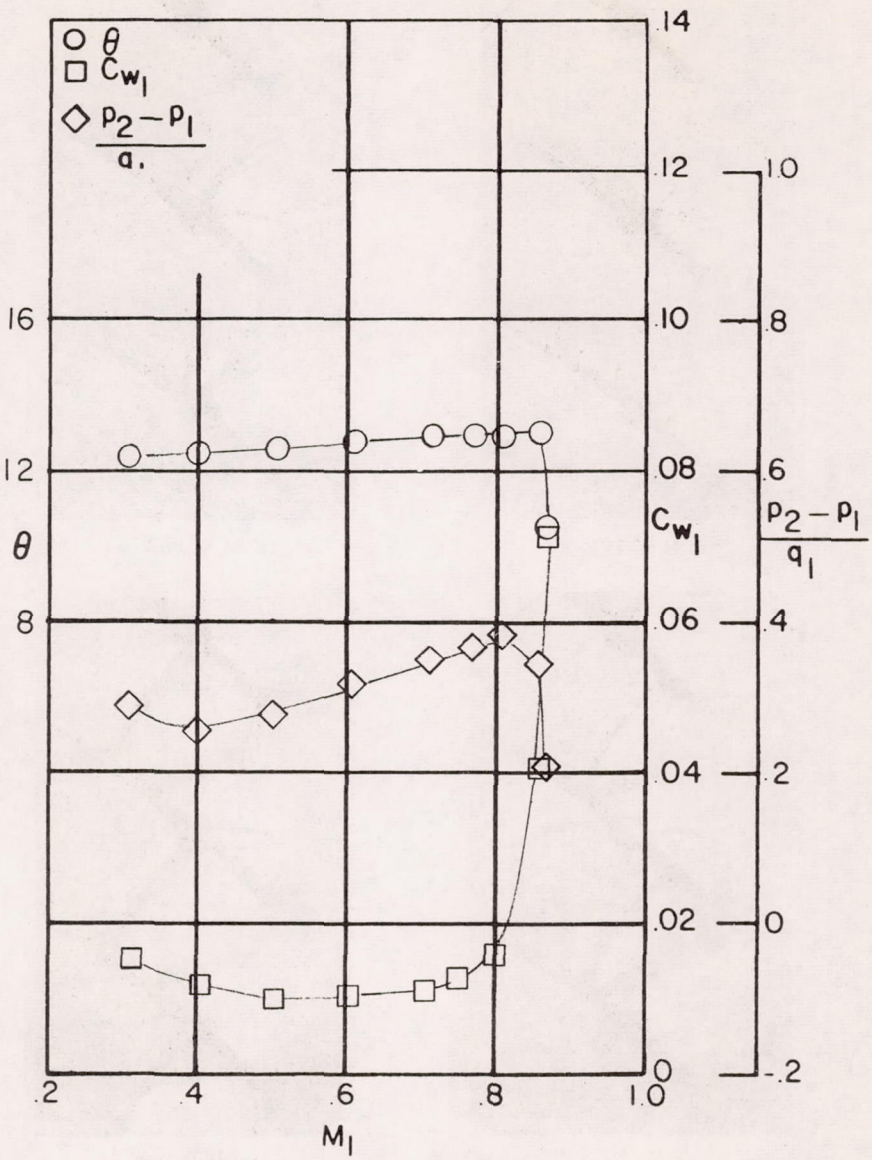
(b) $M_1 = 0.805$.

(c) $M_1 = 0.853$

(d) $M_1 = 0.864$.

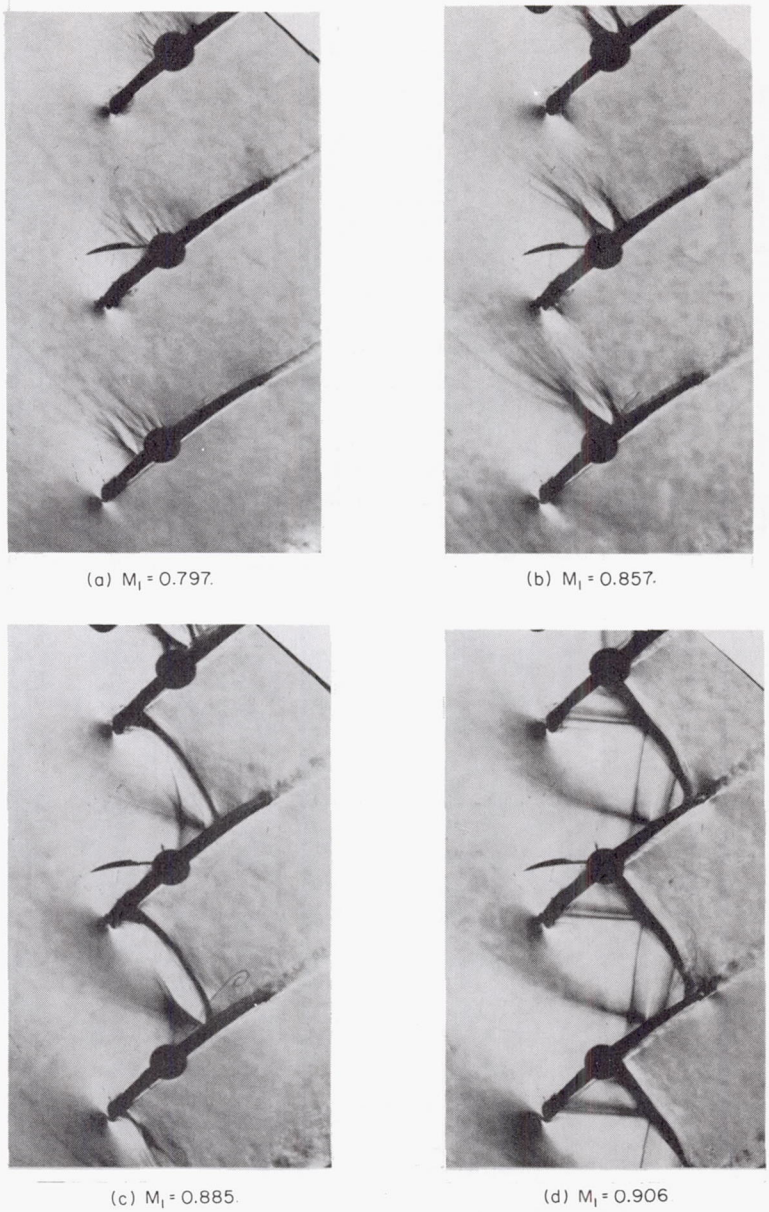
L-57-4482

Figure 90.- Schlieren photographs at various Mach numbers and section characteristics for cascade combination $\beta_1 = 44.0^\circ$, $\alpha = 7.0^\circ$, $\sigma = 1.0$, and NACA 65-$(8A_{10})$06 blade section.




(e) Section characteristics.

Figure 90.- Concluded.



(a) $M_1 = 0.797$.

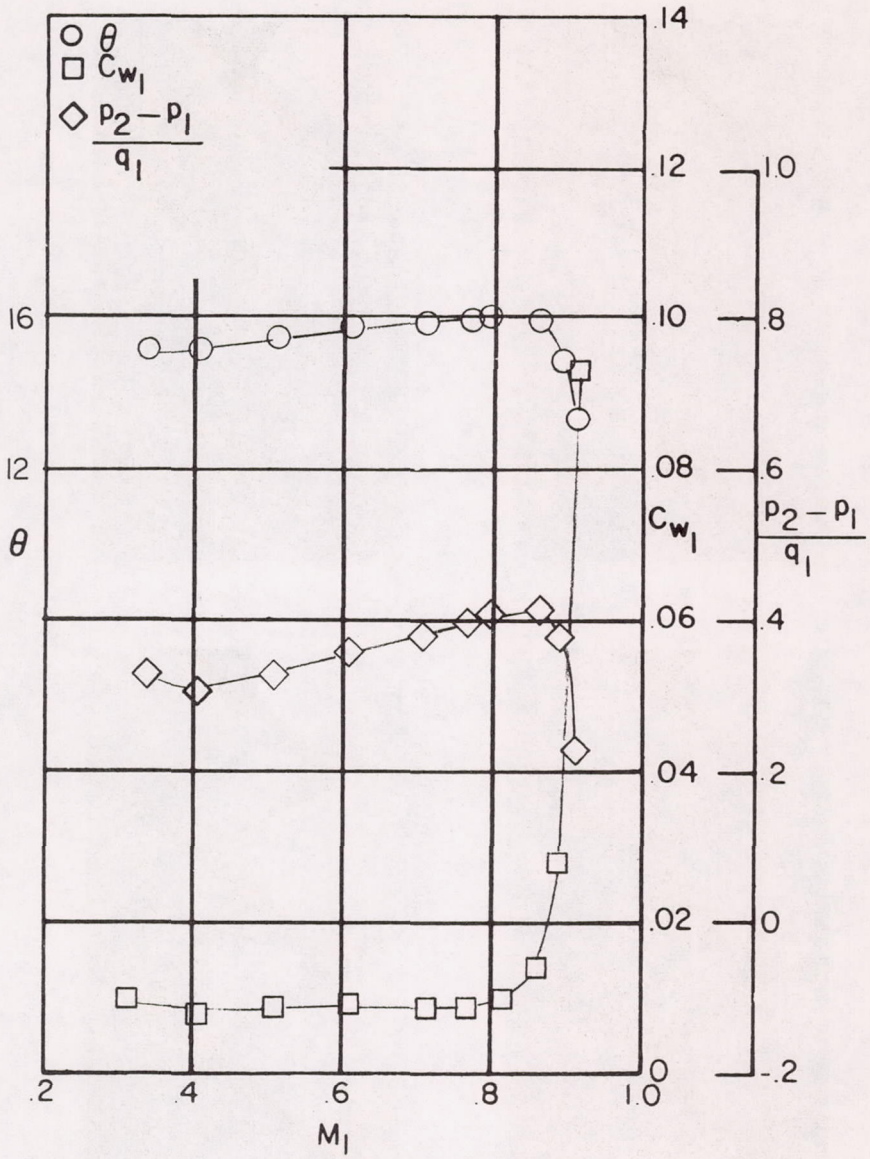
(b) $M_1 = 0.857$.

(c) $M_1 = 0.885$.

(d) $M_1 = 0.906$

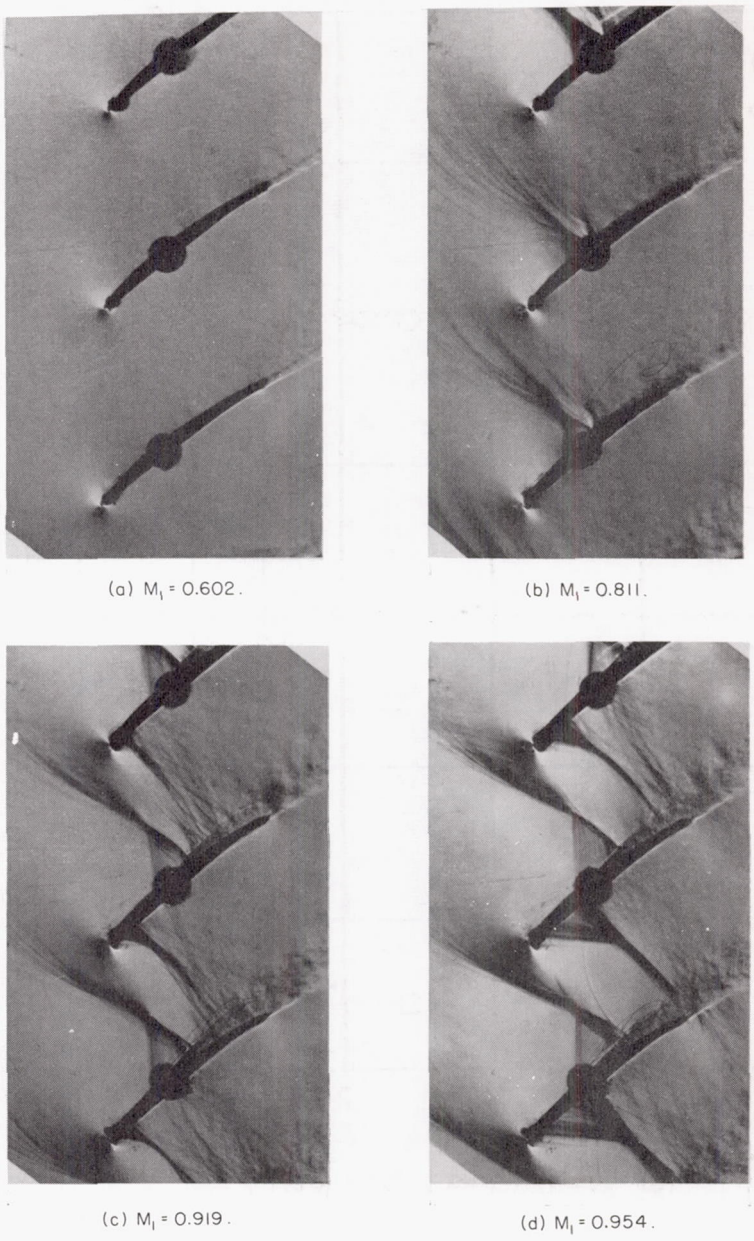
L-57-4483

Figure 91.- Schlieren photographs at various Mach numbers and section characteristics for cascade combination $\beta_1 = 47.0^\circ$, $\alpha = 10.0^\circ$, $\sigma = 1.0$, and NACA 65-$(8A_{10})$06 blade section.




(e) Section characteristics.

Figure 91.- Concluded.



(a) $M_1 = 0.602$.

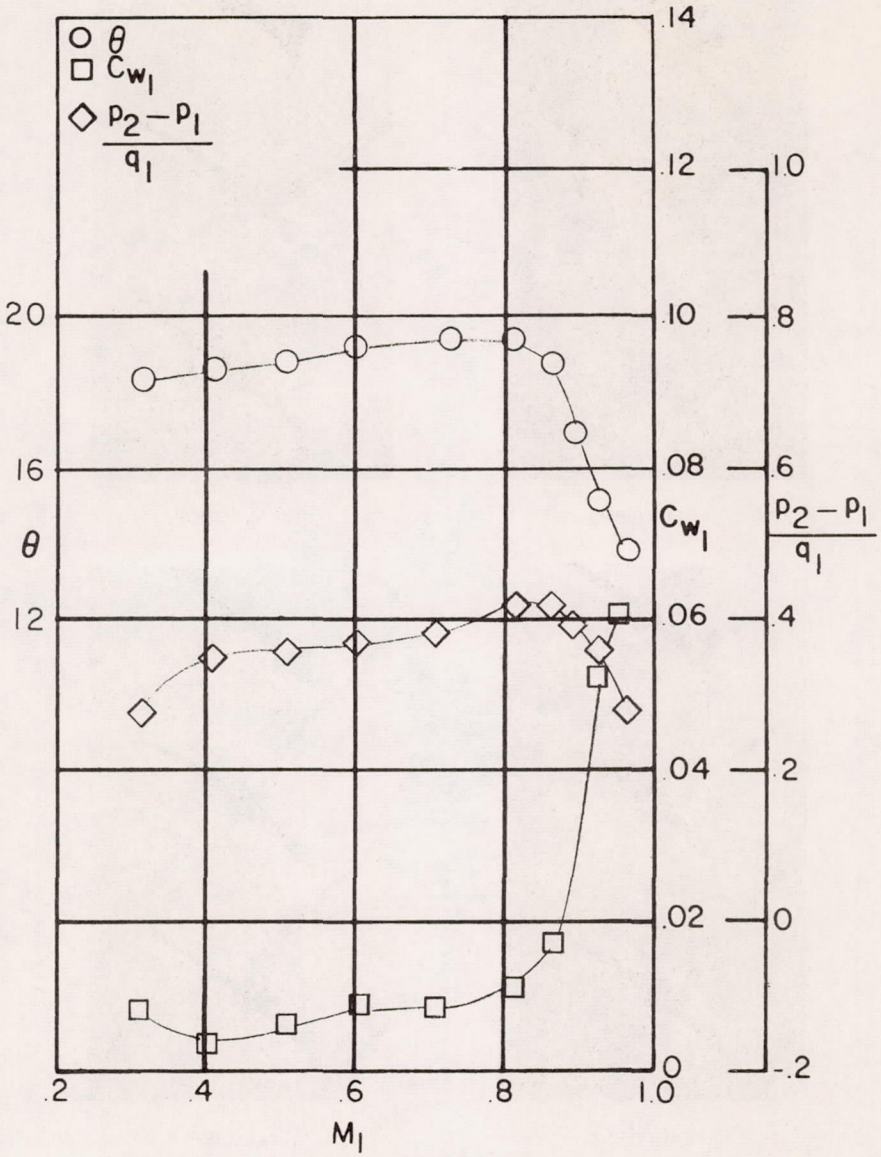
(b) $M_1 = 0.811$.

(c) $M_1 = 0.919$.

(d) $M_1 = 0.954$.

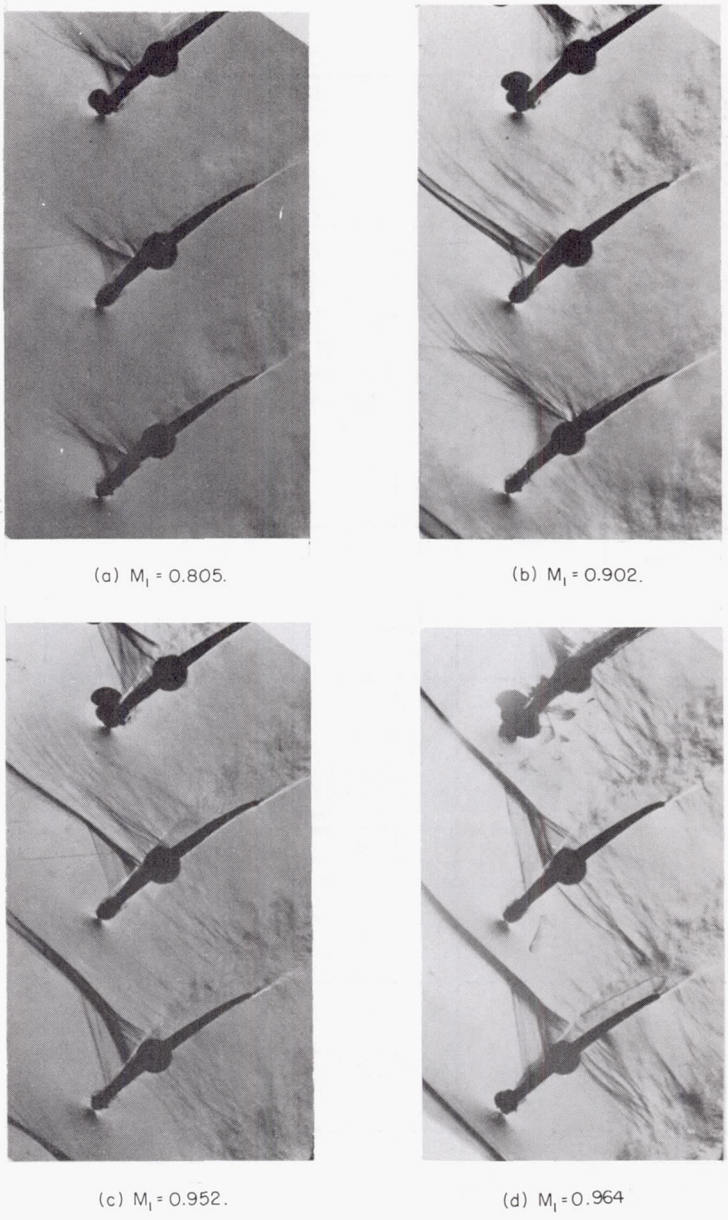
L-57-4484

Figure 92.- Schlieren photographs at various Mach numbers and section characteristics for cascade combination $\beta_1 = 50.0^\circ$, $\alpha = 13.0^\circ$, $\sigma = 1.0$, and NACA 65-$(8A_{10})$06 blade section.




(e) Section characteristics.

Figure 92.- Concluded.



(a) $M_1 = 0.805$.

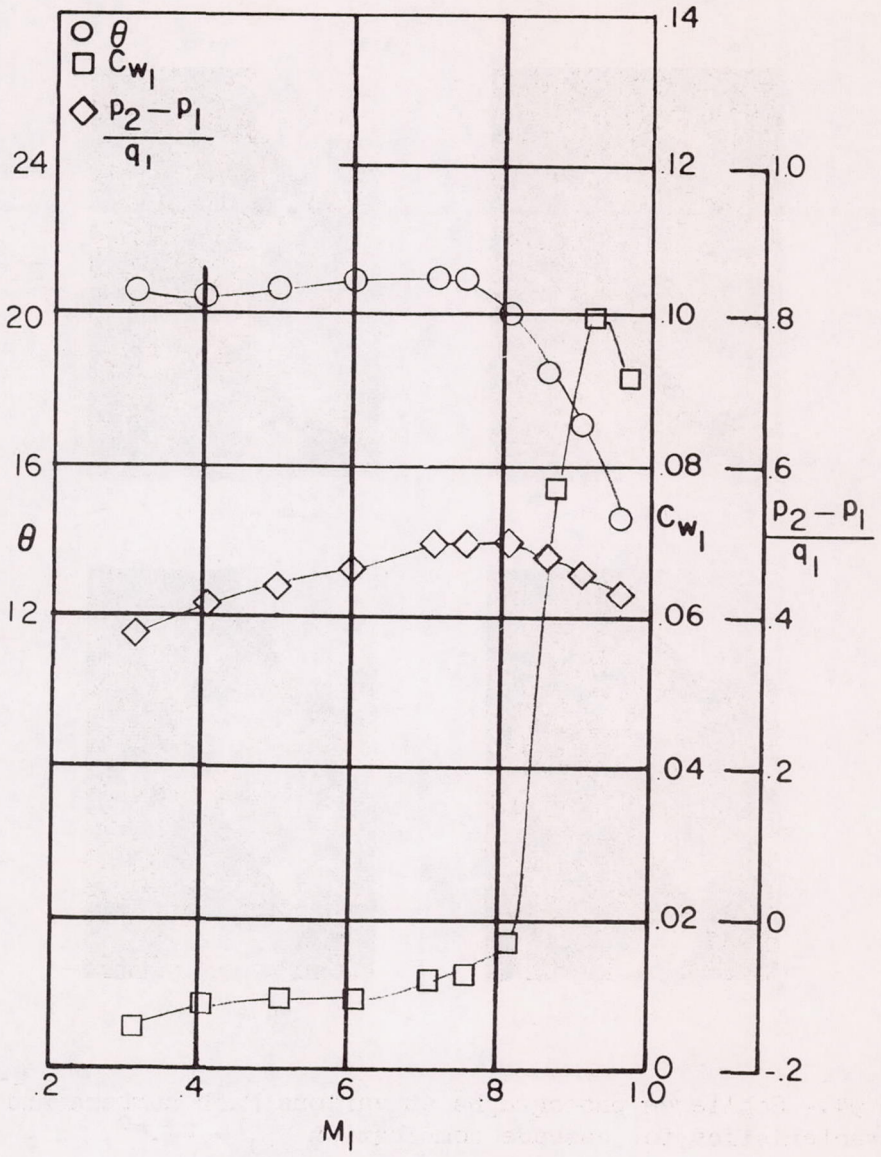
(b) $M_1 = 0.902$.

(c) $M_1 = 0.952$.

(d) $M_1 = 0.964$

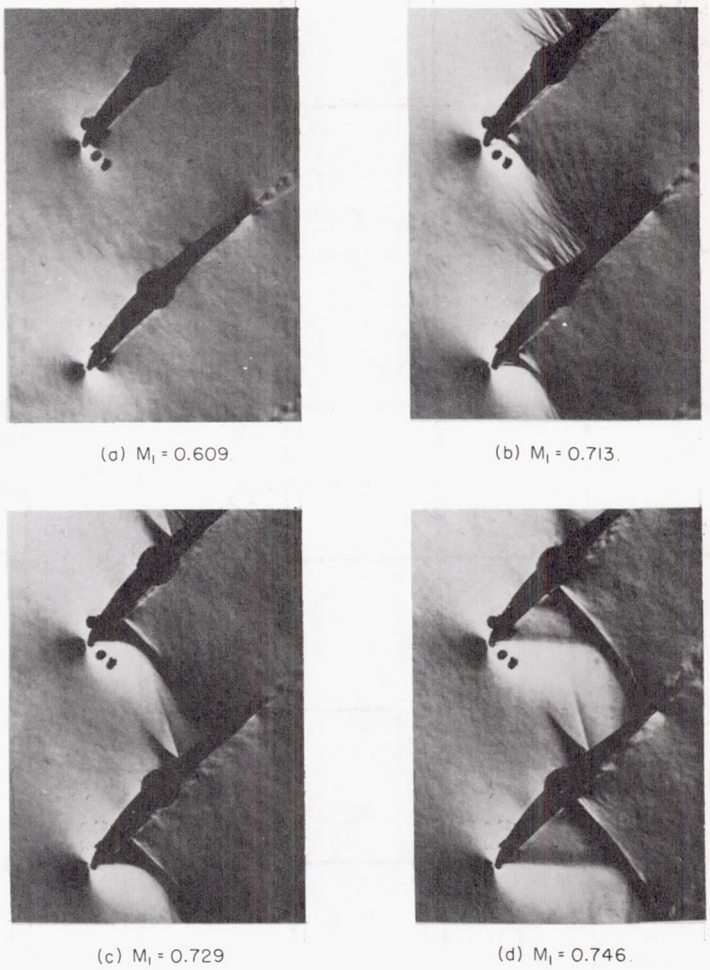
L-57-4485

Figure 93.- Schlieren photographs at various Mach numbers and section characteristics for cascade combination $\beta_1 = 53.0^\circ$, $\alpha = 16.0^\circ$, $\sigma = 1.0$, and NACA 65-$\left(8A_{10}\right)$06 blade section.




(e) Section characteristics.

Figure 93.- Concluded.

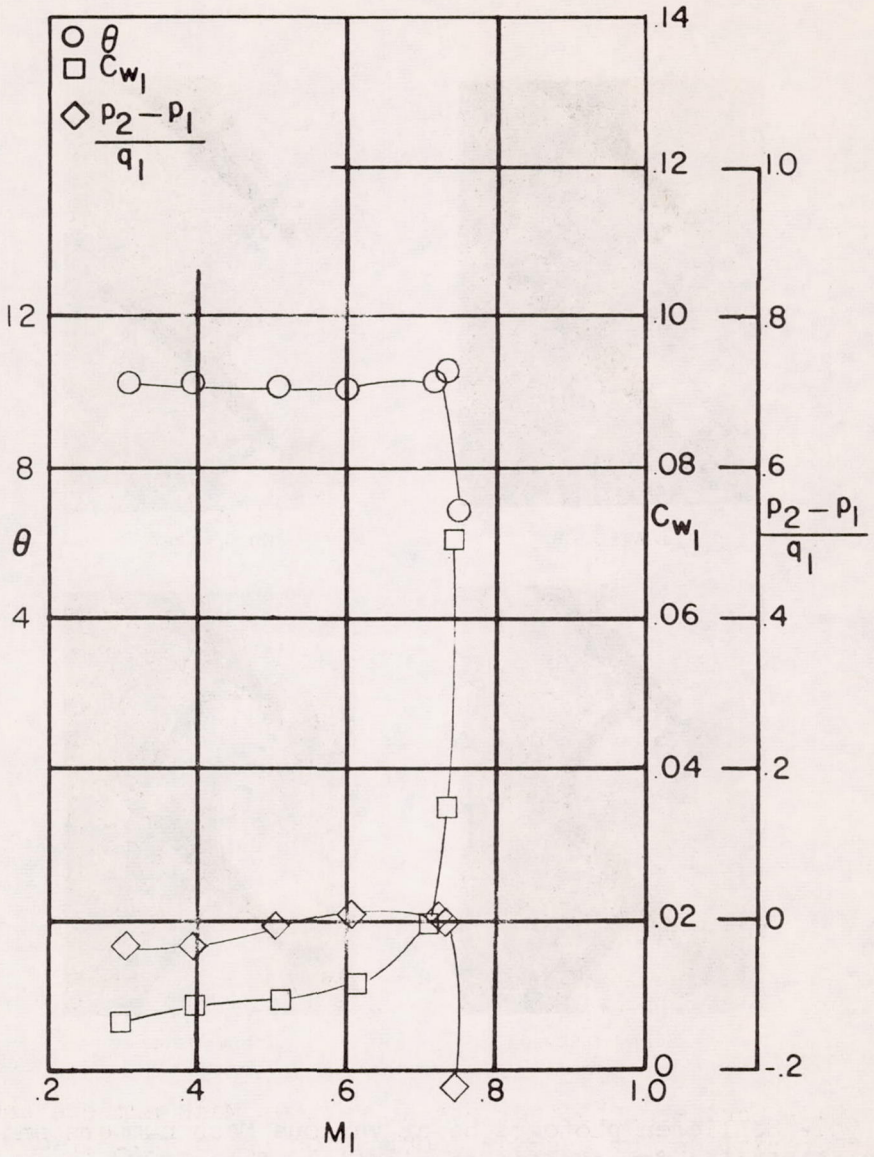


(a) $M_1 = 0.609$ (b) $M_1 = 0.713$

(c) $M_1 = 0.729$ (d) $M_1 = 0.746$

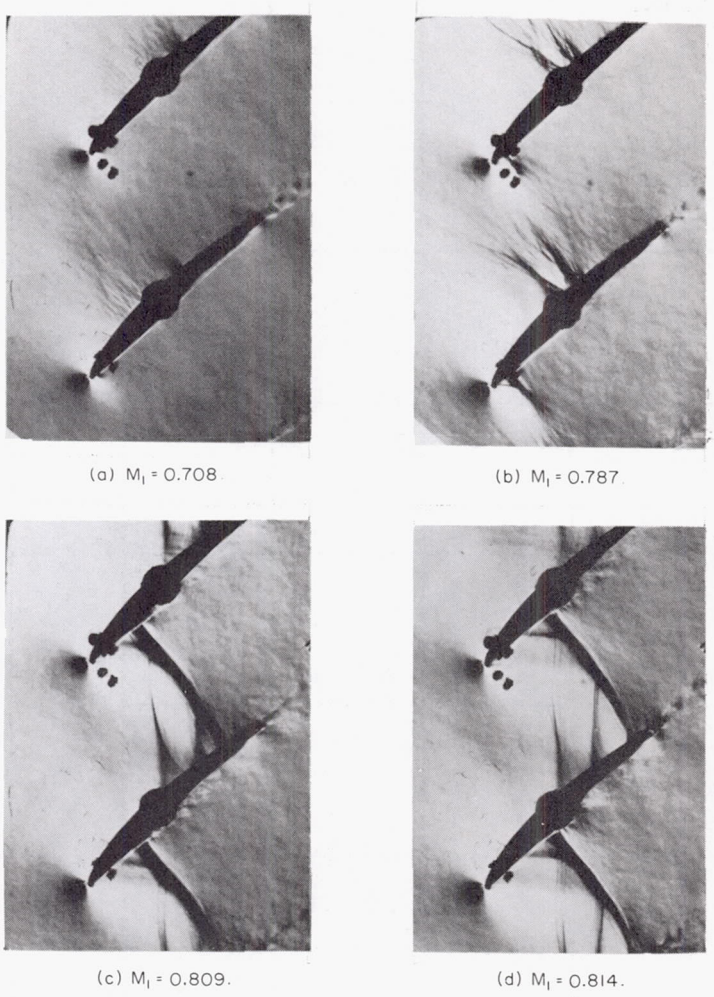
L-57-4486

Figure 94.- Schlieren photographs at various Mach numbers and section characteristics for cascade combination $\beta_1 = 47.0^\circ$, $\alpha = 5.2^\circ$, $\sigma = 1.0$, and NACA 65-$(8A_{10})$10 blade section.




(e) Section characteristics.

Figure 94.- Concluded.

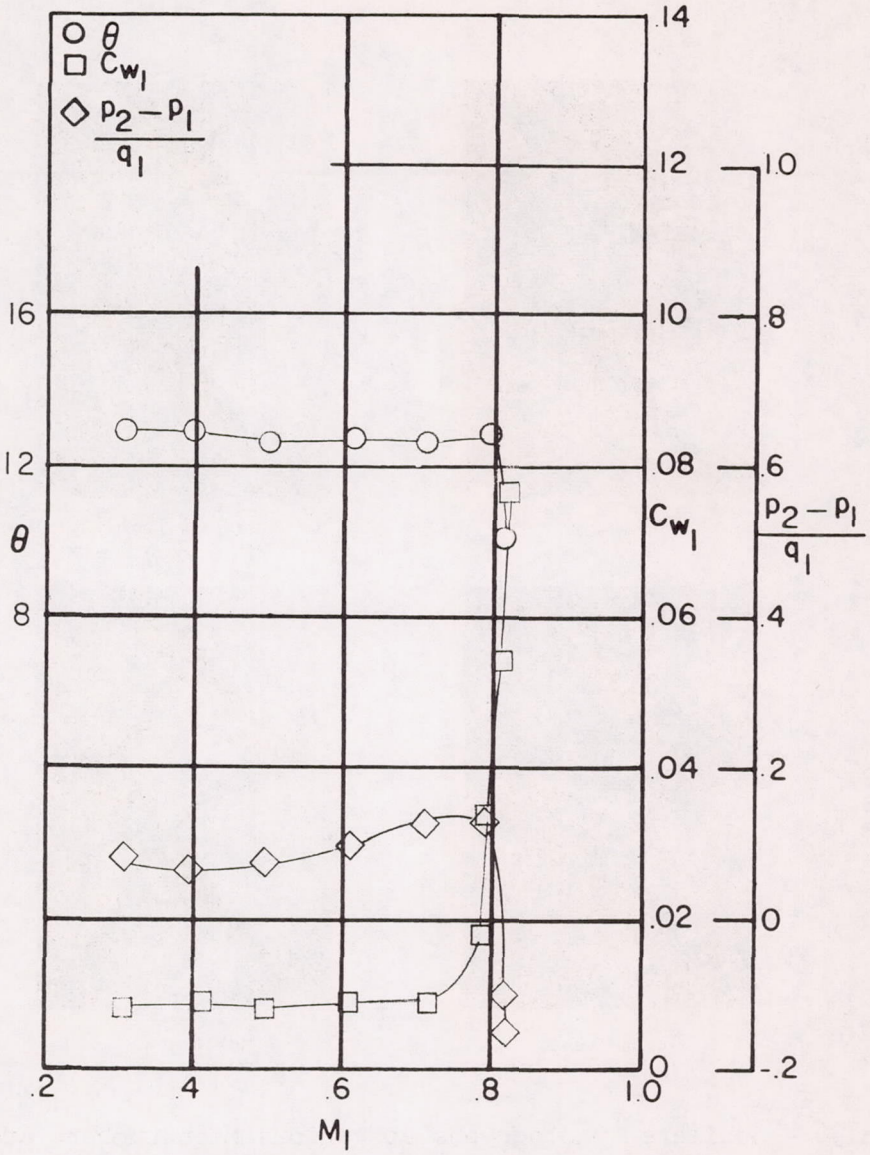


(a) $M_1 = 0.708$. (b) $M_1 = 0.787$.

(c) $M_1 = 0.809$. (d) $M_1 = 0.814$.

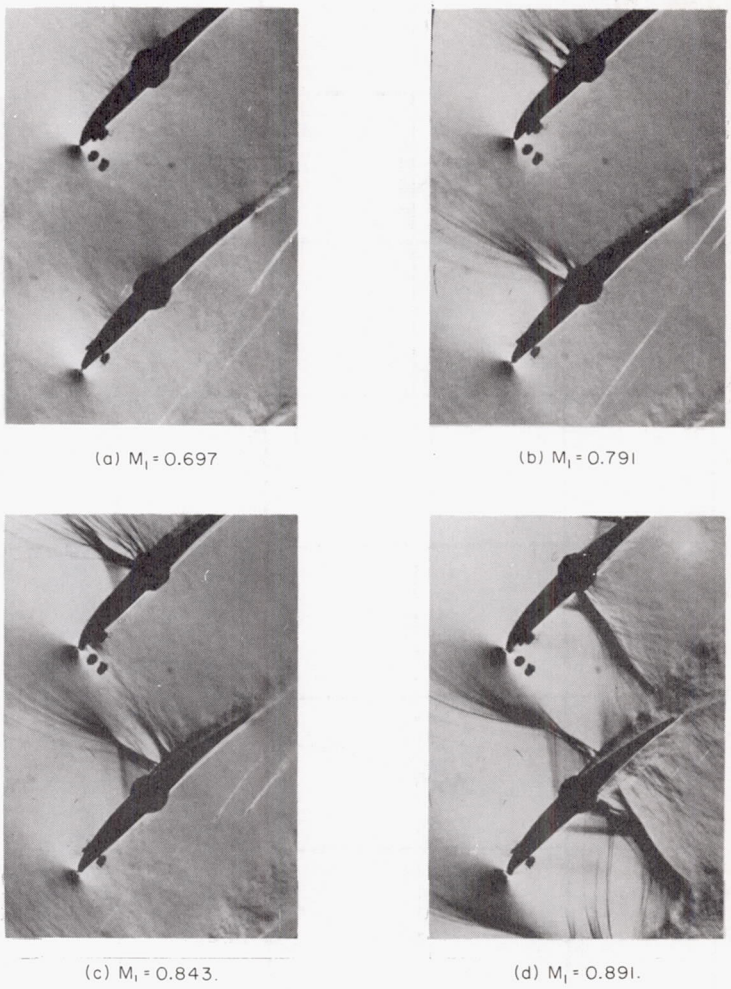
L-57-4487

Figure 95.- Schlieren photographs at various Mach numbers and section characteristics for cascade combination $\beta_1 = 50.0^\circ$, $\alpha = 8.2^\circ$, $\sigma = 1.0$, and NACA 65-$(8A_{10})$10 blade section.




(e) Section characteristics.

Figure 95.- Concluded.

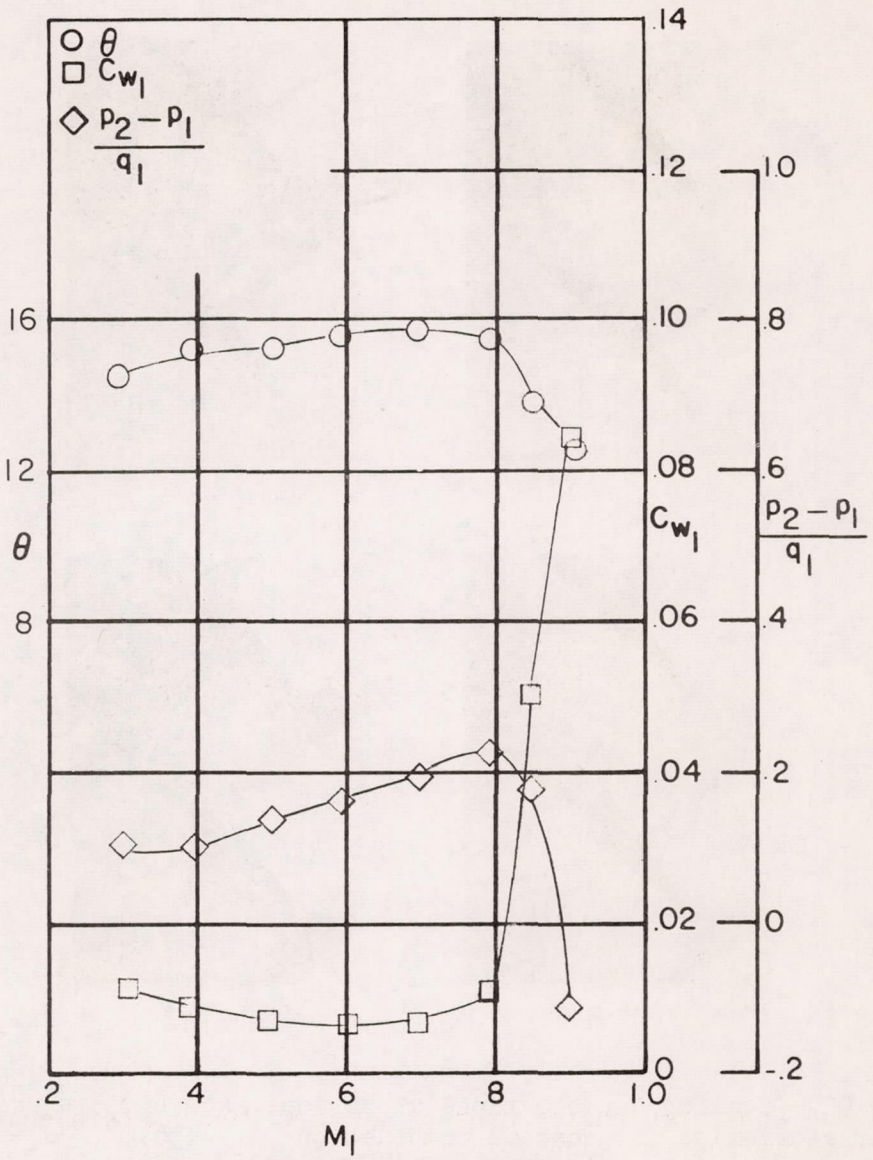


(a) $M_1 = 0.697$ (b) $M_1 = 0.791$

(c) $M_1 = 0.843$. (d) $M_1 = 0.891$.

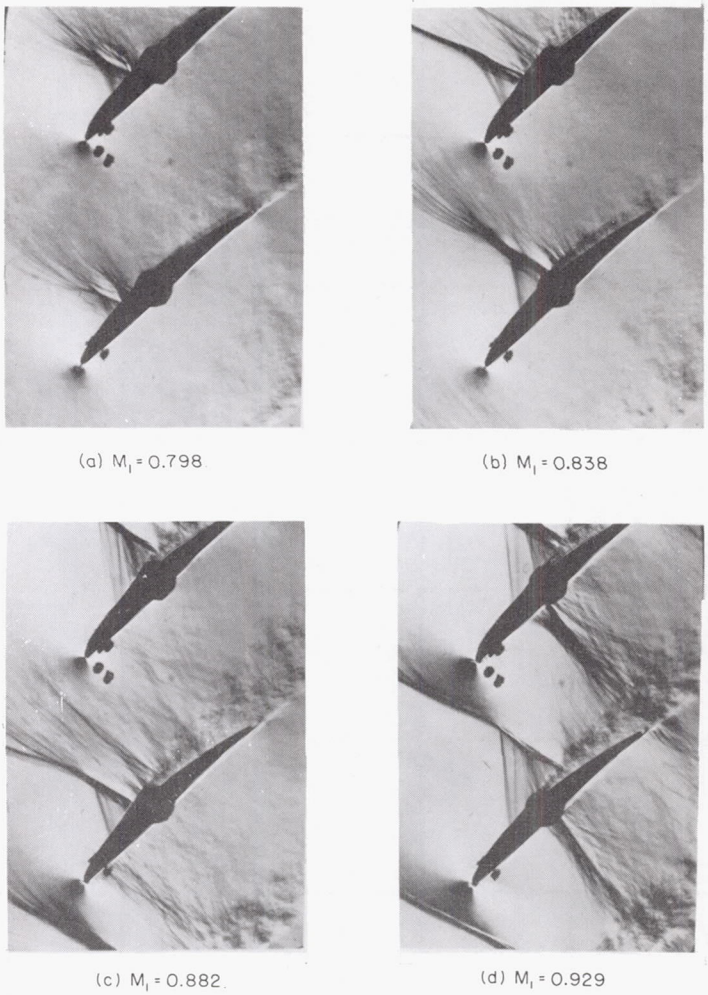
L-57-4488

Figure 96.- Schlieren photographs at various Mach numbers and section characteristics for cascade combination $\beta_1 = 53.0^\circ$, $\alpha = 11.2^\circ$, $\sigma = 1.0$, and NACA 65-$(8A_{10})$10 blade section.




(e) Section characteristics.

Figure 96.- Concluded.

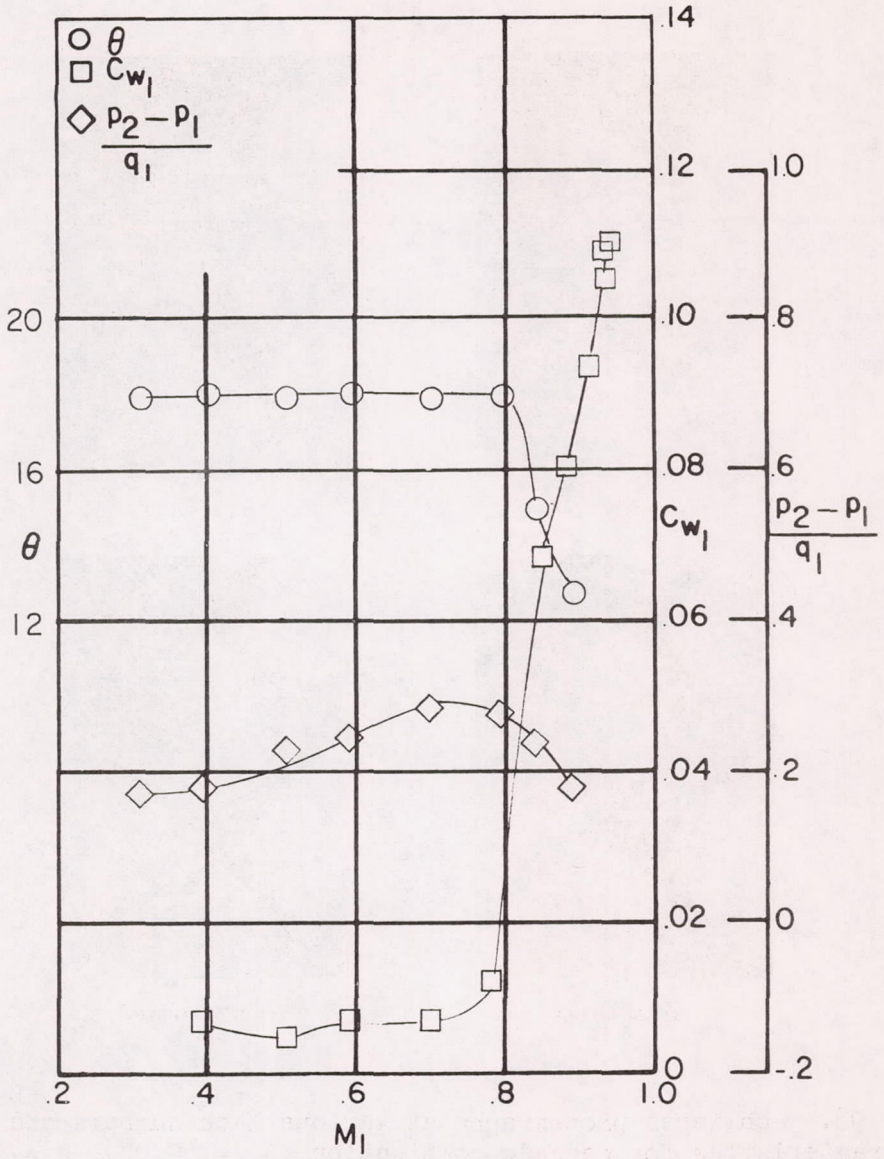


(a) $M_1 = 0.798$ (b) $M_1 = 0.838$

(c) $M_1 = 0.882$ (d) $M_1 = 0.929$

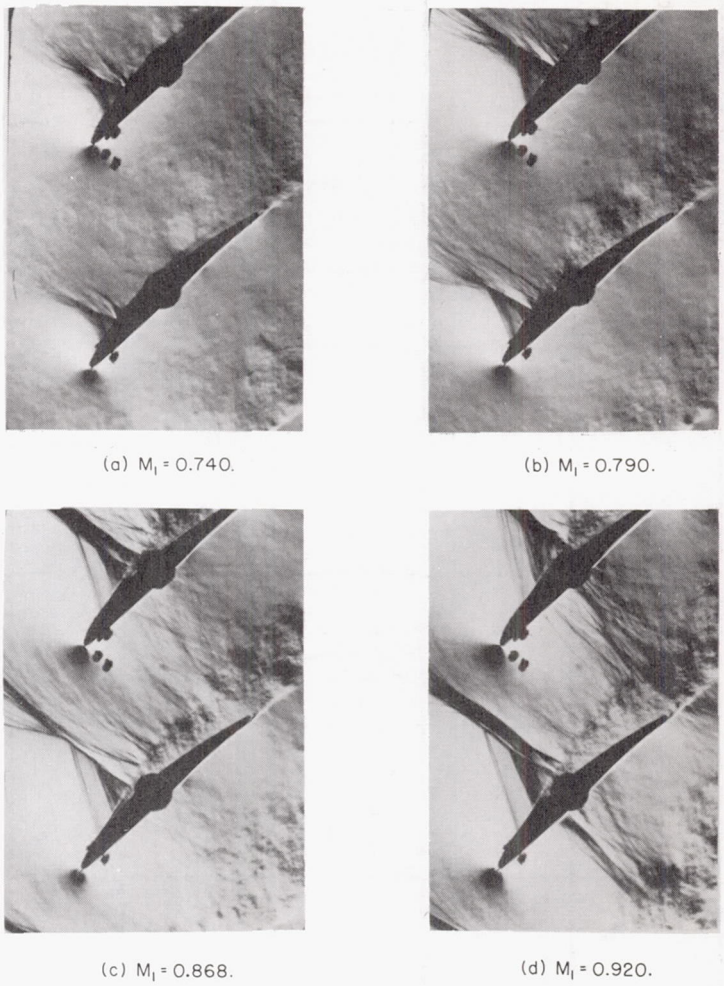
L-57-4489

Figure 97.- Schlieren photographs at various Mach numbers and section characteristics for cascade combination $\beta_1 = 56.0^\circ$, $\alpha = 14.2^\circ$, $\sigma = 1.0$, and NACA 65-$(8A_{10})$10 blade section.




(e) Section characteristics.

Figure 97.- Concluded.



(a) $M_1 = 0.740$.

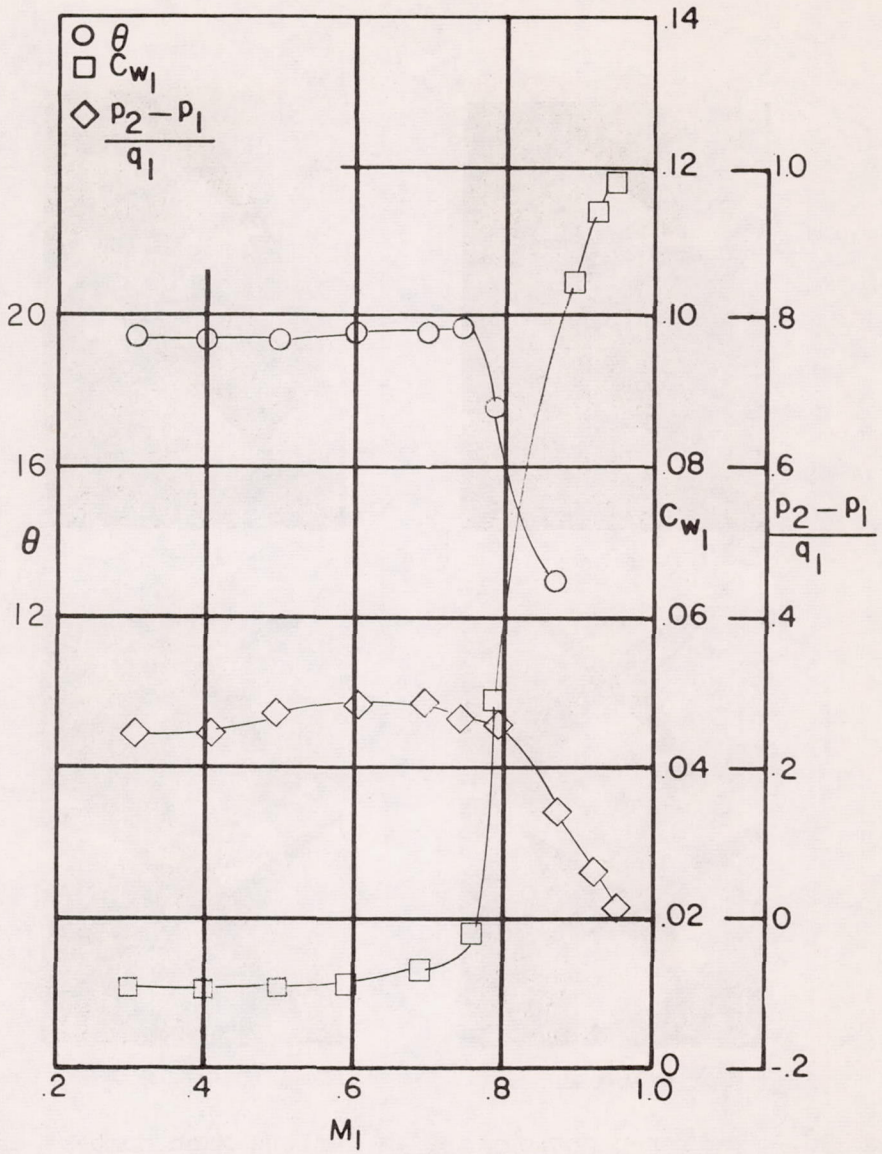
(b) $M_1 = 0.790$.

(c) $M_1 = 0.868$.

(d) $M_1 = 0.920$.

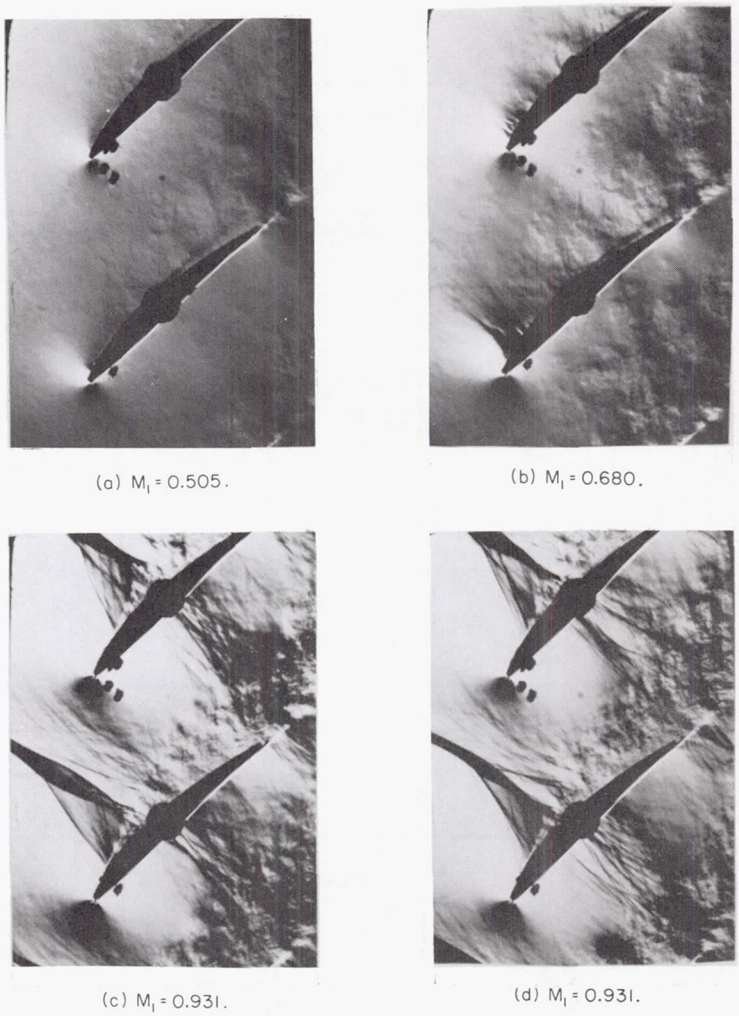
L-57-4490

Figure 98.- Schlieren photographs at various Mach numbers and section characteristics for cascade combination $\beta_1 = 59.0^\circ$, $\alpha = 17.2^\circ$, $\sigma = 1.0$, and NACA 65-$(8A_{10})$10 blade section.




(e) Section characteristics.

Figure 98.- Concluded.



(a) $M_1 = 0.505$.

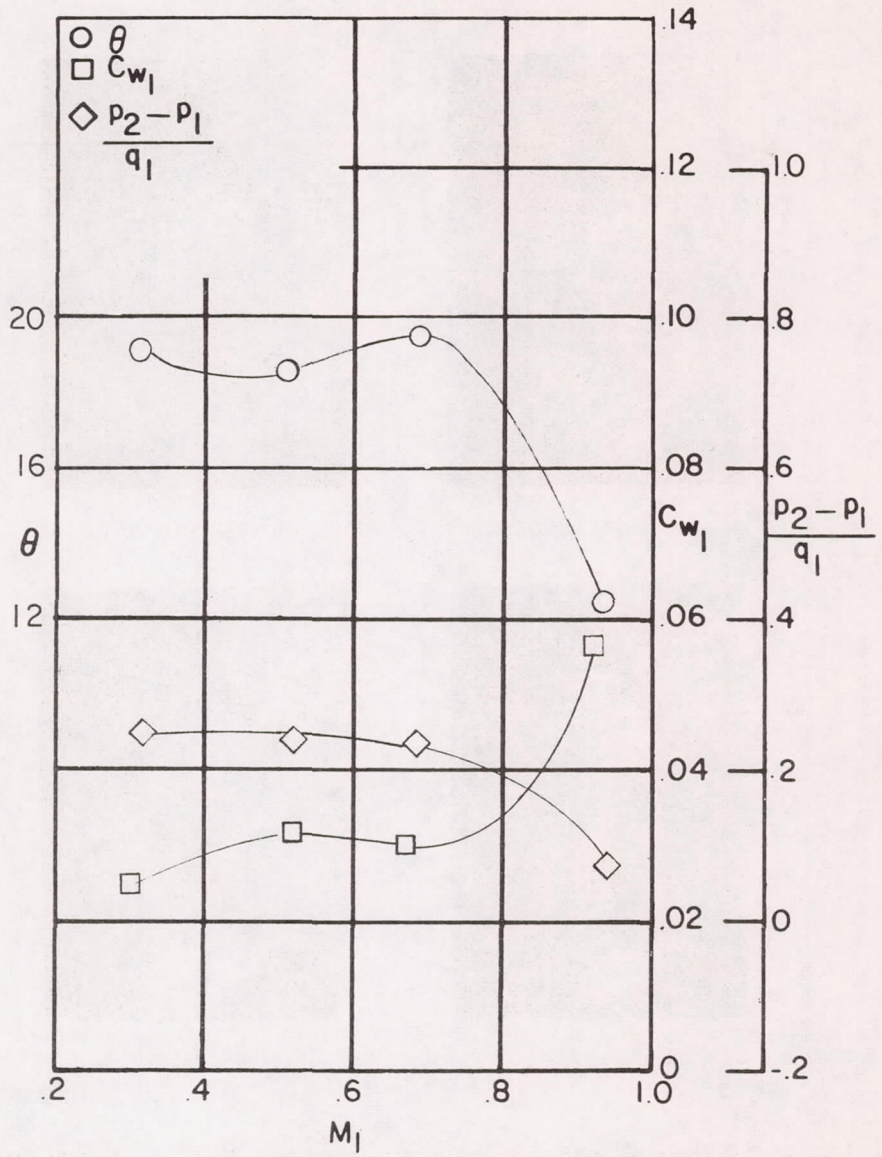
(b) $M_1 = 0.680$.

(c) $M_1 = 0.931$.

(d) $M_1 = 0.931$.

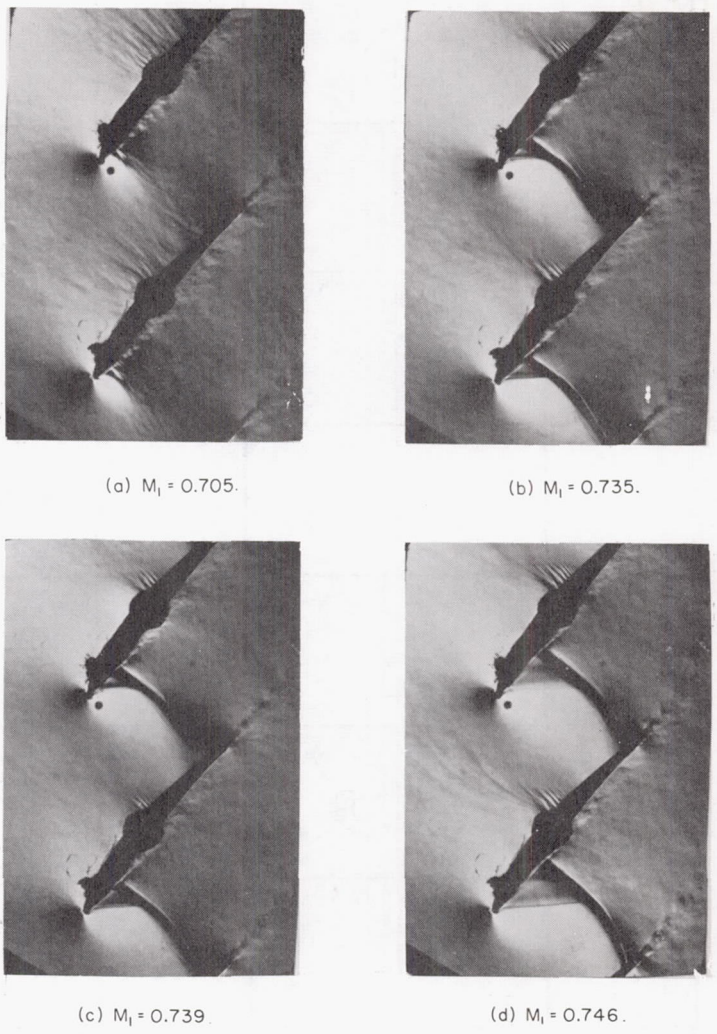
L-57-4491

Figure 99.- Schlieren photographs at various Mach numbers and section characteristics for cascade combination $\beta_1 = 62.0^\circ$, $\alpha = 20.2^\circ$, $\sigma = 1.0$, and NACA 65-$(8A_{10})$10 blade section.




(e) Section characteristics.

Figure 99.- Concluded.



(a) $M_1 = 0.705$.

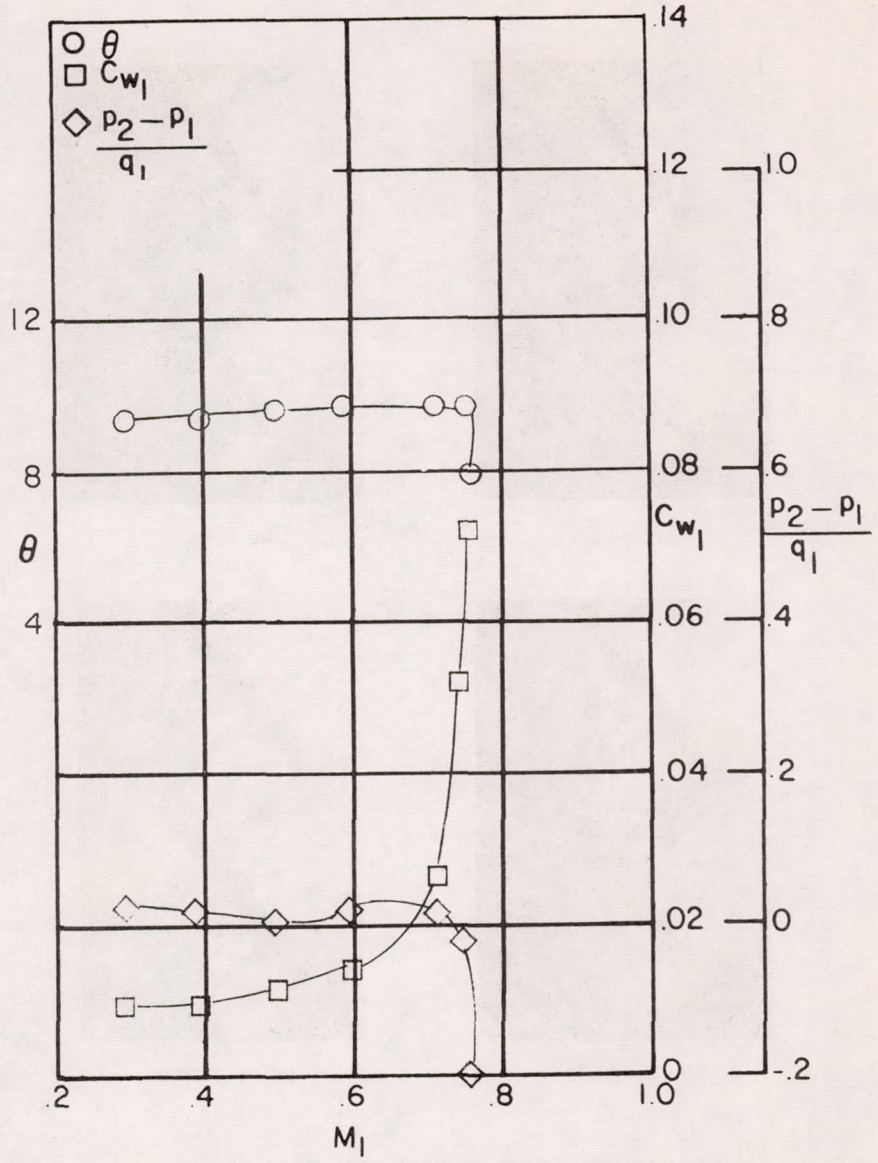
(b) $M_1 = 0.735$.

(c) $M_1 = 0.739$.

(d) $M_1 = 0.746$.

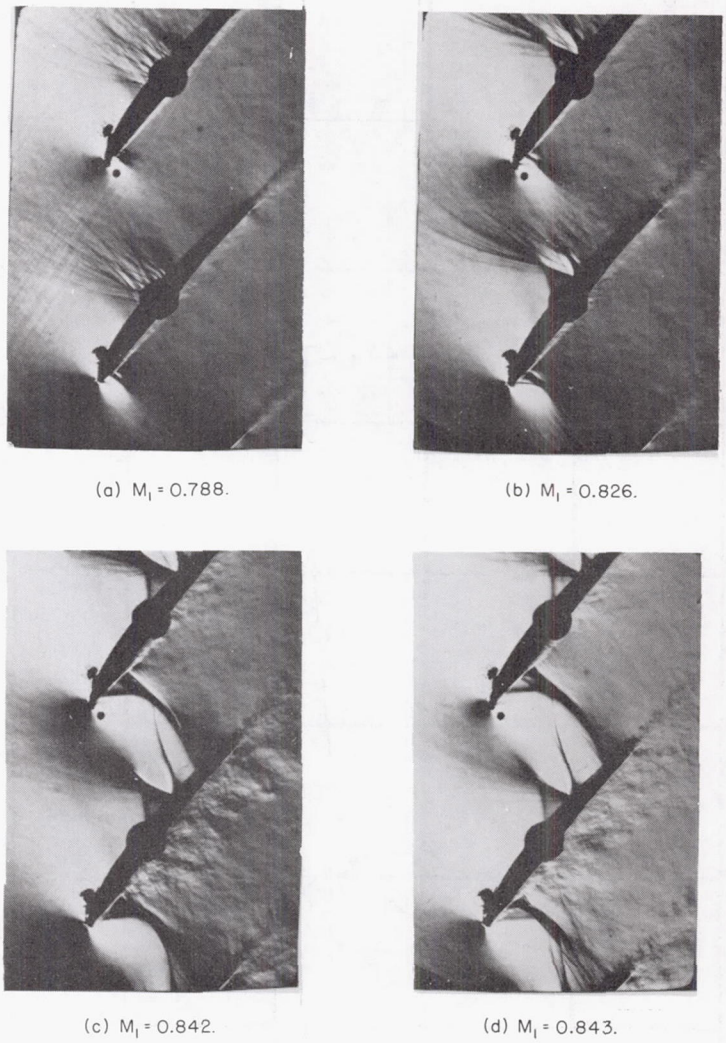
L-57-4492

Figure 100.- Schlieren photographs at various Mach numbers and section characteristics for cascade combination $\beta_1 = 54.0^\circ$, $\alpha = 5.0^\circ$, $\sigma = 1.0$, and NACA 65-$(8A_{10})$10 blade section.




(e) Section characteristics.

Figure 100.- Concluded.



(a) $M_1 = 0.788$.

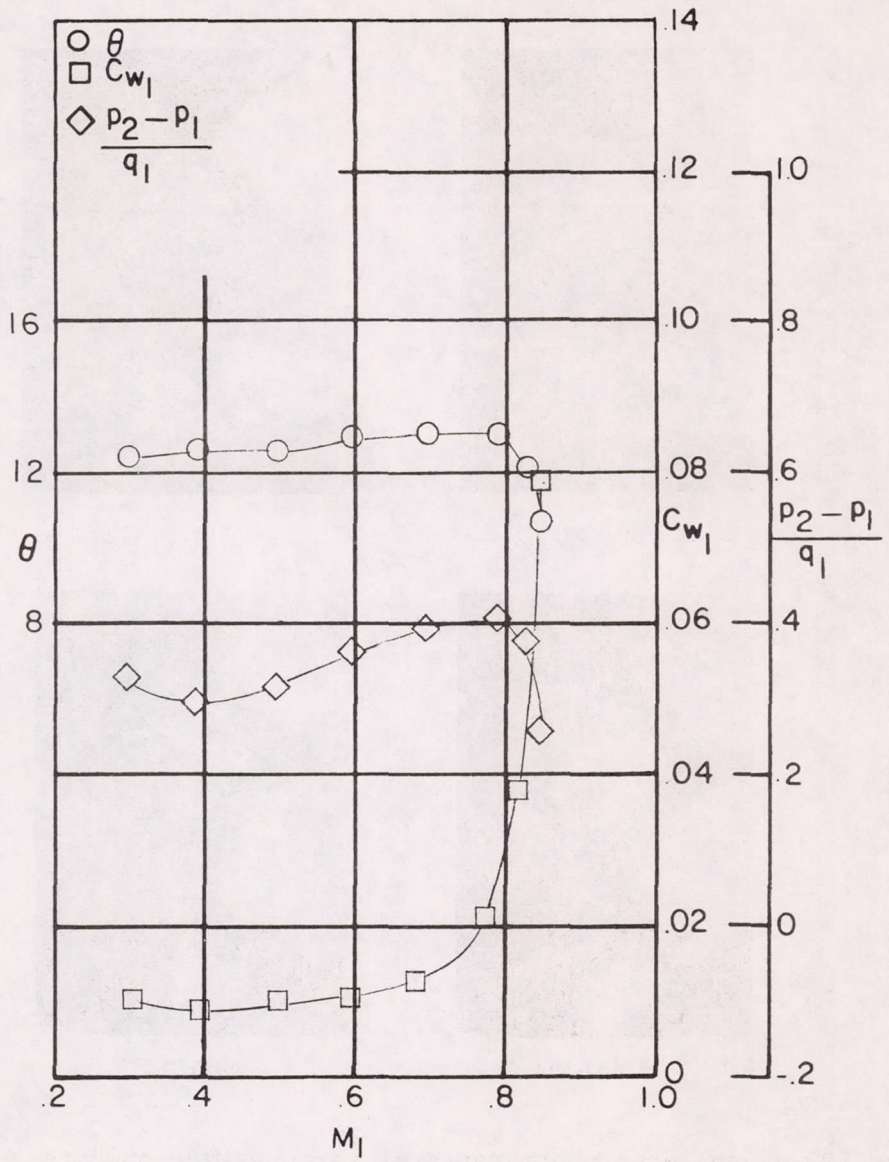
(b) $M_1 = 0.826$.

(c) $M_1 = 0.842$.

(d) $M_1 = 0.843$.

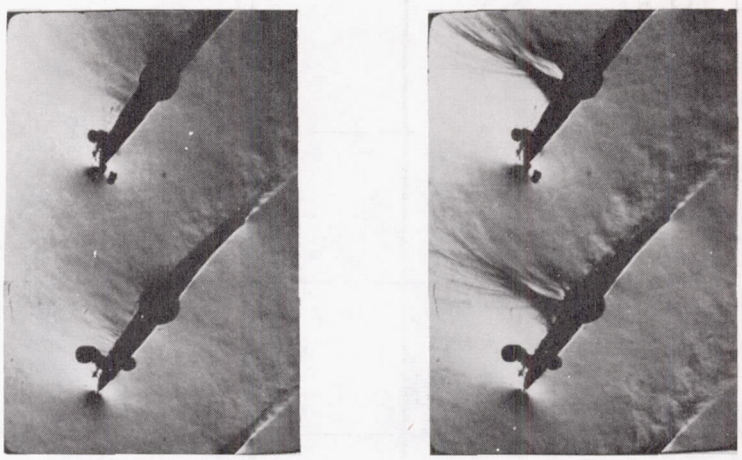
L-57-4493

Figure 101.- Schlieren photographs at various Mach numbers and section characteristics for cascade combination $\beta_1 = 57.0^\circ$, $\alpha = 8.0^\circ$, $\sigma = 1.0$, and NACA 65-$(8A_{10})$10 blade section.




(e) Section characteristics.

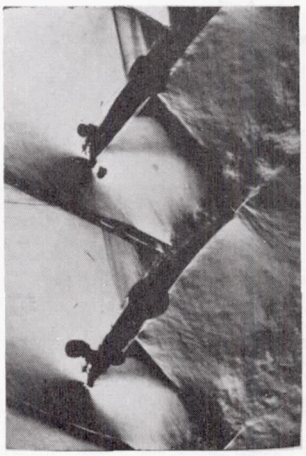
Figure 101.- Concluded.



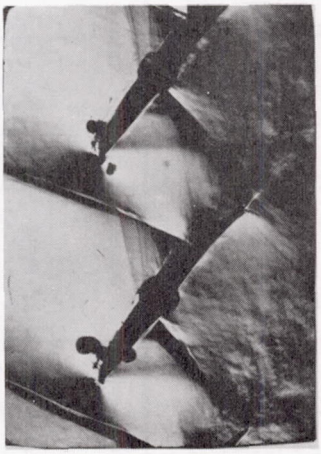
(a) $M_1 = 0.703$.



(b) $M_1 = 0.800$.



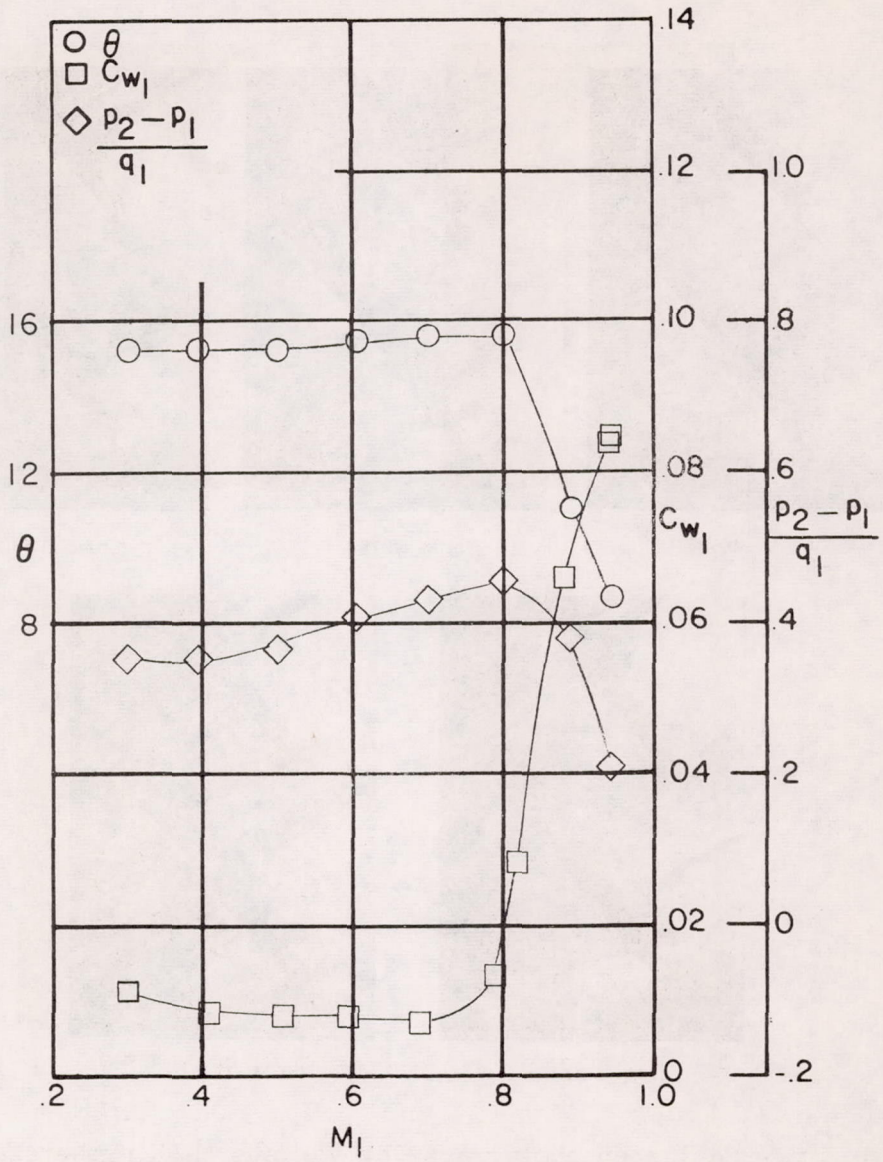
(c) $M_1 = 0.942$.



(d) $M_1 = 0.949$.

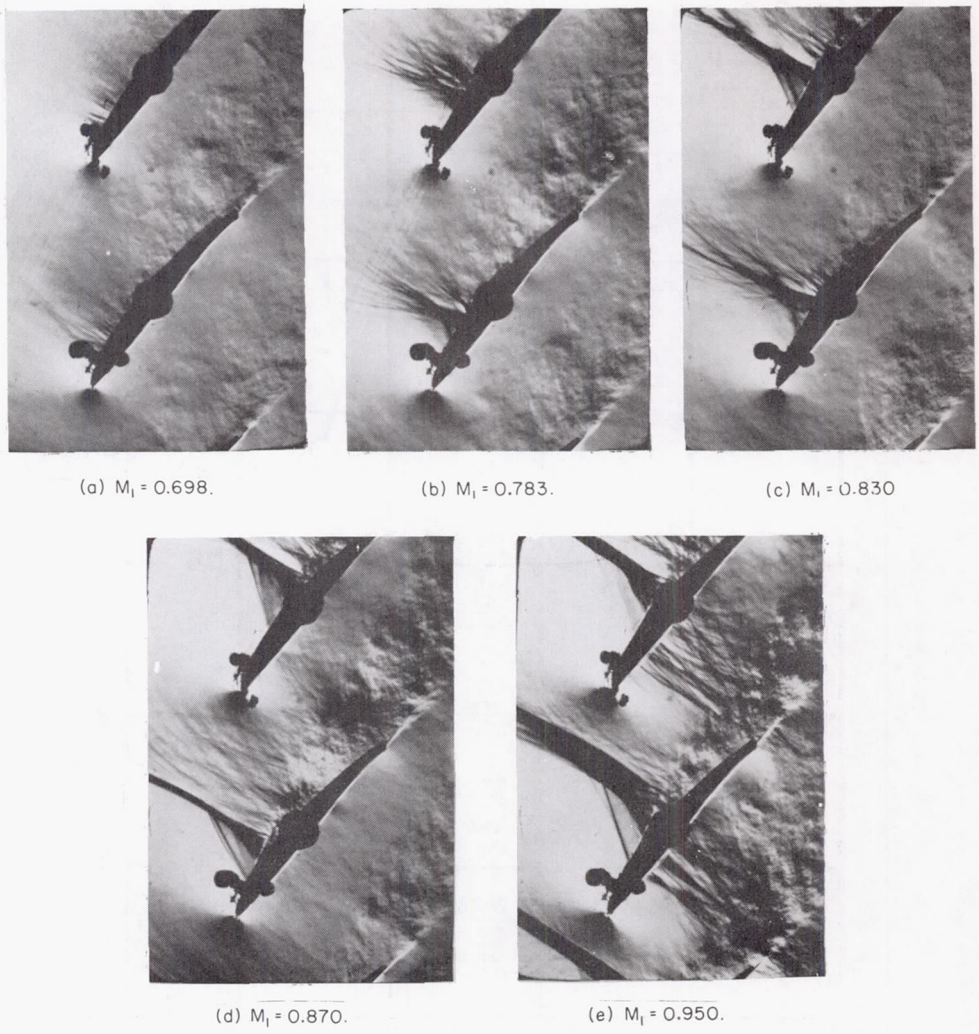
L-57-4494

Figure 102.- Schlieren photographs at various Mach numbers and section characteristics for cascade combination $\beta_1 = 60.0^\circ$, $\alpha = 11.0^\circ$, $\sigma = 1.0$, and NACA 65-$(8A_{10})$10 blade section.




(e) Section characteristics.

Figure 102.- Concluded.

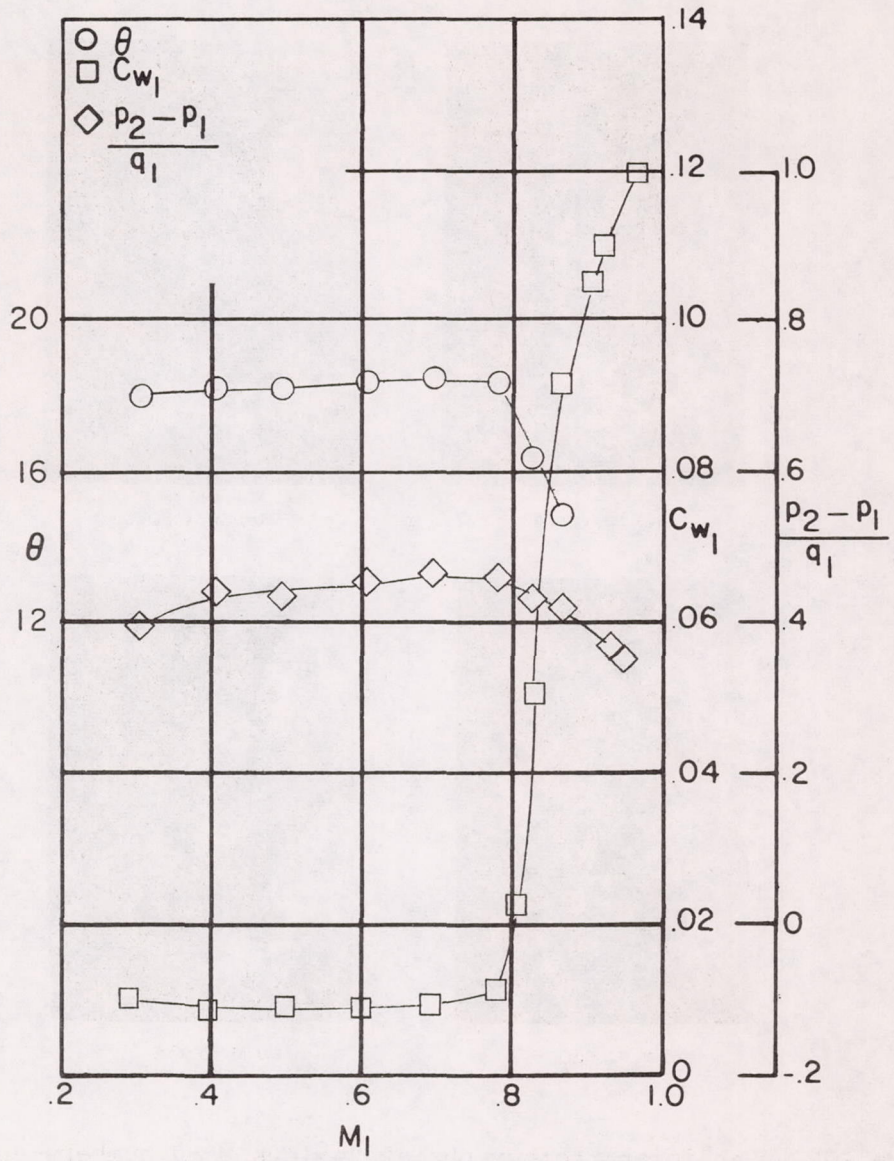


(a) $M_1 = 0.698$. (b) $M_1 = 0.783$. (c) $M_1 = 0.830$

(d) $M_1 = 0.870$. (e) $M_1 = 0.950$.

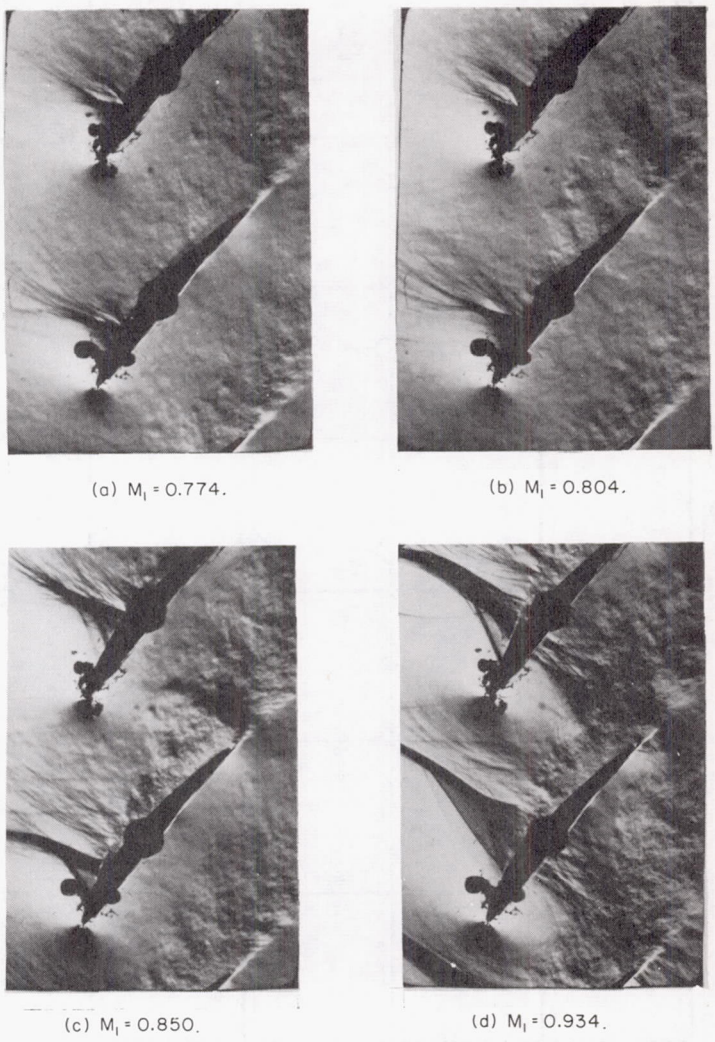
L-57-4495

Figure 103.- Schlieren photographs at various Mach numbers and section characteristics for cascade combination $\beta_1 = 63.0^\circ$, $\alpha = 14.0^\circ$, $\sigma = 1.0$, and NACA 65-$(8A_{10})$10 blade section.




(f) Section characteristics.

Figure 103.- Concluded.



(a) $M_1 = 0.774$.

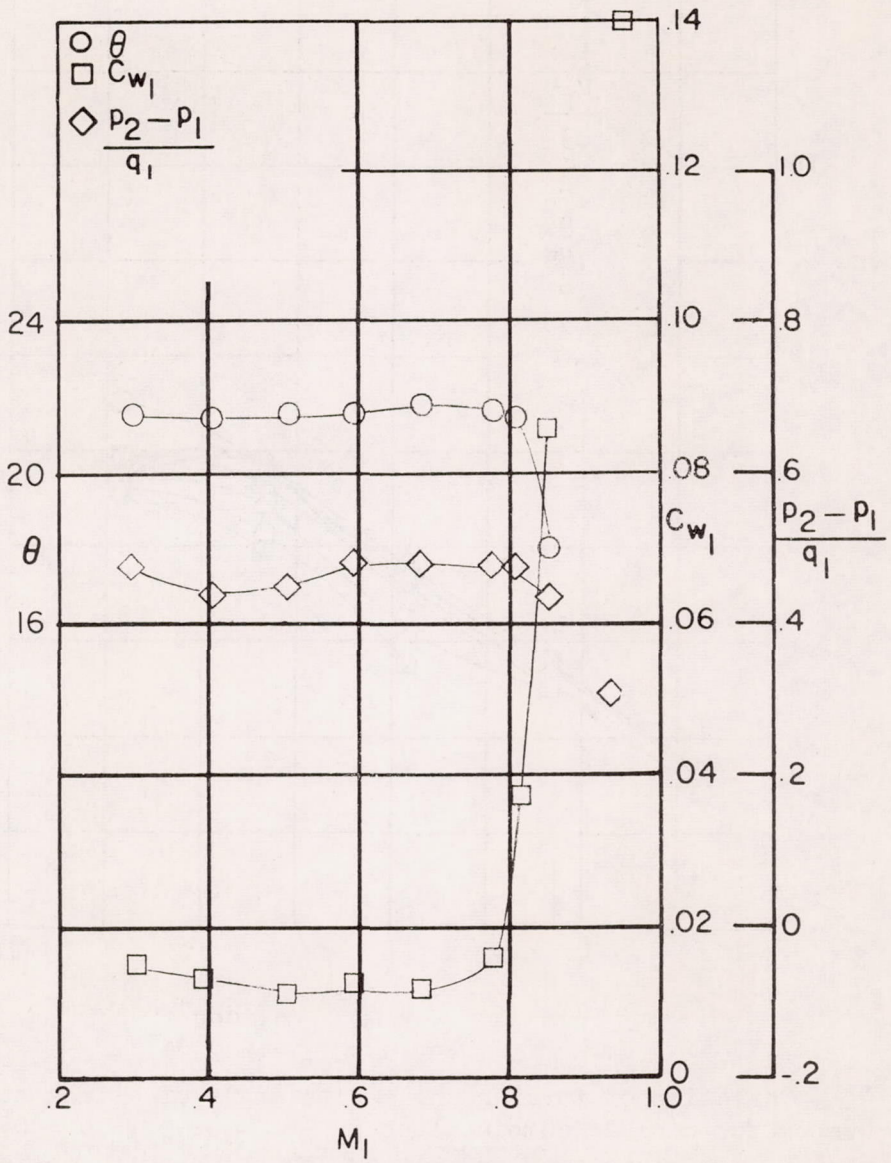
(b) $M_1 = 0.804$.

(c) $M_1 = 0.850$.

(d) $M_1 = 0.934$.

L-57-4496

Figure 104.- Schlieren photographs at various Mach numbers and section characteristics for cascade combination $\beta_1 = 66.0^\circ$, $\alpha = 17.0^\circ$, $\sigma = 1.0$, and NACA 65-$(8A_{10})$10 blade section.




(e) Section characteristics.

Figure 104.- Concluded.

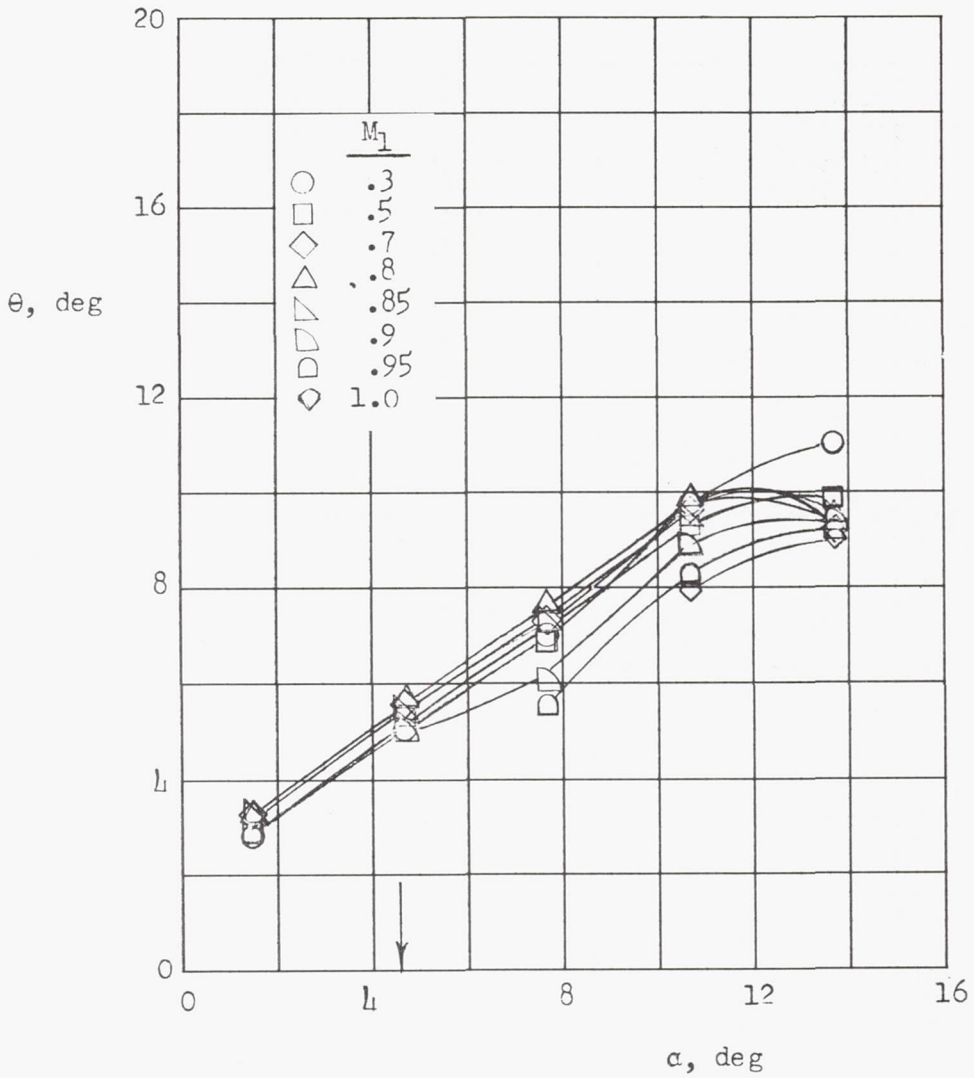



Figure 105.- Variation of turning angle with angle of attack at constant Mach number for cascade combination $\beta_1 - \alpha = 42.3^\circ$, $\sigma = 0.6$, and NACA 65-$(4A_{10})$06 blade section. Arrow shows low-speed design angle of attack.

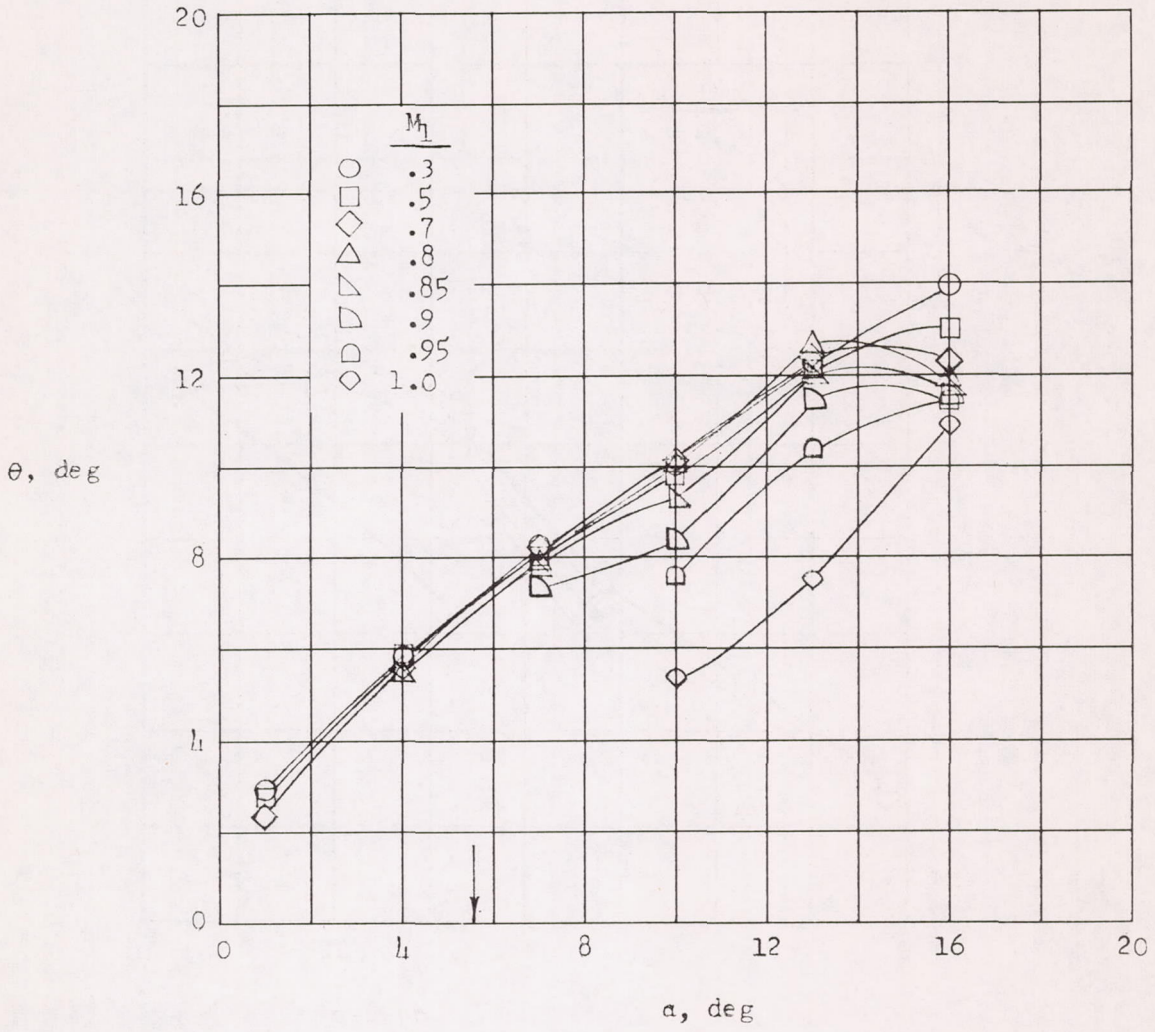



Figure 106.- Variation of turning angle with angle of attack at constant Mach number for cascade combination $\beta_1 - \alpha = 40.0^\circ$, $\sigma = 0.8$, and NACA 65-$(4A_{10})$06 blade section. Arrow shows low-speed design angle of attack.

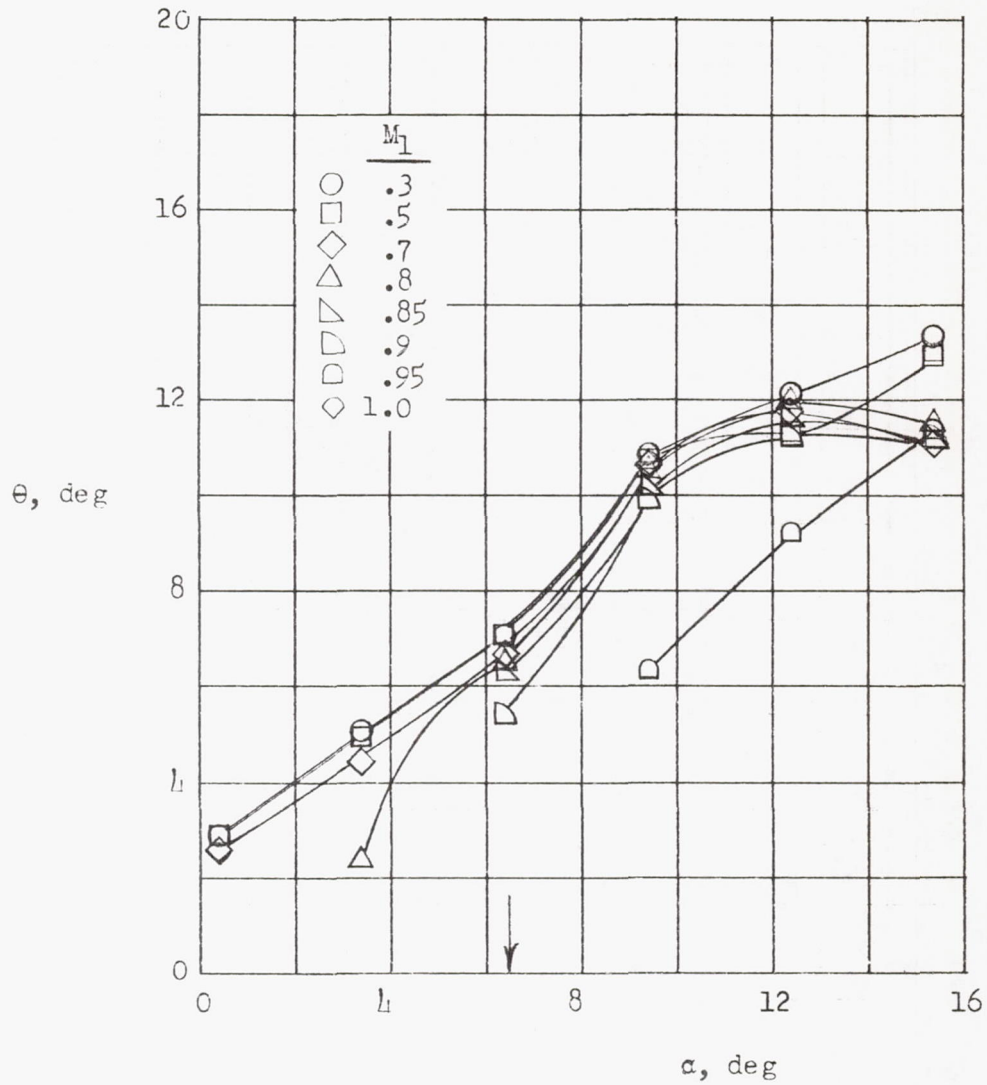



Figure 107.- Variation of turning angle with angle of attack at constant Mach number for cascade combination $\beta_1 - \alpha = 40.6^\circ$, $\sigma = 1.0$, and NACA 65-$\left(4A_{10}\right)$06 blade section. Arrow shows low-speed design angle of attack.

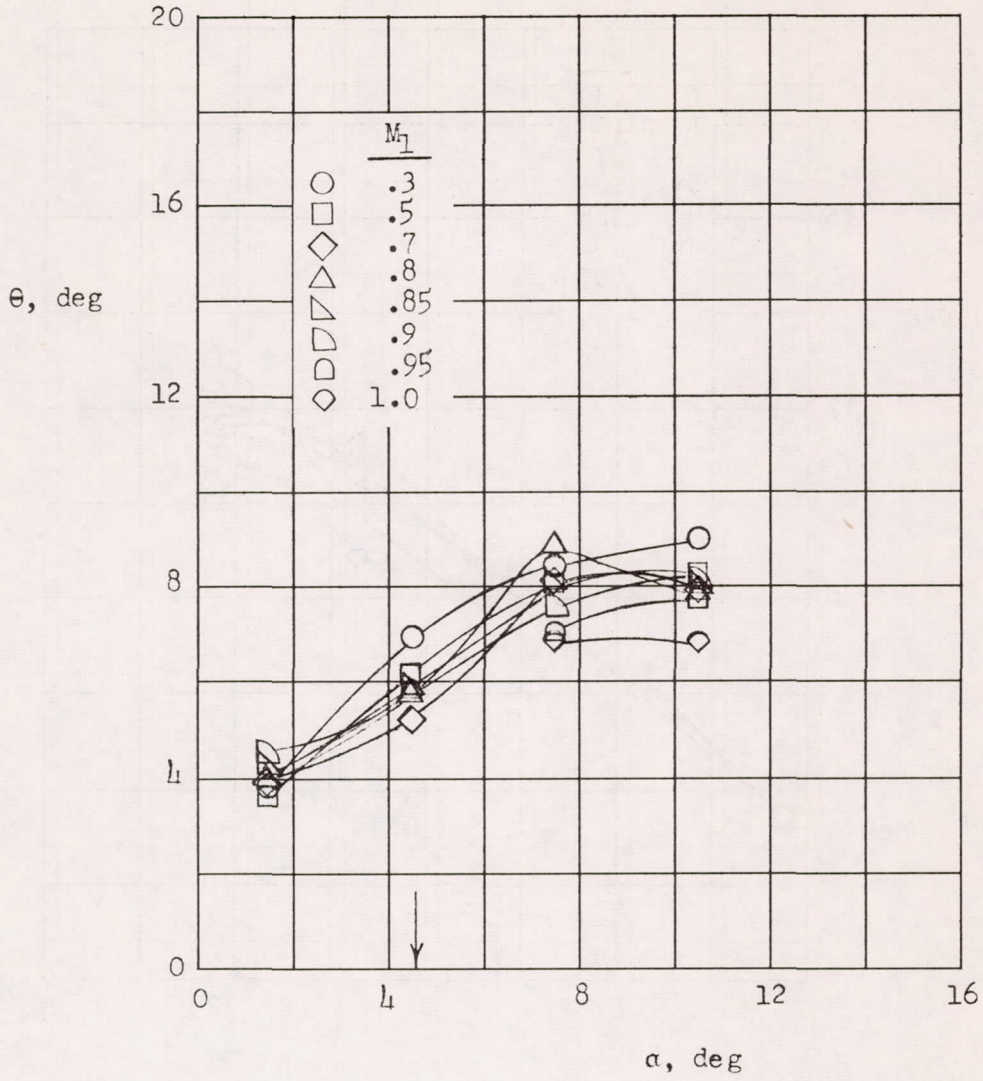



Figure 108.- Variation of turning angle with angle of attack at constant Mach number for cascade combination $\beta_1 - \alpha = 52.5^\circ$, $\sigma = 0.6$, and NACA 65-$(4A_{10})$06 blade section. Arrow shows low-speed design angle of attack.

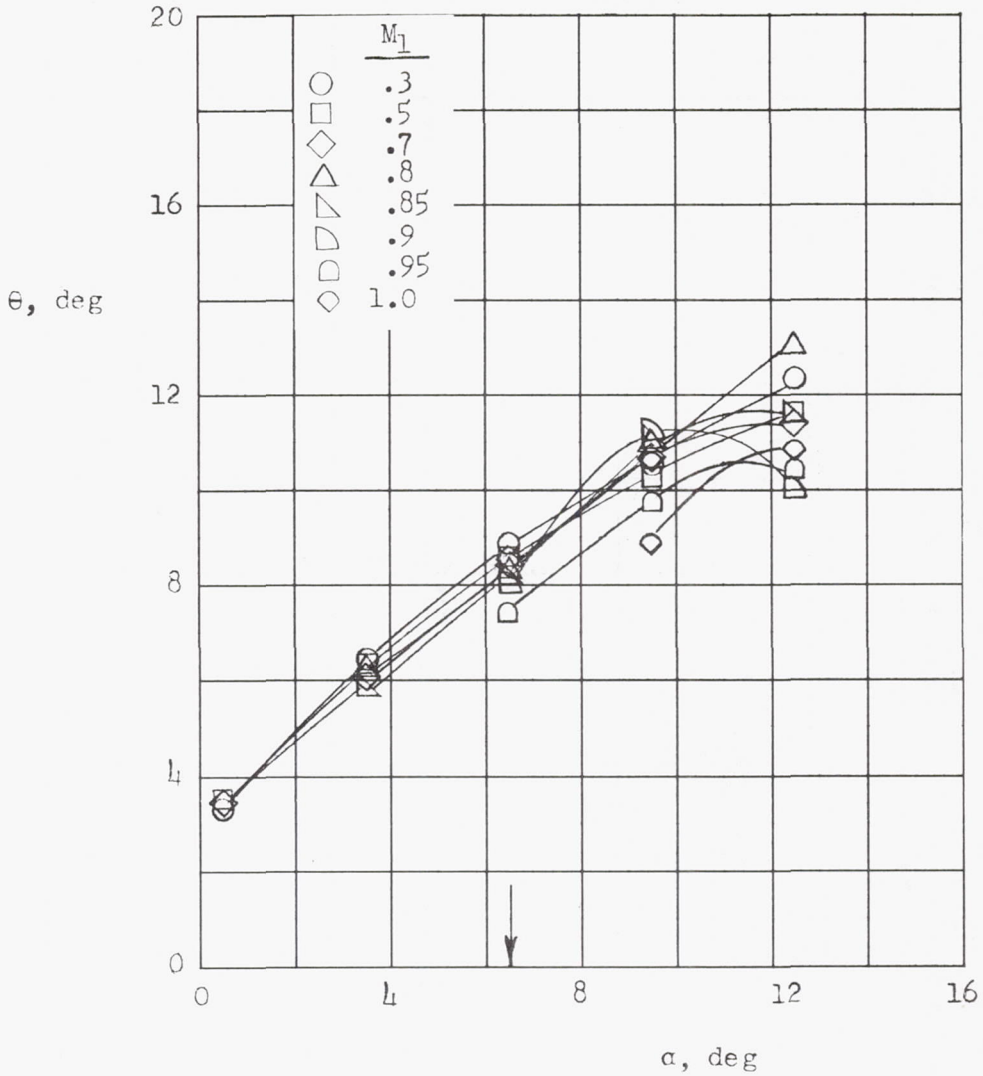



Figure 109.- Variation of turning angle with angle of attack at constant Mach number for cascade combination $\beta_1 - \alpha = 50.5^\circ$, $\sigma = 1.0$, and NACA 65-$(4A_{10})$06 blade section. Arrow shows low-speed design angle of attack.

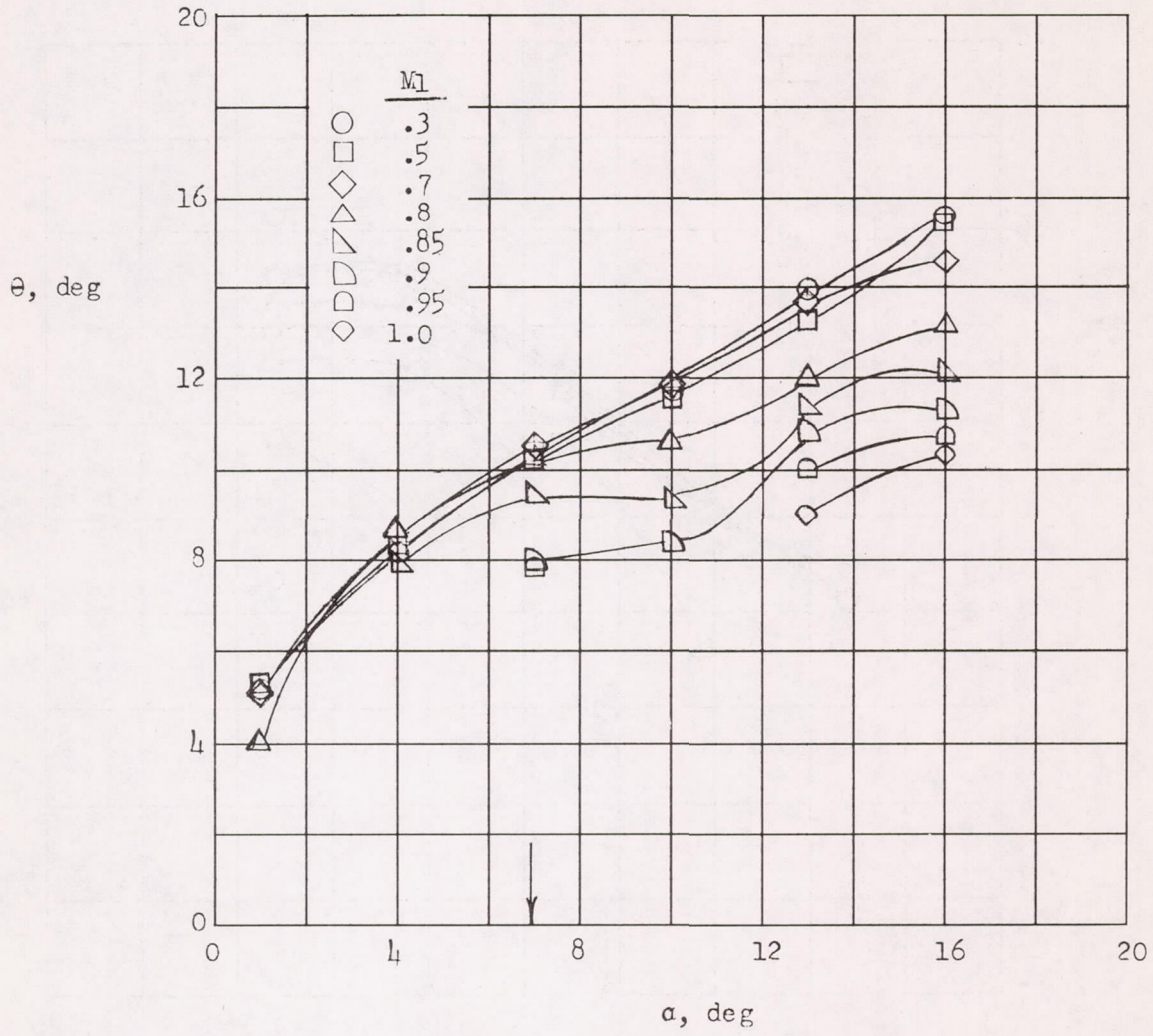



Figure 110.- Variation of turning angle with angle of attack at constant Mach number for cascade combination $\beta_1 - \alpha = 40.0^\circ$, $\sigma = 0.6$, and NACA 65-$(8A_{10})$06 blade section. Arrow shows low-speed design angle of attack.

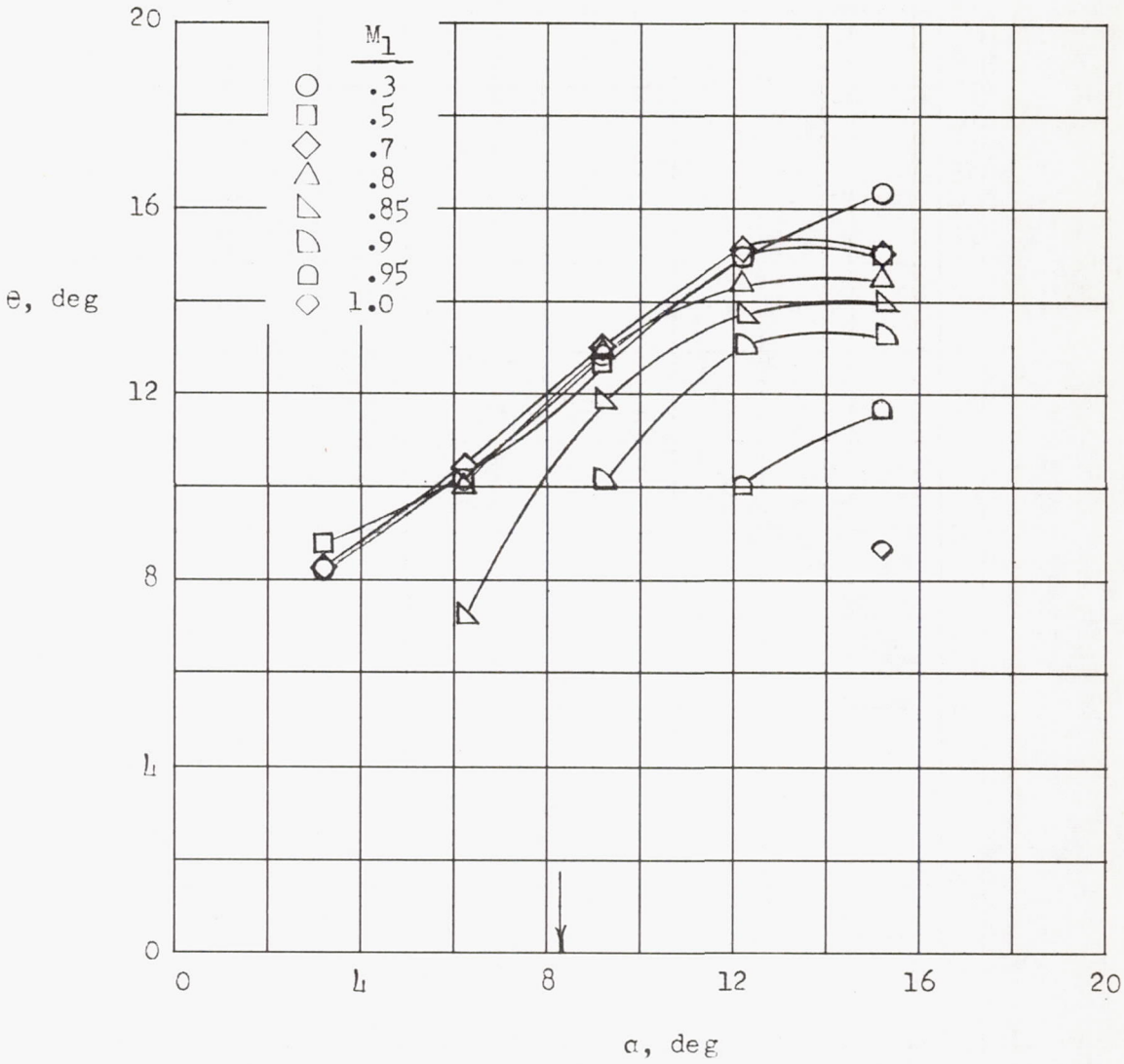



Figure 111.- Variation of turning angle with angle of attack at constant Mach number for cascade combination $\beta_1 - \alpha = 37.8^\circ$, $\sigma = 0.8$, and NACA 65-$(8A_{10})$06 blade section. Arrow shows low-speed design angle of attack.

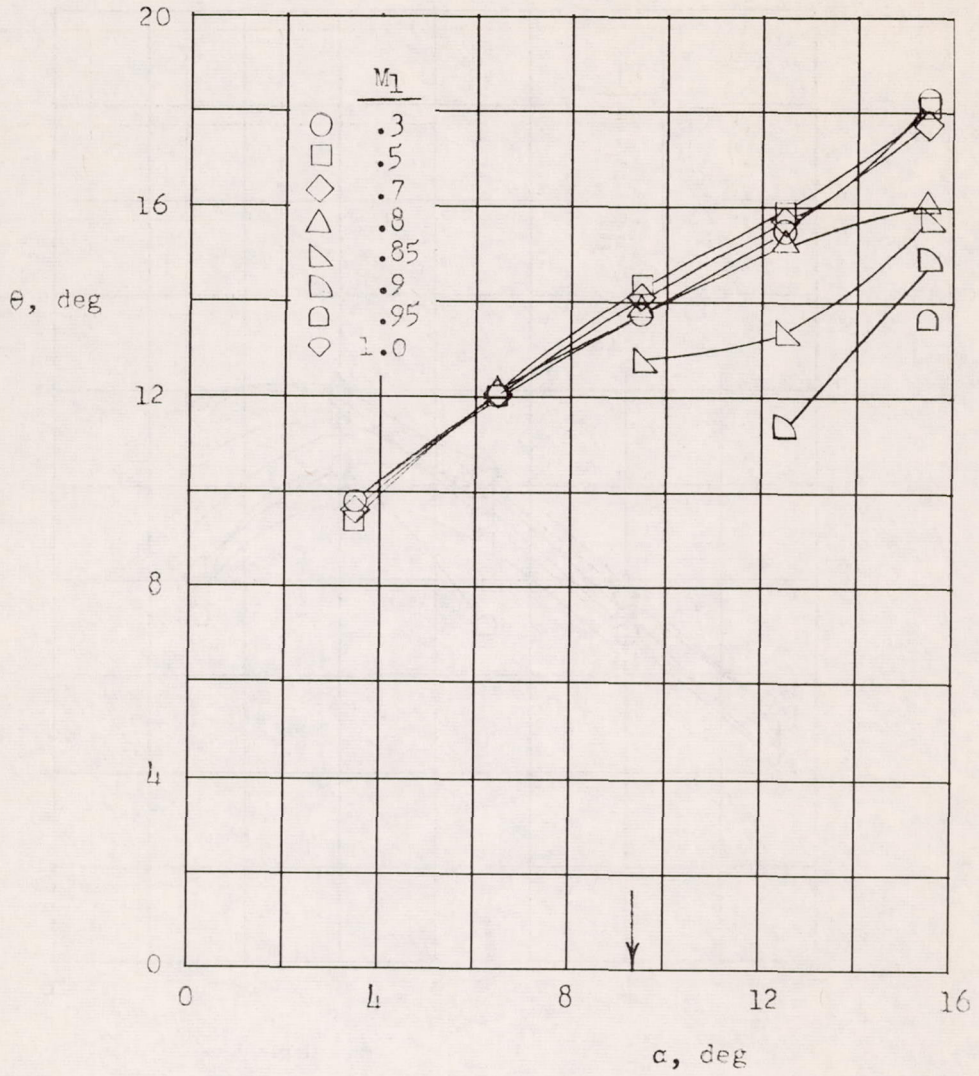



Figure 112.- Variation of turning angle with angle of attack at constant Mach number for cascade combination $\beta_1 - \alpha = 37.5^\circ$, $\sigma = 1.0$, and NACA 65-$(8A_{10})$06 blade section. Arrow shows low-speed design angle of attack.

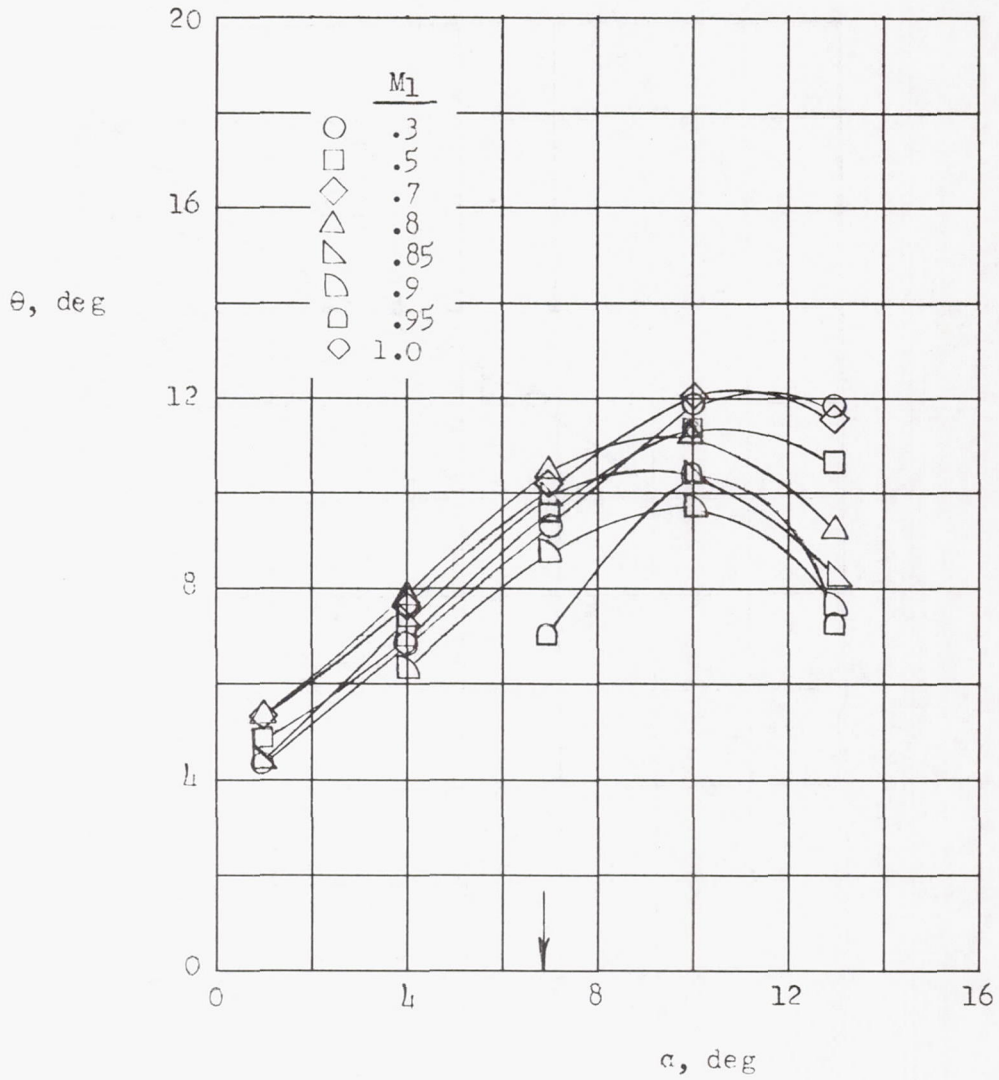



Figure 113.- Variation of turning angle with angle of attack at constant Mach number for cascade combination $\beta_1 - \alpha = 50.0^\circ$, $\sigma = 0.6$, and NACA 65-$(8A_{10})$06 blade section. Arrow shows low-speed design angle of attack.

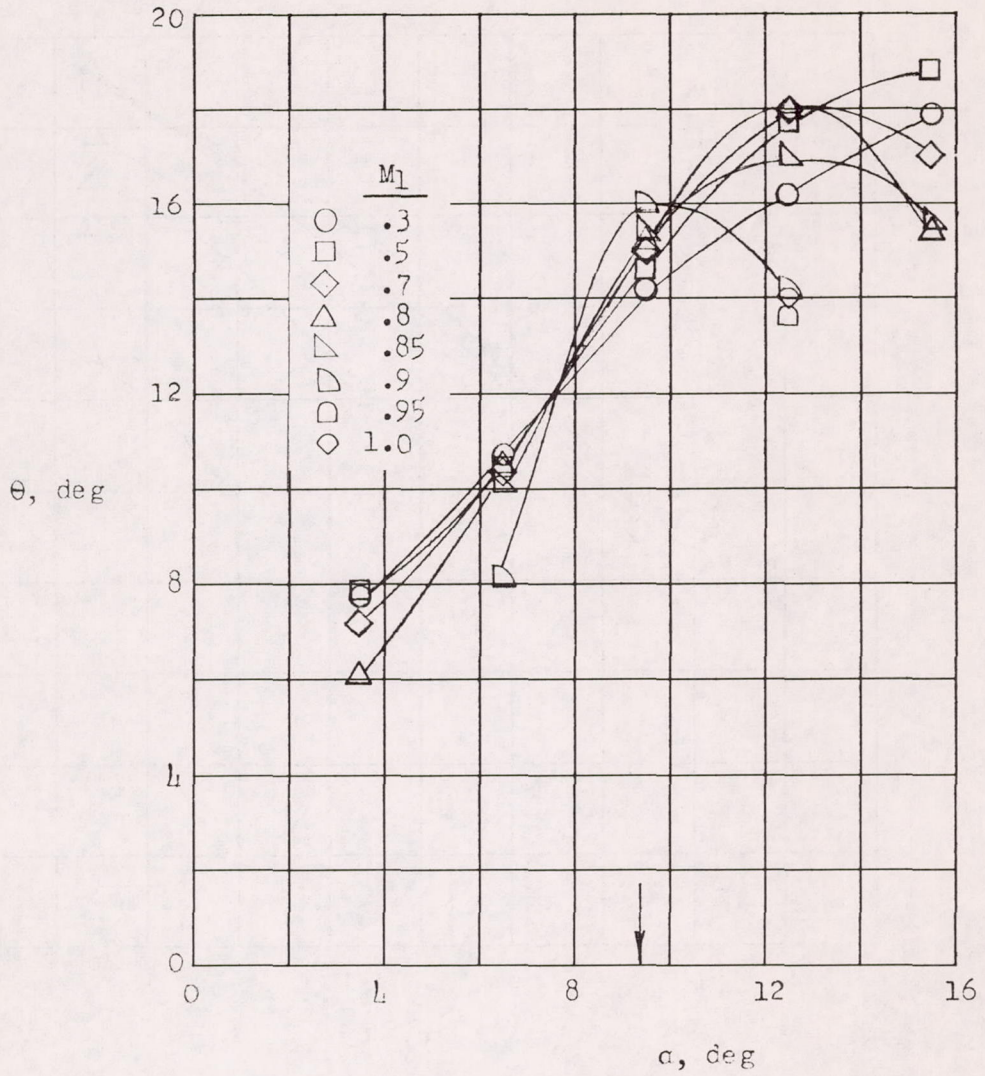



Figure 114.- Variation of turning angle with angle of attack at constant Mach number for cascade combination $\beta_1 - \alpha = 47.5^\circ$, $\sigma = 1.0$, and NACA 65-$(8A_{10})$06 blade section. Arrow shows low-speed design angle of attack.

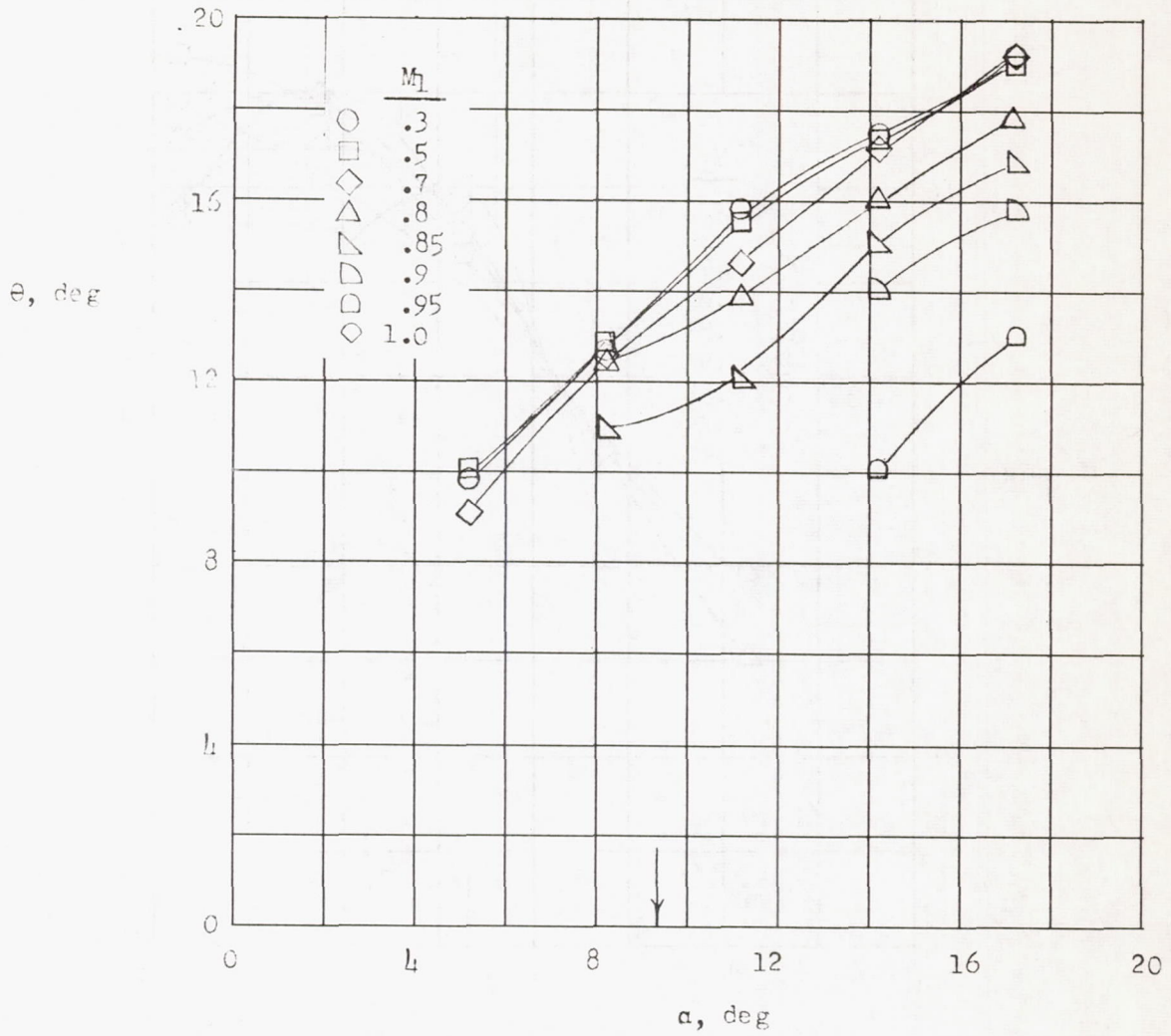



Figure 115.- Variation of turning angle with angle of attack at constant Mach number for cascade combination $\beta_1 - \alpha = 41.8^\circ$, $\sigma = 1.0$, and NACA 65-$(8A_{10})$10 blade section. Arrow shows low-speed design angle of attack.

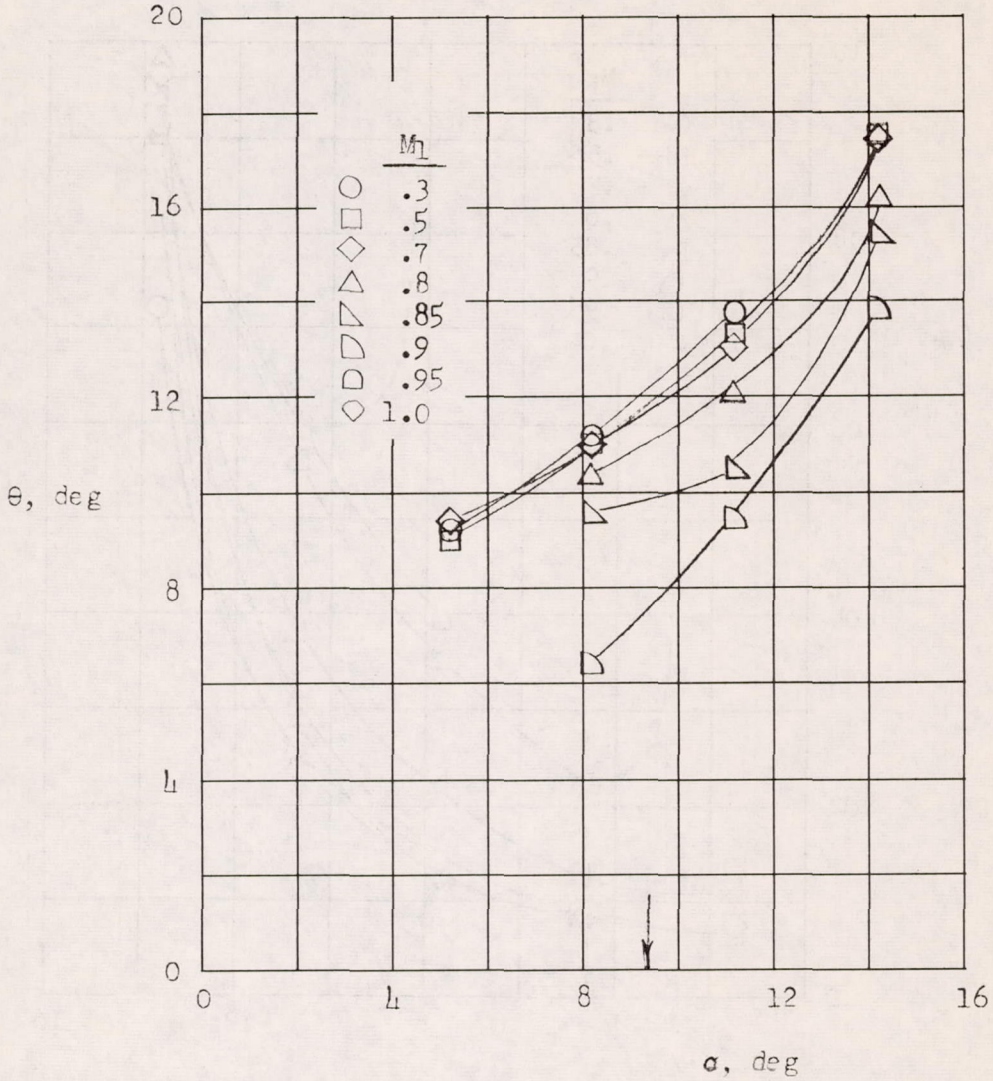



Figure 116.- Variation of turning angle with angle of attack at constant Mach number for cascade combination $\beta_1 - \alpha = 48.8^\circ$, $\sigma = 1.0$, and NACA 65-$(8A_{10})$10 blade section. Arrow shows low-speed design angle of attack.

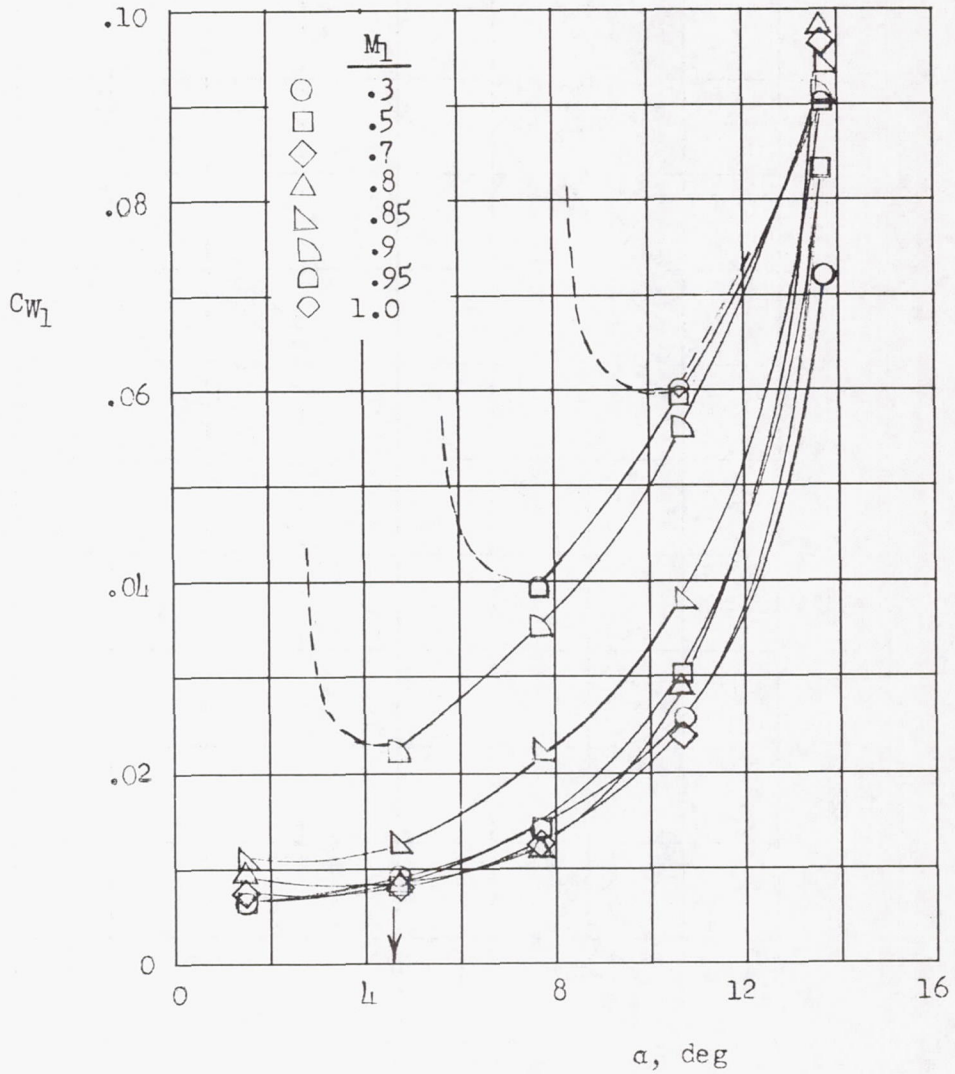



Figure 117.- Variation of momentum-loss coefficient with angle of attack at constant Mach number for cascade combination $\beta_1 - \alpha = 42.3^\circ$, $\sigma = 0.6$, and NACA 65-$(4A_{10})$06 blade section. Arrow shows low-speed design angle of attack.

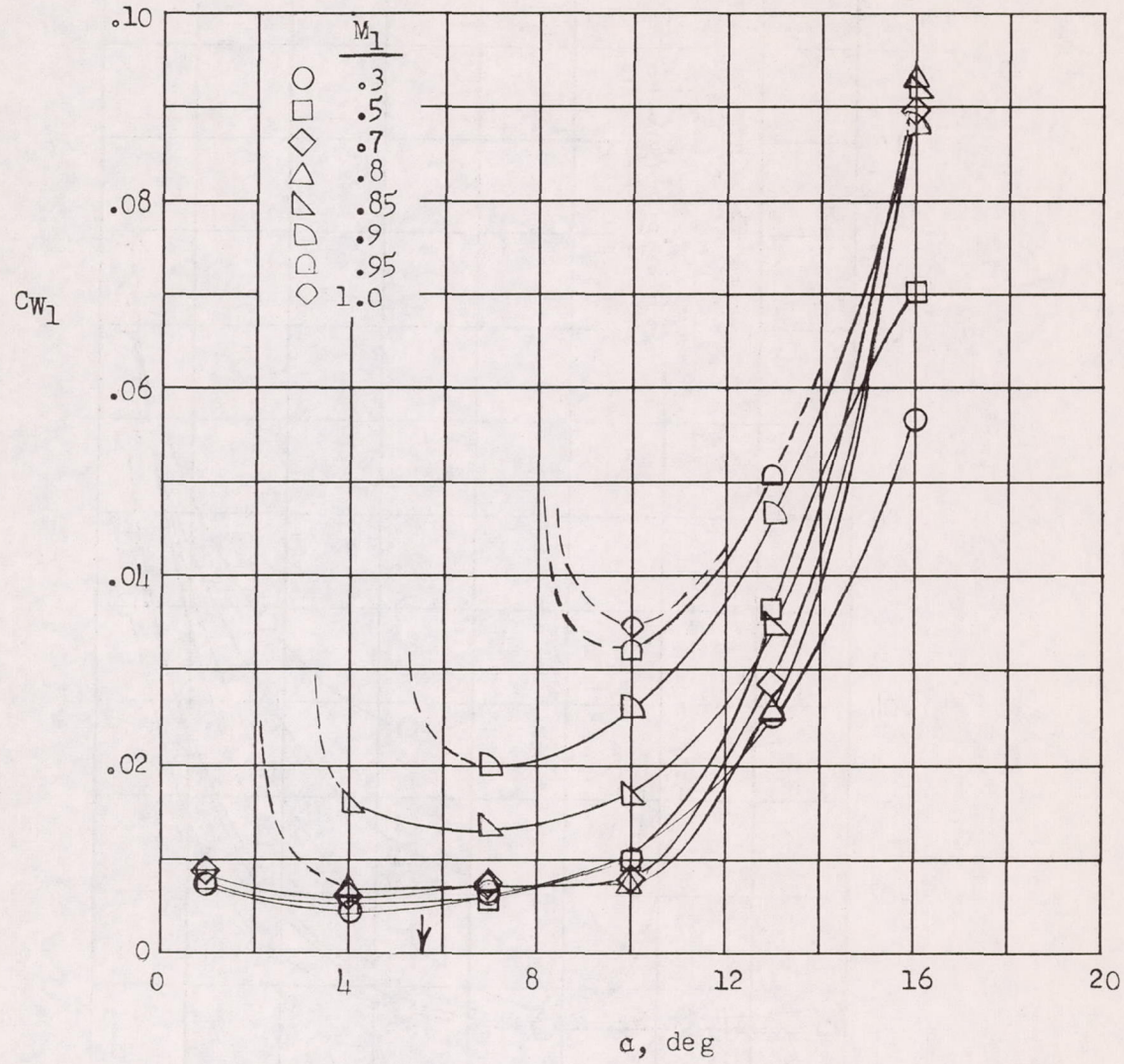



Figure 118.- Variation of momentum-loss coefficient with angle of attack at constant Mach number for cascade combination $\beta_1 - \alpha = 40.0^\circ$, $\sigma = 0.8$, and NACA 65-$(4A_{10})$06 blade section. Arrow shows low-speed design angle of attack.

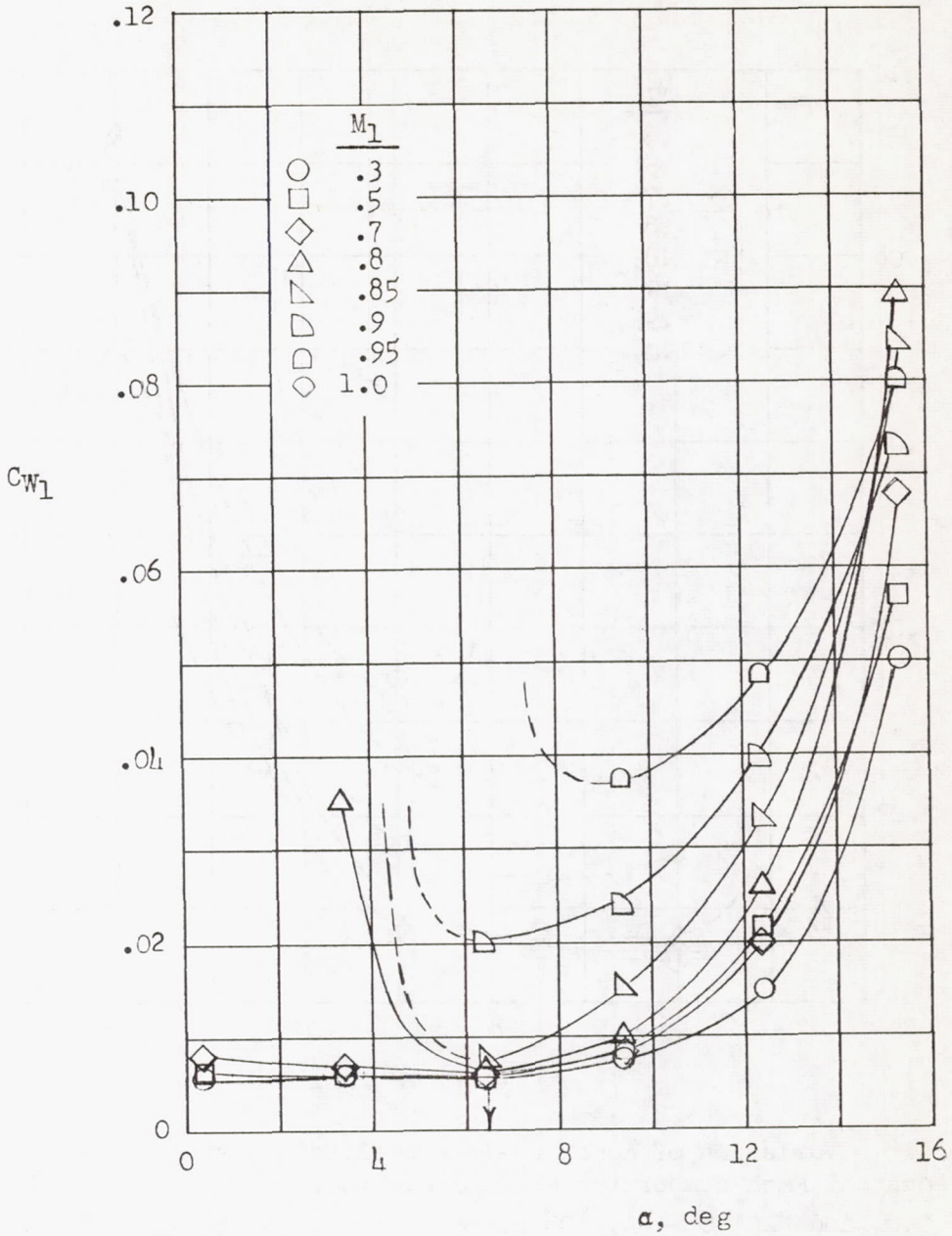



Figure 119.- Variation of momentum-loss coefficient with angle of attack at constant Mach number for cascade combination $\beta_1 - \alpha = 40.6^\circ$, $\sigma = 1.0$, and NACA 65-$\left(4A_{10}\right)$06 blade section. Arrow shows low-speed design angle of attack.

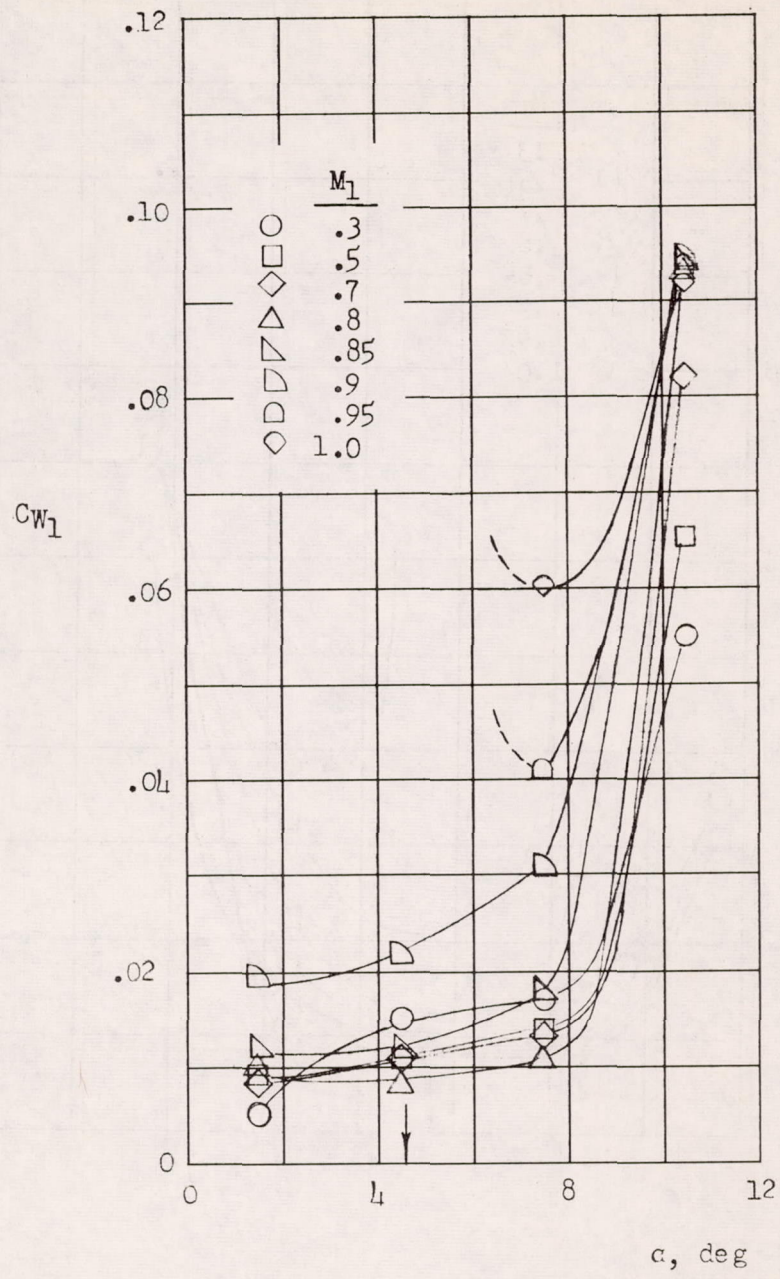



Figure 120.- Variation of momentum-loss coefficient with angle of attack at constant Mach number for cascade combination $\beta_1 - \alpha = 52.5^\circ$, $\sigma = 0.6$, and NACA 65-$\left(4A_{10}\right)$06 blade section. Arrow shows low-speed design angle of attack.

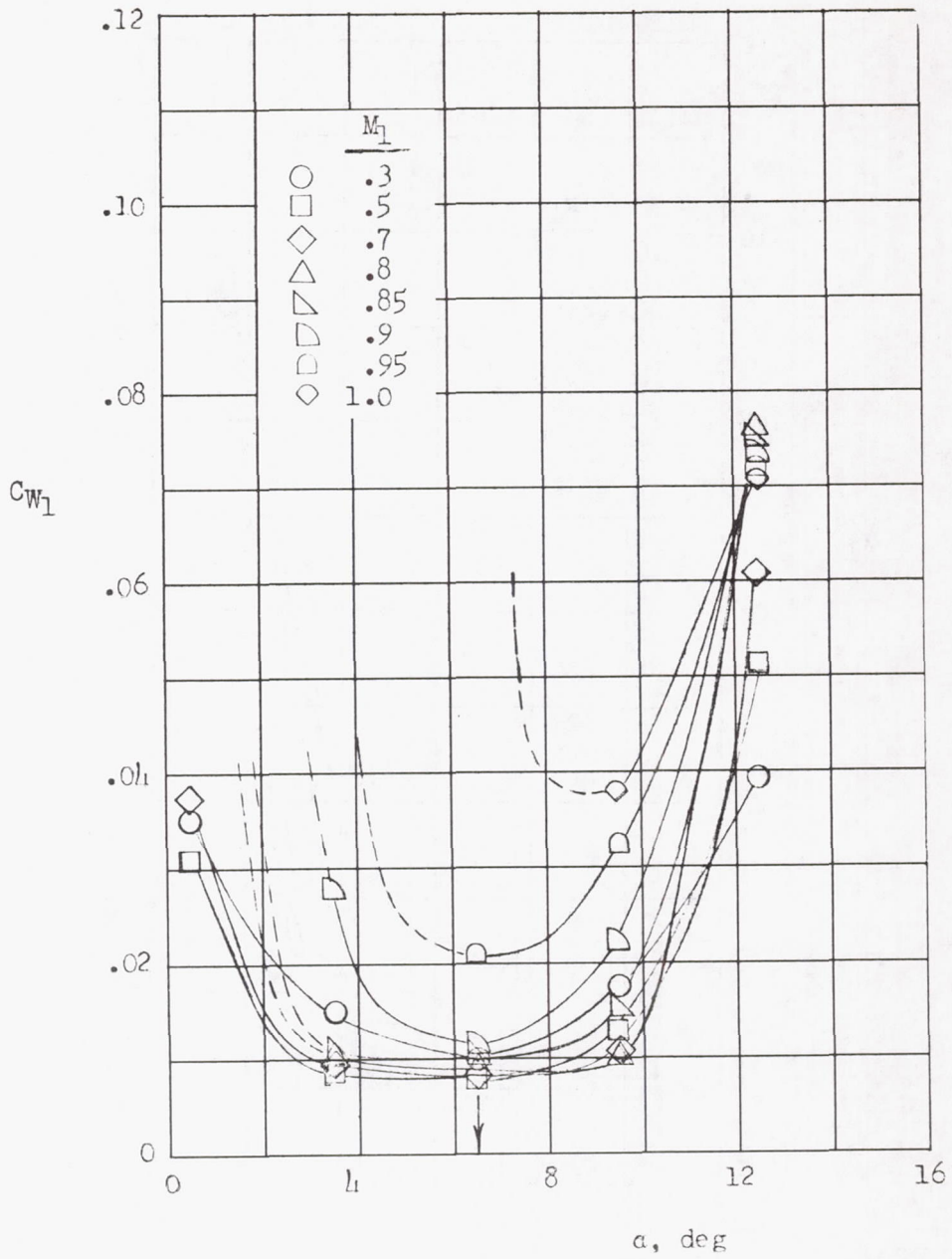



Figure 121.- Variation of momentum-loss coefficient with angle of attack at constant Mach number for cascade combination $\beta_1 - \alpha = 50.5^\circ$, $\sigma = 1.0$, and NACA 65-$\left(4A_{10}\right)$06 blade section. Arrow shows low-speed design angle of attack.

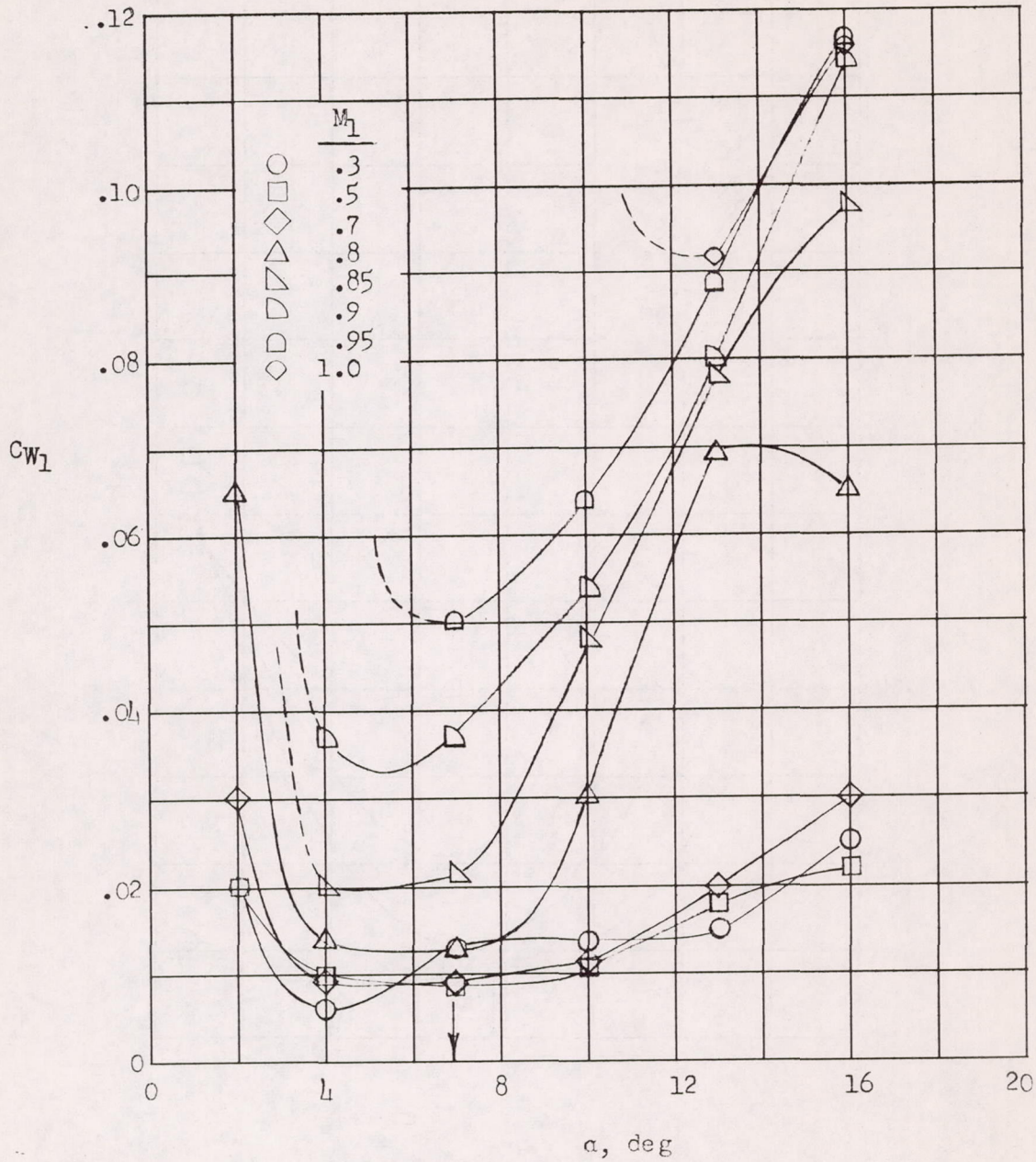



Figure 122.- Variation of momentum-loss coefficient with angle of attack at constant Mach number for cascade combination $\beta_1 - \alpha = 40.0^\circ$, $\sigma = 0.6$, and NACA 65-$(8A_{10})$06 blade section. Arrow shows low-speed design angle of attack.

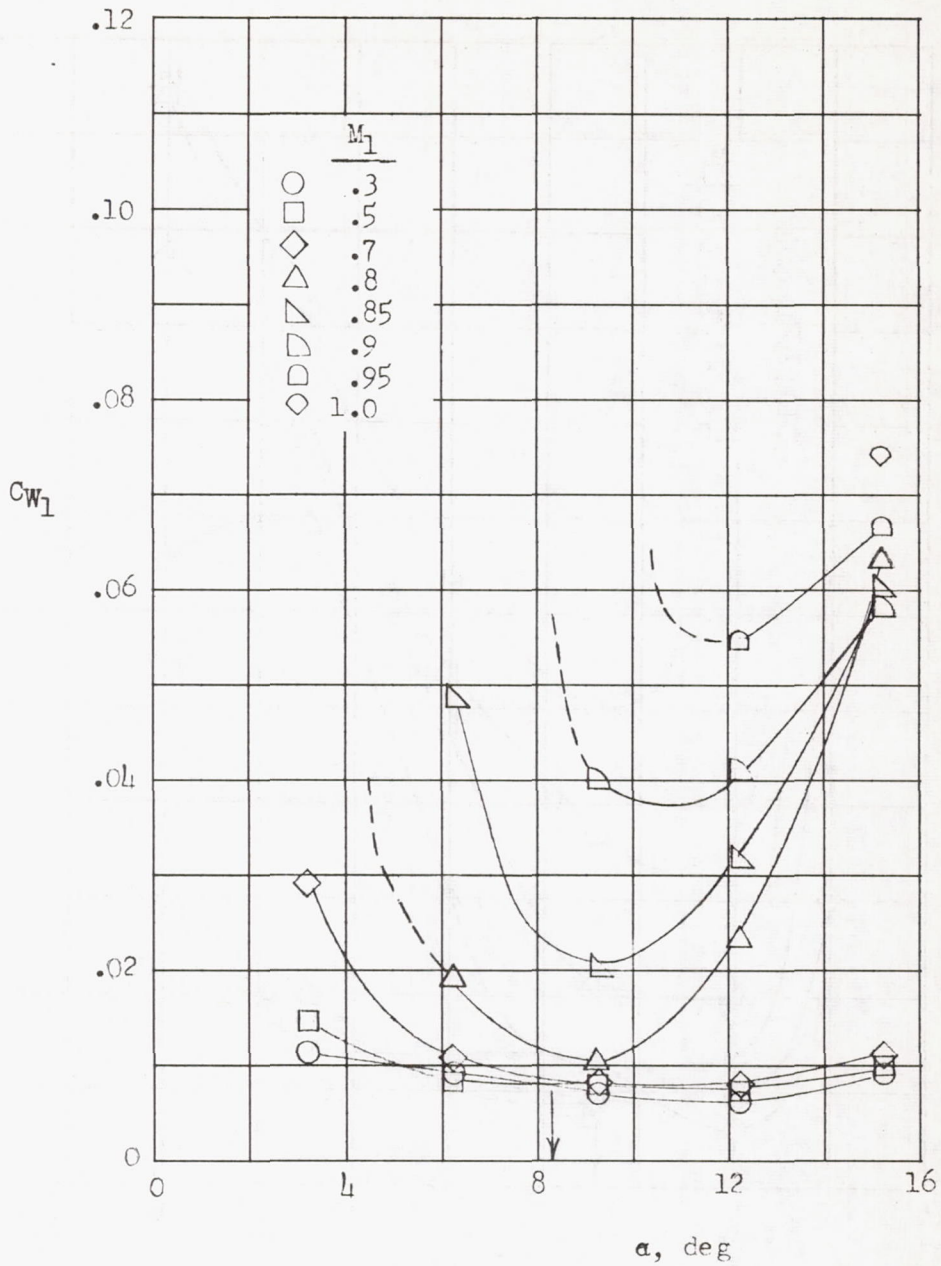



Figure 123.- Variation of momentum-loss coefficient with angle of attack at constant Mach number for cascade combination $\beta_1 - \alpha = 37.8^\circ$, $\sigma = 0.8$, and NACA 65-$(8A_{10})$06 blade section. Arrow shows low-speed design angle of attack.

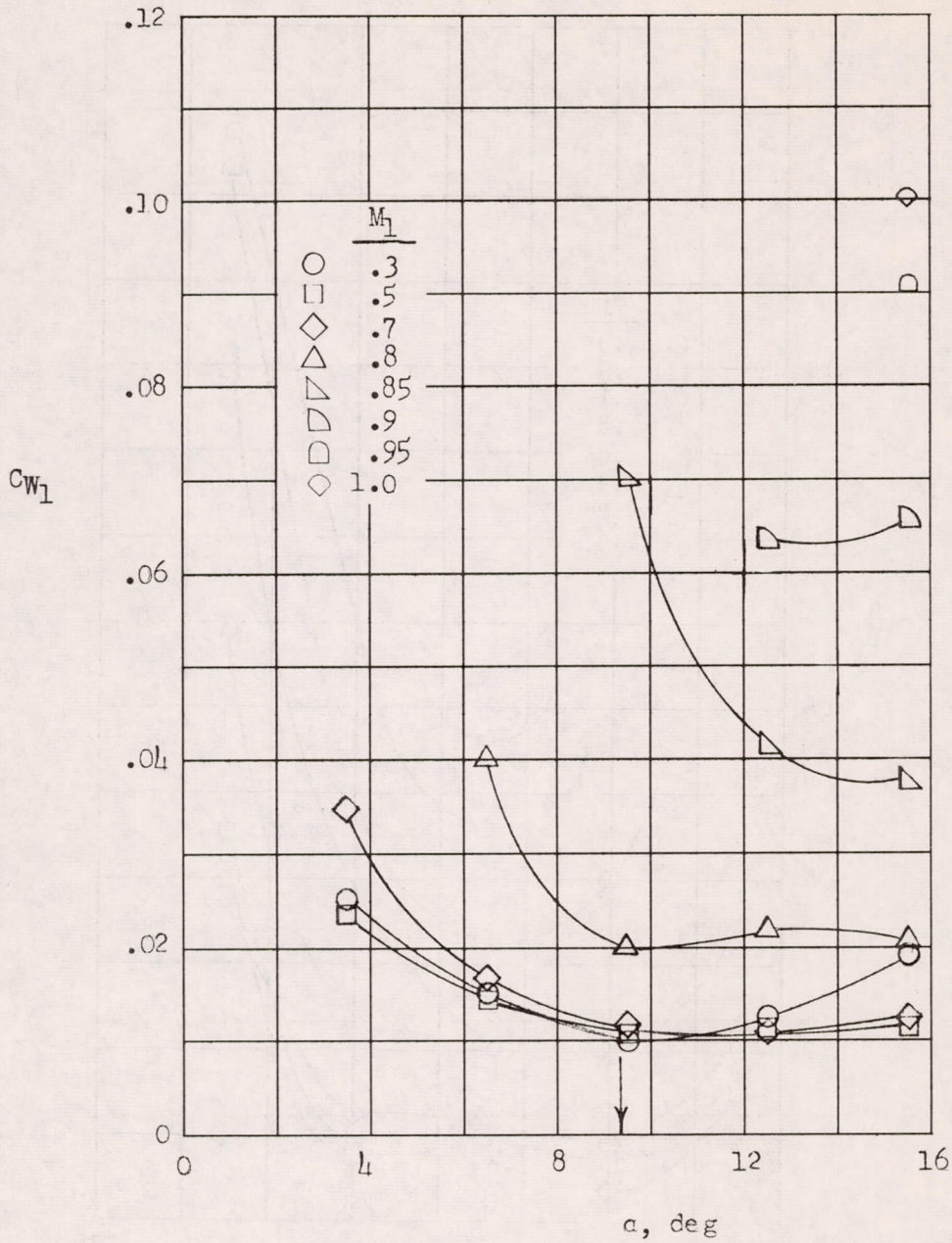



Figure 124.- Variation of momentum-loss coefficient with angle of attack at constant Mach number for cascade combination $\beta_1 - \alpha = 37.5^\circ$, $\sigma = 1.0$, and NACA 65-$(8A_{10})$06 blade section. Arrow shows low-speed design angle of attack.

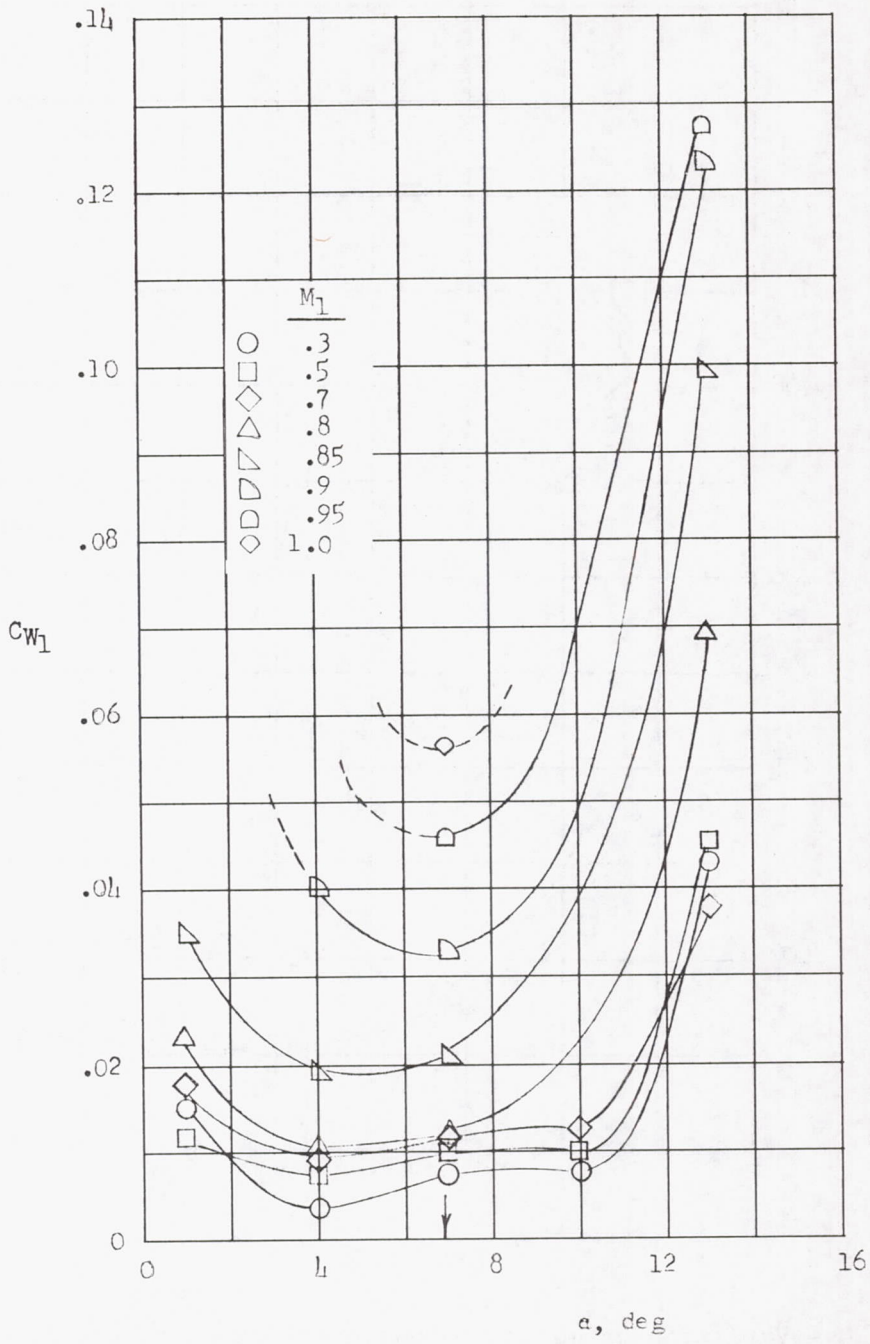



Figure 125.- Variation of momentum-loss coefficient with angle of attack at constant Mach number for cascade combination $\beta_1 - \alpha = 50.0^\circ$, $\sigma = 0.6$, and NACA 65-$(8A_{10})$06 blade section. Arrow shows low-speed design angle of attack.

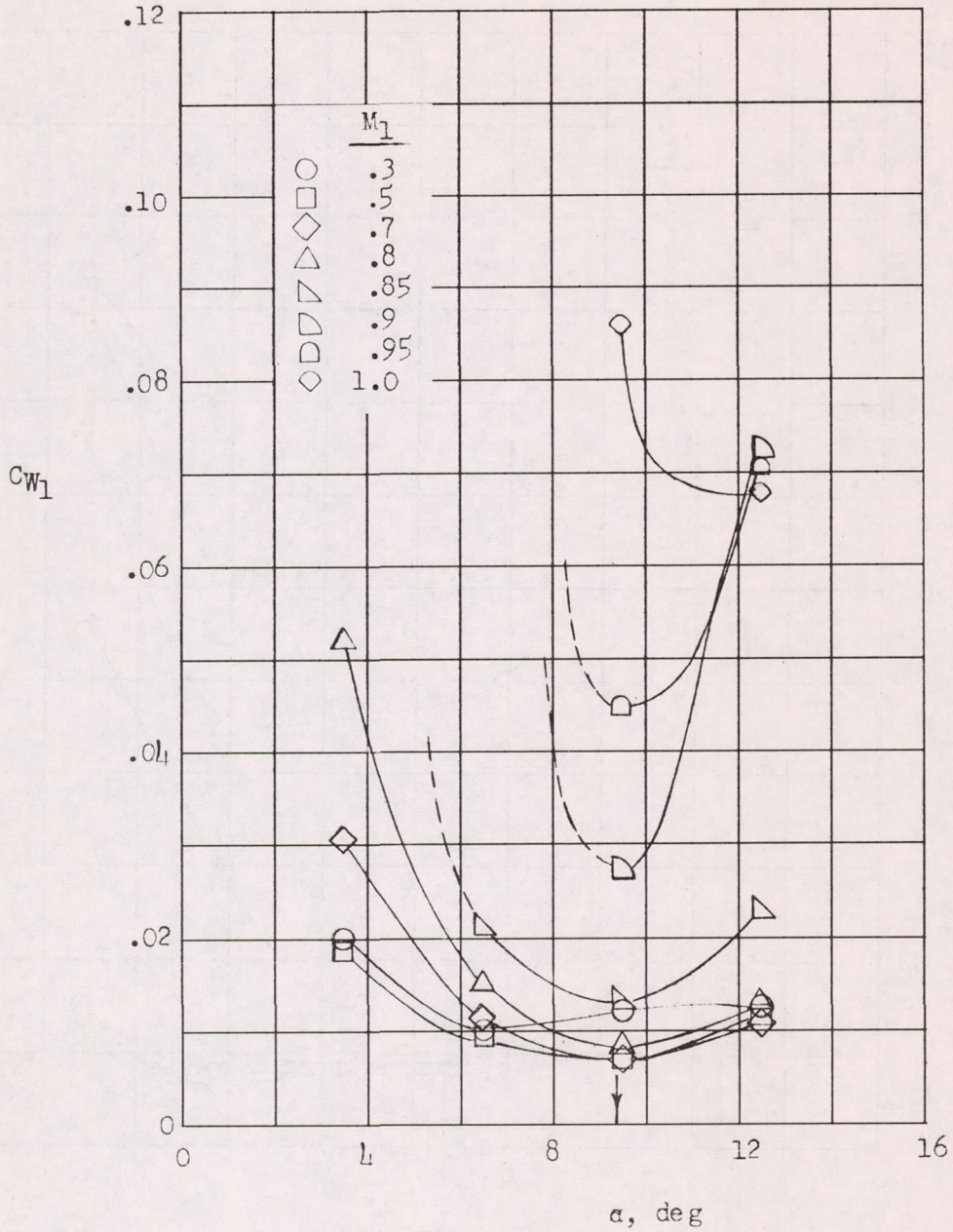



Figure 126.- Variation of momentum-loss coefficient with angle of attack at constant Mach number for cascade combination $\beta_1 - \alpha = 47.5^\circ$, $\sigma = 1.0$, and NACA 65-$(8A_{10})$06 blade section. Arrow shows low-speed design angle of attack.

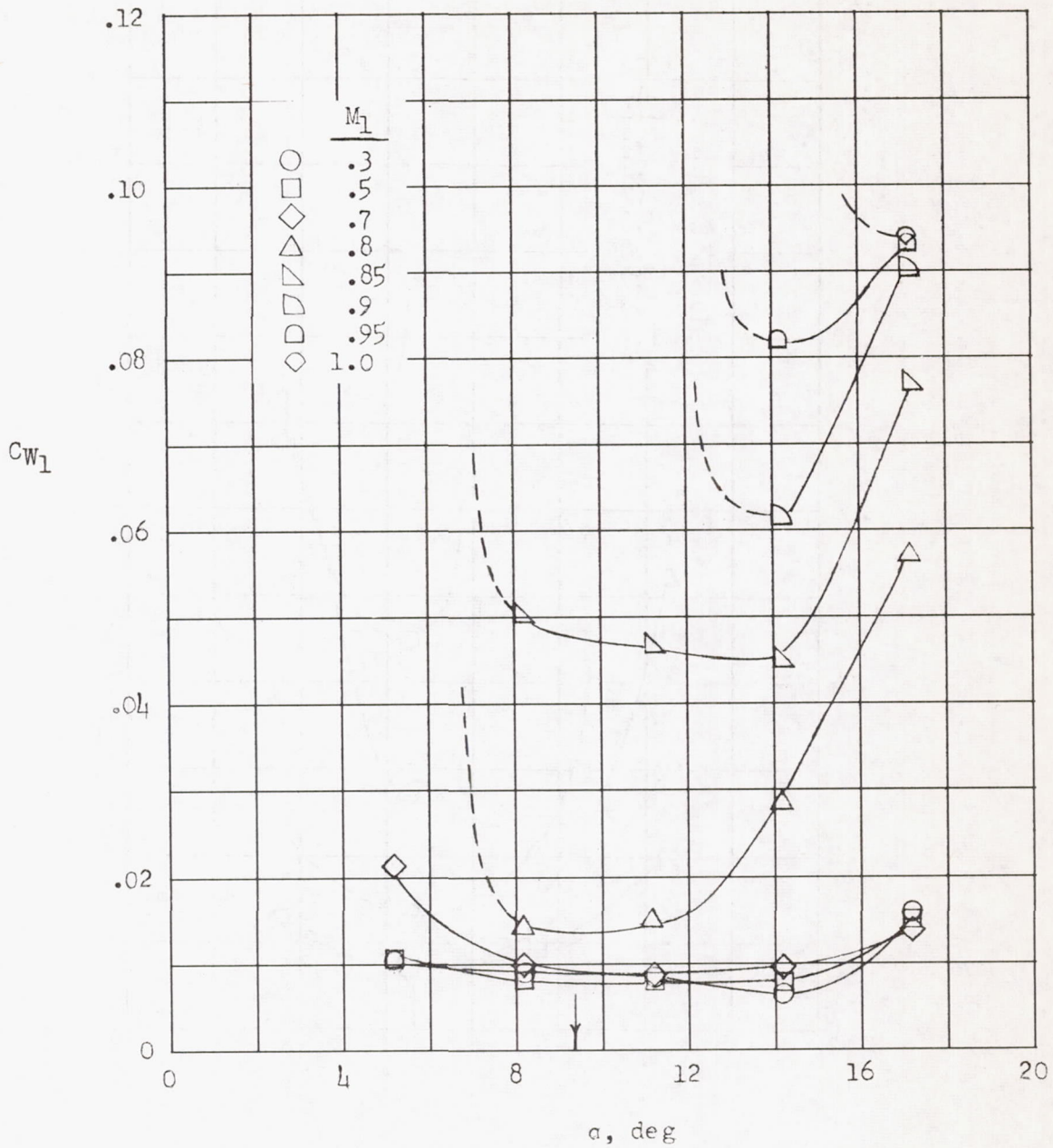



Figure 127.- Variation of momentum-loss coefficient with angle of attack at constant Mach number for cascade combination $\beta_1 - \alpha = 41.8^\circ$, $\sigma = 1.0$, and NACA 65-$(8A_{10})$10 blade section. Arrow shows low-speed design angle of attack.

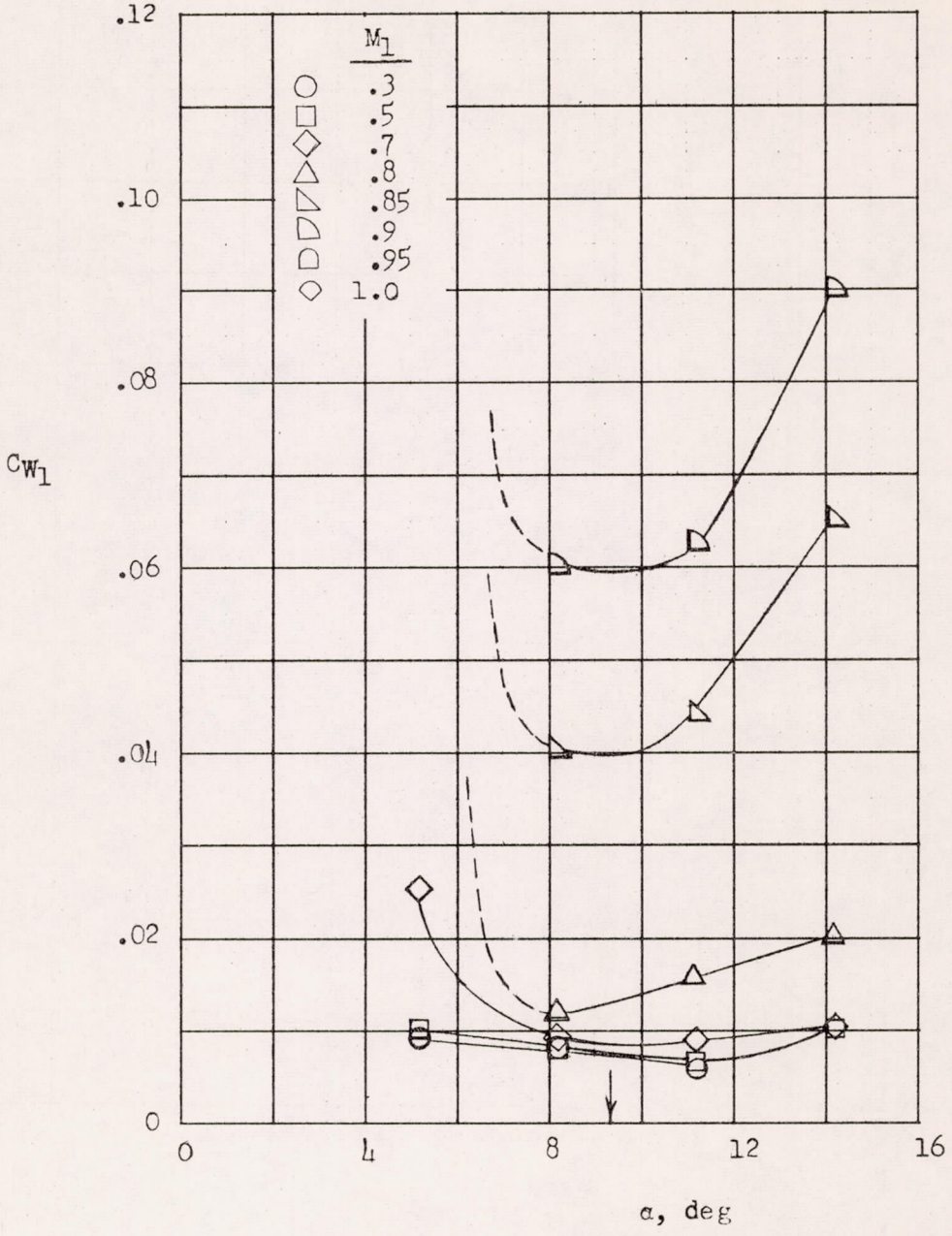



Figure 128.- Variation of momentum-loss coefficient with angle of attack at constant Mach number for cascade combination $\beta_1 - \alpha = 48.8^\circ$, $\sigma = 1.0$, and NACA 65-$\left(4A_{10}\right)$10 blade section. Arrow shows low-speed design angle of attack.